

**Spectroscopic and Photometric Analysis of White Dwarfs in
the Solar Neighbourhood**

by

Mairidgh Williamson O'Brien

Thesis

Submitted to the University of Warwick

for the degree of

Doctor of Philosophy

Department of Physics

June 2025

THE UNIVERSITY OF
WARWICK

Contents

| | |
|------------------------------------------------------|--------------|
| List of Tables | iv |
| List of Figures | vii |
| Acknowledgments | xviii |
| Declarations | xix |
| Abstract | xx |
| Abbreviations | xxi |
| Chapter 1 Introduction | 1 |
| 1.1 Discovery | 1 |
| 1.2 Formation | 2 |
| 1.3 Composition | 3 |
| 1.4 Cooling | 6 |
| 1.5 Spectral evolution | 13 |
| 1.6 Binarity | 13 |
| 1.7 Magnetism | 18 |
| 1.8 Planetary systems | 22 |
| 1.9 Volume samples and the Gaia revolution | 26 |
| 1.10 Thesis outline | 28 |
| Chapter 2 Methodology | 29 |
| 2.1 Observations | 29 |
| 2.1.1 Spectroscopy | 29 |
| 2.1.2 Photometry | 32 |
| 2.2 Models and fitting | 33 |
| 2.2.1 Codes and models | 33 |

| | | |
|------------------|----------------------------------------------------------------------------|-----------|
| 2.2.2 | Fitting | 34 |
| Chapter 3 | New observations of southern hemisphere white dwarfs within 40 pc | 37 |
| 3.1 | Introduction | 38 |
| 3.2 | Observations | 38 |
| 3.2.1 | Catalogue photometry and astrometry | 38 |
| 3.2.2 | Spectroscopy | 39 |
| 3.3 | Atmosphere and evolution models | 40 |
| 3.3.1 | Photometric parameters | 42 |
| 3.3.2 | Spectroscopic parameters | 42 |
| 3.3.3 | Combined spectroscopic and photometric parameters | 43 |
| 3.4 | Results | 43 |
| 3.4.1 | DA white dwarfs | 45 |
| 3.4.2 | Magnetic white dwarfs | 45 |
| 3.4.3 | DB white dwarfs | 53 |
| 3.4.4 | DC white dwarfs | 54 |
| 3.4.5 | DAZ white dwarfs | 55 |
| 3.4.6 | DZ and DZA white dwarfs | 55 |
| 3.4.7 | DQ white dwarfs | 57 |
| 3.4.8 | DQZ and DZQ white dwarfs | 59 |
| 3.4.9 | Main-sequence stars | 60 |
| 3.5 | Discussion | 60 |
| 3.5.1 | Comparison with the overall 40 pc sample | 60 |
| 3.5.2 | Metal-polluted DQ white dwarfs | 63 |
| 3.5.3 | WDJ2140-3637: A warm DQ white dwarf | 63 |
| 3.5.4 | Comparison of DA spectroscopic and photometric parameters | 64 |
| 3.6 | Conclusions | 67 |
| Chapter 4 | The <i>Gaia</i> 40 pc white dwarf sample | 68 |
| 4.1 | Introduction | 69 |
| 4.2 | The 40 pc sample | 70 |
| 4.2.1 | Correction to mass and effective temperature | 74 |
| 4.2.2 | White dwarfs with unreliable <i>Gaia</i> masses and temperatures | 85 |
| 4.2.3 | New spectroscopic observations | 85 |
| 4.2.4 | White dwarfs missing from the 40 pc spectroscopic sample | 89 |
| 4.2.5 | Spectroscopic biases | 90 |
| 4.3 | Discussion | 91 |
| 4.3.1 | Spectral evolution | 91 |

| | | |
|------------------|-----------------------------------------------------------------------------------------------------------------------------------------|------------|
| 4.3.2 | Mass distributions | 92 |
| 4.3.3 | Multiple-star systems containing white dwarfs | 93 |
| 4.3.4 | Space density | 100 |
| 4.3.5 | Multi-wavelength analysis | 102 |
| 4.3.6 | Magnetic white dwarfs | 103 |
| 4.3.7 | Metal-polluted white dwarfs | 109 |
| 4.3.8 | Gaia XP spectra | 109 |
| 4.4 | Conclusions | 111 |
| | | |
| Chapter 5 | Characterising planetary material accreted by cool helium atmosphere white dwarfs using an exponentially decaying disc model | 117 |
| 5.1 | Introduction | 118 |
| 5.2 | Observations and stellar modelling | 119 |
| 5.3 | Methods | 130 |
| 5.3.1 | Exponentially decaying disc model | 130 |
| 5.3.2 | Comparisons to solar system compositions | 133 |
| 5.4 | Results | 135 |
| 5.5 | Discussion | 141 |
| 5.5.1 | Interpretation of WDJ1927-0355 results | 141 |
| 5.5.2 | Interpretation of WDJ2141-3300 results | 142 |
| 5.5.3 | Comparison with constant accretion rate model | 142 |
| 5.5.4 | Future work | 145 |
| 5.6 | Conclusions | 148 |
| | | |
| Chapter 6 | Ultraviolet and optical spectroscopy of white dwarfs within 13 pc | 150 |
| 6.1 | Introduction | 151 |
| 6.2 | Observations | 152 |
| 6.3 | Model atmospheres and fitting | 157 |
| 6.4 | Results | 159 |
| 6.4.1 | Spectrophotometric fits incorporating UV | 159 |
| 6.4.2 | Fits to Balmer lines | 167 |
| 6.5 | Discussion | 168 |
| 6.6 | Future work | 172 |
| | | |
| Chapter 7 | Summary and Outlook | 175 |
| 7.1 | Conclusions | 175 |
| 7.2 | Future work | 177 |

List of Tables

| | | |
|-----|------------------------------------------------------------------------------------------------------------------------------------------------------------------------------------------------------------------------------------------------------------------------------------------------------------------------------------------------------------------------------------------------------------------------------------|----|
| 3.1 | Log of spectroscopic observations, where wavelength ranges are those used for analysis in this chapter. | 40 |
| 3.2 | Definitions of all white dwarf spectral types discussed in this work, where photometric model composition refers to composition-selected Gentile Fusillo et al. (2021) parameters. Adopted parameters for DAZ, DZ and DQ white dwarfs in this work use tailored models and are shown instead in Tables 3.6–3.8. | 41 |
| 3.3 | Spectral types and parameters of the white dwarf sample | 46 |
| 3.3 | Spectral types and parameters of the white dwarf sample (continued) | 47 |
| 3.3 | Spectral types and parameters of the white dwarf sample (continued) | 48 |
| 3.3 | Spectral types and parameters of the white dwarf sample (continued) | 49 |
| 3.3 | Spectral types and parameters of the white dwarf sample (continued) | 51 |
| 3.4 | Estimated magnetic field strengths for newly identified magnetic white dwarfs in the 40 pc sample | 52 |
| 3.5 | Atmospheric parameters and chemical abundances of DB white dwarfs, with fixed $\log(g)$ determined from photometric fitting. | 53 |
| 3.6 | Atmospheric parameters and chemical abundances of newly observed DAZ white dwarfs, where T_{eff} and $\log(g)$ have been determined from a combination of spectroscopic and photometric fitting. | 55 |
| 3.7 | Atmospheric best-fit parameters and chemical abundances of DZ and DZA white dwarfs, where T_{eff} and $\log(g)$ have been determined from a combination of spectroscopic and photometric fitting. Weakly magnetic DZH and DZAH were also fitted. Upper table: Best-fit parameters for white dwarfs with He-dominated atmospheres. Lower table: Best-fit parameters for white dwarfs with H-dominated atmospheres. | 58 |

| | | |
|------|-------------------------------------------------------------------------------------------------------------------------------------------------------------------------------------------------------------------------------------------------------------------------------------------------------------------------------------------------------------------------------------------------------------------------------------------------------------------------------------------------------------------------|-----|
| 3.8 | Atmospheric parameters and chemical abundances of DQ, DQZ and DZQ white dwarfs. T_{eff} and $\log(g)$ were determined from iterative spectroscopic and photometric fitting. The warm DQ WD J2140–3637 is not included here, as it was assumed to have a C-dominated atmosphere when fitting, rather than a He-dominated atmosphere (see Section 3.5.3). | 59 |
| 4.1 | Format of the online 40 pc catalogue, which is accessible at: https://cygnus.astro.warwick.ac.uk/phrtxn/ | 75 |
| 4.2 | White dwarf candidates within 40 pc in the Gentile Fusillo et al. (2021) DR3 catalogue that do not have spectroscopic follow-up. | 77 |
| 4.3 | Confirmed white dwarfs and candidates in the Gentile Fusillo et al. (2021) DR3 catalogue that are within $1\sigma_{\varpi}$ of 40 pc. | 78 |
| 4.4 | White dwarfs within 40 pc that are not in the Gentile Fusillo et al. (2021) DR3 catalogue. | 79 |
| 4.5 | White dwarfs within 40 pc with unreliable <i>Gaia</i> parameters. Best-fit parameters are instead taken from literature. | 80 |
| 4.6 | All white dwarf spectral types listed in the 40 pc sample, where photometric model composition refers to composition-selected Gentile Fusillo et al. (2021) parameters. Spectral types ending with H (Zeeman splitting) or P (polarised) imply magnetism, which does not impact atmospheric composition. In all cases other than for DA and DAH/P, (H/P) were added to spectral types to note that some white dwarfs in that group are magnetic. The lowercase ‘e’ indicates the presence of emission features. | 81 |
| 4.7 | White dwarfs within 40 pc confirmed in this work with spectroscopic follow-up. | 87 |
| 4.8 | Known white dwarfs within 40 pc with new spectroscopic follow-up and updated spectral types. | 88 |
| 4.9 | Double white dwarf binaries with <i>Gaia</i> astrometric periods. | 99 |
| 4.10 | Abundances and upper limits of elements determined from combined fitting of spectra and photometry of newly observed DAZ, DZ, and DQ white dwarfs with Koester (2010) models. | 116 |
| 5.1 | Keck HIRES observation details. | 120 |
| 5.2 | Abundances and upper limits of elements determined from combined fitting of the spectra and photometry of the two DZA white dwarfs with Koester (2010) models. * indicates that the abundance was fixed, not measured. Distances were determined from inverting <i>Gaia</i> DR3 parallaxes, and distance errors incorporated the <i>Gaia</i> astrometric excess noise. | 128 |

| | | |
|-----|----------------------------------------------------------------------------------------------------------------------------------------------------------------------------------------------------------------------------------------------------------------------------------------------------------------------------------------------------------------------------------------------------------------------------------------------------------------------------------------------------------------------------------------------------------|-----|
| 5.3 | Gravitational settling times and masses of heavy elements in the convection zone for WD J1927–0355 and WD J2141–3300, for the models with overshoot. The total mass of heavy elements (i.e. excluding hydrogen) detected in the convection zone is 6.15×10^{21} g for WD J1927–0355 and 1.23×10^{22} g for WD J2141–3300. The * indicates that the hydrogen abundance was fixed at $\log(\text{H}/\text{He}) = -3.5$ | 129 |
| 5.4 | Minimum χ^2_{ν} for solar system abundances compared to the abundances and upper limits of elements in WD J1927–0355 and WD J2141–3300 propagated through the Jura et al. (2009) model. | 135 |
| 6.1 | Details of all spectroscopic observations of white dwarfs within 13 pc that have been analysed in this work. Optical spectroscopy used for fitting in this work is also listed. Distances were determined using <i>Gaia</i> parallaxes in all cases except where indicated by ‡, which were instead taken from Altena et al. (1995). | 154 |
| 6.1 | (continued). Details of all spectroscopic observations of white dwarfs within 13 pc that have been analysed in this work. Optical spectroscopy used for fitting in this work is also listed. Distances were determined using <i>Gaia</i> parallaxes in all cases except where indicated by ‡, which were instead taken from van Altena et al. (1995). | 155 |
| 6.2 | Details of all white dwarfs within 13 pc of the Sun that are part of a multiple-star system. Projected separations were calculated in most cases using <i>Gaia</i> DR3 data, aside from those binaries that are unresolved in <i>Gaia</i> . A colon symbol indicates that the spectral type of the star has not been confirmed. For higher-order systems (triple or quadruple) the periods separated by semicolons are the innermost to outermost periods for the hierarchical system. | 156 |
| 6.3 | Radial velocities of interstellar lines observed in high-resolution <i>HST</i> spectra of 13 pc white dwarfs. | 160 |
| 6.4 | Best-fit parameters for H-atmosphere white dwarfs within 13 pc of the Sun. A fit with UV refers to hybrid spectrophotometric parameters for white dwarfs observed with <i>HST</i> STIS or COS. DD indicates unresolved double degenerate. Symbols indicate the photometry used for the fit. No symbol indicates <i>Gaia</i> , 2MASS and WISE. * indicates <i>Gaia</i> and 2MASS. † indicates <i>Gaia</i> only. ‡ indicates <i>BVRI</i> + 2MASS photometry. § indicates no photometry was used in the fit. Any metal features were masked for these fits. | 161 |

List of Figures

| | | |
|-----|----------------------------------------------------------------------------------------------------------------------------------------------------------------------------------------------------------------------------------------------------------------------------------------------------------------------------------------------------------------------------------------------------------------------------------------------------------------------------------|----|
| 1.1 | An HR diagram with grey datapoints from <i>Gaia</i> DR3. In black is a MESA Isochrones and Stellar Tracks (MIST) stellar evolutionary track for a $1.5 M_{\odot}$ star, from the moment it leaves the main sequence until it reaches the white dwarf cooling track. The MIST models were computed with the Modules for Experiments in Stellar Astrophysics (MESA) code (Choi et al., 2016; Dotter, 2016). | 4 |
| 1.2 | The chemical profile of a typical 12 000 K, $0.6 M_{\odot}$ white dwarf with a hydrogen-dominated atmosphere, where $\log(q) = 0$ corresponds to the centre of the white dwarf, with the surface towards the right. The parameter $\log(q) = \log(1 - m(r)/M_*)$ represents the fraction of the mass that is outside a radius r . $X(Z)$ represents the abundance of element Z in the white dwarf. Reproduced from Saumon et al. (2022) with data provided by A. Bédard. . . | 7 |
| 1.3 | VLT X-shooter and SOAR <i>Goodman</i> spectra of various white dwarf spectral types. The spectra have been offset from each other vertically for clarity. The absorption line labels represent the following elements: blue: H, green: He, red: C, orange: Ca. The example DZ only shows Ca II H+K absorption lines as these are typically the strongest metal lines in optical spectra. . . . | 8 |
| 1.4 | Major contributors to the overall opacity of a hydrogen-atmosphere white dwarf, with parameters $\log(g) = 8$ and $T_{\text{eff}} = 4000$ K (upper) and $T_{\text{eff}} = 12\,000$ K (lower). Minor contributions to the total opacity are not shown. Adapted from Saumon et al. (2022), using models provided by P.-E. Tremblay. . . . | 9 |
| 1.5 | The relative luminosity resulting from neutrino emission (L_{ν}) compared to photon emission (L_{γ}) as a function of white dwarf effective temperature. Reproduced from Saumon et al. (2022) with data provided by A. Bédard. . . | 10 |

| | | |
|------|------------------------------------------------------------------------------------------------------------------------------------------------------------------------------------------------------------------------------------------------------------------------------------------------------------------------------------------------------------------------------------------------------------------------------------------------------------------------------------------------------------------------------------------------------------------------------------------------------------------------------------------------------------------------------------------------------------------------------------------------------------------------------------------------------------------------------------------------------------------------------|----|
| 1.6 | Effective temperature (T_{eff}) against surface gravity ($\log(g)$) for DA white dwarfs within 40 pc, which are shown in grey. Known ZZ Ceti pulsating white dwarfs are shown in black. The red and blue dashed lines represent the boundaries of the hydrogen-atmosphere white dwarf instability strip (Tremblay et al., 2015). | 11 |
| 1.7 | A simplified schematic showing the evolution of a white dwarf with an initially He-rich atmosphere. This figure was inspired by a similar figure in Bédard (2024). | 14 |
| 1.8 | Examples of double white dwarf binaries within 40 pc that have been detected using different methods: spectroscopic (radial velocities), proper motion anomaly, and common proper motion. The dashed line is the <i>Gaia</i> resolution as a function of distance. | 17 |
| 1.9 | VLT X-shooter and WHT ISIS spectra of magnetic hydrogen atmosphere white dwarfs (DAH) of various field strengths. Wavelengths of Balmer lines are indicated by blue lines. Spectra are not flux-calibrated, and have been vertically offset for visual clarity. | 19 |
| 1.10 | A spaghetti diagram showing the Zeeman splitting of $H\alpha$ and $H\beta$ spectral lines in a magnetic white dwarf, depending on the field strength, $\log(B)$, of the white dwarf. Data are from Friedrich et al. (1996). | 20 |
| 1.11 | The fraction of all known polluted white dwarfs with a given number of metals, correct as of Feb. 2025. Data provided by J. T. Williams. | 24 |
| 1.12 | The difference between a magnitude-limited and volume-limited sample of white dwarfs, where both samples were selected from Gentile Fusillo et al. (2021). The volume-limited sample contains all white dwarfs with parallaxes greater than 25 mas, corresponding to the 40 pc volume. The magnitude cut at $G < 16.25$ was chosen to create a magnitude-limited sample with the same number of white dwarf candidates as in the 40 pc sample (≈ 1100), given an additional cut of white dwarf probability > 0.75 (Gentile Fusillo et al., 2021). Cooling ages, τ , were calculated with models from Bédard et al. (2020), assuming a pure-H composition in all cases, as not all white dwarfs in the magnitude-limited sample have been observed spectroscopically. This figure was inspired by a similar figure in Bagnulo and Landstreet (2022). | 27 |

| | | |
|-----|----------------------------------------------------------------------------------------------------------------------------------------------------------------------------------------------------------------------------------------------------------------------------------------------------------------------------------------------------------------------------------------------------------------------------------------------------------------------------------------------------------------------------------------------------|----|
| 2.1 | Demonstration of how model DA white dwarf spectra vary as T_{eff} and $\log(g)$ are varied. Top: Model spectra with $\log(g)$ fixed at 8, and T_{eff} varying from 4000 K to 6500 K. Cool white dwarfs are the primary focus of this thesis, which is why they are shown here. Bottom: Model spectra with T_{eff} fixed at 6500 K, and $\log(g)$ varying from 7 to 9. | 35 |
| 3.1 | $\log(g)$ against T_{eff} distribution for white dwarfs within 40 pc that have been spectroscopically observed in this work, where parameters have been determined by fitting <i>Gaia</i> DR3 photometry. Magnetic stellar remnants have black contours. Data are colour- and symbol-coded by their primary spectral type classification only, for simplicity. | 44 |
| 3.2 | Spectroscopic fits to the normalised Balmer lines for the DAe white dwarf WDJ1653–1001. | 50 |
| 3.3 | Simultaneous fits of spectroscopy and photometry for three metal-rich DZ and DZA white dwarfs: WDJ0808–5300 (left panels), WDJ1935–3252 (middle panels) and WDJ2236–5549 (right panels). The top row of panels compare the best fit models to normalised spectroscopic observations. The spectroscopic observations were re-calibrated onto the models but are still in physical flux units. The bottom panels compare the best fit models to catalogue photometry over a wider wavelength range than the available spectroscopy provides. | 57 |
| 3.4 | A <i>Gaia</i> DR3 HR diagram for the spectroscopic 40 pc sample of 1058 white dwarfs. Magnetic stellar remnants have black contours. Data are colour- and symbol-coded by their primary spectral type classification only, for simplicity. | 61 |
| 3.5 | Incidence of different atmospheric compositions between a sample of 179 X-shooter observations (dark blue) presented in this work, and the full 40 pc sample not including X-shooter observations (light blue). The bars from left to right represent white dwarfs with trace metals in their atmospheres, carbon in their atmospheres, and magnetic white dwarfs. | 62 |
| 3.6 | X-shooter spectrum of WDJ2140–3637 plotted with the combined photometric and spectroscopic fit using Koester (2010) models. The O I absorption features around 7775 Å and 8446 Å are highlighted with ticks. The spectrum was convolved by a Gaussian with a FWHM of 1 Å and shifted by 45 km/s. An inset plot shows the region around the oxygen absorption features without the overplotted model. | 65 |

| | | |
|-----|--------------------------------------------------------------------------------------------------------------------------------------------------------------------------------------------------------------------------------------------------------------------------------------------------------------------------------------------------------------------------------------------------------------------------------------------------------------------------------------------------------------------------------------------------------------------------------------------------------------------------------------------------------------------------------------------------------------------------------|----|
| 3.7 | Differences between <i>Gaia</i> photometric (<i>Photo</i>) and X-shooter spectroscopic (<i>Spectro</i>) T_{eff} (top panel) and $\log(g)$ (bottom panel) for DA white dwarfs, against <i>Gaia</i> photometric T_{eff} (Gentile Fusillo et al., 2021). The spectroscopic fitting method is described in Section 3.3.2. | 66 |
| 4.1 | A <i>Gaia</i> HR diagram showing all spectroscopically confirmed white dwarfs within 40 pc that are in the Gentile Fusillo et al. (2021) catalogue. Confirmed white dwarfs that have unreliable masses determined from <i>Gaia</i> photometry and astrometry are shown as orange diamonds. The remaining unobserved candidates from Gentile Fusillo et al. (2021) are shown as blue squares. The orange line indicates pure-He cooling tracks, the black line indicates pure-H cooling tracks and the blue line indicates mixed H/He = 10^{-5} cooling tracks for a $0.6 M_{\odot}$ white dwarf. The black dashed lines indicate where 7000 K (upper line) and 5000 K (lower line) white dwarfs sit on the cooling tracks. . | 72 |
| 4.2 | The mass distribution of white dwarfs in the 40 pc sample determined from <i>Gaia</i> photometry. Also shown is the mass distribution of simulated white dwarfs, with estimated observational errors drawn from a normal distribution with $\mu = 0$ and $\sigma = 0.02 M_{\odot}$, taken from Cunningham et al. (2024). Double-degenerate candidates have been removed from the observational distribution. Upper panel: white dwarfs with T_{eff} below 6000 K; lower panel: white dwarfs with T_{eff} above 6000 K. | 76 |
| 4.3 | The effect of using pure-H atmosphere models where the Ly α red wing opacity of Kowalski and Saumon (2006) has been multiplied by a factor of 5, on the resulting white dwarf <i>Gaia</i> mass and T_{eff} , for objects with $T_{\text{eff}} < 10\,000$ K. The dashed black line shows the median mass before the model corrections, and the solid blue line shows the median mass after these corrections. The corrections were only applied to white dwarfs with H-rich or assumed H-rich compositions. | 82 |
| 4.4 | Corrected <i>Gaia</i> mass and T_{eff} for all 40 pc white dwarfs below 6000 K (red points) with the ad-hoc mass correction presented in this work, compared to the original mass distribution (grey points). The dashed black line shows the median mass before the mass and T_{eff} corrections, and the solid blue line shows the median mass after these corrections. The median mass in the stable range of $13\,000 > T_{\text{eff}} > 8000$ K was used as a reference for the correction. | 84 |

| | | |
|------|---------------------------------------------------------------------------------------------------------------------------------------------------------------------------------------------------------------------------------------------------------------------------------------------------------------------------------------------------------------------------------------------------------------------------------------------------------------------------------------------------------------------------------|----|
| 4.5 | Corrected <i>Gaia</i> mass and T_{eff} for all 40 pc white dwarfs, where spectral type is indicated by the shape and colour of points. For white dwarfs with unreliable <i>Gaia</i> atmospheric parameters, parameters from Table 4.5 were plotted instead. The average statistical error is shown by the black point on the lower right. More complex spectral types have been simplified to only their most prominent features. | 90 |
| 4.6 | The fractional distribution of He-atmosphere white dwarfs compared to the full 40 pc white dwarf sample. Horizontal error bars represent T_{eff} bins and vertical error bars show the uncertainty of the frequency of the occurrence of He-atmosphere white dwarfs within each bin. | 92 |
| 4.7 | The mass distribution of white dwarfs in the 40 pc sample compared to the published masses from the 100 pc SDSS sample of Kilic et al. (2020b). The mass correction outlined in Section 4.2.1 was applied to the 40 pc parameters. The solid black line represents the bimodal best-fitting Gaussians to the 40 pc mass distribution. | 94 |
| 4.8 | Tangential velocity differences as a function of projected separation for <i>Gaia</i> DR3 sources that are common proper motion companions to white dwarfs in the 40 pc sample. The black dashed line indicates the maximum tangential velocity difference for a binary with $1.4 M_{\odot} + 2.5 M_{\odot}$ stars on a circular orbit. WD+WD systems are shown in dark blue, WD+MS systems are shown in red, and any type of triple or quadruple system containing at least one white dwarf is shown in light blue. | 97 |
| 4.9 | A <i>Gaia</i> HR diagram showing all spectroscopically confirmed white dwarfs within 40 pc as light blue points, alongside all other <i>Gaia</i> sources in the same volume which have <code>parallax_over_error</code> > 1 and <code>astrometric_excess_noise</code> < 1.5 from <i>Gaia</i> DR3 as grey points. White dwarfs in unresolved binaries with main-sequence companions that are not in the Gentile Fusillo et al. (2021) catalogue are shown as red points. Candidate double white dwarfs are in dark blue. | 98 |
| 4.10 | The space density of white dwarfs according to the Galactic simulation presented in this work, as a function of the distance to the Sun, compared to the observed space density from the 40 pc sample. The simulation has been normalised at both 20 pc and 40 pc separately. The filled regions represent an error of 1σ on the numbers of white dwarfs. $N_{\text{WD,Sim}}$ is the number of simulated white dwarfs, and $N_{\text{WD,Obs}}$ is the number of observed white dwarfs. 101 | |

| | | |
|------|----------------------------------------------------------------------------------------------------------------------------------------------------------------------------------------------------------------------------------------------------------------------------------------------------------------------------------------------------------------------------------------------------------------------------------------------------------------------------------------------------------------------------------------------------------------------------------------------------------------------------------------------------------------------------------------------------------------------------------|-----|
| 4.11 | HR diagrams for the 40 pc white dwarf sample. Top: H-atmosphere white dwarfs are in grey, He-atmosphere white dwarfs are in blue, and cool DC white dwarfs with unconstrained composition are in green. Middle: DQ white dwarfs are in red and the rest of the sample is in grey. Bottom: DZ white dwarfs are in purple and the rest of the sample is in grey. In all panels, the black lines indicate pure-H cooling tracks, the red lines indicate mixed H/He = 10^{-5} , and the purple lines indicate mixed C/He cooling tracks with varying initial C mass fractions in the envelope of the PG 1159 star (0.2, 0.4 and 0.6; see Blouin et al. 2023a). In all cases, tracks are for a $0.6 M_{\odot}$ white dwarf. | 104 |
| 4.12 | The mass distribution of magnetic (dark blue) and non-magnetic (light blue) white dwarfs within 40 pc. Top: White dwarfs younger than 2 Gyr. Bottom: White dwarfs older than 2 Gyr. | 105 |
| 4.13 | Frequency of magnetic white dwarfs as a function of mass for white dwarfs within 40 pc with $T_{\text{eff}} > 5000$ K, for H-dominated atmospheres (light blue) and for all spectral types (dark blue). Horizontal error bars represent mass bins and vertical error bars show the uncertainty of the frequency of the occurrence of magnetic fields within each bin. | 106 |
| 4.14 | Fractional cumulative frequency of magnetic white dwarfs as a function of cooling age for corrected masses between $0.49 M_{\odot}$ and $0.8 M_{\odot}$, for all white dwarfs within 40 pc that have H-dominated atmospheres (light blue) and all white dwarfs within 40 pc (dark blue). τ indicates the cooling age of the white dwarf. Cooling ages were derived using updated STELUM evolutionary models (Bédard et al., 2022b; Elms et al., 2023), and the filled regions cover 1σ uncertainty. The black line indicates the cooling age of the onset of crystallisation for core oxygen mass fraction $X(\text{O}) = 0.8$ for a white dwarf with a mass of $0.8 M_{\odot}$ | 107 |
| 4.15 | The fraction of metal-polluted white dwarfs in the 40 pc sample with different numbers of polluting metals. Data for this figure have been compiled from Williams et al. (2024). | 110 |
| 4.16 | Photometry calculated using <i>Gaia</i> XP spectrophotometry in SDSS <i>u</i> and <i>g</i> bands, which we distinguish from catalogue SDSS photometry with a prime symbol. H-atmosphere white dwarfs are shown in grey, and He-atmosphere white dwarfs are in blue. Unconfirmed candidates are in red. The blue line indicates pure-He cooling tracks, the black line indicates pure-H cooling tracks and the red line indicates mixed H/He = 10^{-5} cooling tracks for a $0.6 M_{\odot}$ white dwarf. | 112 |

| | | |
|------|----------------------------------------------------------------------------------------------------------------------------------------------------------------------------------------------------------------------------------------------------------------------------------------------------------------------------------------------------------------------------------------------------------------------------------------------------------------------------------------------------------------------------------------------------------------------------------------------------------------------------------------------------------------------------------------------------------------------------------------------------------------------------------------------------------------------------------------|-----|
| 4.17 | Comparison of catalogue SDSS photometry (u and g) to photometry calculated using <i>Gaia</i> XP spectra in SDSS bands (u' and g'). The difference is shown as a function of apparent SDSS g -magnitude. | 113 |
| 5.1 | Combined, echelle-order-merged, blue portions of the HIRES spectra of WD J1927–0355 (top) and WD J2141–3300 (bottom). The continua and slopes of the spectra are not well flux calibrated, and therefore the spectra do not accurately depict the true spectral shape for each star. | 121 |
| 5.2 | Best-fit model to the metal lines in the HIRES spectra and catalogue photometry for both WD J1927–0355 (top) and WD J2141–3300 (bottom). The model was calculated using code from Koester (2010). | 124 |
| 5.3 | A selection of Ti II, Cr I, Ca I, Mg I, Ni I and Fe I lines in the HIRES spectrum of WD J1927–0355, with the best-fit model overplotted in red. The data were smoothed with a five-point boxcar average and the model spectra were convolved with a Gaussian function. The wavelengths of the models were shifted to match the best-fit radial velocity shift of the data. The spectra and models were normalised to the continuum level and detrended for improved visual clarity. There are many lines of each metal throughout the spectrum. | 125 |
| 5.4 | A selection of Ti II, Cr I, Ca I, Ca II, Mg I, Na I, Si I, Al I, Sr II, and Fe I lines in the HIRES spectrum of WD J2141–3300, with the best-fit model overplotted in red. The data were smoothed with a five-point boxcar average and the model spectra were convolved with a Gaussian function. The wavelengths of the models were shifted to match the best-fit radial velocity shift of the data. The spectra and models were normalised to the continuum level and detrended for improved visual clarity. There are many lines of each metal throughout the spectrum. Some portions of the spectrum are poorly calibrated despite normalisation and detrending. Some fits are also poor due to Zeeman splitting of metal lines caused by the magnetic field at WD J2141–3300, which was not incorporated into the models. | 126 |
| 5.5 | Normalised and binned HIRES spectra of WD J1927–0355 (top) and WD J2141–3300 (bottom) in the region around the $H\alpha$ line. A constant offset has been applied to the flux of WD J2141–3300, for visual clarity. | 127 |

| | | |
|------|---------------------------------------------------------------------------------------------------------------------------------------------------------------------------------------------------------------------------------------------------------------------------------------------------------------------------------------------------------------------------------------------------------------------------------------------------------------------------------------------------------------------------------------------------------------------------------------------------------------------------------------------------------------------------------------------------------------------------------------------------------------------------------------------------------------------------------------|-----|
| 5.6 | A demonstration of the mass abundance (X_{CVZ}) of Mg in the convection zone of WD J1927–0355 for the constant accretion rate model (Dupuis et al., 1993; Koester, 2009) and for the Jura et al. (2009) exponentially decaying model with a 25 Myr disc e -folding characteristic timescale. The accretion was switched off at 25 Myr for the constant accretion rate model scenario, for illustrative purposes. $\dot{M}_{\text{acc}}(t = 0)$ for the exponentially decaying accretion rate model was set equal to \dot{M}_{acc} for the constant accretion rate model. . . . | 131 |
| 5.7 | Element abundances for WD J1927–0355, propagated through the Jura et al. (2009) model for the values of t_{disc} and t_{elapse} corresponding to the minimum χ^2_{ν} , normalised to Mg and CI chondrites, are shown in black. Elements are ordered from left to right in order of increasing atomic weight. Bulk Earth abundances normalised to Mg and CI chondrites are shown by square symbols (Allègre et al., 2001). C chondrite abundances normalised to Mg and CI chondrites are shown by cross symbols (Nittler et al., 2004). Upper limits are denoted with a downwards arrow. CI chondrite abundances are from Lodders (2019). Error bars are propagated using the errors on abundances from Table 5.2. Faded (grey) points represent elements that were not considered in the comparison. | 137 |
| 5.8 | χ^2_{ν} contour plot for the abundances in WD J1927–0355 compared with bulk Earth abundances (relative to magnesium). | 138 |
| 5.9 | Element abundances for WD J2141–3300, propagated through the Jura et al. (2009) model for the values of t_{disc} and t_{elapse} corresponding to the minimum χ^2_{ν} , normalised to Mg and CI chondrites, are shown in black. Elements are ordered from left to right in order of increasing atomic weight. Bulk Earth abundances normalised to Mg and CI chondrites are shown by square symbols (Allègre et al., 2001). C chondrite abundances normalised to Mg and CI chondrites are shown by cross symbols (Nittler et al., 2004). Upper limits are denoted with a downwards arrow. CI chondrite abundances are from Lodders (2019). Error bars are propagated using the errors on abundances from Table 5.2. Faded (grey) points represent elements that were not considered in the comparison. | 139 |
| 5.10 | χ^2_{ν} contour plot for the abundances in WD J2141–3300 compared with C chondrite abundances (relative to magnesium). | 140 |

- 5.11 **Top:** The percentage by mass of all observed elements inferred to be in the parent body accreted by WD J1927–0355, as well as oxygen, as a function of the time since the accretion event began. The disc lifetime is assumed to be 0.05 Myr. At $t_{\text{elapse}} = 0$, the order of elements on the plot from top to bottom is: O, Fe, Mg, Ca, Ni, Cr, Ti. **Bottom:** The inferred total parent body mass (M_{PB}) as a function of the time since the accretion event began. The grey horizontal dashed lines indicate the mass of the dwarf planet Ceres, and the Earth. The grey vertical shaded region is the most likely elapsed time for WD J1927–0355 since accretion began. 143
- 5.12 **Top:** The percentage by mass of all observed elements inferred to be in the parent body accreted by WD J2141–3300, as well as oxygen, as a function of the time since the accretion event began. The disc lifetime is assumed to be 0.05 Myr. At $t_{\text{elapse}} = 0$, the order of elements on the plot from top to bottom is: O, Si, Mg, Fe, Al, Ca, Ni, Na, Cr, Ti, Sr. **Bottom:** The inferred total parent body mass (M_{PB}) as a function of the time since the accretion event began. The grey horizontal dashed lines indicate the mass of the dwarf planet Ceres, and the Earth. The grey vertical shaded region is the most likely elapsed time for WD J2141–3300 since accretion began. 144
- 5.13 Element abundances for WD J1927–0355, propagated through the constant accretion rate model for steady state accretion, normalised to Mg and CI chondrites, are shown in black. Elements are ordered from left to right in order of increasing atomic weight. Bulk Earth abundances normalised to Mg and CI chondrites are shown by square symbols (Nittler et al., 2004). Upper limits are denoted with a downwards arrow. Error bars are propagated using the errors on abundances from Table 5.2. CI chondrite abundances are from Lodders (2019). Faded (grey) points represent elements that were not considered in the comparison. 146
- 5.14 Element abundances for WD J2141–3300, propagated through the constant accretion rate model for steady state accretion, normalised to Mg and CI chondrites, are shown in black. Elements are ordered from left to right in order of increasing atomic weight. LL chondrite abundances normalised to Mg and CI chondrites are shown by cross symbols (Nittler et al., 2004). Upper limits are denoted with a downwards arrow. Error bars are propagated using the errors on abundances from Table 5.2. CI chondrite abundances are from Lodders (2019). Faded (grey) points represent elements that were not considered in the comparison. 147

| | | |
|-----|---------------------------------------------------------------------------------------------------------------------------------------------------------------------------------------------------------------------------------------------------------------------------------------------------------------------------------------------------------------------------------------------------------------------------------------------------------------------------------------------------------------------------------------------------------------------|-----|
| 6.1 | Hybrid spectrophotometric fits of H-atmosphere white dwarfs in the 13 pc sample. Flux is given in units of $\text{erg cm}^{-2} \text{s}^{-1} \text{\AA}^{-1}$. The blue models are best fits to STIS spectra plus <i>Gaia</i> , 2MASS, and WISE photometry, where available. The red models are the fits to just the <i>Gaia</i> , 2MASS, and WISE photometry, where available. All parameters in this figure are from the fits to STIS plus photometry (blue models). | 162 |
| 6.2 | Hybrid spectrophotometric fits of H-atmosphere white dwarfs in the 13 pc sample. Flux is given in units of $\text{erg cm}^{-2} \text{s}^{-1} \text{\AA}^{-1}$. The blue models are best fits to STIS spectra plus <i>Gaia</i> , 2MASS, and WISE photometry, where available. The red models are the fits to just the <i>Gaia</i> , 2MASS, and WISE photometry, where available. All parameters in this figure are from the fits to STIS plus photometry (blue models). | 163 |
| 6.3 | Hybrid spectrophotometric fits to spectra and photometry of the wide DA + DA system WD 0727+482 A+B. Flux is given in units of $\text{erg cm}^{-2} \text{s}^{-1} \text{\AA}^{-1}$. Reliable <i>Gaia</i> photometry is not available for these stars so archive <i>BVRI</i> optical photometry are used in the fit instead. The blue models are best fits to STIS spectra plus <i>BVRI</i> and 2MASS photometry. The red models are the fits to just the photometry. All parameters in this figure are from the fits to STIS plus photometry (blue models). | 164 |
| 6.4 | Fits to photometry DA white dwarfs within 13 pc for which no STIS spectra are available. Flux is given in units of $\text{erg cm}^{-2} \text{s}^{-1} \text{\AA}^{-1}$. The red models show the fits to the photometry. | 165 |
| 6.5 | Fit of the STIS E140H spectra of WD 0642–166 with Tremblay et al. (2013a) models, no additional photometry is available to further constrain the fit. All interstellar lines were masked in the fit and are not shown in the plot. An instrumental defect at 1486\AA was also masked. | 166 |
| 6.6 | Fit of the COS G130M and G160M spectra of WD 1647+591 with Tremblay et al. (2013a) models with additional H_2 molecular lines. | 167 |
| 6.7 | Fits of Balmer lines for white dwarfs the 13 pc sample. Flux is given in units of $\text{erg cm}^{-2} \text{s}^{-1} \text{\AA}^{-1}$ | 169 |
| 6.8 | Fits of Balmer lines for white dwarfs the 13 pc sample. Flux is given in units of $\text{erg cm}^{-2} \text{s}^{-1} \text{\AA}^{-1}$ | 170 |
| 6.9 | Fits of Balmer lines for unresolved double white dwarfs in the 13 pc sample. Flux is given in units of $\text{erg cm}^{-2} \text{s}^{-1} \text{\AA}^{-1}$ | 171 |

6.10 Comparisons of parameters for H-atmosphere white dwarfs. Top panel: The T_{eff} derived from the photometric (phot) optical and IR only fit, compared to the T_{eff} derived from the hybrid STIS, optical and IR fit. Bottom panel: The $\log(g)$ derived from the photometric optical and IR only fit, compared to the $\log(g)$ derived from the hybrid STIS, optical and IR fit. 173

Acknowledgments

I would like to thank my supervisor, Pier, for his enthusiasm, support and guidance throughout the PhD process. Thank you to the European Research Council for funding my PhD programme, which has enabled me to travel to some incredible places and meet many fascinating researchers. Thank you to the many members of the white dwarf community that have collaborated with me or provided data or models, without which the work presented in this thesis would not have been possible. Thank you to the Warwick Astronomy group, particularly the PhD students, who are too many to list, for making my time in the department so enjoyable, and for the lunch chats, board games, pub trips, and parkruns. Thank you to Freya and Viv for being great friends and housemates during my PhD. I would like to thank Sarah, Rachel, Tom, Sara and Emma for their loyal friendship over many years, and for all the amazing times we have had together. Finally, thank you to my family: mum, dad, Rosie and John, for always being there for me and always supporting me with my goals and dreams.

Declarations

This thesis is submitted to the University of Warwick in support of my application for the degree of Doctor of Philosophy. It has been composed by myself and has not been submitted in any previous application for any degree.

The work presented (including data generated and data analysis) was carried out by the author except in the cases outlined below:

Chapter 3 – The VLT X-shooter observing program was led by B. T. Gänsicke and P.-E. Tremblay. Metal-polluted and carbon-atmosphere white dwarf spectra were fitted by M. Hollands and D. Koester. Figure 3.3 was created by M. Hollands. Two helium-atmosphere spectra were fitted by E. Cukanovaite.

Chapter 4 – Two metal-polluted spectra and one carbon-atmosphere white dwarf spectrum were fitted by D. Koester. New model atmospheres with corrections were generated by P.-E. Tremblay. A simulation of a Galactic population of white dwarfs was provided by E. Cukanovaite. A synthetic mass distribution of white dwarfs within 40 pc was provided by T. Cunningham. New spectroscopic observations were provided by B. Klein and C. Melis.

Chapter 6 - The *HST* program was led by B. T. Gänsicke.

Parts of this thesis have been published by the author:

Chapter 3 – Adapted from O’Brien et al. (2023), published in MNRAS.

Chapter 4 – Adapted from O’Brien et al. (2024), published in MNRAS.

Chapter 5 - Adapted from O’Brien et al. (2025), published in MNRAS.

Abstract

Over the past decade, the spacecraft *Gaia* has identified hundreds of thousands of white dwarfs due to the reliable parallaxes and photometry it provides, facilitating the creation of volume-limited samples of white dwarfs. Volume-limited samples are unbiased and span the entire white dwarf cooling sequence, and are therefore vital for population studies.

I analysed the medium-resolution optical spectroscopy of 248 newly-identified white dwarf candidates within 40 pc. I derived their atmospheric compositions using model atmosphere fits to both their spectra and photometry. I then analysed the volume-complete 40 pc sample from *Gaia*. I found that 19 per cent of white dwarfs are in multiple-star systems, that there is a prevalent issue for modelling low-temperature white dwarfs, and that crystallisation cannot solely explain the onset of magnetism in white dwarfs.

I then analysed two nearby cool, helium atmosphere white dwarfs with atmospheres heavily polluted by planetary debris. I used an exponentially decaying disc model to determine the most likely composition of the parent bodies and found that both stars had likely accreted rocky bulk Earth-like bodies at least as massive as a small moon.

The largest volume with complete UV spectroscopy of white dwarfs is 13 pc. Using this sample, I tested the consistency of fitting pure-H white dwarf atmosphere models both to UV data and to optical data, and found a discrepancy below 10 000 K.

Through the work comprising this thesis, I have provided an overview of the statistics of the largest volume-complete optical sample of white dwarfs to date, which will be the benchmark sample for many decades. I have also worked towards analysing the largest UV volume-complete white dwarf sample, and additionally studied the effect of applying an exponentially decaying disc model to infer the composition of material accreted by helium-atmosphere white dwarfs.

Abbreviations

2MASS Two Micron All-Sky Survey

CIA Collision-Induced Absorption

DR Data Release

GALEX Galaxy Evolution Explorer

HIRES High-resolution Echelle Spectrometer

HR Hertzsprung-Russell

HST Hubble Space Telescope

IR Infrared

ISIS Intermediate-dispersion Spectrograph and Imaging System

ISM Interstellar Medium

JWST James Webb Space Telescope

STIS Space Telescope Imaging Spectrograph

UV Ultraviolet

VLT Very Large Telescope

WHT William Herschel Telescope

WISE Wide-field Infrared Survey Explorer

Chapter 1

Introduction

1.1 Discovery

This thesis focuses on the characterisation of white dwarfs in the solar neighbourhood. The closest white dwarfs to us were some of the first to be discovered, and are some of the most well-studied, but there is still much to learn from our stellar neighbours.

The first white dwarf to be discovered, 40 Eridani (Eri) B, located at a distance of 5 pc from the Sun, was discovered by William Herschel in the late 1700s, as a companion to the K dwarf 40 Eri A (Herschel, 1785). However, its unusual properties and stellar classification were not confirmed until the 1900s. The parallaxes of 40 Eri A and B were constrained by Henry Norris Russell, and in 1910 Williamina Paton Fleming conveyed to Russell that the spectral type of 40 Eri B was A-type (Holberg, 2009). However, as noted by Russell and Edward Charles Pickering, 40 Eri B emits just 0.1 per cent of the luminosity of a typical A-type star. Additionally, in 1844, Friedrich Bessel determined that the nearby stars Sirius (A-type) and Procyon (F-type) both had unseen faint companion stars (Bessel, 1844). The companion star Sirius B was first observed by Alvan Graham Clark (Flammarion, 1877), and spectroscopic observations of both Sirius B and 40 Eri B by Adams (1914) again revealed A-type spectral types with broad Balmer lines.

The first isolated white dwarf without a binary stellar companion to be discovered was van Maanen 2 (vMa 2), in 1917 by Adriaan van Maanen (van Maanen, 1917). Due to its strong and broad metal absorption features, it was given an F-type spectral classification, but was recognised as significantly sub-luminous, similar to Sirius B and 40 Eri B. Willem Luyten, a student of Ejnar Hertzsprung, first used the term *white dwarf* to refer to the three stars (40 Eri B, Sirius B, and vMa2) that were sitting in a separate region of the HR diagram (Luyten, 1923). Quantum mechanics provided a reliable description for white dwarfs, and we now know that these stars lie at the end point of stellar evolution.

White dwarfs have masses similar to that of the Sun, but radii of around 1 per cent of that of the Sun. Their spectra are essentially black bodies, like other stars, but due to their small radii they are over ten times fainter than A and F type stars, placing them in a distinct region of the HR diagram. They begin as very hot remnants but cool rapidly, and as such their temperatures range from 100 000 K to 4000 K.

1.2 Formation

Stars with masses below $\approx 10 M_{\odot}$, accounting for over 95 per cent of the stellar population, will eventually end their lives as white dwarfs (Fontaine et al., 2001). The evolution of stars more massive than $10 M_{\odot}$ is not discussed in this section, as they are not white dwarf progenitors. A star less massive than $10 M_{\odot}$ begins its life when a cloud of gas reaches the Jeans mass and undergoes gravitational collapse, forming a protostar (Jeans, 1902). The lifetime of a protostar can be described by the Kelvin–Helmholtz timescale, which is defined as the time it would take an astrophysical body to radiate away its kinetic energy given its current luminosity (Thomson, 1871). If the protostar is less massive than $0.08 M_{\odot}$, hydrogen is fused into deuterium but not subsequently into helium, meaning the main sequence phase will not be reached and a brown dwarf will form instead (Kumar, 1962). However, if the protostar has a mass greater than $\approx 0.08 M_{\odot}$, nuclear fusion of hydrogen into helium can occur through the proton-proton chain reaction or the CNO cycle, which uses carbon, nitrogen, and oxygen as catalysts.

Fusion of hydrogen into helium creates the conditions for the star to be in hydrostatic equilibrium, which is a stable state and corresponds to the main sequence phase of the star (Carroll and Ostlie 2017; Chapter 13). The evolution rate of main sequence stars is governed by the rate of nuclear fusion reactions, and therefore the main sequence lifetime of a star depends primarily on its mass, with more massive stars spending the least amount of time on the main sequence. Zero-age main sequence (ZAMS) stars with masses above $1.2 M_{\odot}$ have convective cores, whereas $0.3 M_{\odot} - 1.2 M_{\odot}$ ZAMS stars have radiative cores (Carroll and Ostlie 2017; Chapter 13). As a star like the Sun evolves along the main sequence, its core steadily contracts as hydrogen fuses into helium, increasing the mean molecular weight of the core (Carroll and Ostlie 2017; Chapter 13).

Once a star has left the main sequence, it enters the post-main sequence phases. Figure 1.1 demonstrates the evolution of a $1.5 M_{\odot}$ star from the end of the main sequence phase to the beginning of the white dwarf phase. Once a star of mass $0.8 M_{\odot} - 8 M_{\odot}$ has fused all the hydrogen in its core, it leaves the main sequence and enters the red giant branch (RGB), where its isothermal helium core contracts due to gravitational pressure from the shell of hydrogen surrounding it, and the hydrogen continues burning in this thick outer

shell, which expands (Iben, 1974). At the top of the RGB, the star reaches a temperature high enough to fuse helium into carbon via the triple- α process, which causes a brief helium core flash. It then enters the horizontal branch phase, where helium is fusing in the core and hydrogen is still fusing in a shell. Once all the helium in the core has been fused, the star evolves onto the asymptotic giant branch (AGB), where hydrogen and helium shell burning prevent the star from collapsing (Karakas, 2011). The AGB phase is analogous to the RGB phase but for helium instead of hydrogen. During the AGB phase, the triple- α process generates both carbon and oxygen in the core of the star. At the top of the AGB, thermal pulses are generated as a result of helium shell flashes caused by the helium products of hydrogen shell burning entering the helium shell. The helium flashes eventually cause the AGB star to eject its envelope, forming a cloud of ionised gas known as a planetary nebula which enriches the ISM (Seaton, 1966).

The remaining core of the star, revealed after the ejection of the shell, is a white dwarf. Most currently observed isolated white dwarfs were formed via the pathway described in this section. Only B, A, F, and G-type main sequence stars have had time to evolve into white dwarfs within the age of the Universe, and therefore the typical mass of a white dwarf in the solar neighbourhood is $\approx 0.6 M_{\odot}$ (Bergeron et al., 2019), corresponding to a ZAMS progenitor mass of $1.4 M_{\odot}$ (Cummings et al., 2018). For a main sequence star of mass $0.8 M_{\odot} - 8 M_{\odot}$, the subsequent white dwarf will have a carbon-oxygen core composition. Main sequence stars with masses between $8 M_{\odot} - 10 M_{\odot}$ are the progenitors for high-mass oxygen-neon core white dwarfs as a result of carbon burning (Werner et al., 2005). Another white dwarf formation pathway exists for the lowest-mass main sequence stars, with masses less than $0.3 M_{\odot}$, which are fully convective and in which helium cannot fuse into carbon, therefore forming helium-core white dwarfs. These helium-core white dwarfs have formed via binary evolution, but have not yet formed from single stars within the age of the Universe (Althaus and Benvenuto, 1997).

1.3 Composition

The extremely high densities of white dwarfs cause the matter in their cores to exist in the form of fully ionised, electron-degenerate plasma. The ions in the white dwarf core are non-degenerate, and can be treated as an ideal gas at sufficiently high temperatures. The Pauli exclusion principle, which states that two electrons in an atom cannot occupy the same quantum state simultaneously, generates electron degeneracy pressure in the white dwarf (Pauli, 1925). Electron degeneracy pressure prevents the white dwarf from collapsing under its extreme gravity, therefore keeping the star in hydrostatic equilibrium. Conduction of energy by the degenerate electrons is the dominant source of energy transport within

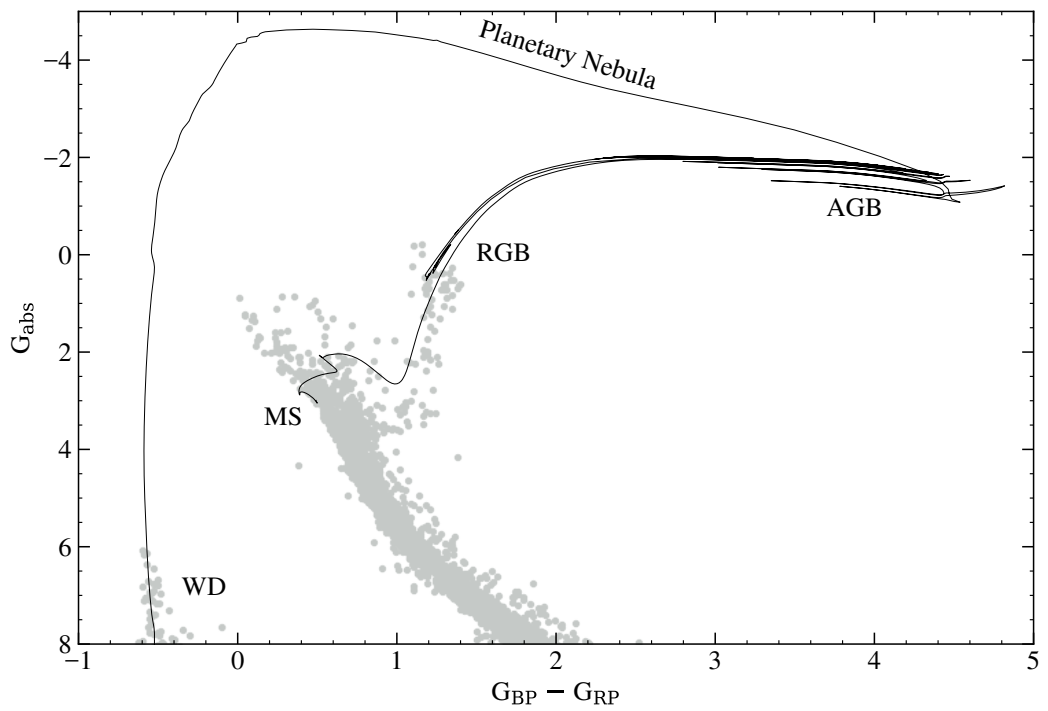


Figure 1.1: An HR diagram with grey datapoints from *Gaia* DR3. In black is a MESA Isochrones and Stellar Tracks (MIST) stellar evolutionary track for a $1.5 M_{\odot}$ star, from the moment it leaves the main sequence until it reaches the white dwarf cooling track. The MIST models were computed with the Modules for Experiments in Stellar Astrophysics (MESA) code (Choi et al., 2016; Dotter, 2016).

the white dwarf core, and this efficient transport mechanism makes the core effectively isothermal.

The mass-radius relation for white dwarfs implies that higher masses correspond to smaller radii. For a typical-mass white dwarf, the degenerate electron gas can be assumed to be non-relativistic, with an equation of state of the form $P \propto \rho^{5/3}$, where P is the pressure and ρ is the density (Koester and Chanmugam, 1990). The electrons in the cores of the most massive white dwarfs are travelling close to the speed of light, and their relativistic equation of state becomes $P \propto \rho^{4/3}$ (Koester and Chanmugam, 1990). Relativistic electron degeneracy pressure can support a white dwarf up to a finite mass – the Chandrasekhar mass, $\sim 1.4 M_{\odot}$ – above which the white dwarf will undergo gravitational collapse (Chandrasekhar, 1931).

The extreme gravity of white dwarfs causes chemical stratification, a process in which heavier elements sink towards the centre of the star and light elements float to the surface (Koester, 1989). Figure 1.2 demonstrates the stratified composition of a white dwarf, where the left-hand side of the horizontal axis represents the centre of the star, and with each increase on the log scale, more of the star is encased. The carbon-oxygen core makes up 99 per cent of a typical white dwarf by mass (Saumon et al., 2022). Almost all of the remaining 1 per cent of the mass is contained in the envelope, comprising of a helium layer encased by a thin hydrogen layer. Further out is the photosphere, the depth of which is defined as $\frac{2}{3}$ of the Rosseland mean optical depth (Saumon et al., 2022). The majority of the photons that we observe from white dwarfs originate from the photosphere. The outermost layer, the atmosphere, makes up $\approx 10^{-14}$ of the white dwarf by mass.

The spectral type of a white dwarf is determined from the strength of atomic lines from optical spectroscopy (Sion et al., 1983). When Balmer lines are the strongest optical features, a white dwarf is classified as a DA. Neutral helium gives the classification DB, and DO implies the detection of ionised helium lines. DQ white dwarfs have detectable carbon, which is typically dredged up from the stellar interior (classical DQ), or brought to the surface during a merger (hot DQ or warm DQ), and DZ white dwarfs display metal lines which are generally attributed to the accretion of planetary debris. A DC white dwarf has a completely featureless spectrum. In all cases, ‘D’ stands for degenerate. Combinations of these letters as an overall spectral type forms a picture of the atmospheric composition of the white dwarf, however the spectral type depends on the signal-to-noise and resolution of the spectra and therefore does not always reflect the relative abundances of each element (Doyle et al., 2023). Below 10 500 K, helium lines are no longer visible in a white dwarf spectrum, and below 5000 K hydrogen lines also disappear. Therefore the atmospheric composition for a white dwarf cooler than 5000 K, where both hydrogen and helium lines are absent, is generally uncertain. A selection of optical spectra of white dwarfs demonstrating the

variety in their spectral types is shown in Fig. 1.3. Despite the many spectral types of white dwarfs, the primary constituent of most atmospheres is either hydrogen or helium. Helium-dominated atmosphere white dwarfs must have burned most of their hydrogen in a previous evolutionary phase (Saumon et al., 2022).

The opacity of the atmosphere of a white dwarf varies as a function of wavelength, and the dominant sources of opacity depend on the effective temperature of the star, as shown in Fig. 1.4. For a hydrogen-atmosphere white dwarf at 12 000 K, the bound-bound opacity (orange line; Fig. 1.4) corresponds to the Balmer lines in the optical and Lyman α in the UV. There is an additional H bound-free continuum opacity (blue line; Fig. 1.4), and these combine to produce an overall opacity, with some weaker sources providing minor contributions. At 4000 K, the thermal energy is too low to excite the bound-bound transitions. The major opacity contributions at these cooler temperatures for hydrogen-atmosphere white dwarfs are threefold:

1. In the IR, collision-induced absorption (CIA) effects dominate the opacity profile, caused by collisions of molecular and atomic hydrogen (purple line; Fig. 1.4).
2. In the optical, bound-free absorption from the H^- ion dominates (red line; Fig. 1.4).
3. In the UV and blue part of the optical, the opacity generated by the red wing of the Lyman α line dominates (green line; Fig. 1.4). Even though the line is centred in the UV, H_2 -H collisions broaden the absorption line profile into the optical at high densities (Kowalski and Saumon, 2006).

Helium-atmosphere white dwarfs have similar opacity sources but with helium included, and at low temperatures the photospheric density is so high that it becomes liquid-like (Saumon et al., 2022). State-of-the-art white dwarf model atmospheres, which are discussed in Chapter 2, are unable to reliably fit the full UV-to-IR range of a white dwarf spectral energy distribution, especially at low temperatures, and therefore there may be missing opacity sources from white dwarf models (see Chapters 4 and 6).

1.4 Cooling

White dwarfs are not undergoing fusion and therefore they cool down as they age and evolve. The process dominating the rate of cooling depends on the temperature of the white dwarf. In this section, only the cooling of isolated white dwarfs is discussed.

The youngest and therefore hottest white dwarfs have hot enough interiors for neutrinos to be generated via electroweak interactions. Photon, pair, plasma and bremsstrahlung neutrino processes generate neutrinos in hot white dwarfs, with the plasma neutrino process

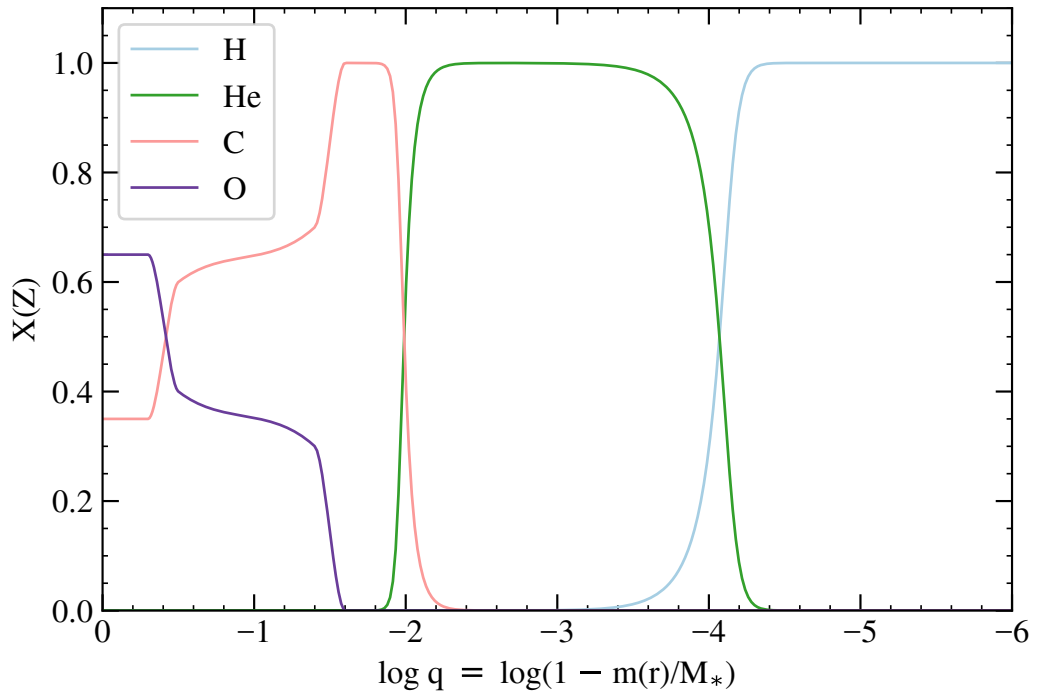


Figure 1.2: The chemical profile of a typical 12 000 K, $0.6 M_{\odot}$ white dwarf with a hydrogen-dominated atmosphere, where $\log(q) = 0$ corresponds to the centre of the white dwarf, with the surface towards the right. The parameter $\log(q) = \log(1 - m(r)/M_*)$ represents the fraction of the mass that is outside a radius r . $X(Z)$ represents the abundance of element Z in the white dwarf. Reproduced from Saumon et al. (2022) with data provided by A. Bédard.

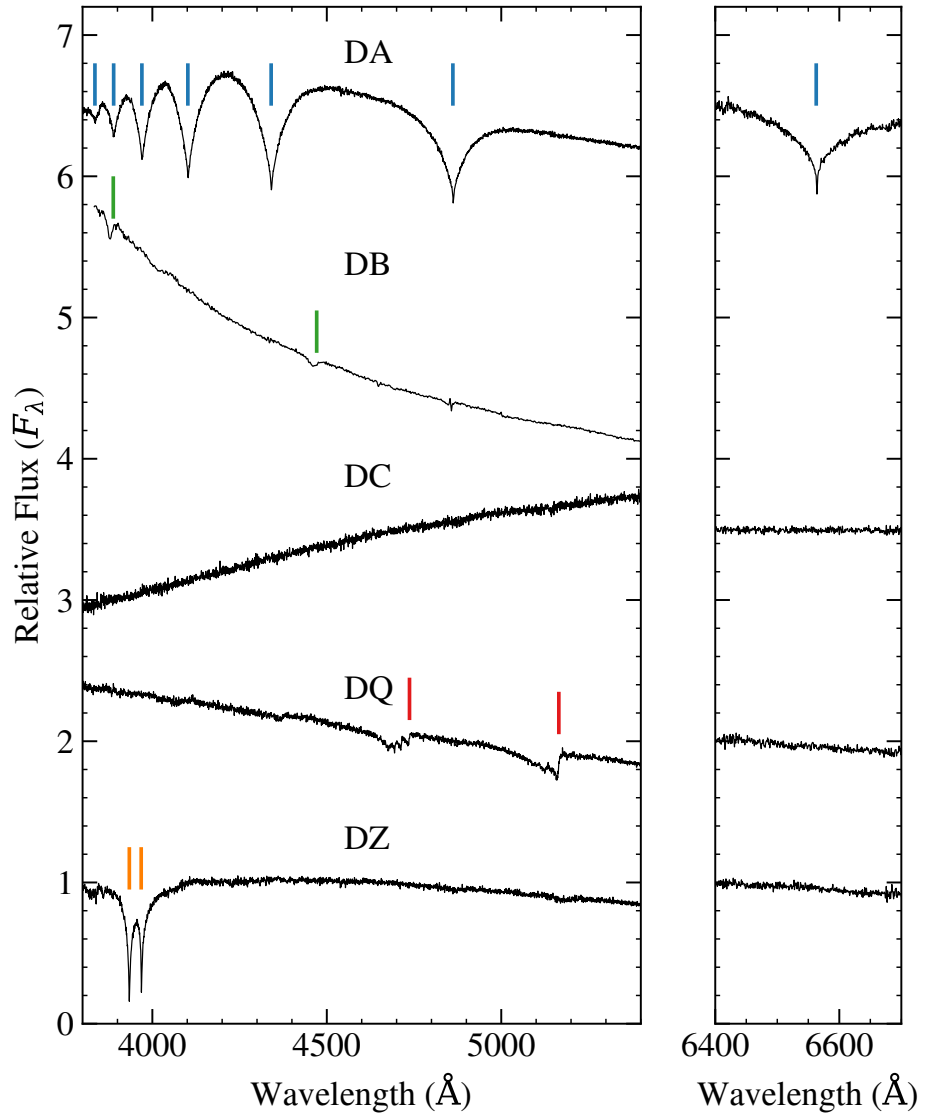


Figure 1.3: VLT X-shooter and SOAR *Goodman* spectra of various white dwarf spectral types. The spectra have been offset from each other vertically for clarity. The absorption line labels represent the following elements: blue: H, green: He, red: C, orange: Ca. The example DZ only shows Ca II H+K absorption lines as these are typically the strongest metal lines in optical spectra.

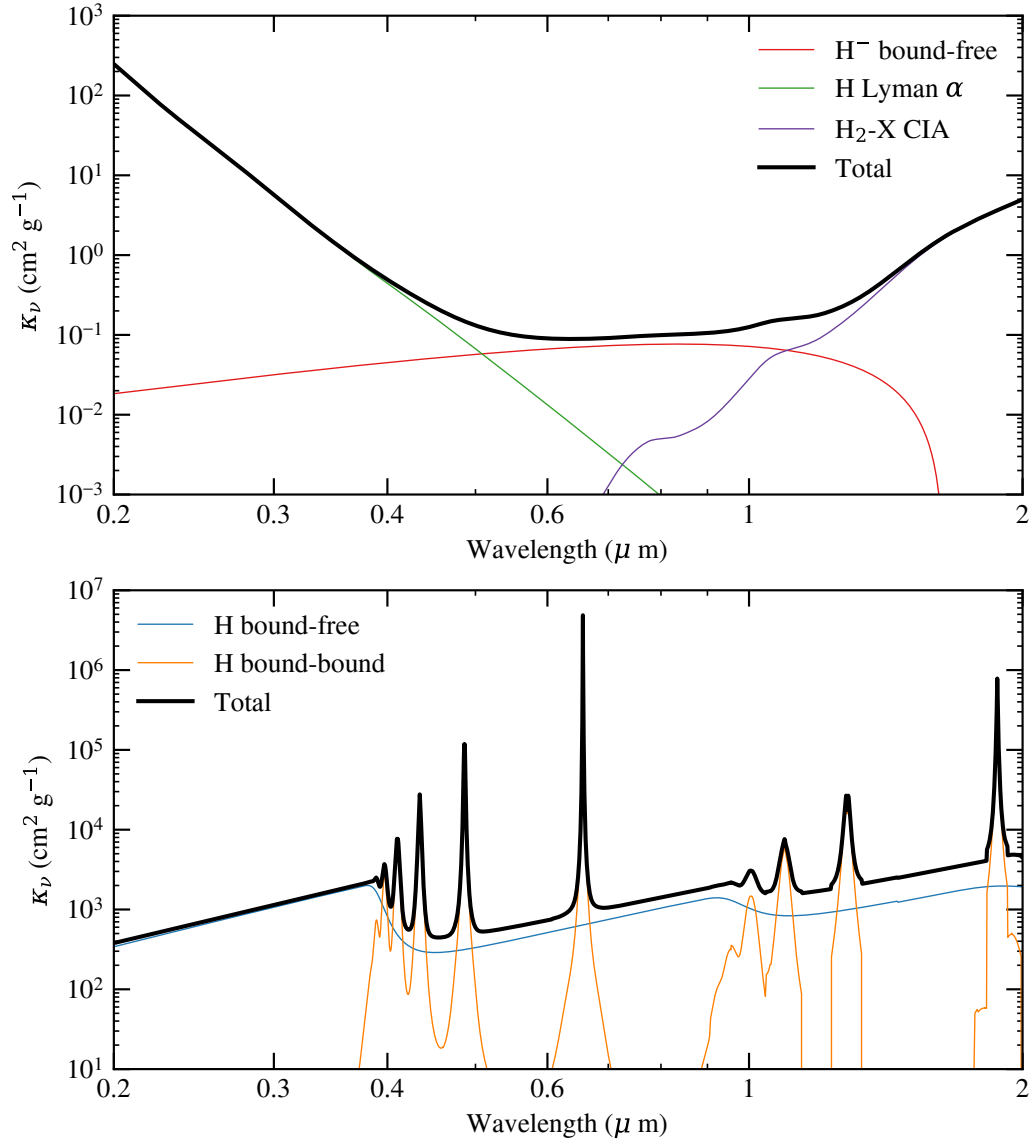


Figure 1.4: Major contributors to the overall opacity of a hydrogen-atmosphere white dwarf, with parameters $\log(g) = 8$ and $T_{\text{eff}} = 4000 \text{ K}$ (upper) and $T_{\text{eff}} = 12\,000 \text{ K}$ (lower). Minor contributions to the total opacity are not shown. Adapted from Saumon et al. (2022), using models provided by P.-E. Tremblay.

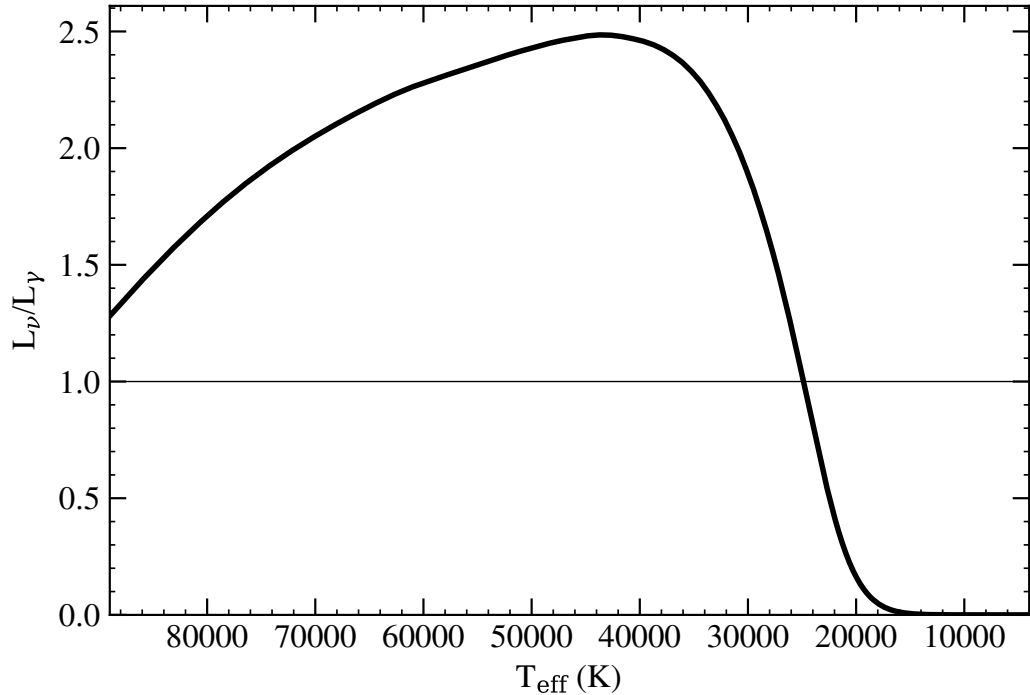


Figure 1.5: The relative luminosity resulting from neutrino emission (L_{ν}) compared to photon emission (L_{γ}) as a function of white dwarf effective temperature. Reproduced from Saumon et al. (2022) with data provided by A. Bédard.

typically dominating (Koester and Chanmugam, 1990). Plasma neutrino processes are generated by plasmons, which are quasiparticle quanta of electromagnetic fields in a plasma, in the same way as photons and phonons are described as quanta of light and mechanical vibrations respectively. Plasmons in white dwarfs can decay into a neutrino-antineutrino pair, since plasmons acquire an effective mass due to plasma interactions, and the decay rate of this process is highly temperature dependent (Kantor and Gusakov, 2007). The neutrinos escape from the white dwarf without interacting with it, causing energy loss, and enabling the white dwarf to cool very rapidly in its early stages. Fig. 1.5 shows that neutrino cooling is the dominant source of energy release for the first 50 Myr of the cooling of the white dwarf, or until the white dwarf has cooled down to $\approx 25\,000$ K (Winget et al., 2004).

As they cool and evolve, most white dwarfs go through at least one period of pulsational instability, aside from some of the most highly magnetic white dwarfs (Córscico et al., 2019). The pulsations are caused by partial ionisation of the envelope, which increases the envelope opacity and inhibits thermal emission, making the white dwarf unstable so it begins to pulsate (Fontaine and Brassard, 2008). The pulsations manifest as global non-radial g -mode oscillations in the white dwarf, for which gravity is the restoring force (Córscico

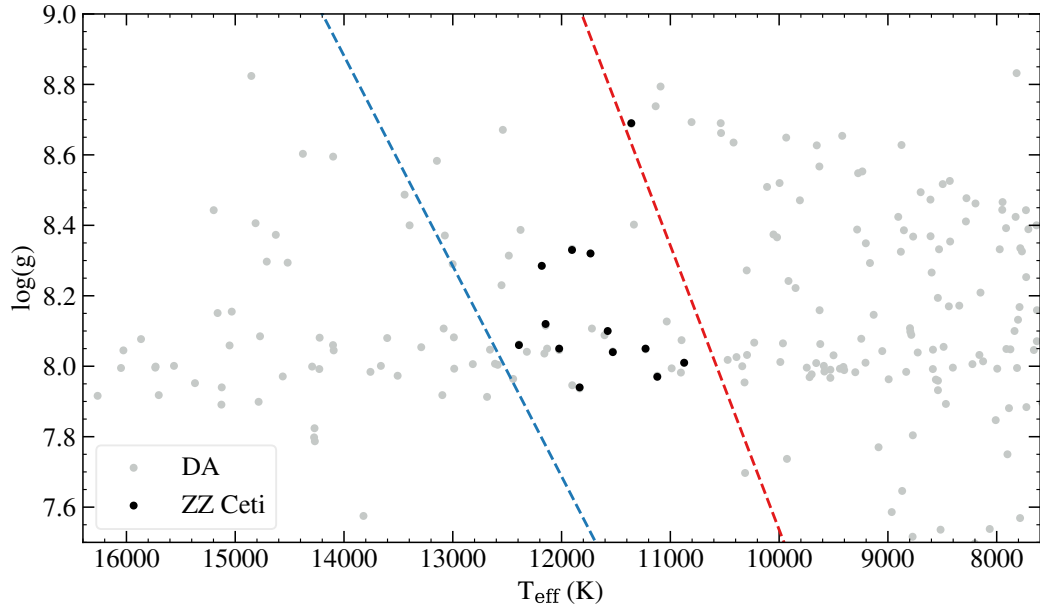


Figure 1.6: Effective temperature (T_{eff}) against surface gravity ($\log(g)$) for DA white dwarfs within 40 pc, which are shown in grey. Known ZZ Ceti pulsating white dwarfs are shown in black. The red and blue dashed lines represent the boundaries of the hydrogen-atmosphere white dwarf instability strip (Tremblay et al., 2015).

et al., 2019). DB white dwarfs pulsate between approximately 32 000 K and 22 000 K (DBV, Winget et al. 1982), and DA white dwarfs pulsate between 12 500 K and 10 500 K (DAV or ZZ Ceti), because hydrogen and helium partially ionise at different temperatures. The instability strip for ZZ Ceti stars is shown in Fig. 1.6, with boundaries from Tremblay et al. (2015), demonstrating that the exact temperature range for which DA white dwarfs pulsate is a function of surface gravity. The study of these pulsations, known as asteroseismology, is used to characterise the interiors of white dwarfs, as the temperature and composition of the interior of the star affects the speed at which the g -mode waves can travel.

Once the effective temperature of the white dwarf drops below $\approx 25\,000$ K, thermal cooling is the dominant source of energy release. The ions in the degenerate core leak thermal energy which escapes through the envelope and photosphere, and this process is much slower than neutrino cooling. There are small changes in the radius of the star during thermal cooling, due to thermal expansion. However, this change in radius is not as significant as the gravitational contraction that occurs in young white dwarfs, which itself is a source of luminosity (D’Antona and Mazzitelli, 1990). At the thermal cooling stage, the energy release is limited by the radiative opacities of the envelope layers.

As the white dwarf cools further, the carbon and oxygen plasma that makes up the

core undergoes a first-order phase transition from liquid to solid. This phase transition is known as crystallisation, and causes the release of $\approx \frac{3}{4}k_B T$ of latent heat per ion. White dwarfs crystallise from the inside and the crystallisation front propagates outwards. It typically takes 1 – 3 Gyr for 90 per cent of the core to crystallise (Saumon et al., 2022). This phase transition releases energy, providing an additional heating source and keeping the white dwarf at roughly the same temperature for longer. Crystallisation therefore ‘delays’ the cooling process of a standard white dwarf by about 1 Gyr. The prediction by van Horn (1968) that there should be a mass-dependent pile up of white dwarfs at a certain point along the cooling sequence while they crystallise was observed by the *Gaia* satellite (Tremblay et al., 2019b). The most massive white dwarfs undergo crystallisation earlier in their cooling, and therefore the *Gaia* HR diagram only demonstrates a pile up at high masses. Alongside the latent heat release, cooling is further slowed by the release of gravitational energy from the partial separation of carbon and oxygen in the crystallising core (Tremblay et al., 2019b). Some massive carbon-oxygen core white dwarfs, likely merger remnants, experience an extreme cooling delay of more than an 8 Gyr as a result of the distillation of ^{22}Ne impurities in the core (Bédard et al., 2024).

Hydrogen-rich atmosphere white dwarfs develop convective instabilities at the photosphere due to the partial ionisation of hydrogen at $T_{\text{eff}} \approx 18\,000\text{ K}$ (Saumon et al., 2022). The convection zone extends as the hydrogen-atmosphere white dwarf cools, reaching sub-photospheric layers at $T_{\text{eff}} \approx 12\,000\text{ K}$. Eventually, at $T_{\text{eff}} \approx 6000\text{ K}$, the convection zone extends to reach the core. The surface is then coupled with the core, which is known as convective coupling, and at that point convection becomes the dominant mechanism for energy release, and the rate of energy transfer increases (Fontaine et al., 2001). Therefore following convective coupling, the opacity of the atmosphere layer controls the cooling rate. For helium-rich atmosphere white dwarfs, convective coupling occurs at $T_{\text{eff}} \approx 12\,000\text{ K}$ because helium has a higher ionisation potential than hydrogen.

Following the crystallisation of the core, the specific heat capacity of the solid state phase becomes significant. Once the temperature of the core drops to below the Debye temperature, the white dwarf enters a final stage of rapid cooling. Below the Debye temperature, the ions in the white dwarf core vibrate collectively as a lattice rather than independently, and these collective vibrations can be quantised in the form of phonons (Debye, 1912). The phonons release thermal energy rapidly, and the specific heat capacity of the star scales as T^3 . Some very massive white dwarfs have already reached this stage of Debye cooling.

1.5 Spectral evolution

As a white dwarf goes through the stages of cooling discussed in the previous section, various element transport mechanisms can work against stratification and gravitational settling to change the spectral type over time. Hydrogen-rich atmosphere white dwarfs start off on the white dwarf cooling track with the spectral type DA, or possibly DAO if there is some ionised helium. Any trace helium will subsequently sink out of the atmosphere, and the star remains as a DA until it reaches 5000 K, at which point the Balmer lines are so weak that they are no longer detectable, making the spectrum appear as a featureless DC white dwarf.

The spectral evolution of helium-atmosphere white dwarfs is more complex. Figure 1.7 shows a schematic diagram demonstrating the cooling of helium-atmosphere white dwarfs. They begin as spectral type DO with ionised helium, and the radiative wind slows chemical stratification in the outer envelope (Unglaub and Bues, 1998, 2000). Once they cool, the wind fades and the white dwarfs stratify. If a DO has a high hydrogen content, it will develop a thick enough hydrogen atmosphere following gravitational settling to appear to have a DA spectral type. If not, it will appear as a DB. The DA white dwarfs undergo one of two processes as they cool further: convective dilution or convective mixing, depending on the hydrogen content in the envelope. If the hydrogen layer is thin, the helium layer below it becomes convective, and overshoot processes cause the dilution of the hydrogen layer, leading to the spectral type DBA. If the hydrogen layer is thicker, it can become convective. The convection eventually reaches the helium layer below, causing mixing and again leading to the spectral type DBA.

Once the DB(A) white dwarf cools down to below 10 500 K, its helium features are no longer detectable, and it appears as a featureless DC white dwarf. However, as shown in Fig. 1.7, the convective dredge-up of carbon as the white dwarf cools further can change the spectral type yet again. If there is sufficient dredge-up that the trace carbon becomes detectable, the spectral type of the white dwarf becomes DQ. The carbon is dredged up as the white dwarf cools, until the helium convection zone reaches its maximum depth, at which point the carbon sinks again due to partial recombination (Pelletier et al., 1986). It is thought that all helium-atmosphere white dwarfs experience some form of carbon dredge-up, though in many cases the carbon is below the current detection limit (Blouin et al., 2023a; Camisassa et al., 2023).

1.6 Binarity

The white dwarf evolution and physics discussed so far is under the assumption that all white dwarfs are formed in isolation. However, five out of the ten closest white dwarfs

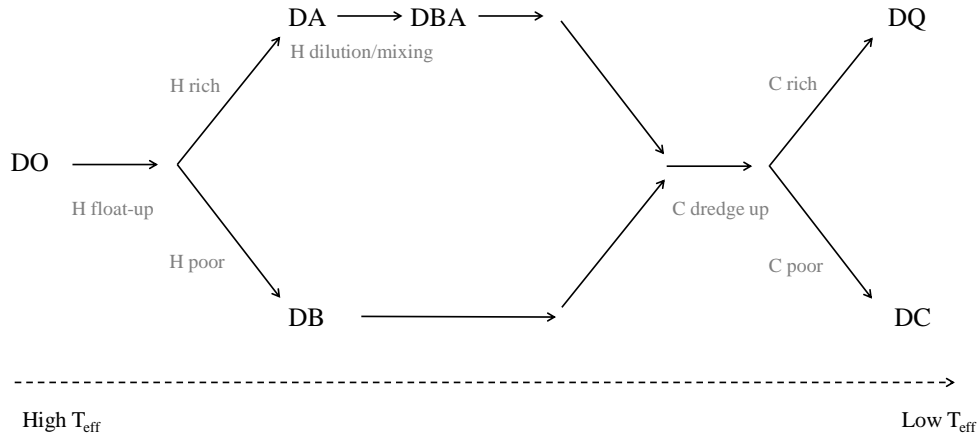


Figure 1.7: A simplified schematic showing the evolution of a white dwarf with an initially He-rich atmosphere. This figure was inspired by a similar figure in Bédard (2024).

to the Sun are members of binary or higher-order systems. The types and architectures of white dwarf binary systems vary greatly. All the binary systems considered in this thesis are split into two categories: wide and unresolved. This distinction is based on the ability of *Gaia* to resolve the two (or more) stars individually, where the on-sky resolution of *Gaia* is 0.4 arcsec.

Binary star systems are formed when a single collapsing gas cloud fragments during the star formation process (e.g. Kratter 2011). The stars are gravitationally bound to each other and orbit the centre of mass of the system. Higher-order systems are hierarchical; there is a close inner binary orbited by a wide tertiary, or in the case of quadruple systems, two pairs of stars are on short-period orbits and both pairs orbit each other on a longer period. If two stars are sufficiently close, the gravitational pull of the more massive star will cause the less massive star to undergo Roche lobe overflow, and the more massive star will begin accreting. All the binary systems containing a white dwarf within 40 pc (the distance limit considered in this thesis) are not currently accreting, and therefore I will not discuss interacting binaries in this chapter. There are a handful of local white dwarfs that are part of post-common envelope binary systems, which were close enough to each other that the system underwent common envelope evolution, during which the stars were interacting.

There are various ways of confirming the binarity of white dwarf systems, outlined below, which depend on the separation of the stars. The resulting orbital period distribution of some of these detection methods, specifically for double white dwarf systems, is shown

in Fig. 1.8.

Common proper motion

The proper motion of a source determines its astrometric movement across the sky. The proper motions of individual white dwarfs are calculated and compared to other stars within their vicinity to determine if the white dwarfs have any common proper motion companions. *Gaia* provides two-dimensional astrometry, enabling common proper motion stars to be easily identified. The combination of tangential velocity and projected separation from position and parallax are used to determine if two stars are in a bound system (Hollands et al., 2018b). This technique is utilised in Chapter 4 in order to identify all white dwarfs within 40 pc that have a wide companion. The radial velocity parameter can provide a further confirmation of binarity, however this parameter is challenging to determine for a large sample of white dwarfs without time-resolved high-resolution spectroscopy, and appropriate spectral features for this calculation are not always available. Wide double white dwarf binaries have been used to determine the initial-final mass relation, since they both formed at the same time but have different cooling ages, meaning their main-sequence lifetimes can be inferred (Andrews et al., 2015; Hollands et al., 2024).

Proper motion anomaly

Gaia provided, as part of its DR3, a non-single star catalogue. Sources for which the proper motion changes over time due to orbital acceleration were identified by *Gaia*, and these are provided in the two-body orbit catalogue (El-Badry, 2024). As shown in Fig. 1.8, the proper motion anomaly solutions in *Gaia* cover a narrow range of periods, as they depend on the baseline of *Gaia* and *Hipparcos*. This binary detection method is reliable for nearby sources, but becomes less effective at larger distances.

Spectroscopic binaries

The observed spectral features of an unresolved compact binary system will be redshifted or blueshifted throughout the orbital period of the system. In some cases, such as for two almost equally bright hot white dwarfs, the spectral features of both stars will be visible, clearly indicating that the system is a binary. However, in many double white dwarf systems the absorption lines from only one of the stars is detectable (Napiwotzki et al., 2020). Similarly, in close white dwarf – main sequence binaries, the light from the white dwarf is outshined by the main sequence star, so only the main sequence spectral features are visible. By measuring radial velocities, the mass ratio of the components of the binary can be calculated. Time-series high-resolution spectroscopic observations around key absorption lines are required to determine radial velocities of spectroscopic binaries.

Eclipsing

If the orbital plane of the binary is in the line-of-sight of the observer, the stars in a binary

may eclipse each other. This is unusual for white dwarf systems because the white dwarf radius is so small, and therefore only systems with favourable orientations will eclipse. However, within 40 pc there are some known eclipsing binary systems containing a white dwarf, such as the white dwarf – M-dwarf system RR Cae (Bruch and Diaz, 1998). Eclipses are identified through photometric light curves. If the baseline of photometric observations is long enough, multiple eclipses may be detected, and the orbital period of the system can be determined.

Evidence of a stellar merger

From simulations, Temmink et al. (2020) predicted that 10–30 per cent of all observable single white dwarfs are the products of binary mergers. Many merger products are challenging to identify, but there are some properties that certain merger products have that single white dwarfs do not. Temmink et al. (2020) found that 30–45 per cent of white dwarfs with masses above $0.9 M_{\odot}$ are merger products. Therefore, white dwarfs with high masses are more likely to have formed from a merger than average mass white dwarfs. Kinematic properties of white dwarfs provide observational evidence of mergers; they can place white dwarfs in old stellar populations, and yet their ages make them appear inconsistently young. The reason for this discrepancy is that white dwarf merger products take longer to evolve than single white dwarfs, and therefore the ages of these merger products would be underestimated if fitted with single star models. Therefore, the kinematic inconsistency is indicative of a merger event. Hot DQ, warm DQ and DAQ spectral types are all typically massive, and also show photometric variability consistent with fast rotation, both of which are characteristics of merger products (Dunlap and Clemens, 2015; Kilic et al., 2024). The carbon in the atmospheres of these white dwarfs may have been brought to the surface during a merger event (Dufour et al., 2007b). Finally, it was recently observed that 5–9 per cent of massive white dwarfs stop cooling for at least 8 Gyr due to ^{22}Ne distillation (Bédard et al., 2024). An explanation for these ^{22}Ne -rich white dwarfs are that they are the products of the mergers of white dwarfs with subgiant stars (Shen et al., 2023). This observational evidence of a cooling delay has identified a subset of the merger product population.

Over-luminosity

An indirect method for detecting candidate unresolved double white dwarfs consists of fitting their photometry or spectra with a single-star model and checking for inconsistencies. The combined light from an unresolved double white dwarf system will make it appear over-luminous compared to a single white dwarf, and therefore the assumed radius when fitted with a single star model will be overestimated, and the mass underestimated. When fitting a sample of white dwarfs, as in Chapter 4, candidate double white dwarfs can be identified by implementing a mass or $\log(g)$ cut to identify those stars that are not massive

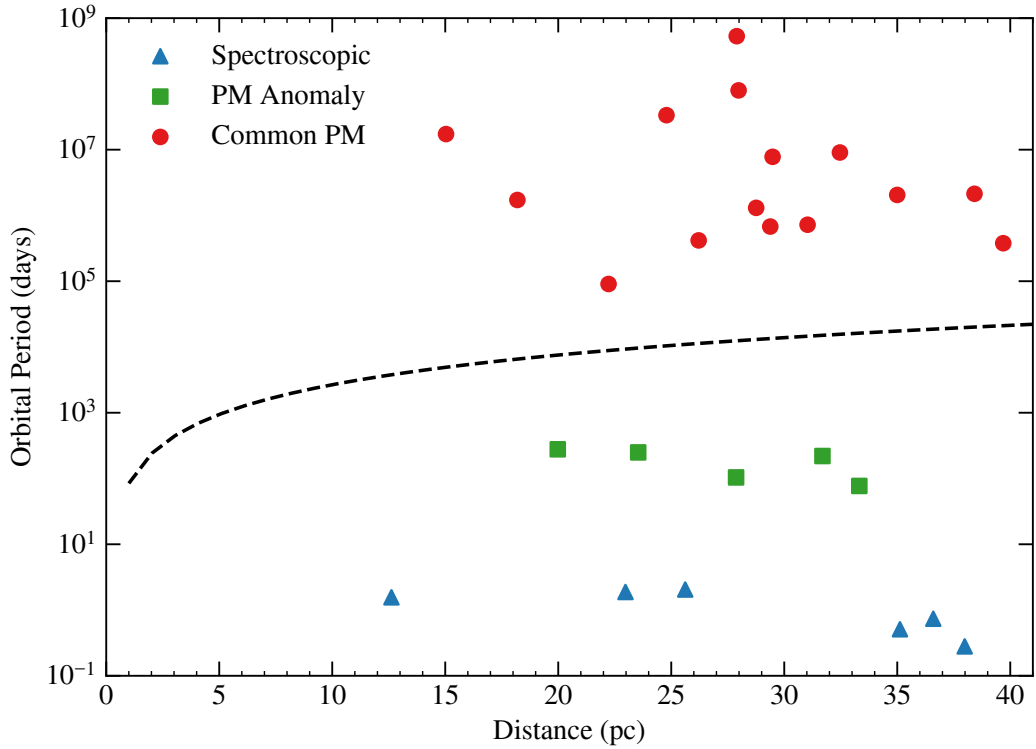


Figure 1.8: Examples of double white dwarf binaries within 40 pc that have been detected using different methods: spectroscopic (radial velocities), proper motion anomaly, and common proper motion. The dashed line is the *Gaia* resolution as a function of distance.

enough to have become white dwarfs within the age of the Universe. In some cases, both stars will have similar masses and appear over-luminous, but occasionally one of the white dwarfs is genuinely very low-mass (Sun and Arras, 2018). These extremely low-mass white dwarfs can only have formed in binary systems where the companion has stripped some of its mass (Marsh et al., 1995). Therefore, either way, a low-mass white dwarf is likely to be an unresolved double white dwarf system.

Renormalised unit weight error

The renormalised unit weight error (RUWE) parameter is another parameter provided by *Gaia* (Lindgren et al., 2018). In *Gaia* DR3, all sources were fitted with a single-star astrometric model, and the RUWE provides a metric for how well the single-star model fits to the astrometry. Belokurov et al. (2020) determined that *Gaia* sources with $\text{RUWE} \geq 1.4$ could possibly be unresolved multiple-star systems, but mentioned that a high RUWE could also be caused by other contamination effects such as a nearby on-sky source. Therefore high-RUWE white dwarfs do not confirm a hidden companion, but are ideal targets for observational follow-up by methods such as those listed above.

1.7 Magnetism

Circularly polarised light originating from a white dwarf was first detected by Kemp et al. (1970), which corresponded to a surface magnetic field strength of tens to hundreds of MG. The spectrum of the first magnetic white dwarf, WD 1900+705, is labelled as the 300 MG spectrum in Fig. 1.9. Following this discovery, many white dwarfs have been found to harbour magnetic fields ranging from 10^4 to 10^9 G, although the lower observational limit depends on the spectral type and the availability of spectropolarimetric observations. The exact origin of these order-of-magnitude spanning magnetic fields in white dwarfs is still debated, and some leading theories will be discussed in this section.

As shown in Fig. 1.9, the presence of a magnetic field in a white dwarf causes Zeeman splitting of spectral features, and depending on the field strength, the splitting is in one of three regimes. Weakly magnetic white dwarfs experience linear splitting, corresponding to the removal of the quantum number m_l degeneracy, which causes the Balmer lines to split into three components: π corresponding to $\Delta m_l = 0$ and σ_{\pm} corresponding to $\Delta m_l = \pm 1$ (Ferrario et al., 2015). Higher field strengths induce quadratic splitting, which is caused by the removal of the quantum number l degeneracy. The π components are shifted in this regime, and it impacts higher-order lines at lower field strengths. The most highly magnetic white dwarfs experience fully mixed splitting, where the n quantum number becomes degenerate. The effect of increasing field strength on the splitting is demonstrated in Fig. 1.10, which demonstrates Zeeman splitting of the $H\alpha$ and $H\beta$ lines from 10 G up to 1000 MG.

The technique used for the detection of magnetic fields in white dwarfs depends on both the spectral type of the white dwarf and the strength of its field. In many cases, the field strength can be determined directly by comparing the curves in Fig. 1.10 with the spectrum of the white dwarf. The field strengths of white dwarfs with no spectral features (DC), those with weaker fields than can be picked up with Zeeman splitting, and those with such strong fields that features are blended and indistinguishable, can be determined using spectropolarimetry. Light from a magnetic white dwarf can be linearly and/or circularly polarised, and spectropolarimetry measures the polarisation of the light as a function of wavelength, via the quantity Stokes V/I (Landstreet, 2015). The $\Delta m_l = \pm 1$ transitions are circularly polarised in opposite directions, and the extent of this polarisation quantifies the magnetic field strength.

Based on statistics from the 20 pc white dwarf sample, which has been exhaustively analysed for magnetism, 22 per cent of white dwarfs harbour a detectable magnetic field (Bagnulo and Landstreet, 2021). Leading theories for the generation and retention of magnetic fields in white dwarfs include:

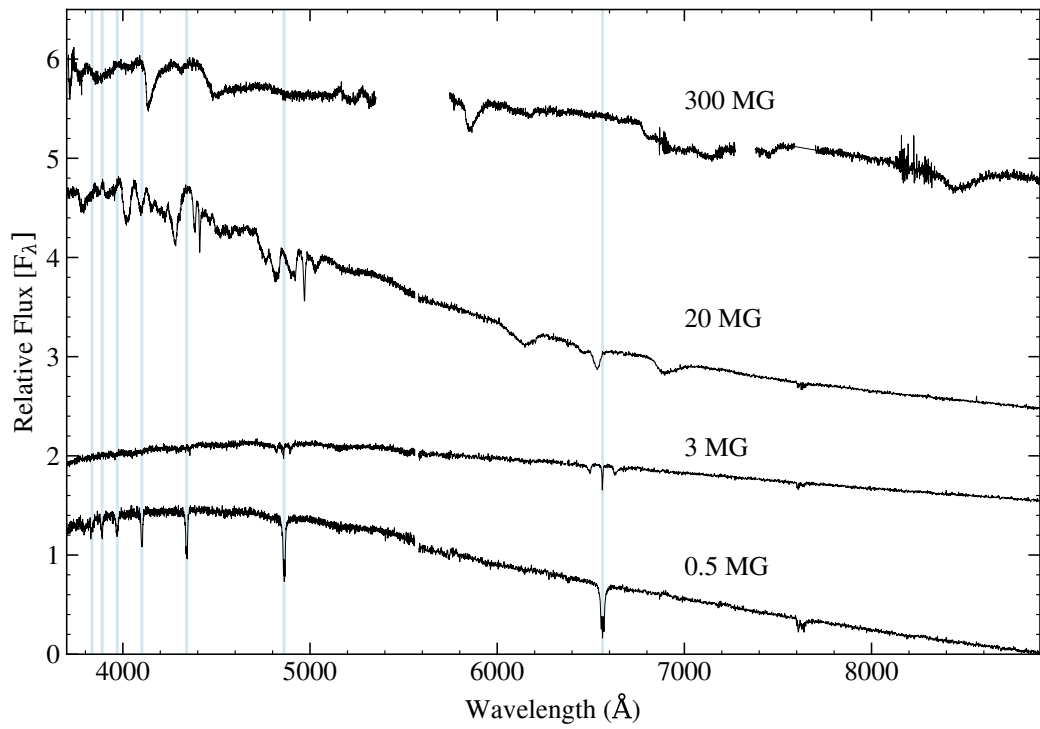


Figure 1.9: VLT X-shooter and WHT ISIS spectra of magnetic hydrogen atmosphere white dwarfs (DAH) of various field strengths. Wavelengths of Balmer lines are indicated by blue lines. Spectra are not flux-calibrated, and have been vertically offset for visual clarity.

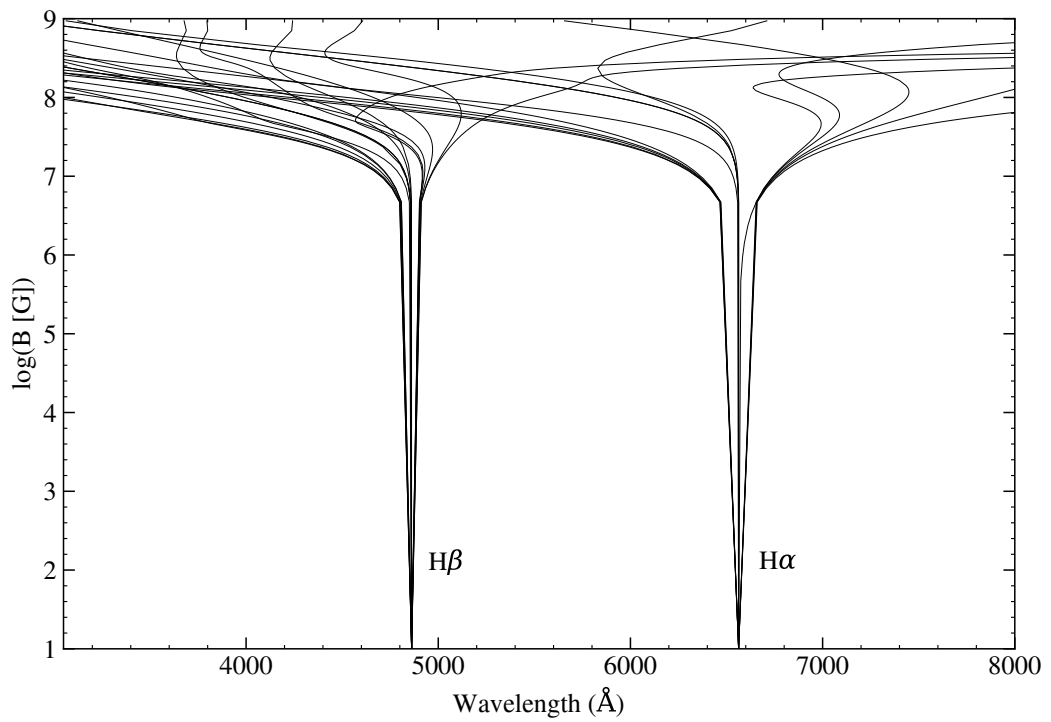


Figure 1.10: A spaghetti diagram showing the Zeeman splitting of H α and H β spectral lines in a magnetic white dwarf, depending on the field strength, $\log(B)$, of the white dwarf. Data are from Friedrich et al. (1996).

1. (a) The present field is a fossil remnant from a previous evolutionary stage of the star and was amplified as the star evolved.
(b) The field emerged due to the generation of a dynamo during the main sequence or giant phase.
2. The field emerged due to the generation of a dynamo in the white dwarf which formed as the white dwarf cooled.
3. The field was generated by a dynamo that formed as a result of binary evolution or a merger event.

If it were the case that magnetic fields in white dwarfs were caused by fossil fields originating from their progenitor stars, these progenitors could be the magnetic chemically peculiar Ap and Bp stars, which have magnetic fields of the order of kG. The fields would then need to be amplified in order to produce the MG fields commonly detected in white dwarfs (Wickramasinghe and Ferrario, 2005). Few young, typical-mass white dwarfs are magnetic, and the frequency of magnetism in white dwarfs appears to increase as a function of age, which contradicts the fossil field theory (Bagnulo and Landstreet, 2022).

As a white dwarf crystallises, carbon and oxygen in the core are separated during phase separation. The crystallisation process causes Rayleigh–Taylor instabilities in the interface between the liquid mantle and the solid core. The convective region in which these instabilities occur can induce a dynamo (Isern et al., 2017; Ginzburg et al., 2022). A dynamo requires an electrically conductive fluid medium (white dwarf plasma), kinetic energy provided by rotation, and an internal energy source to drive convection within the fluid. The onset of magnetism in a typical mass white dwarf as it ages, as observed by Bagnulo and Landstreet (2022), indicates that crystallisation could be a potential mechanism for magnetic field generation. A crystallisation dynamo can generate fields up to 0.1 MG in field strength (Isern et al., 2017), which could explain some currently observed white dwarfs, however many observed magnetic white dwarfs have much stronger fields than 0.1 MG, and additionally many magnetic white dwarfs have not begun to crystallise, so there must be additional mechanisms responsible for generating magnetic fields in white dwarfs.

Binary evolution processes could also potentially generate magnetic fields in white dwarfs. During common envelope evolution, a low-mass stellar companion can be disrupted by the white dwarf into an accretion disc and engulfed into the star, which would generate a dynamo that amplifies the magnetic field in the white dwarf (Nordhaus et al., 2011). This engulfment process means that the resulting magnetic white dwarf would be a single star once the common envelope phase has ceased. Additionally, the merger of two white dwarfs could also generate a dynamo in the differentially rotating and convective corona that forms

as a result of the merger (García-Berro et al., 2012). A high-mass white dwarf ($> 1 M_{\odot}$) could have formed from the merger of two more typical-mass white dwarfs. Most high-mass magnetic white dwarfs have high field strengths, indicating a separate formation channel to the lower-field average mass white dwarfs, however there are many exceptions (Bagnulo and Landstreet, 2022).

Light curves of magnetic white dwarfs are often variable (see e.g. Hernandez et al. 2024). This variability may be caused by magnetic spots that cause the brightness to vary as the star rotates, however this is only possible if the atmosphere of the white dwarf is convective, and magnetism may inhibit convection in white dwarfs. Another possibility is that the non-uniform field causes varying Zeeman shifts as the star rotates, and therefore the brightness varies over the rotation period (Hernandez et al., 2024). Metal-polluted magnetic white dwarfs have been observed to display photometric variability, which line blanketing cannot account for (Bagnulo et al., 2024a,b).

1.8 Planetary systems

In recent years, scientific and instrumental improvements have enabled the precise characterisation and interpretation of the atmospheric composition of exoplanets (see reviews by Madhusudhan, 2019; Kempton and Knutson, 2024). In contrast, much less is known about the composition of exoplanet interiors (see chapter by Noack et al., 2024). White dwarfs present a unique opportunity to characterise the chemical composition of the interiors of exoplanets via the observation of disrupted planetesimals. Most known planetary systems around main-sequence stars will eventually end up orbiting a white dwarf, and thus the study of current white dwarf planetary systems should on average reproduce main sequence exoplanet properties.

Atmospheric pollution

White dwarfs are chemically stratified, meaning metals (i.e. not hydrogen or helium) should not be visible in their atmospheres. Internal processes can cause metals to become visible, such as radiative levitation processes in white dwarfs above 20 000 K (Chayer et al., 1995), and the dredge up of carbon producing broad Swan band features in DQ white dwarfs (Blouin and Dufour, 2019). Additionally, metal lines originating from nearby ISM clouds can be detected in white dwarf spectra (e.g. Sahu et al. 2024). However, metal lines of photospheric origin imply accretion of planetary material caused by the tidal disruption of planetary bodies (Jura, 2003; Farihi et al., 2009), and provide a unique insight into the interior composition of exoplanets. Accretion onto these so-called ‘polluted’ white dwarfs must be ongoing or recent, otherwise the metals would have sunk out of the atmosphere and would no longer be detectable.

The first metal polluted white dwarf observed was vMa 2, a cool DZ, which is the closest single white dwarf to the Sun (van Maanen, 1917). The observations of vMa 2 with photographic plates, which showed calcium spectral features, were the first evidence of exoplanetary systems (Farihi, 2016). For subsequent decades the composition of vMa 2 was thought to be typical for cool, helium-rich white dwarfs, and models of a ‘vMa 2 composition’ were used to fit DC spectra (e.g. Liebert 1976). However, the metal features are instead a result of the accretion of planetary debris.

High-resolution optical spectroscopy has since revealed that 25 per cent of DA white dwarfs have photospheric metals (Zuckerman et al., 2003), and UV spectroscopy has showed that over 50 per cent of DA white dwarfs in the T_{eff} range 17 000 – 27 000 K have photospheric metal detections (Koester et al., 2014). Photospheric metal lines have been detected in the atmospheres of over 1700 polluted white dwarfs (Coutu et al., 2019; Williams et al., 2024). As shown in Fig. 1.11, 75 per cent of polluted white dwarf spectra contain only one metal line, due to observational biases or targeted searches (Williams et al., 2024), but a subset show many metal species in their spectra. This subset is particularly useful, as the relative fractions of the different metals in the atmosphere inform on the composition of the accreted planetary material.

Most polluted white dwarfs in the solar neighbourhood have accreted rocky material (e.g. Zuckerman et al. 2007; Trierweiler et al. 2023), the compositions of which typically correspond to chondritic meteorite or bulk Earth compositions. White dwarfs have also been observed to have accreted core, crust or mantle-rich fragments of differentiated planetesimals (e.g. Gänsicke et al. 2012; Hollands et al. 2018a; Buchan et al. 2022). There are additionally some detections of an excess of volatile species and hydrogen, possibly due to the accretion of water-rich or icy planetary bodies, which commonly requires UV spectroscopy to detect (e.g. Farihi et al. 2013; Raddi et al. 2015; Klein et al. 2021).

Dust and gas discs

Tidally disrupted planetary bodies produce circumstellar discs of material which are then accreted by their white dwarf host (Debes and Sigurdsson, 2002; Jura, 2003; Veras et al., 2014). Once material is within the Roche radius, the point inside which material becomes tidally disrupted by the white dwarf, it forms a dust disc. Closer to the white dwarf, the dust sublimates such that only gas is present, which is subsequently accreted onto the white dwarf (Veras et al., 2024). A white dwarf gas disc reveals itself through emission features in optical white dwarf spectra (e.g. Gänsicke et al. 2006, 2007, 2008). The morphology of these gas discs can be determined with the Doppler tomography technique, which indicates that gas discs can be dynamically variable (Manser et al., 2016), and can undergo general relativistic precession (Cauley et al., 2018).

The first white dwarf dust disc was observed by Zuckerman and Becklin (1987) at the

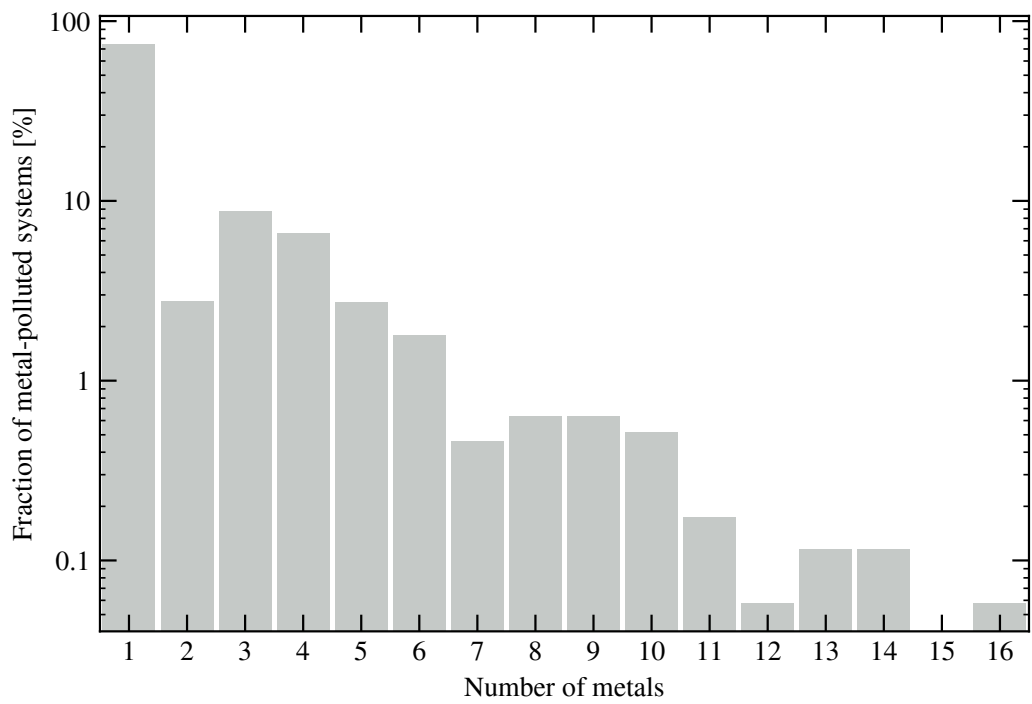


Figure 1.11: The fraction of all known polluted white dwarfs with a given number of metals, correct as of Feb. 2025. Data provided by J. T. Williams.

nearby polluted white dwarf G 29–38, for which there have since been detections of x-rays indicating ongoing accretion (Cunningham et al., 2022). Dust discs have been observed in 1–3 per cent of metal polluted white dwarfs (Farihi et al., 2009) via the detection of an excess at IR wavelengths (e.g. Jura et al. 2007a,b; von Hippel et al. 2007). These discs should be commonplace around polluted white dwarfs, however most white dwarf dust discs emit insufficient flux to be detected by IR facilities such as *Spitzer* (Rocchetto et al., 2015). Recently, *JWST* has detected dust discs showing silicate molecular features in the spectra of 12 out of a sample of 36 polluted white dwarf targets (Farihi et al., 2025).

It is debated if dust discs are generated from the stochastic accretion of larger objects, meaning the disc is not replenished during the accretion event (Jura et al., 2009; Farihi et al., 2012), or if the discs are created from the continuous accretion of small rocks (Jura, 2008; Wyatt et al., 2014). If the former were the case, the accretion rates onto the white dwarf would decay exponentially over time until the disc is fully depleted (Jura et al., 2009). If the latter were true, a balance between long-term accretion from a continuously replenished disc, and diffusion of metals, could be reached, forming a so-called steady state of accretion and diffusion (Koester, 2009).

Direct planetary detections

To date, there have only been a handful of major planet candidates detected orbiting white dwarfs, all with different architectures (Veras, 2021). The first to be detected was a circumbinary planet orbiting a white dwarf–pulsar binary (Thorsett et al., 1993). The second, a $7 M_{\text{Jup}}$ gas giant, is in a wide orbit with a white dwarf (Luhman et al., 2011; Voyer et al., 2025). The third is an evaporating ice giant on a 10-day orbit with spectral features indicating a volatile-rich gas disc (Gänsicke et al., 2019). The fourth detection was the transit of a gas giant orbiting a white dwarf at 0.02 au, where the white dwarf is a wide companion to a close M dwarf–M dwarf binary (Vanderburg et al., 2020). Recently, a possible gas giant planet orbiting between 0.1–2 au was observed by *JWST* (Limbach et al., 2024). All the intact planet candidate detections so far have been giant planets due to observational biases favouring giant planet detections.

A subset of white dwarfs display periodic transits with depths of up to 50 per cent, caused by eclipsing material (e.g. Vanderburg et al. 2015; Vanderbosch et al. 2020). These transits are not from intact planets but instead from debris that produces many transit features that repeat on periodic timescales, the fundamental periods of which can drift over weeks to months (Farihi et al., 2022).

Delivery of polluting material

The mechanisms used to perturb planetary material and deliver it to the within the Roche radius of the white dwarf depend on the size of the polluting material. Small objects, such as

pebbles, can be pulled in towards the Roche sphere by forces from radiation and magnetism (Veras et al., 2024). However, bodies that are asteroid-sized or larger require gravitational interactions from planets in the system or even stellar companions in order to deliver the bodies to within the Roche radius. The wealth of observational evidence from atmospheric pollution indicates that the most common type of planetary material polluting white dwarfs is from dry, rocky asteroids (Jura, 2003). Only one planet is required to perturb the orbits of asteroids sufficiently that they become eccentric enough to pass within the Roche radius (e.g. Bonsor et al. 2011). Based on dynamical arguments, moons make up a non-negligible portion (≈ 1 per cent) of white dwarf polluters (Trierweiler et al., 2022). It is unlikely that objects as large as terrestrial planets or giant planets are the origin of polluting material, although they are likely to be the cause of the perturbations of orbits of smaller bodies.

1.9 Volume samples and the Gaia revolution

Some of the brightest and closest white dwarfs to the Sun were identified and observed spectroscopically as long ago as the 1910s. However, the white dwarf luminosity function peaks at faint magnitudes, and therefore most white dwarfs are cool and faint, and even some of the most nearby white dwarfs are challenging to identify. Within the last two decades, many local white dwarfs have been discovered through spectroscopic and photometric observations (Bergeron et al., 1997, 2001; Liebert et al., 2005; Kawka and Vennes, 2006; Gianninas et al., 2011; Sayres et al., 2012; Kawka and Vennes, 2012, and others). The Research Consortium on Nearby Stars (RECONS) produced a dedicated series of explicit searches for local white dwarfs based on parallax measurements (Subasavage et al., 2007, 2008, 2009, 2017). Many local white dwarfs were missed from these surveys because of a lack of comprehensive parallax measurements for faint, nearby objects. The first space-based mission designed to determine the parallaxes of nearby stars, *Hipparcos*, was launched in 1989 and provided high-precision astrometry and parallax measurements for over 100 000 stars via the *Hipparcos* catalogue (Perryman et al., 1997), however due to their faintness just 20 white dwarfs were observed by *Hipparcos* (Vauclair et al., 1997).

Volume-limited samples of astronomical objects are unbiased and often representative of the overall population of those objects. Magnitude-limited samples instead provide a subset of the brightest objects. In the case of white dwarfs, a magnitude-limited sample would eliminate a large portion of the white dwarf population, as shown in Fig. 1.12, since they cool rapidly and cooler white dwarfs are faint. Studies of the local white dwarf population within 13 pc, 20 pc and 25 pc volumes were carried out by Holberg et al. (2002, 2008, 2016) and Giammichele et al. (2012). Limoges et al. (2015) carried out the first dedicated effort to identify white dwarfs within a 40 pc volume, which was limited to the

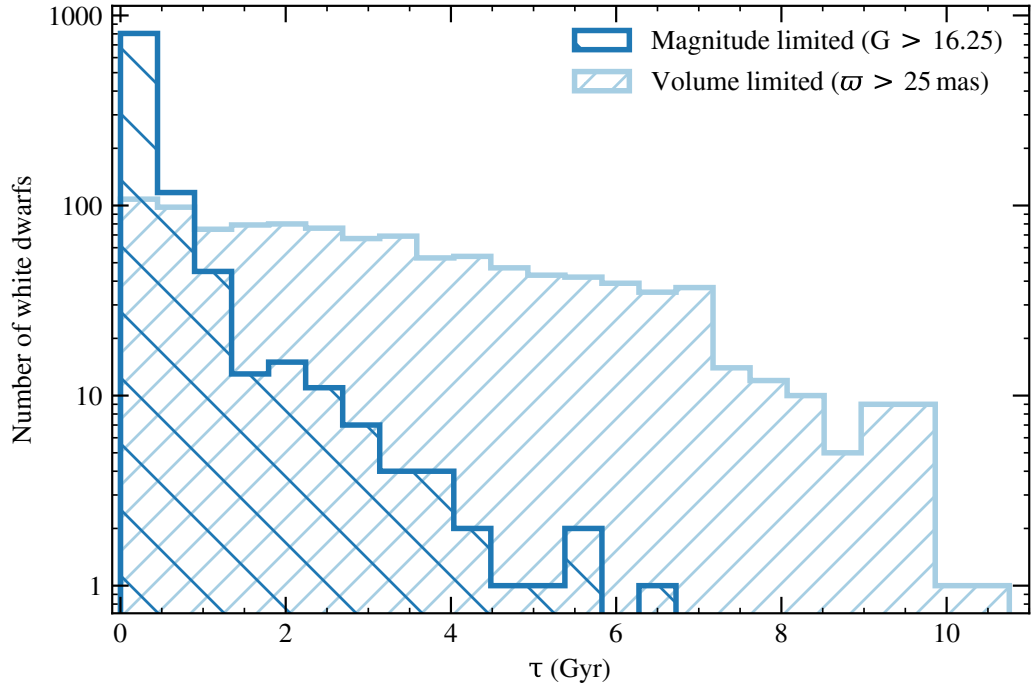


Figure 1.12: The difference between a magnitude-limited and volume-limited sample of white dwarfs, where both samples were selected from Gentile Fusillo et al. (2021). The volume-limited sample contains all white dwarfs with parallaxes greater than 25 mas, corresponding to the 40 pc volume. The magnitude cut at $G < 16.25$ was chosen to create a magnitude-limited sample with the same number of white dwarf candidates as in the 40 pc sample (≈ 1100), given an additional cut of white dwarf probability > 0.75 (Gentile Fusillo et al., 2021). Cooling ages, τ , were calculated with models from Bédard et al. (2020), assuming a pure-H composition in all cases, as not all white dwarfs in the magnitude-limited sample have been observed spectroscopically. This figure was inspired by a similar figure in Bagnulo and Landstreet (2022).

northern hemisphere and resulted in 281 new discoveries. None of these volume surveys were complete with spectroscopic follow-up.

The *Gaia* satellite was launched in 2013 as a successor to *Hipparcos*, and has observed over a billion objects in the Milky Way (Gaia Collaboration et al., 2016). *Gaia* provides photometry in three bands: a broad G band, and narrower (but still relatively broad) BP and RP bands. *Gaia* additionally provides low-resolution spectra of a subset of sources (Gaia Collaboration et al., 2023) and radial velocity measurements from the onboard radial velocity spectrometer (Recio-Blanco et al., 2023). The magnitude limit of *Gaia*, $G = 20.7$, is substantially fainter than *Hipparcos*, and therefore over 350 000 white dwarfs had their parallaxes determined for the first time by *Gaia* (Gentile Fusillo et al., 2021).

Following *Gaia* DR2, the first all-sky *Gaia* catalogues of white dwarf candidates with precise parallaxes were released (Jiménez-Esteban et al., 2018; Gentile Fusillo et al., 2019). Hollands et al. (2018b) compiled and analysed the volume-complete 20 pc white dwarf sample from *Gaia* DR2. *Gaia* DR3 has further improved our understanding of the local stellar population within 100 pc, which is nearly volume-complete (Gaia Collaboration et al., 2021b; Gentile Fusillo et al., 2021; Jiménez-Esteban et al., 2023). Cooling white dwarfs have a relatively large range of absolute *Gaia* magnitudes ($8 \lesssim M_G \lesssim 18$ mag). In particular, the very faint end of the white dwarf luminosity function, which includes ultra-cool white dwarfs from old disc and halo stars (Hollands et al., 2021; Kaiser et al., 2021; Bergeron et al., 2022; Elms et al., 2022), can only be observed up to a distance of 40–100 pc given the *Gaia* limiting magnitude. A sample which includes all ages and types of white dwarfs can only be achieved for 40–100 pc, therefore a volume-limited sample out to these distances is necessary. Almost every white dwarf candidate within the 40 pc volume has now been confirmed with optical spectroscopy at medium resolution ($R > 1000$) and high signal-to-noise of > 30 (see Chapters 3 and 4 of this thesis).

1.10 Thesis outline

In this thesis, I will present my work on characterising and analysing white dwarfs in the solar neighbourhood. Chapter 2 describes the primary methodology used to identify and characterise white dwarfs and the fitting of white dwarf observations with atmosphere models. Chapter 3 outlines the optical spectroscopic observations and analysis of 248 new white dwarfs within 40 pc of the Sun, mostly within the southern hemisphere. Following the analysis in Chapter 3, the sample of white dwarfs within 40 pc is > 99 per cent complete with optical spectroscopic follow-up. The analysis of the full 40 pc white dwarf sample, the largest volume-complete white dwarf sample to date, is presented in Chapter 4. Chapter 5 presents a detailed analysis of two white dwarfs within 40 pc which are heavily polluted by planetary debris, and adopts an exponentially decaying disc model in order to constrain the type and mass of accreted material. Chapter 6 presents analysis of a smaller volume-limited sample of white dwarfs, within 13 pc, for which UV spectroscopy is available, and compares optical and UV parameters. Conclusions and avenues for future work are presented in Chapter 7.

Chapter 2

Methodology

2.1 Observations

2.1.1 Spectroscopy

Most of the observational data analysed in this thesis is spectroscopic data. Spectroscopic instruments disperse the light from an astronomical source into colours, outputting the flux of the source as a function of wavelength. Isaac Newton published his work on the refraction of white light through a prism (Newton, 1672), laying the groundwork for spectroscopy as a discipline. Joseph von Fraunhofer used prisms to observe the Sun, and detected not only the solar continuum but also many absorption lines (Fraunhofer, 1817). These features, known as ‘Fraunhofer lines’ are due to the absorption of the Sun’s light by elements in the solar atmosphere. The analysis of stellar absorption lines is fundamental in the study of white dwarfs, in order to determine not just the atmospheric composition, but also the temperature, mass, and age, as well as to interpret any pollution by planetary debris.

Modern spectroscopy utilises diffraction gratings to split light into its wavelength-dependent components. Astronomical diffraction gratings contain grooves that are similar in width to the wavelength of the incident light waves. These grooves are parallel and are etched onto transparent glass. Light with shorter wavelengths is diffracted more than light with longer wavelengths according to the grating equation,

$$n\lambda = d\sin(\theta), \tag{2.1}$$

where n is the order of the spectrum, λ is the wavelength, d is the spacing between the grooves, and θ is the angle of diffraction. Modern spectroscopic instruments tend to use arrays of charge-coupled devices (CCDs) in order to detect light. Once the telescope is pointed at an astronomical source, the CCDs count the number of photons emitted per

second from that source, since the number of electrons generated in each pixel of the CCD is proportional to the incoming flux from the source.

The resolution of a spectrograph, R , is given by $\lambda/\Delta\lambda$ where $\Delta\lambda$ is the spacing between two wavelength points. The diffraction-limited resolution is,

$$R = \frac{Wn}{d}, \quad (2.2)$$

where W is the grating width. Spectrographs are typically categorised into three groups: low-resolution ($R < 1000$), medium-resolution ($1000 < R < 10\,000$), and high-resolution ($R > 10\,000$). Low-resolution spectroscopic instruments use conventional gratings. High-resolution spectrographs such as Keck HIRES, as well as some medium-resolution spectrographs, such as VLT X-shooter, are instead comprised of echelle gratings. Echelle gratings are optimised to obtain high-order spectra by reducing the density of grooves and increasing the incidence angle according to equation 2.1, which therefore increases n in equation 2.2. A cross-disperser is used to ensure the high-order spectra that overlap in the wavelength plane do not overlap in the spatial direction of the detector, and are offset to form a two-dimensional grid of spectra. This setup removes the need for very long gratings or a very fine groove spacing, which are the alternative requirements for high-resolution spectra.

The spectra used in this thesis are either optical or UV, are either ground-based or space-based, and have different resolutions, depending on the observational requirements. Spectroscopic observations targeting the UV part of the electromagnetic spectrum must be undertaken by space-based instruments, since roughly 90 per cent of UV-B light is blocked by the Earth's atmosphere (Döhning, 2017). Ground-based spectroscopic instruments are effective at observing in the optical, however, because much less light in this region is blocked by the atmosphere. There is some telluric contamination from the Earth's atmosphere in optical ground-based observations, but this can be mitigated by dividing the spectrum by the telluric response of a calibration star, and by modelling the Earth's atmospheric absorption and correcting for it (e.g. Smette et al. 2015).

The effects of noise in spectra are reduced using binning and smoothing techniques. Spectral binning takes the data and places it into a desired number of bins, and returns the mean flux in each bin. This method preserves the information from the spectrum while reducing noise. Smoothing methods such as boxcar averaging can also mitigate the effects of noise. In boxcar averaging, for each wavelength point the data returned is the mean of some number of flux points around it. For example in a five-point boxcar average, each flux value becomes the mean of the original flux and the two datapoints either side of it. Reducing the noise in spectra enables genuine spectral features to be more reliably identified, and simplifies the process of fitting with models.

Most of the spectra presented in Chapter 3 were taken with the X-shooter spectro-

graph, Chapter 5 is an in-depth study of two Keck HIRES spectra, and Chapter 6 presents fits of mostly *HST* STIS spectra. Therefore in the below subsections, I will briefly discuss each of these three instruments in turn.

VLT X-shooter

The X-shooter spectrograph was installed on the VLT in Paranal, Chile (Vernet et al., 2011). It is mounted on the UT3, one of the four 8 m reflector telescopes on the VLT, at the Cassegrain focus. X-shooter has three spectral arms: UV-Blue (UVB), visible (VIS), and near-IR (NIR). These arms correspond to wavelengths of 3000 – 5600 Å, 5500 – 10 200 Å, and 10 200 – 24 800 Å, respectively. The medium-resolution capabilities of the UVB and VIS arms of X-shooter make it an ideal instrument for studying nearby white dwarfs; it has a broad wavelength coverage while maintaining sufficient resolution to detect key optical absorption features for white dwarfs. The limiting magnitude for X-shooter to achieve a signal-to-noise of 10 in one hour is 20–22 depending on the wavelength region, which corresponds well to the faintest white dwarfs within 40 pc of the Sun (see Chapters 3 and 4).

Keck HIRES

HIRES is a high-resolution optical spectrograph mounted at the 10 m Keck I telescope in Mauna Kea, Hawaii, USA (Vogt et al., 1994). The wavelength range of the spectrograph is roughly 3000 – 10 000 Å, and the resolution of HIRES ranges from 25 000 to 85 000 depending on the configuration. The high-resolution capabilities of HIRES make it ideal for studying metal-pollution in white dwarfs, as there are often many weak and narrow metal lines that would not be detected with a lower-resolution instrument. HIRES extends to the very blue part of the optical (3000 Å), which corresponds to the location of many optical metal lines that would be missed with other redder optical spectrographs.

HST STIS

STIS is a UV, optical, and near-IR spectrograph onboard *HST*, a space telescope in a low-Earth orbit. It has three detectors: one CCD which covers UV, optical and near-IR wavelengths (1710 – 10 270 Å), and two Multi-Anode Microchannel Arrays (MAMAs) that cover the far-UV (1150 – 1740 Å) and near-UV (1570 – 3180 Å). There are choices of low, medium, and high-resolution (echelle) gratings for these detectors, depending on the science objective. For the low-resolution gratings, wider long-slit apertures can be used to provide flux calibrated spectrophotometry. Narrower apertures improve the spectral purity and resolution but reduce flux calibration. The UV capabilities of STIS make it vital for observing white dwarfs, since the fluxes of hot white dwarfs peak in the UV, and many photospheric metal lines are easily detectable in the UV. Bright targets, such as some of the hot and nearby white dwarfs analysed in Chapter 6, can damage the MAMA detectors when they are observed with wide apertures. To mitigate for this, smaller apertures or higher

resolution gratings can be used.

2.1.2 Photometry

Photometric data is defined as the integrated flux, or magnitude, of an astronomical source. By obtaining photometric data over a range of UV, optical and IR wavelengths, a spectral energy distribution of a source can be created, and the parameters of the object can be determined via fitting of appropriate models. Photometric surveys such as GALEX, Pan-STARRS, 2MASS, and WISE provide data for the whole sky, or a portion of the sky. Due to surveys such as these, most white dwarfs within the solar neighbourhood have archival photometry available from the UV to the IR. Additionally, all *Gaia*-identified white dwarfs have *Gaia* photometry in three optical filters, which is sufficient for fitting with white dwarf atmosphere models to determine fundamental parameters (Gentile Fusillo et al., 2021).

The flux, F , which is the brightness of a source as observed from the distance, D , of the detector, is related to the source's inherent luminosity, L , via,

$$F = \frac{L}{4\pi D^2}. \quad (2.3)$$

Flux is often quoted in terms of flux density, either in per unit frequency (f_ν) or per unit wavelength (f_λ). These flux densities can be integrated across all frequencies or wavelengths to obtain the bolometric flux F_{bol} , as

$$F_{\text{bol}} = \int_0^\infty f_\nu d\nu = \int_0^\infty f_\lambda d\lambda. \quad (2.4)$$

Photometric data is often expressed in terms of magnitudes, which can be converted from fluxes according to the relation,

$$m_2 - m_1 = 2.5 \log_{10} \frac{F_1}{F_2}, \quad (2.5)$$

where m_1 and m_2 are the magnitudes of two sources, and F_1 and F_2 are the fluxes of those two sources. The second source in this equation is usually a zeropoint, based on a given magnitude system. Magnitudes are often calculated within a specific passband filter, for example the SDSS *ugriz* filters. The fluxes in this case will not be bolometric but instead integrated over the filter transmission function.

Magnitudes are commonly represented in one of two main systems: Vega and AB. The Vega magnitude system takes the magnitude of the star Vega as the zeropoint against which all astronomical sources are referenced. Vega was chosen as a standard star because it was known to be relatively bright and stable. However, Vega has a dust disc which appears as an excess above the photosphere at IR wavelengths (Sibthorpe et al., 2010), making it a

less-than-ideal calibration star. AB magnitudes are calibrated in terms of flux density, such that the equation,

$$m_{AB} = -2.5 \log_{10}(f_\nu) - 48.6, \quad (2.6)$$

always holds (Oke, 1974). Therefore a source with $f_\nu = 3.63 \times 10^{-20} \text{ erg cm}^{-2} \text{ s}^{-1} \text{ Hz}^{-1}$ has an AB magnitude of zero in every filter.

2.2 Models and fitting

2.2.1 Codes and models

Despite only making up the very outermost portion of the white dwarf, the atmosphere is the main region that is directly observable by spectroscopy and photometry. In recent decades, codes have been created that can model the atmosphere of a white dwarf for a given set of fundamental input parameters: effective temperature (T_{eff}), surface gravity ($\log(g)$) and in some cases abundances of H, C or other metals (e.g. Koester 2010; Bergeron et al. 2011; Tremblay et al. 2011a, 2013b, 2015; Blouin et al. 2018a). The codes calculate the physical structure of the atmosphere, including the temperature, density, pressure, and absorption coefficients as a function of depth, and then produce the surface intensities for UV, optical and IR wavelengths, which corresponds to the synthetic spectrum. The spectral line profiles are calculated considering pressure broadening effects including Stark broadening from charged particles (Tremblay and Bergeron, 2009) and neutral broadening for the Lyman series (Kowalski and Saumon, 2006). The atomic data used in the codes is taken from databases like the NIST Atomic Spectra Database. Examples of various synthetic spectra of pure hydrogen atmosphere white dwarfs are shown in Fig. 2.1.

In order to determine the best-matching parameters to a white dwarf spectrum or set of photometric points, a grid of models are created such that they can be run through a χ^2 or similar fitting mechanism. To generate these grids, a model atmosphere code is run many times for a variety of combinations of input parameters. This grid will have columns of T_{eff} , $\log(g)$, abundances if necessary, and the corresponding synthetic spectrum. In order to reduce the parameter space in which a χ^2 calculation will have to iterate through, the grids of models are generated to be within a certain range, e.g. $7 \leq \log(g) \leq 9$.

Evolutionary codes, such as STELUM, can model a white dwarf from its centre out to its atmosphere, and can then predict the evolution of these modelled stars (Bédard et al. 2022b and references therein). The physical processes incorporated into the white dwarf models include: the cooling processes discussed in Section 1.4, the equation of state, and stellar opacities. The chemical transport mechanisms that are modelled include:

chemical diffusion, gravitational settling, thermal diffusion, stellar winds, external accretion, convection, convective overshoot, semi-convection, and thermohaline mixing (a process where a gradient in temperature stabilises an unstable compositional gradient). STELUM and other evolutionary codes can determine both the mass and cooling age of a white dwarf, given a particular T_{eff} and $\log(g)$ (Bédard et al., 2020). The cooling age of a white dwarf is the time since the star became a white dwarf, and hence how long it has been cooling. To determine the total age of the star, the mass of the progenitor must first be calculated using an initial–final mass relation (e.g. Cummings et al. 2018; El-Badry et al. 2018). Then, the main-sequence lifetime can be determined using stellar evolution tracks, and can be combined with the cooling age to produce the total age.

2.2.2 Fitting

The method used for spectroscopic fitting of white dwarfs depends on the spectral type of the white dwarf, as well as the wavelength coverage and resolution of the spectrum. The general procedure is that the flux of the spectrum, or some portion of it, is compared to individual atmosphere models using a χ^2 calculation, and then least-squares fitting is used to minimise the reduced χ^2 value. The reduced χ^2 (χ^2_{ν}) statistic is determined using,

$$\chi^2_{\nu} = \frac{1}{\nu} \sum_i \frac{(O - E)^2}{E}, \quad (2.7)$$

where ν is the degrees of freedom, O is the observed value, and E is the expected value (i.e. the model value) at each datapoint i . The fit of the data to the model improves as χ^2_{ν} approaches one. The number of degrees of freedom is equivalent to the number of datapoints being fitted minus the number of free parameters in the model.

The models must be scaled to the distance of the star before fitting. The models are also convolved with a Gaussian prior to fitting in order to match the resolution to that of the spectroscopic observation. Tremblay et al. (2011a) models provide the absolute Eddington flux per unit stellar surface area, $F_{\text{Edd}}(\lambda) = F(\lambda)/4\pi$, which must be scaled according to the white dwarf distance, D , and the white dwarf radius, R , as,

$$f(\lambda) = 4\pi \left(\frac{R}{D} \right)^2 F_{\text{Edd}}(\lambda), \quad (2.8)$$

before the χ^2 calculation occurs. The value $f(\lambda)$ denotes the monochromatic flux at a given wavelength, with units dependent on the context, and the radius is determined from T_{eff} and $\log(g)$ using the mass-radius relation (e.g. Althaus et al. 2013; Bédard et al. 2020). The best-fitting model with the lowest χ^2_{ν} value corresponds to best-matching T_{eff} , $\log(g)$, and abundances to the data, along with uncertainties.

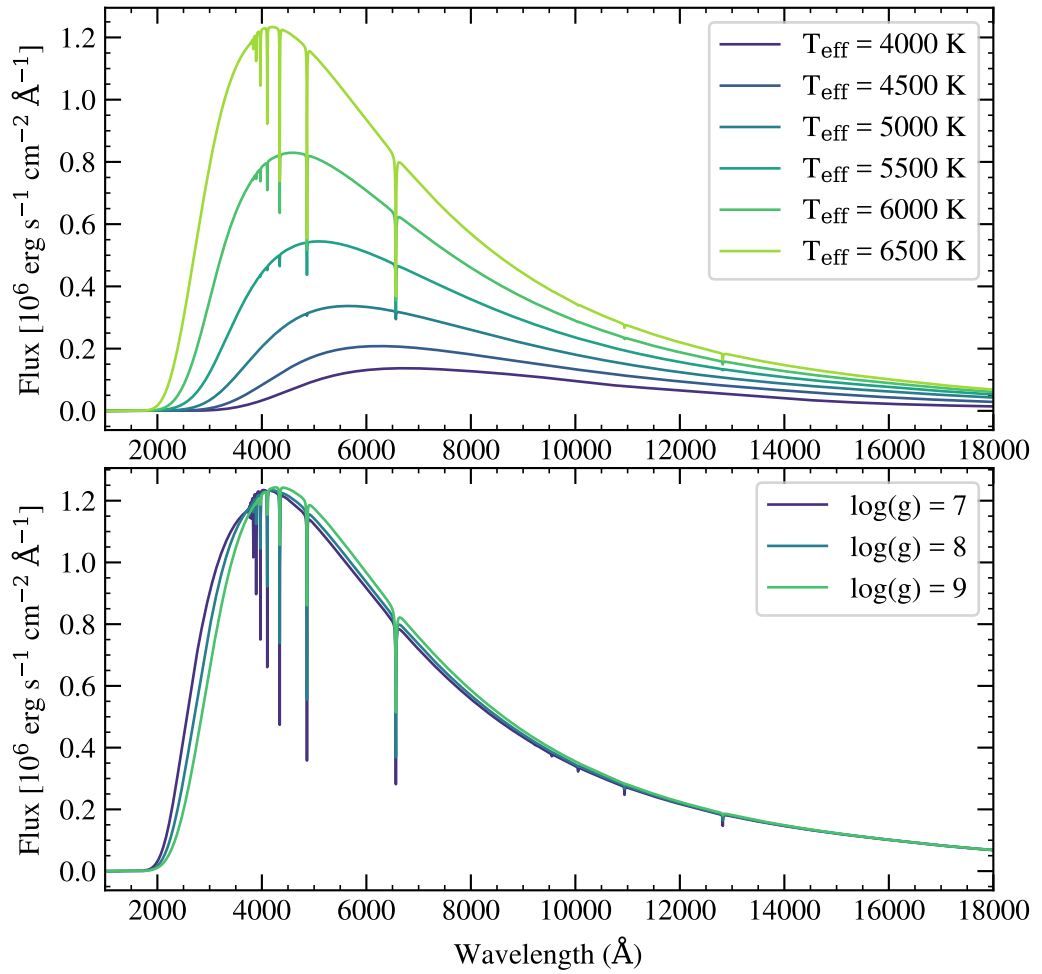


Figure 2.1: Demonstration of how model DA white dwarf spectra vary as T_{eff} and $\log(g)$ are varied. Top: Model spectra with $\log(g)$ fixed at 8, and T_{eff} varying from 4000 K to 6500 K. Cool white dwarfs are the primary focus of this thesis, which is why they are shown here. Bottom: Model spectra with T_{eff} fixed at 6500 K, and $\log(g)$ varying from 7 to 9.

For spectrophotometric data, such as *Gaia* XP spectra, or highly flux-calibrated spectra, such as *HST* STIS spectra, full white dwarf synthetic spectra can be compared to the data, provided the wavelengths of the synthetic spectrum have been interpolated onto the wavelength spacing of the observation (see e.g. Sahu et al. 2023).

To fit a set of photometric datapoints, the grid of models with the correct atmospheric composition (or an estimated composition) is selected, and synthetic apparent magnitudes, m , are calculated using the model fluxes. For photometric data with a photon-counter detector type, such as *Gaia* DR3 photometry, the following equation is used,

$$m = -2.5 \log \left(\frac{\int S(\lambda) f(\lambda) \lambda d\lambda}{\int S(\lambda) \lambda d\lambda} \right) + f_0, \quad (2.9)$$

where $S(\lambda)$ is the filter response function, $f(\lambda)$ is the model flux scaled to the distance of the white dwarf, and f_0 is the zeropoint flux for the given filter in the chosen magnitude system (Vega or AB, depending on instrument specifications). If instead the photometric data is from an energy-counter detector type, such as 2MASS and WISE, synthetic magnitudes are calculated using the equation,

$$m = -2.5 \log \left(\frac{\int S(\lambda) f(\lambda) d\lambda}{\int S(\lambda) d\lambda} \right) + f_0. \quad (2.10)$$

These synthetic magnitudes, calculated for the correct photometric filters for every model in the grid, are then compared with the observed magnitudes using a χ^2 calculation, and the best-fitting model is calculated using least-squares fitting.

For helium-atmosphere white dwarfs, a third parameter, H abundance, must be incorporated into the models alongside T_{eff} and $\log(g)$ prior to fitting. Similarly, for DQ white dwarfs with carbon features, the carbon abundance must be incorporated as a free parameter. For metal-polluted white dwarfs, only one metal abundance is varied in the models at a time. The grids of models from e.g. Koester (2010) will be generated for different values of T_{eff} , $\log(g)$, and abundance. An iterative procedure is commonly used when fitting DB, DQ and DZ white dwarf spectra. In this procedure, the abundance of H, C or metal is fixed and T_{eff} and $\log(g)$ are determined from a photometric fit. Then, T_{eff} and $\log(g)$ are fixed and the H, C or metal abundance is determined from a spectroscopic fit. These two fits are repeated until convergence.

For DA white dwarf optical spectra with at least two Balmer lines, those Balmer lines can be fitted using atmosphere models for an independent determination of T_{eff} and $\log(g)$. For this Balmer line fitting procedure, a section around each line is selected from the spectrum, and this line section is then normalised and a DA model from e.g. Tremblay et al. (2011a) is fitted in a similar way as outlined above (see e.g. Gianninas et al. 2011).

Chapter 3

New observations of southern hemisphere white dwarfs within 40 pc

In this chapter, I present a spectroscopic survey of 248 white dwarf candidates within 40 pc of the Sun; of these 244 are in the southern hemisphere. Observations were performed mostly with VLT X-shooter and the Southern Astrophysical Research Telescope (SOAR). Almost all candidates were selected from *Gaia* DR3. A total of 246 white dwarfs were confirmed, 209 of which had no previously published spectra, and two main-sequence star contaminants were identified. Of the confirmed white dwarfs, 100 displayed hydrogen Balmer lines, 69 had featureless spectra, and two showed only neutral helium lines. Additionally, 14 white dwarfs displayed traces of carbon, while 37 had traces of other elements that are heavier than helium. Thirty-five white dwarfs were found to be magnetic through the detection of Zeeman splitting of their hydrogen Balmer or metal spectral lines. High spectroscopic completeness (> 97 per cent) has now been reached, such that 1058 *Gaia* DR3 white dwarfs have been confirmed out of 1083 candidates within 40 pc of the Sun at all declinations, following the results of this chapter. The work presented in this chapter, plus additional plots of all new white dwarf spectra, was published in O'Brien et al. (2023). The majority of the spectra presented in this chapter were observed under European Southern Observatory programmes 0102.C-0351, 1103.D-0763, and 105.20ET.001, all with PI B. T. Gänsicke. The spectroscopic observations presented in this chapter were obtained between 2018 and 2023 by a large team of people (see co-author list of O'Brien et al. (2023)).

3.1 Introduction

Prior to the work presented in this chapter, the 40 pc *Gaia* sample was missing a significant number of southern hemisphere observations. Gentile Fusillo et al. (2021) identified 542 white dwarf candidates in the northern hemisphere within 40 pc using *Gaia* DR3, 531 of which were spectroscopically confirmed from the literature prior to this work (e.g. Tremblay et al. 2020; Gianninas et al. 2011; Kawka and Vennes 2012; Limoges et al. 2015; Subasavage et al. 2017). In McCleery et al. (2020), the 40 pc northern sample was analysed based on a DR2 catalogue, which contained 521 confirmed white dwarfs (Gentile Fusillo et al., 2019). In the southern hemisphere, Gentile Fusillo et al. (2021) identified 541 white dwarf candidates within 40 pc, of which 304 were spectroscopically confirmed from the literature prior to this work. This significant observational gap in the southern hemisphere needed to be filled before meaningful analysis of the volume-limited 40 pc white dwarf sample could occur.

In this chapter, I discuss the nature of 246 *Gaia* white dwarf candidates within 40 pc of the Sun, 34 of which have previous spectral type classifications in the literature. These newly confirmed white dwarfs were primarily observed with the X-shooter spectrograph on the VLT. Four of the sources lie outside of 40 pc but are within $1\sigma_{\varpi}$ of that distance. The majority of targets, 242, are located in the southern hemisphere ($\delta < 0$ deg), while the remaining 4 are in the northern hemisphere. In addition, 2 white dwarfs are presented that are not in the DR3 catalogue. Following the results presented in this chapter, the full *Gaia* 40 pc sample of white dwarf candidates has 1058 confirmed white dwarfs out of 1083 initial DR3 candidates (97 per cent spectroscopic completeness). Of the 25 remaining 40 pc white dwarf candidates in DR3, two were confirmed as main-sequence stars in this work, and 23 remained unobserved. In this chapter I analyse the composition and provide the fundamental parameters of these new white dwarfs. A detailed statistical analysis of the full 40 pc white dwarf sample appears in Chapter 4.

3.2 Observations

3.2.1 Catalogue photometry and astrometry

Gentile Fusillo et al. (2021) used spectroscopically confirmed white dwarfs from the Sloan Digital Sky Survey (SDSS) (Ahumada et al., 2020) to select regions of the *Gaia* DR3 HR diagram likely to be populated by white dwarfs. I selected white dwarf candidates from the catalogue of Gentile Fusillo et al. (2021) with a parallax cut of $\varpi - \sigma_{\varpi} > 25$ mas such that all sources are within $1\sigma_{\varpi}$ of 40 pc. For each source, Gentile Fusillo et al. (2021) provided a parameter, the probability of being a white dwarf (P_{WD}). Gentile Fusillo et al.

(2021) suggested using $P_{\text{WD}} > 0.75$ as a cut for the best compromise between completeness and contamination, and within 40 pc only eight candidates out of 1083 do not meet this cut, so I therefore included all 1083 candidates in the 40 pc sample for completeness. Observations of high-confidence candidates within the southern hemisphere that had no previously published spectral type or an ambiguous classification were prioritised, as the goal of this work was to increase the spectroscopic completeness of the overall 40 pc white dwarf sample. I use the `WDJhhmmss.ss ± ddmss.ss` naming convention introduced by Gentile Fusillo et al. (2019) throughout this chapter. For simplicity, I often shorten their WDJ names to `WDJhhmm ± ddm`.

The Gentile Fusillo et al. (2021) catalogue does not include white dwarfs in unresolved binaries with brighter main-sequence companions. Toonen et al. (2017) predicted that 0.5–1 per cent of white dwarfs are part of an unresolved WD+MS binary, therefore in 40 pc one would expect that only 5–10 of these systems would be excluded from the Gentile Fusillo et al. (2021) DR3 catalogue. These systems will be discussed in Chapter 4.

3.2.2 Spectroscopy

A total of 248 white dwarf candidates were observed, and details of these observations are presented in Table 3.1. The majority of targets (181) were observed by the VLT with the X-shooter spectrograph (Vernet et al., 2011), where slit widths of 1.0, 0.9 and 0.9 arcsec in the UVB (3000 – 5600 Å, $R = 5400$), VIS (5500 – 10 200 Å, $R = 8900$) and NIR (10 200 – 24 800 Å, $R = 5600$) arms, respectively, were employed. The X-shooter spectra were reduced following a standard procedure employing the `Reflex` pipeline (Freudling et al., 2013). The flux calibration technique used observations of hot DA white dwarfs obtained with the same instrument setup as the science spectroscopy, while telluric correction was performed using `molecfit` (Kausch et al., 2015; Smette et al., 2015). The signal-to-noise ratio of the X-shooter NIR spectra was insufficient for meaningful analysis, so is not discussed or analysed further.

Forty nine white dwarfs were observed using the Goodman spectrograph (Clemens et al., 2004) mounted on SOAR. The 930 line mm^{-1} grating was used in the M2 mode (3850 – 5550 Å) with a 1.5 arcsec slit. The data were reduced using the `iraf` package `ccdproc`, and extracted using `noao.twodspec.apextract`. Flux calibration was carried out using spectrophotometric standard stars observed on the same night and with the same setup. The 930–M2 mode does not cover any skylines, and since arcs were not taken close in time to the observations, radial velocities (RVs) from these observations are not reliable.

Two observations are presented which were taken with the ISIS instrument on the WHT and three observations using the Optical System for Imaging and low-Resolution Integrated Spectroscopy (OSIRIS) on the Gran Telescopio Canarias (GTC) (Cepa et al.,

Table 3.1: Log of spectroscopic observations, where wavelength ranges are those used for analysis in this chapter.

| Telescope/ Instrument | Programme IDs | No. of objects in this work | Wavelength Coverage [\AA] | Resolution (R) |
|--------------------------|----------------------------|--------------------------------|-----------------------------------------|--------------------------|
| VLTX-shooter | 0102.C-0351 | 181 | 3600 – 10 200 | UVB: 5400, VIS: 8900 |
| SOAR/Goodman | 1103.D-0763 | 49 | 3850 – 5550 | 1100 |
| | 105.20ET.001 | | | |
| | SO2017B-009 | | | |
| | SO2018A-013 SO2018B-015 | | | |
| Shane/Kast | – | 11 | 3600 – 7800 | 1900 |
| GTC/OSIRIS | GTC103-21A | 3 | 3950 – 5700 | 2200 |
| WHT/ISIS | ITP08 | 2 | 3730 – 7290 | Blue: 2000, Red: 3900 |
| Tillinghast/FAST | – | 2 | 3600 – 5500 | 1500 |

2000, 2003), which have the same setup as the observations reported in Tremblay et al. (2020)

Eleven observations were taken from the Kast Double Spectrograph mounted on the Shane 3 m telescope at the Lick Observatory. The 600/4310 grism was used for the blue, and either 830/8460 or 600/7500 gratings for the red, and slit widths of 1, 1.5, or 2 arcsec were adopted. Two observations from the FASt Spectrograph for the Tillinghast Telescope (FAST) at the F. L. Whipple Observatory are also shown. Instrument details for FAST can be found in Fabricant et al. (1998).

3.3 Atmosphere and evolution models

I have used spectroscopic and photometric data to determine spectral types by human inspection for all 248 observed white dwarf candidates. The classifications are based on the spectral types described in Table 3.2 (Sion et al., 1983). Spectral types were allocated visually according to the relative strength of absorption lines in the spectrum, with ‘H’ representing Zeeman splitting from the presence of a magnetic field. I have derived atmospheric parameters and chemical abundances using photometric and spectroscopic fitting, where appropriate. The notation $\log(X/Y)$ used in Table 3.2 and throughout this thesis refers to the logarithm of the number abundance ratio of any two chemical elements, X and Y.

Table 3.2: Definitions of all white dwarf spectral types discussed in this work, where photometric model composition refers to composition-selected Gentile Fusillo et al. (2021) parameters. Adopted parameters for DAZ, DZ and DQ white dwarfs in this work use tailored models and are shown instead in Tables 3.6–3.8.

| Spectral type (SpT) | Number in this work | Spectral features in order of strength | Photometric model composition |
|---------------------|---------------------|-----------------------------------------------|-------------------------------------------------------------------------------------|
| DA | 100 | Hydrogen Balmer | pure-H |
| DAH | 28 | Hydrogen Balmer + magnetic | pure-H |
| DB | 2 | Neutral helium | $\log(\text{H}/\text{He}) = -5$ |
| DC | 69 | Featureless | $\log(\text{H}/\text{He}) = -5$, pure-He below 7000 K, assumed pure-H below 5200 K |
| DAZ | 10 | Hydrogen Balmer + metal | pure-H |
| DZ | 12 | Metal | $\log(\text{H}/\text{He}) = -5$, pure-He below 7000 K |
| DZH | 5 | Metal + magnetic | $\log(\text{H}/\text{He}) = -5$, pure-He below 7000 K |
| DZA | 4 | Metal + hydrogen Balmer | $\log(\text{H}/\text{He}) = -5$, pure-He below 7000 K |
| DZAH | 2 | Metal + hydrogen Balmer + magnetic | $\log(\text{H}/\text{He}) = -5$, pure-He below 7000 K |
| DQ | 7 | Carbon (molecular bands) | $\log(\text{H}/\text{He}) = -5$, pure-He below 7000 K |
| warm DQ | 1 | Carbon (atomic lines) | pure-He |
| DQpec | 2 | Carbon (molecular bands, shifted wavelengths) | $\log(\text{H}/\text{He}) = -5$, pure-He below 7000 K |
| DQZ | 2 | Carbon + metal | $\log(\text{H}/\text{He}) = -5$, pure-He below 7000 K |
| DZQ | 1 | Metal + carbon | $\log(\text{H}/\text{He}) = -5$, pure-He below 7000 K |
| DZQH | 1 | Metal + carbon + magnetic | $\log(\text{H}/\text{He}) = -5$, pure-He below 7000 K |

3.3.1 Photometric parameters

T_{eff} and stellar radius can be derived for most white dwarfs using photometric and parallax fits to model atmospheres, providing the composition of the white dwarf atmosphere is known (Koester et al., 1979; Bergeron et al., 2001; Gentile Fusillo et al., 2021). In this work, I relied on the photometric parameters already made available in Gentile Fusillo et al. (2021). In brief, either pure-hydrogen (Tremblay et al., 2011b), pure-helium (Bergeron et al., 2011), or mixed hydrogen and helium (Tremblay et al., 2014) model atmospheres were used, depending on the spectral type (see Table 3.2), to fit the *Gaia* DR3 photometry to determine T_{eff} and radii of all white dwarfs in the sample. The H/He ratio for the mixed atmosphere models was fixed at $\log(\text{H}/\text{He}) = -5$ for all photometric fitting of DC white dwarfs above 7000 K. For DC stars within $5200 \text{ K} < T_{\text{eff}} < 7000 \text{ K}$ pure-helium models were used, as any hydrogen would be detectable at these temperatures. For DC white dwarfs below 5200 K it is difficult to constrain the atmospheric composition, as the $\text{H } \alpha$ line is difficult to detect with most ground- and space-based current or near-future spectroscopic instruments, so I assumed pure-hydrogen atmospheres (McCleery et al., 2020; Gentile Fusillo et al., 2020).

The $\log(g)$, masses and cooling ages were derived using evolutionary models (Bédard et al., 2020). Table 3.3 shows the derived parameters from a homogeneous set of photometric fits from Gentile Fusillo et al. (2021) using *Gaia* data only. In this work I also derived independent parameters from hybrid fits using spectroscopy and photometry for the DQ and DZ stars (see Section 3.3.3 for details).

3.3.2 Spectroscopic parameters

I derived T_{eff} and $\log(g)$ from spectroscopic fits of Balmer lines in non-magnetic DA white dwarfs using a Python implementation adapted from previous Balmer line fitting procedures described extensively in Tremblay et al. (2020); Liebert et al. (2005); Tremblay et al. (2011a) and Gianninas et al. (2011). This modern fitting code is part of the 4MOST multi-object spectroscopic (MOS) survey consortium pipeline (Chiappini et al., 2019; de Jong et al., 2019) and will also be a key resource for other MOS surveys such as WEAVE (Dalton et al., 2020). For these fits, I relied on DA models from Tremblay et al. (2011a) with 3D corrections from Tremblay et al. (2013a). Table 3.3 shows the spectroscopic parameters determined from this method. Only DA spectra with at least two visible Balmer lines were fitted spectroscopically. If there is only one spectral line available, either due to the T_{eff} and $\log(g)$ of the white dwarf or incomplete spectral coverage, the best-fit parameters cannot be well constrained. For DA white dwarfs below $\approx 5200 \text{ K}$ observed with X-shooter, Balmer lines from $\text{H } \beta$ and above become very weak, while T_{eff} and $\log(g)$ become degenerate when predicting the equivalent width of the $\text{H } \alpha$ line.

For the two DB white dwarfs in the sample, the 3D model atmospheres of Cukanovaite et al. (2021) were applied to obtain $\log(\text{H}/\text{He})$ and T_{eff} , under a fitting procedure similar to that of Bergeron et al. (2011). *Spectra of DB white dwarfs were fitted by E. Cukanovaite.* The DC white dwarfs and highly magnetic white dwarfs in the sample were not fitted spectroscopically, but best-fit parameters from *Gaia* photometry are presented in Table 3.3. Best-fit parameters for confirmed unresolved binary systems are also not provided. The two *Gaia* white dwarf candidates that were found to be main-sequence stars are not analysed further in this work.

3.3.3 Combined spectroscopic and photometric parameters

Atmospheres with carbon traces and metal-polluted white dwarfs were fitted using models from Koester (2010) and improvements described therein. Fits are presented in Sections 3.4.6 and 3.4.7. An iterative approach of combined photometric and spectroscopic fitting was adopted, which starts with computing a small grid of models with an initial guess on the metal abundances to fit the photometry for T_{eff} and $\log(g)$. A new grid of models is then calculated with variable metal abundances at fixed atmospheric parameters in order to fit chemical composition. These two steps are repeated until convergence. *Spectra of DQ and DAZ white dwarfs were fitted by D. Koester, and spectra of DZ and DZA white dwarfs were fitted by M. Hollands.*

3.4 Results

In this chapter I have confirmed the classification of 246 *Gaia* white dwarfs within $1\sigma_{\varpi}$ of 40 pc, 213 of which had no previous observations from literature. All white dwarf spectra are presented in the Appendix of O’Brien et al. (2023). The distribution of $\log(g)$ as a function of T_{eff} for all white dwarfs in the sample, based on *Gaia* DR3 photometric parameters (Gentile Fusillo et al., 2021), is shown in Fig. 3.1. There is a visible second track at $\log(g) \sim 7.4$ below the main $\log(g) \sim 8.0$ distribution in Fig. 3.1, where double degenerate binary candidates with about twice the luminosity of a single white dwarf are located. Their $\log(g)$ values are underestimated because their photometry was fitted as if they were single stars. In Fig. 3.1 there is a downward trend in photometric $\log(g)$ against T_{eff} below around 6000 K. A similar trend has been discussed following *Gaia* DR2 (Hollands et al., 2018b; Bergeron et al., 2019; Tremblay et al., 2020; McCleery et al., 2020), and could be due to *Gaia* temperatures being too low or luminosities being too large. This issue is discussed in detail in Chapter 4.

Only the two DZH white dwarfs WD J0548–7507 and WD J2147–4035, and the DA WD J1956–5258 do not have atmospheric parameters determined from *Gaia* DR3

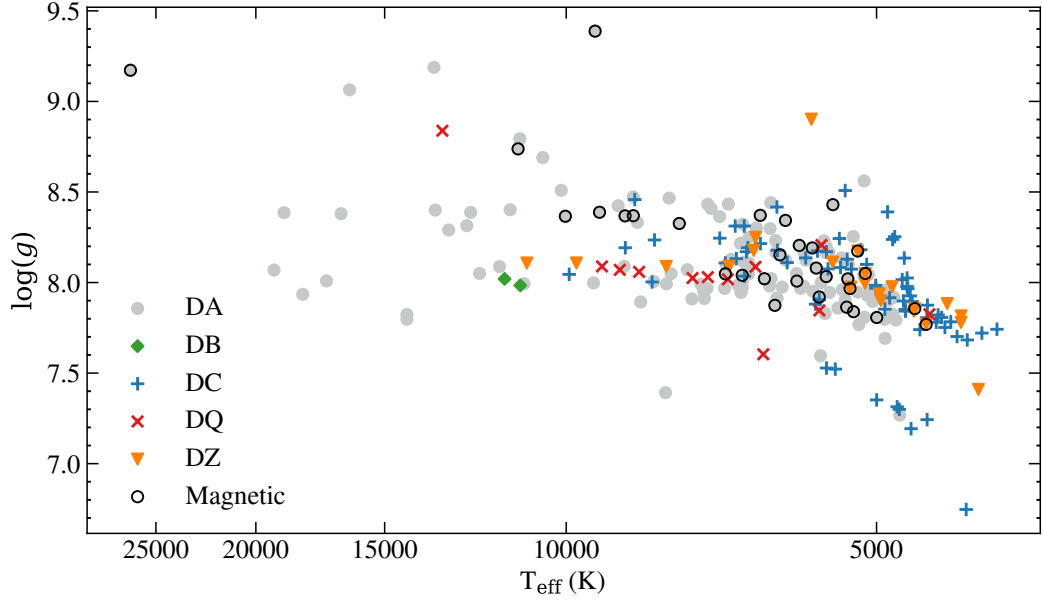


Figure 3.1: $\log(g)$ against T_{eff} distribution for white dwarfs within 40 pc that have been spectroscopically observed in this work, where parameters have been determined by fitting *Gaia* DR3 photometry. Magnetic stellar remnants have black contours. Data are colour- and symbol-coded by their primary spectral type classification only, for simplicity.

photometry in Gentile Fusillo et al. (2021). WDJ2147–4035 was identified by Gentile Fusillo et al. (2021), but is a very cool IR-faint white dwarf (Apps et al., 2021), and its spectroscopy and photometry was fitted with tailored models in Elms et al. (2022). WDJ0548–7507 was selected as a white dwarf candidate by Gentile Fusillo et al. (2019) in *Gaia* DR2, but it was not selected in the DR3 catalogue due to failing the BP–RP excess factor rule, as it is in the Large Magellanic Cloud region (Gentile Fusillo et al., 2021). WDJ0548–7507 has parameters of $T_{\text{eff}} = 4720 \pm 170$ K and $\log(g) = 7.9 \pm 0.1$ from *Gaia* DR2 photometric fitting. WDJ1956–5258 was not selected in either of the DR2 or DR3 white dwarf catalogues, due to a bright, *Gaia* G=10 M-dwarf companion separated by 4.7 arcsec on the sky from the white dwarf. All objects with a parallax below 25 mas are flagged with an asterisk in Table 3.3; these objects may be a member of the 40 pc sample within $1\sigma_{\varpi}$.

I have updated the spectral types of five white dwarfs in the sample which were previously classified as DC, owing to the higher-quality spectroscopy that has been obtained. The white dwarfs were reclassified as follows: WDJ1821–5951 (Subasavage et al., 2017) and WDJ1430–2403 (Reid and Gizis, 2005) are DAs, WDJ0252–7522 (Subasavage et al., 2007) and WDJ1412–1842 (Dupuis et al., 1994) are DAHs and WDJ2112–2922 (Raddi et al., 2017) is a DZQ. These updated spectral types are shown in italics in Table 3.3.

While observations primarily focused on southern hemisphere white dwarfs, four northern hemisphere targets were also observed. Spectroscopy of three northern hemisphere targets omitted from Tremblay et al. (2020) due to low P_{WD} values in DR2 were obtained: WD J1318+7353, WD J1815+5532, and WD J1919+4527. In DR3 (Gentile Fusillo et al., 2021), the P_{WD} values of these white dwarfs increased to 0.96, 0.75, and 0.87 respectively. The highly-polluted northern white dwarf WD J0358+2157 was also re-observed with X-shooter.

The best estimates of spectroscopic atmospheric parameters and chemical abundances are displayed in Table 3.5 for DB white dwarfs, Table 3.6 for DAZ white dwarfs, Table 3.7 for DZ and DZA white dwarfs, and Table 3.8 for all white dwarfs with carbon features. The observations of main-sequence stars that contaminate the 40 pc sample are briefly discussed in Section 3.4.9.

3.4.1 DA white dwarfs

All DA white dwarfs with *Gaia* $T_{\text{eff}} > 5200$ K, and with more than one spectral line visible, were fitted spectroscopically using the fitting code described in Section 3.3, with best-fit atmospheric parameters corrected for 3D convection (Tremblay et al., 2013a), identified in Table 3.3. I did not fit the spectrum of WD J0312–6444 as it is a known unresolved DA+DA binary (Kilic et al., 2020a).

WD J1653–1001 is a DA white dwarf with emission in the core of the $H\alpha$ and $H\beta$ lines (see Fig. 3.2). This emission appears to be similar to that seen in the DAe white dwarf WD J0412+7549, observed in Tremblay et al. (2020). Therefore I made the tentative classification of WD J1653–1001 as a DAe. A detailed discussion of these two systems is provided in Elms et al. (2023).

3.4.2 Magnetic white dwarfs

It is not simple to determine the mass of a highly magnetic white dwarf by photometric fitting in the optical, due to Zeeman splitting and displacement of spectral lines. Therefore the error bars of the $\log(g)$ values quoted in Table 3.3 for cool magnetic white dwarfs may be slightly underestimated (McCleery et al., 2020).

WD J0103–0522 has the largest *Gaia* photometric surface gravity of any white dwarf in the sample. It was analysed in Tremblay et al. (2020), where a quadratic wavelength shift of the π -component was observed, due to a complex field geometry. Even from the higher resolution X-shooter observations, the line cores have round shapes and do not show evidence of the typical multiple sub-components found in DAH stars.

WD J0317–8532 B is a $1.27 \pm 0.02 M_{\odot}$ DAH which has a high field strength of \approx

Table 3.3: Spectral types and parameters of the white dwarf sample

| WD J name | SpT | T_{eff} [K] 3D Spectro | $\log(g)$ 3D Spectro | T_{eff} [K] Gaia | $\log(g)$ Gaia | Note |
|-----------------------|------------|------------------------------------|-------------------------|------------------------------|-------------------|-----------|
| 001349.89–714954.26 | DAH | – | – | 6280 (30) | 7.87 (0.02) | (a) |
| 001830.36–350144.71 | DAH | – | – | 7010 (60) | 8.05 (0.03) | |
| 003036.62–685458.25 | DA | 8640 (40) | 7.98 (0.05) | 8790 (230) | 8.09 (0.06) | |
| 003713.77–281449.81 | DC: | – | – | 5340 (60) | 8.13 (0.04) | |
| 004126.61–503258.58 | DC | – | – | 4180 (60) | 7.70 (0.04) | |
| 004434.77–114836.05 | DZ | – | – | 5300 (70) | 7.98 (0.06) | |
| 005311.22–501322.87 | DC | – | – | 5570 (60) | 8.08 (0.03) | |
| 005411.42–394041.53 | DA | 6580 (20) | 8.43 (0.02) | 6260 (40) | 8.23 (0.02) | |
| 010338.56–052251.96 | DAH | – | – | 9380 (290) | 9.39 (0.05) | (b) |
| 012953.18–322425.86 | DA | 6770 (80) | 8.1 (0.1) | 6720 (50) | 8.11 (0.03) | |
| 013843.16–832532.89 | DA | 7750 (70) | 8.14 (0.09) | 7630 (60) | 8.07 (0.02) | |
| * 014240.09–171410.85 | DAH | – | – | 5560 (50) | 8.00 (0.03) | |
| 014300.98–671830.35 | DAZ | – | – | 6350 (30) | 7.98 (0.02) | (c) |
| 015038.47–720716.54 | DC | – | – | 6840 (60) | 8.13 (0.03) | (d) |
| 021228.98–080411.00 | DA | 9020 (20) | 8.14 (0.02) | 8470 (110) | 7.89 (0.03) | |
| 024300.36–603414.82 | DA | 5760 (120) | 8.5 (0.3) | 5600 (50) | 8.20 (0.03) | |
| 024527.76–603858.32 | DA | 6150 (70) | 8.4 (0.1) | 5880 (50) | 7.98 (0.03) | |
| 025017.18–224130.53 | DA | – | – | 5620 (60) | 8.23 (0.03) | |
| 025245.61–752244.56 | <i>DAH</i> | – | – | 6200 (50) | 8.15 (0.02) | (e) |
| 025332.00–654559.93 | DA | 5600 (60) | 8.0 (0.1) | 5450 (50) | 7.86 (0.03) | |
| 025759.87–302709.99 | DA | 6330 (60) | 8.1 (0.1) | 6170 (40) | 7.98 (0.02) | |
| 030154.44–831446.19 | DA | 6860 (60) | 8.0 (0.1) | 6810 (50) | 7.99 (0.02) | |
| 030407.15–782454.62 | DA | 5500 (30) | 7.99 (0.04) | 5360 (60) | 7.90 (0.04) | |
| 031225.70–644410.89 | DA | – | – | – | – | DA+DA (f) |
| 031318.66–560734.99 | DA | 11 230 (60) | 8.03 (0.03) | 10990 (120) | 7.99 (0.02) | |
| 031646.48–801446.19 | DA | 7510 (50) | 8.0 (0.1) | 7360 (60) | 7.95 (0.02) | |
| 031715.85–853225.56 | DAH | – | – | 26470 (1370) | 9.17 (0.05) | (g) |
| 031719.13–853231.29 | DA | 17 050 (230) | 8.43 (0.03) | 16 530 (290) | 8.38 (0.02) | (h) |
| 032646.69–592700.23 | DA | 6380 (90) | 8.5 (0.2) | 6330 (60) | 8.44 (0.02) | |
| 034010.17–361038.22 | DA | 5870 (60) | 8.2 (0.1) | 5610 (40) | 7.83 (0.03) | (i) |
| 034347.42–512516.55 | DAZ | – | – | 6740 (50) | 8.01 (0.02) | |
| 035005.27–685307.56 | DA | – | – | 4910 (50) | 7.80 (0.03) | |
| 035531.89–561128.32 | DAH | – | – | 5770 (50) | 8.19 (0.03) | |
| 035826.49+215726.16 | DAZ | – | – | 6780 (80) | 8.22 (0.03) | (b) |
| 041630.04–591757.19 | DA | 15 540 (70) | 7.96 (0.01) | 14 270 (240) | 7.82 (0.02) | (j) |
| 041823.34–500424.14 | DC | – | – | 4700 (40) | 8.14 (0.03) | |
| 042021.33–293426.26 | DAH | – | – | 6420 (40) | 8.02 (0.02) | |
| 042357.67–455042.27 | DA | 5900 (40) | 8.49 (0.06) | 5550 (40) | 7.95 (0.02) | (k) |
| 042643.98–415341.44 | DAZ | – | – | 6130 (60) | 8.12 (0.03) | |
| 042731.73–070802.80 | DC | – | – | 6720 (60) | 8.04 (0.03) | (b) |
| 044538.42–423255.05 | DAZ | – | – | 6750 (50) | 7.97 (0.02) | |
| 044903.21–241239.20 | DA | – | – | 4870 (50) | 7.96 (0.04) | |
| 045943.21–002238.86 | DA | 11 060 (100) | 8.81 (0.04) | 11 090 (120) | 8.79 (0.02) | (l) |
| 050552.46–172243.48 | DAH | – | – | 5350 (30) | 7.86 (0.02) | (m) |
| 051942.85–701401.50 | DC | – | – | 4540 (70) | 7.74 (0.05) | |
| 052436.27–053510.52 | DA | 17 330 (120) | 8.08 (0.03) | 17 080 (310) | 8.01 (0.02) | (b) |
| 052844.01–430449.21 | DA | 10 620 (140) | 8.70 (0.04) | 10 540 (140) | 8.69 (0.02) | (n) |
| 053446.50–524150.29 | DA | 6110 (60) | 8.2 (0.1) | 5980 (70) | 8.05 (0.04) | |

Notes: (a) Landstreet and Bagnulo (2019), (b) Tremblay et al. (2020), (c) Subasavage et al. (2017), (d) Subasavage et al. (2008), (e) Subasavage et al. (2007), (f) Külebi et al. (2010), (g) Kilic et al. (2020a), (h) Barstow et al. (1995), (i) Reid and Gizis (2005), (j) Bédard et al. (2017), (k) Scholz et al. (2000), (l) Gianninas et al. (2011), (m) Blouin et al. (2019b), (n) O’Donoghue et al. (2013), (o) Kepler et al. (2000), (p) Dufour et al. (2005), (q) Bergeron et al. (2001), (r) Coutu et al. (2019), (s) Hollands et al. (2017), (t) Dupuis et al. (1994), (u) Bagnulo and Landstreet (2021), (v) Kirkpatrick et al. (2016), (w) Raddi et al. (2017), (x) Bergeron et al. (2021), (y) Elms et al. (2022). Objects with an asterisk before their name have a parallax value outside of 40 pc but may still be within that volume at 1σ . A spectral type in italics indicates we have updated the classification in this work. A spectral type followed by a colon represents a tentative classification. Table 3.2 shows which atmospheric composition was used for the photometric fits of each white dwarf. All quoted uncertainties represent the intrinsic fitting errors. The *3D Spectro* column for DA white dwarfs presents fitted Balmer line parameters.

Table 3.3: Spectral types and parameters of the white dwarf sample (continued)

| WDJ name | SpT | T_{eff} [K] 3D Spectro | $\log(g)$ 3D Spectro | T_{eff} [K] Gaia | $\log(g)$ Gaia | Note |
|-----------------------|-------|------------------------------------|-------------------------|------------------------------|-------------------|------|
| 054249.69–190107.34 | DC | – | 8763 (80) | 8.19 (0.02) | | |
| * 054858.25–750745.20 | DZH | – | 4720 (170) | 7.9 (0.1) | DR2 Parameters | |
| 055118.71–260912.89 | DC | – | 4750 (40) | 7.30 (0.03) | | |
| 055443.04–103521.34 | DZ | – | 6580 (40) | 8.12 (0.02) | (b) | |
| 055802.46–722848.43 | DC | – | 6720 (80) | 8.31 (0.03) | | |
| 055808.89–542804.68 | DA | – | 4850 (60) | 7.92 (0.05) | | |
| 061813.08–801155.22 | DA | 14 800 (240) | 8.37 (0.06) | 13 400 (230) | 8.40 (0.01) | (o) |
| 062620.54–185006.83 | DAZ | – | – | 7300 (60) | 7.97 (0.02) | |
| 064604.27–224633.04 | DC | – | – | 4380 (60) | 7.78 (0.04) | |
| 064806.66–205839.53 | DA | – | – | 5040 (30) | 7.91 (0.02) | |
| 070551.92–083526.76 | DC | – | – | 4620 (340) | 7.9 (0.3) | |
| 071550.55–370642.20 | DA | 7260 (90) | 8.3 (0.2) | 7240 (70) | 8.41 (0.02) | |
| 072251.38–304234.38 | DA | – | – | 5140 (40) | 8.56 (0.02) | |
| 073326.40–445325.34 | DA | 9500 (40) | 7.98 (0.04) | 9410 (80) | 8.00 (0.02) | |
| 075328.47–511436.98 | DAH | – | – | 9280 (100) | 8.39 (0.02) | |
| 075447.40–241527.71 | DAH | – | – | 5940 (50) | 8.21 (0.03) | |
| 080151.04–282831.73 | DQpec | – | – | 5680 (40) | 7.85 (0.03) | |
| 080833.93–530059.48 | DZA | – | – | 4140 (100) | 7.78 (0.06) | |
| 081200.29–610809.79 | DA | 6340 (60) | 8.2 (0.1) | 6260 (60) | 8.17 (0.03) | |
| 081227.07–352943.32 | DC | – | – | 6240 (30) | 8.18 (0.01) | |
| 081630.14–464113.24 | DC | – | – | 4240 (40) | 7.78 (0.03) | |
| 081716.19–680838.31 | DQpec | – | – | 4440 (100) | 7.83 (0.07) | |
| 081843.92–151208.31 | DZ | – | – | 3980 (210) | 7.4 (0.2) | |
| 082533.15–510730.83 | DC: | – | – | 5010 (40) | 7.98 (0.03) | |
| 083759.16–501745.76 | DA | 12 860 (40) | 8.33 (0.02) | 12 490 (160) | 8.31 (0.01) | |
| 084635.27–362206.68 | DA | – | – | 4890 (40) | 7.91 (0.03) | |
| 085021.30–584806.21 | DZA | – | – | 5600 (50) | 8.90 (0.02) | |
| 085430.49–250848.99 | DA | 6720 (90) | 8.2 (0.1) | 6650 (60) | 8.25 (0.02) | |
| 090212.89–394553.32 | DAH | – | – | 8770 (100) | 8.37 (0.02) | |
| 090633.51–262656.02 | DA | – | – | 4990 (40) | 7.95 (0.03) | |
| 090734.25–360907.93 | DA | 5500 (130) | 8.2 (0.3) | 5220 (60) | 7.95 (0.04) | |
| 091228.06–264201.50 | DA | 12 730 (40) | 9.47 (0.03) | 13 440 (280) | 9.19 (0.02) | |
| 091600.94–421520.68 | DZH: | – | – | 5130 (30) | 8.05 (0.02) | |
| 091620.71–631117.21 | DA | 10 270 (40) | 8.50 (0.03) | 10 110 (100) | 8.51 (0.02) | |
| 091708.67–454613.68 | DAZ | – | – | 6330 (40) | 8.02 (0.02) | |
| 091808.59–443724.25 | DAH | – | – | 5330 (40) | 8.02 (0.03) | |
| 092449.05–491529.60 | DC: | – | – | 5420 (30) | 8.08 (0.02) | |
| 093011.42–295943.38 | DA | – | – | 5100 (60) | 7.93 (0.05) | |
| 093659.79–372130.80 | DQ | – | – | 9230 (90) | 8.09 (0.02) | (p) |
| 093659.94–372126.91 | DA | 8130 (60) | 8.0 (0.1) | 7910 (60) | 8.05 (0.02) | (l) |
| 093736.24–385223.21 | DA | 5930 (40) | 8.43 (0.06) | 5660 (50) | 8.00 (0.03) | |
| 094052.75–423225.46 | DC | – | – | 5860 (60) | 8.14 (0.03) | |
| 094240.23–463717.68 | DAH | – | – | 5970 (30) | 8.01 (0.02) | |
| 095522.89–711808.37 | DA | 14 420 (260) | 7.87 (0.05) | 14 280 (210) | 7.80 (0.02) | (l) |
| 101039.30–471729.83 | DA | 5980 (40) | 8.24 (0.08) | 5850 (40) | 8.12 (0.02) | |
| 101341.21–523400.86 | DA | 7230 (40) | 8.49 (0.06) | 6920 (60) | 8.13 (0.02) | |
| 101812.80–343846.05 | DA | – | – | 5090 (50) | 8.04 (0.04) | |
| 101947.34–340221.88 | DAH | – | – | 6480 (50) | 8.37 (0.02) | |
| 103427.04–672239.24 | DA | 19 430 (150) | 8.44 (0.02) | 18 780 (350) | 8.39 (0.02) | |
| 103706.75–441236.96 | DAH | – | – | 5680 (50) | 7.92 (0.03) | |
| 104646.00–414638.85 | DAH | – | – | 6750 (40) | 8.04 (0.02) | |
| 105735.13–073123.18 | DC | – | – | 7100 (50) | 8.25 (0.02) | (q) |
| 105747.61–041330.16 | DZ | – | – | 6950 (60) | 8.09 (0.03) | (r) |
| 105915.98–281955.96 | DAZ | – | – | 6650 (60) | 8.05 (0.03) | |
| 111717.11–441134.49 | DC | – | – | 5590 (30) | 7.53 (0.02) | |
| 113216.54–360204.95 | DZH | – | – | 4590 (70) | 7.86 (0.06) | |
| 114122.38–350406.93 | DZA | – | – | 4600 (40) | 7.84 (0.04) | |
| 114734.45–745759.24 | DC: | – | – | 3820 (80) | 7.74 (0.05) | |
| 114901.67–405114.98 | DC | – | – | 4290 (60) | 7.75 (0.05) | |
| 115020.14–255335.40 | DC | – | – | 6690 (60) | 8.17 (0.02) | |

Table 3.3: Spectral types and parameters of the white dwarf sample (continued)

| WDJ name | SpT | T_{eff} [K] 3D Spectro | $\log(g)$ 3D Spectro | T_{eff} [K] Gaia | $\log(g)$ Gaia | Note |
|----------------------|-----|------------------------------------|-------------------------|------------------------------|-------------------|------|
| 115403.49–310145.29 | DC | – | – | 6110 (60) | 8.11 (0.03) | |
| 121456.38–023402.84 | DZH | – | – | 5220 (60) | 8.17 (0.04) | (s) |
| 121616.94–375848.13 | DC | – | – | 4460 (70) | 7.88 (0.07) | |
| 121724.77–632945.73 | DZ | – | – | 8000 (70) | 8.09 (0.02) | |
| * 122257.77–742707.7 | DA | 6020 (50) | 8.6 (0.1) | 5580 (60) | 7.95 (0.04) | |
| 123156.66–503247.99 | DA | 19 110 (20) | 8.0 (0.2) | 18 010 (350) | 7.94 (0.02) | |
| 123445.37–444001.75 | DC | – | – | 6670 (70) | 8.19 (0.03) | |
| 124112.37–243428.54 | DZ | – | – | 6550 (70) | 8.25 (0.03) | |
| 124155.92–133501.27 | DC | – | – | 8250 (80) | 8.00 (0.03) | |
| 124504.52–491336.69 | DQ | – | – | 8500 (70) | 8.06 (0.02) | |
| 130744.29–792511.64 | DC | – | – | 4670 (80) | 7.98 (0.07) | |
| 131727.39–543808.28 | DA | 5710 (40) | 7.90 (0.08) | 5760 (30) | 7.95 (0.02) | |
| 131830.01+735318.25 | DC: | – | – | 5000 (40) | 7.35 (0.04) | |
| 131958.95–563928.42 | DC | – | – | 7010 (50) | 8.11 (0.02) | |
| 132550.44–601508.04 | DB | 11 080 (130) | – | 11 510 (120) | 7.98 (0.03) | |
| 132756.43–281716.98 | DQ | – | – | 6440 (140) | 7.60 (0.06) | |
| 133216.49–440838.71 | DC | – | – | 5710 (80) | 8.17 (0.04) | |
| 133314.60–675117.19 | DZ | – | – | 5510 (90) | 8.11 (0.05) | |
| 134349.01–344749.39 | DA | – | – | 5140 (80) | 7.81 (0.05) | |
| 134441.03–650942.13 | DA | – | – | 4790 (130) | 7.79 (0.09) | |
| 140115.27–391432.21 | DAH | – | – | 5510 (60) | 8.43 (0.03) | |
| 140608.61–695726.60 | DA | 6910 (40) | 7.99 (0.05) | 6770 (50) | 7.95 (0.02) | |
| 141041.67–751030.18 | DZA | – | – | 4950 (40) | 7.90 (0.04) | |
| 141159.17–592044.99 | DA | 6780 (40) | 8.07 (0.05) | 6650 (40) | 8.11 (0.02) | |
| 141220.36–184241.64 | DAH | – | – | 5720 (90) | 8.08 (0.05) | (t) |
| 141622.47–653126.81 | DA | 9130 (80) | 8.58 (0.08) | 8610 (90) | 8.47 (0.02) | |
| 142254.17–460549.72 | DC | – | – | 6480 (60) | 8.22 (0.03) | |
| 142428.39–510233.63 | DQ | – | – | 6550 (60) | 8.09 (0.03) | |
| 143015.38–240326.12 | DA | – | – | 4870 (60) | 7.90 (0.05) | (i) |
| 143019.96–252040.40 | DA | 6930 (40) | 8.33 (0.06) | 6740 (70) | 8.32 (0.03) | |
| 143826.23–560110.20 | DC | – | – | 8210 (80) | 8.24 (0.02) | |
| 144710.68–694040.21 | DC | – | – | 4470 (30) | 7.24 (0.02) | |
| 150324.74–244129.02 | DA | 6100 (30) | 8.7 (0.8) | 5670 (30) | 7.60 (0.02) | |
| 151431.85–462555.28 | DQZ | – | – | 7540 (60) | 8.03 (0.02) | |
| 151907.38–485423.83 | DQZ | – | – | 8870 (80) | 8.07 (0.02) | |
| 152915.63–642811.20 | DA | 5550 (30) | 8.00 (0.04) | 5200 (60) | 7.77 (0.04) | |
| 152926.39–141614.44 | DA | 5310 (100) | 8.2 (0.2) | 5270 (90) | 8.25 (0.06) | |
| 153044.96–620304.10 | DAZ | – | – | 5880 (60) | 8.17 (0.03) | |
| 154053.08–485837.95 | DZA | – | – | 4830 (50) | 7.98 (0.04) | |
| 155131.68–385049.90 | DC | – | – | 5290 (40) | 8.07 (0.03) | |
| 160027.92–131949.93 | DC | – | – | 5010 (100) | 7.97 (0.08) | |
| 160137.01–383209.35 | DA | – | – | 4910 (40) | 7.69 (0.03) | |
| 160454.29–720347.59 | DC | – | – | 4090 (40) | 6.75 (0.04) | |
| 162224.44–551132.01 | DA | 5640 (200) | 8.0 (0.5) | 5400 (80) | 7.96 (0.05) | |
| 162558.78–344145.71 | DAH | – | – | 5000 (60) | 7.81 (0.04) | |
| 163029.74–373936.84 | DC | – | – | – | – | |
| 163058.32–281815.48 | DC | – | – | 3950 (140) | 7.72 (0.09) | |
| 163337.05–371314.28 | DC | – | – | 5430 (40) | 8.24 (0.02) | |
| 163626.53–873706.08 | DQ | – | – | 5660 (70) | 8.21 (0.04) | |
| 164725.24–544237.58 | DA | 8800 (30) | 8.34 (0.02) | 8530 (70) | 8.33 (0.02) | |
| 165335.21–100116.33 | DAe | 7360 (40) | 7.84 (0.06) | 7350 (90) | 7.91 (0.03) | |
| 165538.10–232555.73 | DA | 7120 (40) | 8.09 (0.05) | 6990 (50) | 8.10 (0.02) | |
| 165823.76–805857.14 | DC | – | – | 4690 (30) | 7.85 (0.03) | |
| 170054.19–690832.65 | DA | 8160 (40) | 8.59 (0.03) | 7950 (70) | 8.47 (0.02) | |
| 170427.96–005026.31 | DA | 6650 (700) | 8.39 (0.08) | 6540 (50) | 8.30 (0.02) | |
| 170430.68–481953.11 | DC | – | – | 5180 (40) | 8.18 (0.03) | |

Table 3.3: Spectral types and parameters of the white dwarf sample (continued)

| WDJ name | SpT | T_{eff} [K] 3D Spectro | $\log(g)$ 3D Spectro | T_{eff} [K] Gaia | $\log(g)$ Gaia | Note |
|---------------------|------|------------------------------------|-------------------------|------------------------------|-------------------|-------------|
| 170641.36–264334.71 | DAH | – | – | 6130 (30) | 8.34 (0.01) | (u) |
| 171436.16–161243.30 | DAH | – | – | 11 140 (140) | 8.74 (0.02) | |
| 171652.09–590636.29 | DAH | – | – | 8600 (90) | 8.37 (0.02) | |
| 172239.79–355441.65 | DA | 7120 (50) | 8.32 (0.08) | 7100 (130) | 8.36 (0.04) | |
| 173351.73–250759.90 | DA | 5520 (40) | 8.00 (0.08) | 5560 (60) | 8.17 (0.04) | |
| 173800.77–311237.21 | DC | – | – | 4660 (70) | 7.97 (0.06) | |
| 173837.46–342729.28 | DA | – | – | 4830 (120) | 7.83 (0.09) | |
| 174220.63–203935.92 | DC | – | – | 5590 (50) | 8.17 (0.03) | |
| 174246.61–650514.67 | DC | – | – | 8580 (90) | 8.46 (0.02) | |
| 174349.28–390825.95 | DA | 11 700 (20) | 7.89 (0.01) | 11 610 (210) | 8.09 (0.03) | |
| 174611.08–625141.41 | DA | 7530 (40) | 8.00 (0.06) | 7400 (60) | 7.99 (0.02) | |
| 174736.82–543631.16 | DC | – | – | 4360 (30) | 7.82 (0.02) | (v) |
| 175325.53–840510.03 | DC | – | – | 5110 (70) | 8.10 (0.05) | |
| 175554.31–245648.94 | DA | 12 830 (10) | 8.395 (0.006) | 13 000 (200) | 8.29 (0.02) | |
| 175931.34–620108.87 | DA | 17 000 (70) | 9.14 (0.02) | 16 220 (270) | 9.06 (0.01) | |
| 180314.84–805750.43 | DC | – | – | 4800 (70) | 8.25 (0.05) | |
| 180315.18–371725.54 | DA | 5500 (50) | 8.1 (0.1) | 5410 (50) | 8.14 (0.03) | |
| 180345.86–752318.35 | DAH | – | – | 5600 (40) | 8.03 (0.03) | |
| 180853.83–704231.62 | DC | – | – | 4720 (60) | 8.02 (0.05) | |
| 180901.95–410140.69 | DC | – | – | 5730 (100) | 7.9 (0.6) | |
| 181311.31–860811.23 | DA | – | – | 4950 (70) | 7.95 (0.06) | |
| 181548.96+553232.22 | DC: | – | – | 4630 (50) | 7.19 (0.04) | |
| 182159.54–595148.52 | DA | – | – | 4750 (30) | 7.27 (0.03) | (c) |
| 182228.37–653738.06 | DA | – | – | 5050 (40) | 7.96 (0.04) | |
| 183351.29–694203.57 | DA | 8120 (50) | 7.87 (0.06) | 8010 (60) | 7.39 (0.02) | |
| 183852.85–441631.32 | DA | 5770 (110) | 8.5 (0.2) | 5560 (100) | 8.17 (0.06) | |
| 183856.35–535726.05 | DA | 5260 (30) | 8.00 (0.04) | 5150 (60) | 8.04 (0.04) | |
| 184650.69–452139.33 | DC | – | – | 4860 (40) | 7.92 (0.04) | |
| 184947.86–095744.38 | DA | 12 130 (20) | 8.24 (0.01) | 12 130 (160) | 8.05 (0.02) | |
| 185005.58–285117.29 | DA | 5700 (180) | 8.5 (0.4) | 5330 (90) | 8.02 (0.07) | |
| 185709.09–265059.22 | DA | 7110 (100) | 8.2 (0.2) | 7020 (60) | 7.97 (0.03) | |
| 185934.75–162656.29 | DA | 8510 (150) | 8.00 (0.05) | 8000 (90) | 8.0 (0.6) | |
| 190255.35–044012.64 | DC | – | – | 4670 (90) | 8.03 (0.08) | |
| 190525.34–495625.77 | DZ | – | – | 10 920 (120) | 8.11 (0.02) | |
| 191100.25–382031.89 | DC: | – | – | 4080 (120) | 7.68 (0.08) | |
| 191144.26–272954.76 | DB | 11 680 (150) | – | 11 480 (140) | 8.02 (0.03) | |
| 191858.23–434920.40 | DC | – | – | 5360 (130) | 8.51 (0.07) | |
| 191936.23+452743.55 | DC: | – | – | 4780 (20) | 7.31 (0.02) | |
| 193538.63–325225.56 | DZAH | – | – | 5310 (50) | 7.97 (0.04) | |
| 194522.76–490420.23 | DC | – | – | 4320 (100) | 7.81 (0.08) | |
| 194549.13–153135.63 | DA | 12 590 (40) | 8.422 (0.008) | 12 380 (170) | 8.39 (0.02) | |
| 195211.78–732235.48 | DC | – | – | – | – | |
| 195616.36–525819.16 | DA | 7670 (620) | 8.65 (0.06) | – | – | Not in GF21 |
| 195639.81–511544.83 | DC | – | – | 4640 (70) | 7.93 (0.06) | |
| 200348.80–474800.18 | DA | 6060 (40) | 8.07 (0.07) | 5920 (50) | 7.97 (0.03) | |
| 200707.98–673442.18 | DAH | – | – | 7770 (70) | 8.33 (0.02) | |
| 201722.68–401043.73 | DZA | – | – | 4970 (80) | 7.94 (0.0) | |
| 201756.19–124639.44 | DC | – | – | 4820 (50) | 8.24 (0.04) | |
| 202011.65–382445.66 | DA | 7400 (40) | 8.44 (0.06) | 7290 (70) | 8.43 (0.02) | |
| 202016.78–652523.10 | DAZ | – | – | 6340 (70) | 8.30 (0.03) | |
| 202025.46–302714.65 | DC | – | – | 9930 (110) | 8.04 (0.02) | |
| 202030.93–420256.74 | DQ | – | – | 6970 (70) | 8.02 (0.03) | |
| 202748.03–563031.58 | DZ | – | – | 4140 (120) | 7.82 (0.09) | |
| 202749.54–430115.21 | DC: | – | – | 4880 (40) | 8.39 (0.03) | |
| 202837.91–060842.77 | DA | 11 860 (100) | 8.49 (0.02) | 11 340 (290) | 8.40 (0.04) | |
| 202956.94–643420.13 | DQ | – | – | 7290 (70) | 8.03 (0.02) | |
| 204911.00–544617.50 | DA | 7670 (30) | 8.02 (0.03) | 7550 (60) | 7.91 (0.02) | |
| 205050.50–612235.61 | DA | 7050 (80) | 8.28 (0.09) | 6960 (70) | 8.43 (0.03) | |

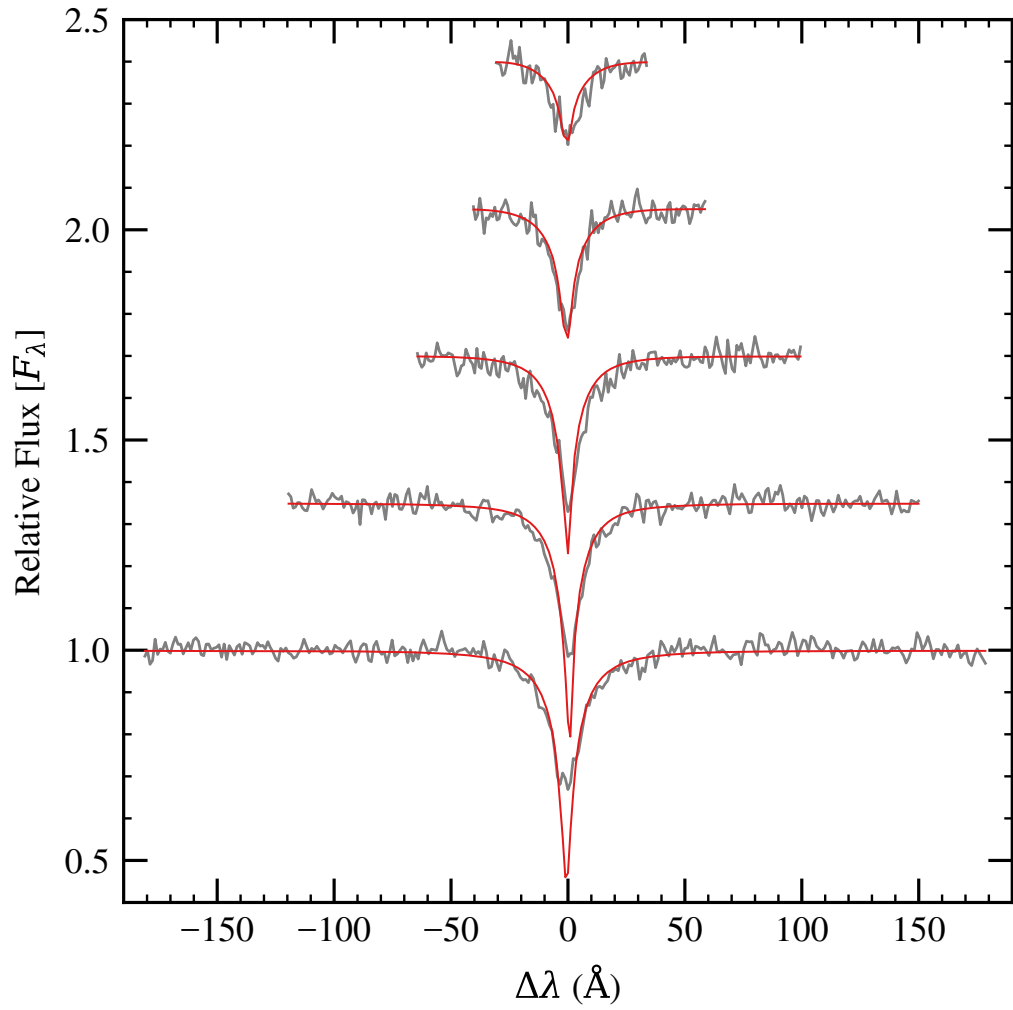


Figure 3.2: Spectroscopic fits to the normalised Balmer lines for the DAe white dwarf WDJ1653–1001.

Table 3.3: Spectral types and parameters of the white dwarf sample (continued)

| WDJ name | SpT | T_{eff} [K] 3D Spectro | $\log(g)$ 3D Spectro | T_{eff} [K] Gaia | $\log(g)$ Gaia | Note |
|-----------------------|------------|------------------------------------|-------------------------|------------------------------|-------------------|------|
| 205213.41–250415.13 | DC | – | – | 4910 (20) | 7.85 (0.02) | |
| 211240.64–292217.96 | <i>DZQ</i> | – | – | 9770 (110) | 8.11 (0.03) | (w) |
| 212121.30–255716.33 | DA | 19 450 (20) | 8.11 (0.05) | 19 210 (370) | 8.07 (0.02) | |
| 212602.02–422453.76 | DC: | – | – | 5480 (30) | 7.52 (0.03) | |
| 213721.24–380838.22 | DC | – | – | 6860 (70) | 8.31 (0.03) | |
| 214023.96–363757.44 | warm DQ | – | – | 13 190 (230) | 8.84 (0.02) | (x) |
| 214324.09–065947.99 | DA | 9390 (80) | 8.5 (0.06) | 8910 (80) | 8.42 (0.02) | |
| 214756.59–403527.79 | DZQH | – | – | – | – | (y) |
| * 214810.74–562613.14 | DAH | – | – | 5930 (60) | 8.08 (0.03) | |
| 220437.98–312713.76 | DA | – | – | 4810 (30) | 7.92 (0.03) | |
| 220552.11–665934.73 | DAH | – | – | 5260 (40) | 7.84 (0.03) | |
| 220655.28–600135.32 | DA | – | – | 5040 (40) | 7.90 (0.04) | |
| 223418.67–553403.40 | DC | – | – | 4690 (70) | 7.84 (0.05) | |
| 223601.50–554852.02 | DZ | – | – | 5130 (40) | 8.00 (0.03) | |
| 223607.66–014059.65 | DAH | – | – | 10 020 (160) | 8.37 (0.03) | |
| 223634.58–432911.11 | DA | 6730 (30) | 8.02 (0.04) | 6240 (40) | 7.92 (0.02) | |
| 223700.03–542241.81 | DA | 8320 (10) | 8.184 (0.008) | 8220 (70) | 8.01 (0.02) | |
| 225335.70–143828.19 | DA | 5500 (30) | 8.20 (0.05) | 5320 (100) | 8.10 (0.07) | |
| 230232.34–330907.96 | DC | – | – | 4710 (90) | 7.90 (0.07) | |
| 230345.52–371051.56 | DZ | – | – | 4270 (90) | 7.88 (0.07) | |
| 234300.85–644737.90 | DC | – | – | 5800 (50) | 7.98 (0.03) | |
| 234935.57–521528.02 | DC | – | – | 6250 (60) | 8.42 (0.02) | |
| 235419.41–814104.96 | DZH | – | – | 4480 (40) | 7.77 (0.04) | |
| 235422.99–514930.65 | DC: | – | – | 4470 (50) | 7.81 (0.03) | |

340 MG (Barstow et al., 1995), and is part of a wide double-degenerate binary system with a DA companion, WD J0317–8532 A. This system has been studied extensively pre-*Gaia*, as WD J0317–8532 B is potentially a double-degenerate merger product due to its large mass (Ferrario et al. 1997; Külebi et al. 2010). I calculated the *Gaia* best-fit parameters of the two components of this binary system (see Table 3.3), and used these to determine the total ages of both stars (Hurley et al. 2000; Cummings et al. 2018; Bédard et al. 2020). The total age of the DAH WD J0317–8532 B is 315 ± 80 Myr, and the total age of the companion is 450 ± 40 Myr, where errors are statistical and likely underestimated, especially for the hot magnetic component. These total ages are in agreement within 2σ with single-star evolution for both objects. A merger could cause a cooling delay, such that the magnetic star would appear younger than its companion, and this cannot be ruled out for WD J0317–8532 B if there is a moderate cooling delay of the order of 200 Myr.

WD J1706–2643 was observed by Bagnulo and Landstreet (2021) who determined a field strength of 8 MG from spectropolarimetry. The field strengths of the remaining DAH white dwarfs have been estimated by visual comparison with theoretical λ -B curves (Friedrich et al., 1996) and are displayed in Table 3.4. Uncertainties in field strength are estimated based on the width of the Zeeman split lines.

WD J2236–0140 is magnetic, but its field strength is poorly constrained due to the limited number of spectral features in the spectrum. There is a broad feature at ≈ 4400 – 4600 Å. There is also a narrower, stationary component at 4140 Å. The field strength is

Table 3.4: Estimated magnetic field strengths for newly identified magnetic white dwarfs in the 40 pc sample

| WD J name | SpT | $\langle B \rangle$ (MG) |
|-----------------------|------|--------------------------|
| 001349.89–714954.26 | DAH | 0.4 (0.2) |
| 001830.36–350144.71 | DAH | 6.8 (0.4) |
| * 014240.09–171410.85 | DAH | 15.1 (0.2) |
| 025245.61–752244.56 | DAH | 22 (3) |
| 035531.89–561128.32 | DAH | 2.3 (0.2) |
| 042021.33–293426.26 | DAH | 0.4 (0.2) |
| 050552.46–172243.48 | DAH | 3.9 (0.2) |
| * 054858.25–750745.20 | DZH | 1.1 (0.2) |
| 075328.47–511436.98 | DAH | 19 (2) |
| 075447.40–241527.71 | DAH | 10.5 (0.2) |
| 090212.89–394553.32 | DAH | 21 (1) |
| 091808.59–443724.25 | DAH | 0.4 (0.2) |
| 094240.23–463717.68 | DAH | 3.4 (0.2) |
| 101947.34–340221.88 | DAH | 110 (10) |
| 103706.75–441236.96 | DAH | 0.3 (0.1) |
| 104646.00–414638.85 | DAH | 3.6 (0.2) |
| 113216.54–360204.95 | DZH | 0.25 (0.02) |
| 121456.38–023402.84 | DZH | 2.1 (0.2) |
| 140115.27–391432.21 | DAH | 7.7 (0.5) |
| 141220.36–184241.64 | DAH | 21 (3) |
| 162558.78–344145.71 | DAH | 4.0 (0.2) |
| 171436.16–161243.30 | DAH | 55 (7) |
| 171652.09–590636.29 | DAH | 0.7 (0.2) |
| 180345.86–752318.35 | DAH | 0.2 (0.2) |
| 193538.63–325225.56 | DZAH | 0.10 (0.01) |
| 200707.98–673442.18 | DAH | 6.4 (0.2) |
| * 214810.74–562613.14 | DAH | 12.4 (0.4) |
| 220552.11–665934.73 | DAH | 2.2 (0.3) |
| 223607.66–014059.65 | DAH | > 250 |
| 235419.41–814104.96 | DZH | 0.6 (0.2) |

Notes: Objects with an asterisk before their name have a parallax value outside of 40 pc but may still be within that volume at $1\sigma_{\varpi}$.

Table 3.5: Atmospheric parameters and chemical abundances of DB white dwarfs, with fixed $\log(g)$ determined from photometric fitting.

| WD J name | T_{eff} [K] (Spectro) | $\log(g)$ (<i>Gaia</i>) | $\log(\text{H/He})$ |
|-----------|-----------------------------------|------------------------------|---------------------|
| 1325–6015 | 11550 (120) | 7.98 (0.02) | –5.03 (0.08) |
| 1911–2729 | 11680 (150) | 8.02 (0.02) | –5.5 (0.3) |

Note: All quoted uncertainties represent the intrinsic fitting errors. I recommend adding systematics of 1 per cent in T_{eff} to account for data calibration errors.

estimated to be $250 < B < 750$ MG from these components, although H α spectroscopy is needed to confirm this.

WD J2354–8141 and WDJ1132–3602 show splitting of the Ca II H line into two groups of two, and the Ca II K line into six because of the large spin-orbit effect for the 4p state of Ca II (Kawka and Vennes, 2011). WD J0916–4215 has been confirmed as a highly magnetic DZH white dwarf with complex splitting of its spectral features (Vennes et al., 2024). The field strengths of new DZH white dwarfs have been estimated and are displayed in Table 3.4. WDJ1935–3252 is weakly magnetic (100 kG) with spectral type DZAH.

The lower limit of detectable magnetic field strength depends on the object; the best case for a magnetic field detection is for a spectrum with very narrow Ca lines and a high signal-to-noise. In this case, I found that field strengths of less than ≈ 50 kG could not be detected using X-shooter spectroscopy.

For all magnetic white dwarfs, I estimated field strengths in Table 3.4 from Zeeman splitting but did not derive spectroscopic atmospheric parameters, which is notoriously difficult for such systems (Külebi et al., 2009). Spectropolarimetry is required to determine the magnetic status of the remaining newly observed white dwarfs which do not display Zeeman splitting, for example WD J0812–3529 has been classified as a DC in this work from a Goodman spectrum but Bagnulo and Landstreet (2020) classify it as a DAH with a field strength of 30 MG, determined from their high-quality spectropolarimetric observations.

3.4.3 DB white dwarfs

The T_{eff} of the two DB white dwarfs were derived using 3D model atmospheres (Cukanovaite et al., 2021), and their parameters are displayed in Table 3.5. These are in reasonable agreement with *Gaia* values. These white dwarfs are at the cool end of the DB range, where spectroscopic fits are difficult (Koester and Kepler, 2015; Rolland et al., 2018). The $\log(g)$ values were therefore fixed at the values derived with *Gaia* photometry.

3.4.4 DC white dwarfs

Nineteen of the DC spectra were observed with the Goodman or FAST spectrographs, which both only provide spectra in the optical blue range 3000 – 6000 Å such that H α coverage is missing from the data. This is often the only diagnostic line for DA white dwarfs with low temperatures. Therefore, further spectroscopy may reveal that a subset of these DC systems are in fact DA white dwarfs. The coolest DA in the sample that was observed with Goodman is WDJ1317–5438, which has a T_{eff} of ≈ 5800 K. For white dwarfs below ≈ 5600 K, the resolution and typical signal-to-noise ratio achieved with Goodman are not high enough to detect the H β line. Therefore the eleven optical blue-only DCs with temperatures above 5600 K are likely to be genuine DCs as one would observe the H β line if they were DA. The remaining eight DCs with lower temperatures could have unobserved H α lines, and require further observations. These are classified as tentative DC (DC: spectral type in Table 3.3). Three new white dwarf candidates in the north, WDJ1815+5532, WDJ1919+4527, and WDJ1318+7353, were all confirmed as white dwarfs spectroscopically. I classified them as tentative DC (DC:) as their OSIRIS spectra are noisy, and potential spectral features cannot be excluded.

On the *Gaia* HR diagram (see Fig. 3.4), WDJ1952–7322 has the faintest absolute *Gaia* G-band magnitude for any DC white dwarf within 40 pc. The spectrum of WDJ1952–7322 displays hints of mild optical collision-induced absorption (CIA), which would be consistent with a mixed H and He atmospheric composition and IR-faint categorisation (Bergeron et al., 2022). Only *Gaia* photometry is available for this white dwarf, so its parameters cannot be constrained given the degeneracy between $\log(\text{H}/\text{He})$ and T_{eff} for such broad *Gaia* bandpasses. WDJ1630–2818 shows signs of mild optical CIA in its spectrum. For both of these white dwarfs, I therefore did not infer T_{eff} and $\log(g)$ from *Gaia* photometry.

WDJ1147–7457 is potentially an ultra-cool (< 4000 K) DC white dwarf and a candidate halo white dwarf, as it has a tangential velocity of ≈ 160 km/s.

WDJ1604–7203 is a low-probability ($P_{\text{WD}} = 0.28$) white dwarf candidate in the Gentile Fusillo et al. (2021) catalogue. It has a *Gaia* photometric $\log(g)$ of 6.75, and a T_{eff} of 4090 K, when fitted as a single star. This object is likely a double degenerate system.

There are Ca II H+K emission features in the spectrum of WDJ0519–7014 which are not associated with the white dwarf and are due to less than ideal sky subtraction as the result of contamination from the Large Magellanic Cloud. This white dwarf is still classified as a DC, as these emission features do not originate from the star itself.

Table 3.6: Atmospheric parameters and chemical abundances of newly observed DAZ white dwarfs, where T_{eff} and $\log(g)$ have been determined from a combination of spectroscopic and photometric fitting.

| WD J name | T_{eff} [K] | $\log(g)$ | $\log(\text{Ca}/\text{H})$ |
|-----------|----------------------|-------------|----------------------------|
| 0143–6718 | 6230 (10) | 7.91 (0.01) | –11.05 |
| 0343–5125 | 6710 (10) | 7.99 (0.01) | –9.60 |
| 0445–4232 | 6650 (10) | 7.92 (0.01) | –10.70 |
| 0626–1850 | 7280 (10) | 7.96 (0.01) | –10.50 |
| 0917–4546 | 6260 (10) | 7.97 (0.01) | –10.30 |
| 1059–2819 | 6530 (10) | 7.99 (0.01) | –9.30 |
| 1530–6203 | 5860 (10) | 8.15 (0.02) | –11.00 |
| 2020–6525 | 6120 (10) | 8.20 (0.02) | –10.65 |

Note: All quoted uncertainties represent the intrinsic fitting errors. I recommend adding systematics of 1 per cent in T_{eff} to account for data calibration errors.

3.4.5 DAZ white dwarfs

WD J0358+2157 (reported in Tremblay et al. (2020)) and WD J0426–4153 are both highly metal-polluted DAZ white dwarfs that will have a dedicated analysis in a future study, and therefore no spectral fits are presented here.

The other eight DAZ stars were fitted using the combined photometry and spectroscopy method of Koester (2010). The fitting of T_{eff} and $\log(g)$ relies on photometry from *Gaia*, GALEX (Martin et al., 2005), Pan-STARRS (Chambers et al., 2016), SkyMapper (Keller et al., 2007), 2MASS (Skrutskie et al., 2006) and WISE (Wright et al., 2010). Not all photometry was available for every object. The best-fit parameters, including $\log(\text{Ca}/\text{H})$ abundances, of the remaining 8 DAZ white dwarfs are displayed in Table 3.6.

3.4.6 DZ and DZA white dwarfs

The combined spectroscopy and photometry of 19 DZ and DZA white dwarfs were fitted using the techniques described in Section 3.3.3. WD J0548–7507 and WD J2354–8141 are DZH white dwarfs and were not fitted due to the complexity of the splitting of their lines. The high-field DZH WD J0916–4215 was also not fitted for the same reason (see Vennes et al. 2024 for a detailed study of this object). The X-shooter spectra of WD J2147–4035 and WD J1214–0234 have already been fitted by Elms et al. (2022) and Hollands et al. (2021), respectively. In this section, I discuss all DZ and DZA white dwarfs for which their combined spectroscopy and photometry have been fitted using the model atmosphere code of Koester (2010). The fitting of T_{eff} and $\log(g)$ relies on photometry from *Gaia*, GALEX, PanSTARRS, SkyMapper, 2MASS and WISE. Not all photometry was available for every object. Ca was detected in the atmospheres of all DZ and DZA spectra in the observed

sample.

WD J1057–0413, WD J1217–6329, WD J1905–4956, and WD J2236–5548 are DZ white dwarfs with He-dominated atmospheres, and no H is detected. Ca was detected in the atmosphere of WD J1057–0413 by Coutu et al. (2019), and I additionally detected Mg and Fe in this white dwarf. WD J2236–5548 is a cool DZ which shows strong metal lines and has a He-dominated atmosphere, abundances are constrained for five metals: Ca, Na, Mg, Fe, and Cr (See Fig. 3.3 for fit).

WD J0044–1148, WD J0554–1035, WD J1241–2434, and WD J1333–6751 are all DZ white dwarfs with He-dominated atmospheres and trace H that was inferred indirectly from their spectra. There are no visible H α lines in these spectra, however there are narrow and sharp metal lines. The electron density in the atmosphere, and therefore the opacity of the atmosphere, is significantly increased by the presence of H which causes the metal lines to appear narrower. WD J0044–1148 has a companion separated by a few arcseconds. WD J0554–1035 was identified as a DZ with Ca in Tremblay et al. (2020); the $\log(\text{H}/\text{He})$ abundance was measured, which was not previously constrained. There is a blend of Fe lines in the spectra of WD J1241–2434 and WD J1333–6751.

WD J0818–1512, WD J1132–3602, WD J2027–5630, and WD J2303–3710 have very narrow Ca lines, indicating a H-dominated atmosphere. Therefore their abundances presented in Table 3.7 are in relation to hydrogen, despite their spectral classification of DZ. There is Zeeman splitting in the spectrum of WD J1132–3602 which indicates a magnetic field of about 280 kG, which has been accounted for in the modelling. WD J2027–5630 is a potential ultra-cool DZ, with a combined spectroscopic and photometric T_{eff} of around 3700 K.

WD J0808–5300, WD J0850–5848, WD J1141–3504, WD J1410–7510, WD J1540–4858, WD J1935–3252, and WD J2017–4010 are DZA white dwarfs with sharp metal lines and a very narrow H α line, indicating almost pure-H atmospheres.

WD J0850–5848 has a high photometric $\log(g)$ of ≈ 8.9 derived from fits with mixed H/He models, and has a combined spectroscopic and photometric $\log(g)$ of ≈ 8.7 . I determined that the white dwarf mass is $1.045 \pm 0.005 M_{\odot}$, corresponding to a progenitor mass of $5.4 \pm 0.1 M_{\odot}$ (Cummings et al., 2018). The spectrum of WD J0850–5848 does not indicate the presence of CIA, so I inferred that this is indeed a massive white dwarf, and is among the most massive metal-polluted white dwarfs ever observed.

WD J1410–7510 and WD J1540–4858 both display sharp Fe lines. The DZAH WD J1935–3252 displays strong metal lines from four elements: Ca, Mg, Fe and Al, and has a weak magnetic field of 100 kG (see Fig. 3.3 for the fit to this spectrum).

WD J0808–5300 displays atmospheric CIA caused by H₂–H₂ and H₂–H, seen in IR photometry from 2MASS and WISE. This white dwarf is polluted by Ca, Na, Mg, Fe,

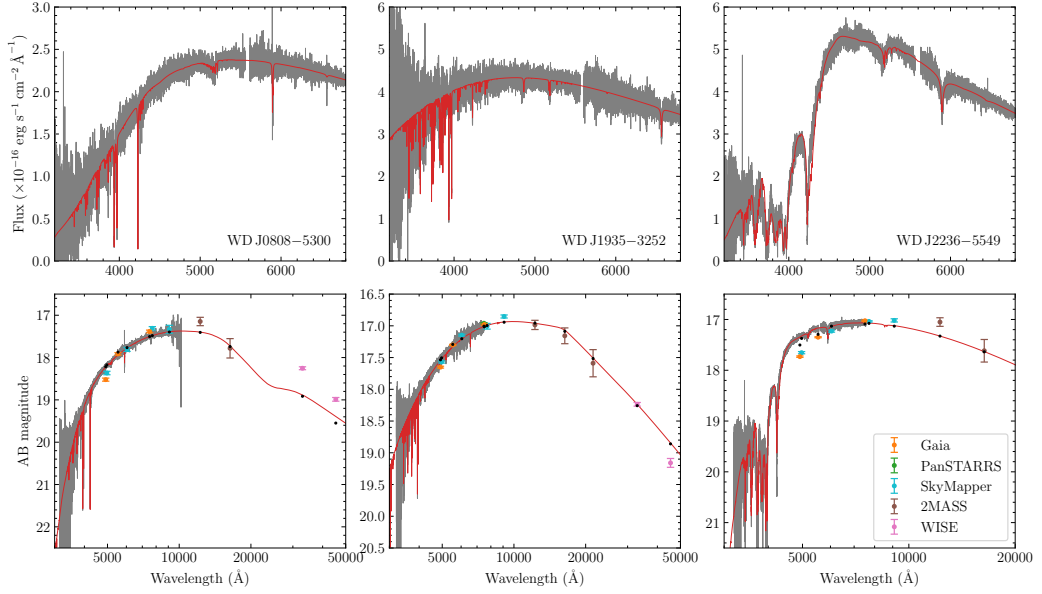


Figure 3.3: Simultaneous fits of spectroscopy and photometry for three metal-rich DZ and DZA white dwarfs: WD J0808–5300 (left panels), WD J1935–3252 (middle panels) and WD J2236–5549 (right panels). The top row of panels compare the best fit models to normalised spectroscopic observations. The spectroscopic observations were re-calibrated onto the models but are still in physical flux units. The bottom panels compare the best fit models to catalogue photometry over a wider wavelength range than the available spectroscopy provides.

Al and Cr. I detected an absorption feature caused by MgH molecules at around 5200 Å, a feature that has been detected in white dwarfs with mixed H/He atmospheres (Blouin et al., 2019a; Kaiser et al., 2021). This is the first detection of MgH in a H-dominated atmosphere white dwarf. The hybrid fit to this white dwarf is shown in Fig. 3.3.

The abundances of Li, Na, Mg, K, Ca, Cr and Fe for the DZH white dwarf WD J1214–0234 were calculated in Hollands et al. (2021).

3.4.7 DQ white dwarfs

All DQ white dwarf spectra were fitted with the Koester (2010) model atmosphere code using an iterative procedure. Results from the fitting procedure are shown in Table 3.8. The fitting of T_{eff} and $\log(g)$ relies on photometry from *Gaia*, GALEX, SkyMapper and 2MASS. Not all photometry was available for every object.

Two of the DQ white dwarfs in the sample, WD J0801–2828 and WD J1636–8737, display CH molecular absorption features in their spectra near 4300 Å. I classified WD J0801–2828 and WD J0817–6808 as peculiar DQ (DQpec) white dwarfs. This classification describes

Table 3.7: Atmospheric best-fit parameters and chemical abundances of DZ and DZA white dwarfs, where T_{eff} and $\log(g)$ have been determined from a combination of spectroscopic and photometric fitting. Weakly magnetic DZH and DZAH were also fitted. Upper table: Best-fit parameters for white dwarfs with He-dominated atmospheres. Lower table: Best-fit parameters for white dwarfs with H-dominated atmospheres.

| WDJ name | SpT | T_{eff} [K] | $\log(g)$ | $\log(\text{H}/\text{He})$ | $\log(\text{Ca}/\text{He})$ | $\log(\text{Na}/\text{He})$ | $\log(\text{Mg}/\text{He})$ | $\log(\text{Fe}/\text{He})$ | $\log(\text{Cr}/\text{He})$ |
|-----------|------|----------------------|---------------|----------------------------|-----------------------------|-----------------------------|-----------------------------|-----------------------------|-----------------------------|
| 0044–1148 | DZ | 5310 (30) | 7.99 (0.02) | -1.23 (0.03) | -11.53 (0.04) | - | - | - | - |
| 0554–1035 | DZ | 6230 (20) | 8.04 (0.01) | -4.52 (0.05) | -11.78 (0.03) | - | - | - | - |
| 1057–0413 | DZ | 6500 (20) | 8.03 (0.01) | - | -10.30 (0.01) | - | -8.88 (0.02) | -9.60 (0.03) | - |
| 1217–6329 | DZ | 7420 (80) | 7.96 (0.03) | - | -10.43 (0.05) | - | - | - | - |
| 1241–2434 | DZ | 6310 (30) | 8.13 (0.01) | -2.78 (0.04) | -11.42 (0.01) | - | - | -10.29 (0.03) | - |
| 1333–6751 | DZ | 5640 (60) | 8.17 (0.03) | -1.97 (0.02) | -11.41 (0.03) | - | - | -10.62 (0.04) | - |
| 1905–4956 | DZ | 10600 (40) | 8.08 (0.01) | - | -8.99 (0.03) | - | - | - | - |
| 2236–5548 | DZ | 5350 (10) | 8.17 (0.01) | - | -9.17 (0.01) | -9.16 (0.01) | -7.41 (0.01) | -8.64 (0.01) | -9.9 (0.1) |
| WDJ name | SpT | T_{eff} [K] | $\log(g)$ | $\log(\text{Ca}/\text{H})$ | $\log(\text{Na}/\text{H})$ | $\log(\text{Mg}/\text{H})$ | $\log(\text{Fe}/\text{H})$ | $\log(\text{Al}/\text{H})$ | $\log(\text{Cr}/\text{H})$ |
| 0808–5300 | DZA | 4910 (10) | 8.34 (0.01) | -9.74 (0.02) | -9.60 (0.02) | -8.16 (0.02) | -9.05 (0.03) | -9.54 (0.03) | -10.48 (0.03) |
| 0818–1512 | DZ | 4720 (10) | 7.68 (0.01) | -11.50 (0.04) | - | - | - | - | - |
| 0850–5848 | DZA | 5430 (20) | 8.73 (0.01) | -10.65 (0.01) | - | - | - | - | - |
| 1132–3602 | DZH | 4990 (10) | 8.12 (0.01) | -10.84 (0.03) | - | - | - | - | - |
| 1141–3504 | DZA | 4880 (20) | 8.07 (0.01) | -11.11 (0.02) | - | - | - | - | - |
| 1410–7510 | DZA | 5180 (10) | 8.011 (0.007) | -10.64 (0.01) | - | - | -9.36 (0.02) | - | - |
| 1540–4858 | DZA | 5000 (30) | 8.10 (0.02) | -10.57 (0.03) | - | - | -9.77 (0.03) | - | - |
| 1935–3252 | DZAH | 5430 (10) | 8.00 (0.01) | -9.68 (0.02) | - | -7.89 (0.03) | -8.61 (0.02) | -9.12 (0.04) | - |
| 2017–4010 | DZA | 5250 (20) | 8.08 (0.01) | -10.62 (0.03) | - | - | - | - | - |
| 2027–5630 | DZ | 3750 (130) | 7.7 (0.1) | -12.6 (0.1) | - | - | - | - | - |
| 2303–3710 | DZ | 4790 (50) | 8.28 (0.03) | -10.76 (0.06) | - | - | - | - | - |

Note: All quoted uncertainties represent the intrinsic fitting errors. I recommend adding systematics of 1 per cent in T_{eff} to account for data calibration errors.

Table 3.8: Atmospheric parameters and chemical abundances of DQ, DQZ and DZQ white dwarfs. T_{eff} and $\log(g)$ were determined from iterative spectroscopic and photometric fitting. The warm DQ WD J2140–3637 is not included here, as it was assumed to have a C-dominated atmosphere when fitting, rather than a He-dominated atmosphere (see Section 3.5.3).

| WDJ name | SpT | T_{eff} [K] | $\log(g)$ | $\log(\text{C}/\text{He})$ | $\log(\text{H}/\text{He})$ | $\log(\text{Ca}/\text{He})$ |
|-----------|-------|----------------------|-------------|----------------------------|----------------------------|-----------------------------|
| 0801–2828 | DQpec | 5970 (10) | 7.96 (0.01) | –5.90 (0.01) | –4.25 | – |
| 0817–6808 | DQpec | 4620 (20) | 8.02 (0.02) | –7.70 (0.01) | – | – |
| 0936–3721 | DQ | 8890 (20) | 7.96 (0.01) | –4.94 (0.02) | – | – |
| 1245–4913 | DQ | 8120 (20) | 7.94 (0.01) | –5.30 (0.02) | – | – |
| 1327–2817 | DQ | 7510 (50) | 7.90 (0.02) | –5.74 (0.01) | – | – |
| 1424–5102 | DQ | 6340 (30) | 7.98 (0.01) | –7.45 (0.01) | – | – |
| 1514–4625 | DQZ | 7470 (20) | 7.99 (0.01) | –5.96 (0.02) | – | –11.7 |
| 1519–4854 | DQZ | 8960 (20) | 8.06 (0.01) | –4.60 (0.02) | – | –11.6 |
| 1636–8737 | DQ | 5370 (40) | 8.11 (0.02) | –7.60 (0.01) | –3.40 | – |
| 2020–4202 | DQ | 6870 (30) | 7.99 (0.01) | –6.6 (0.2) | – | – |
| 2029–6434 | DQ | 7120 (20) | 7.97 (0.01) | –6.30 (0.01) | – | – |
| 2112–2922 | DZQ | 8960 (40) | 7.87 (0.01) | –4.80 (0.01) | – | –11.6 |

Note: All quoted uncertainties represent the intrinsic fitting errors. I recommend adding systematics of 1 per cent in T_{eff} to account for data calibration errors.

cool DQs below 6000 K with molecular absorption bands with central wavelengths that have been shifted 100–300 Å from the positions of the C₂ Swan bands (Hall and Maxwell, 2008). The warm DQ WD J2140–3637 is discussed further in Section 3.5.3.

3.4.8 DQZ and DZQ white dwarfs

WD J1514–4625 and WD J1519–4854 are classified as DQZ, and WD J2112–2922 is classified as DZQ. All three show both carbon absorption features and metal lines in their spectra. In all three cases, I detected metals from the Ca II H+K lines, and carbon from the C₂ Swan bands. WD J1514–4625 and WD J1519–4854 were both observed by the Goodman spectrograph, for which the field of view is 10 arcmin. The two stars are separated by over a degree on the sky, so they are not a duplicate observation, despite their physical proximity. These stars are unlikely to be DQ + DZ binaries, as all three stars have photometric $\log(g)$ values close to or above the canonical value of 8.0 for single stars. Elms et al. (2022) tentatively detected carbon in the ultra-cool DZ WD J2147–4035; this star would notionally be a DZQpecH. The origin of DQZ white dwarfs is discussed further in Section 3.5.2.

3.4.9 Main-sequence stars

Two white dwarf candidates with $P_{\text{WD}} = 1$ from Gentile Fusillo et al. (2021) turned out to be main-sequence stars following spectroscopic observations: WD J0924–1818 and WD J1732–1710. The issues of contamination from *Gaia* DR2 white dwarf samples (Gentile Fusillo et al., 2019) have mostly been solved in DR3 (Gentile Fusillo et al., 2021), such that there are now minimal contaminant sources in the 40 pc sample (< 1 per cent of this 40 pc south sample has main-sequence contaminants). It is likely that these sources have spurious *Gaia* parallaxes placing them on the white dwarf sequence of the HR diagram, hence their high P_{WD} values. Both stars have high excess flux error values in *Gaia*, indicating either variability or issues with photometry.

3.5 Discussion

3.5.1 Comparison with the overall 40 pc sample

The *Gaia* DR3 HR diagram for the volume-limited 40 pc spectroscopic white dwarf sample, following the new confirmations presented in this work, is shown in Fig. 3.4. The faintest and reddest white dwarf in the sample is WD J2147–4035, at the bottom right of Fig. 3.4 (Elms et al., 2022).

The mean *Gaia* photometric T_{eff} of the sample of the 246 white dwarfs presented in this work is 6930 K, whereas for the full 40 pc sample the mean *Gaia* T_{eff} is 7530 K. Both samples have a standard deviation of ≈ 3000 K. It is expected that the sub-sample presented in this work has a lower mean T_{eff} than in 40 pc overall because the new observations are biased towards fainter white dwarfs at lower T_{eff} , as these had not previously been observed spectroscopically.

The mean *Gaia* photometric mass of both the sub-sample and the overall 40 pc sample is $0.63 M_{\odot}$. The mean mass is biased by the cool white dwarfs with $T_{\text{eff}} < 5000$ K for which masses may have been incorrectly calculated from models (see Fig. 3.1). The mean mass for white dwarfs with $T_{\text{eff}} > 5000$ K is $0.66 M_{\odot}$ (McCleery et al., 2020).

Within this work, 179 white dwarfs were observed with X-shooter. This X-shooter sample provides a set of white dwarf spectra with a large wavelength coverage and high signal-to-noise ratio. Metal-polluted, carbon-rich, and magnetic white dwarfs are over-represented in this X-shooter sub-sample compared to the remaining 40 pc white dwarfs that have not been observed with X-shooter, as shown in Fig. 3.5. An over-abundance of magnetic and of metal-polluted white dwarfs may be due to the resolution of X-shooter, a medium-resolution spectrograph, compared to the observations for the existing 40 pc sample, providing the opportunity to detect low levels of metal abundances and weaker

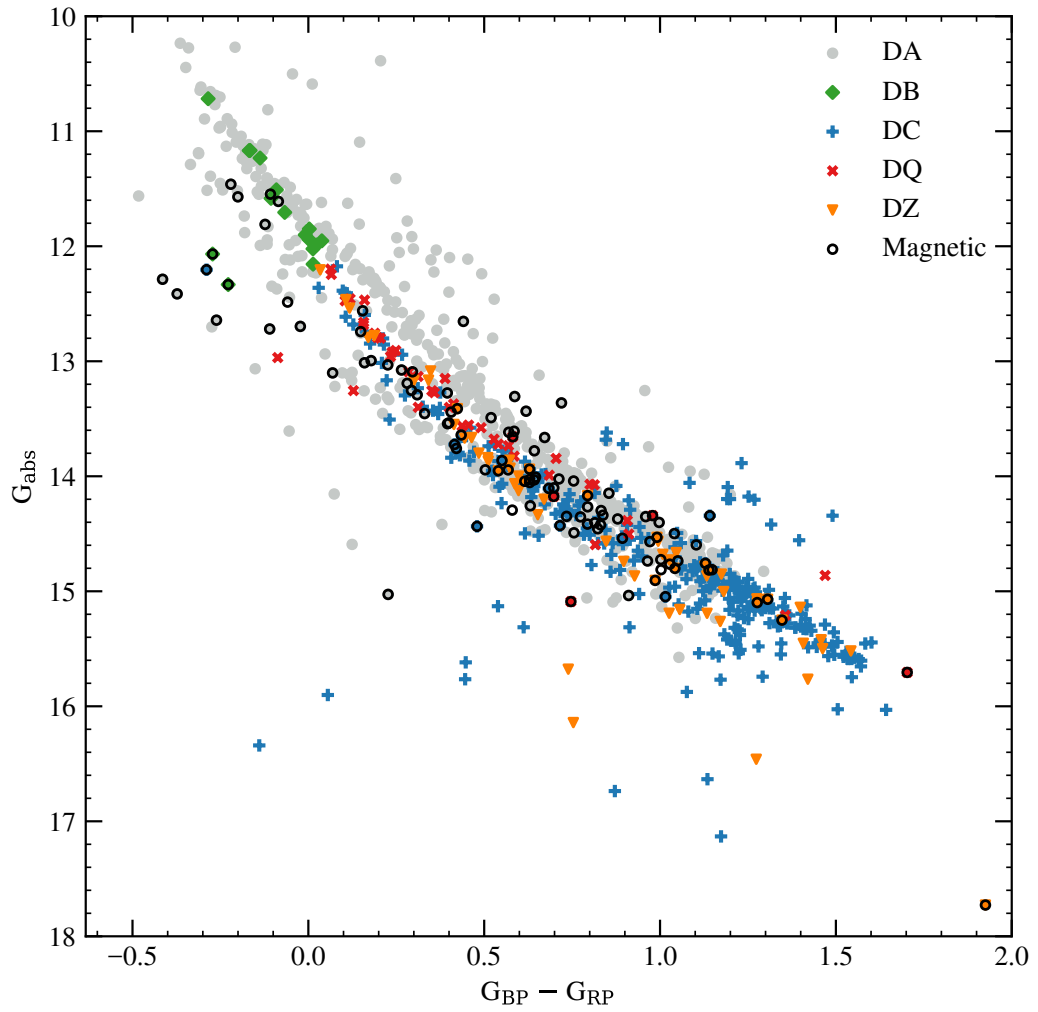


Figure 3.4: A *Gaia* DR3 HR diagram for the spectroscopic 40 pc sample of 1058 white dwarfs. Magnetic stellar remnants have black contours. Data are colour- and symbol-coded by their primary spectral type classification only, for simplicity.

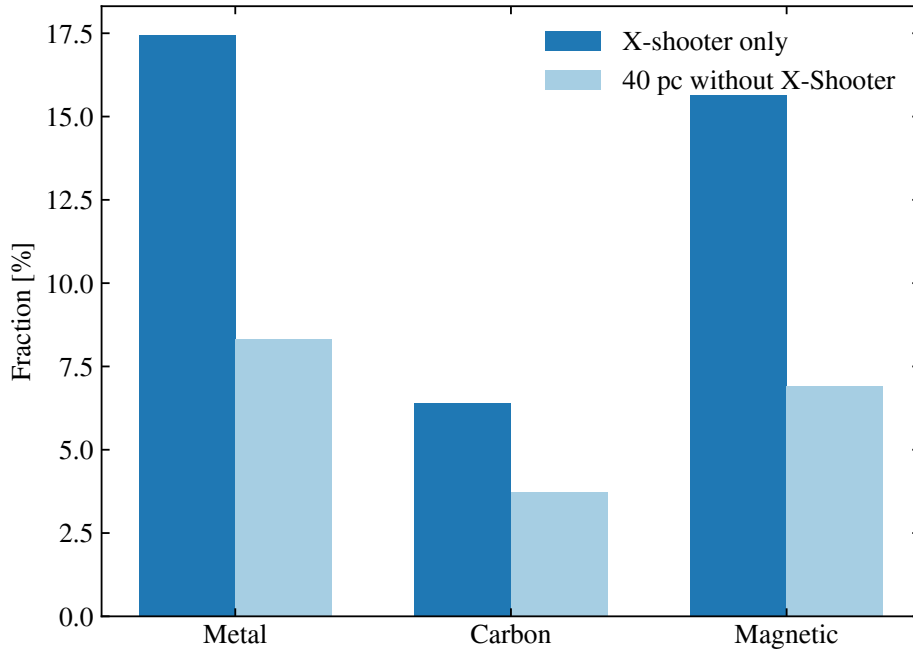


Figure 3.5: Incidence of different atmospheric compositions between a sample of 179 X-shooter observations (dark blue) presented in this work, and the full 40 pc sample not including X-shooter observations (light blue). The bars from left to right represent white dwarfs with trace metals in their atmospheres, carbon in their atmospheres, and magnetic white dwarfs.

Zeeman splitting. Since the X-shooter sub-sample is biased towards lower T_{eff} , there might also be a greater incidence of metal-pollution, trace carbon and magnetism due to this bias. It is critical to obtain higher resolution and quality spectra of the remaining 40 pc white dwarfs to update fractions of metal-polluted and magnetic white dwarfs and determine the underlying distributions for this volume-limited sample.

Using Keck HIRES high-resolution spectra, Zuckerman et al. (2003) observed that 25 per cent of DA white dwarfs with T_{eff} below 10 000 K were metal-polluted. In the 40 pc south sub-sample, I detected a metal-pollution rate of around 15 per cent for DA white dwarfs with T_{eff} below 10 000 K. It is possible that such a high fraction of polluted white dwarfs were not observed compared to Zuckerman et al. (2003) due to the intrinsic fainter nature of the presented sub-sample. The sub-sample also comprises of medium-resolution spectroscopic observations rather than high-resolution, so less metal lines will be detected.

3.5.2 Metal-polluted DQ white dwarfs

Both Coutu et al. (2019) and Farihi et al. (2024a) observed a significant deficit in the frequency of metal pollution in DQ stars, and observed only a 2 per cent pollution rate in DQ white dwarfs. To explain this deficit, Hollands et al. (2022) and Blouin (2022) modelled the effect of metal pollution on the presence of Swan bands in DQ white dwarf spectra, and showed that for above a relatively low level of pollution, Swan bands will be suppressed such that a DQZ would present as a DZ. Therefore, the only metal-polluted DQ stars that can be observed spectroscopically should have relatively low levels of pollution (Blouin, 2022), which aligns with what has been observed in the 40 pc sample. Another explanation for this observed deficit is that DQ white dwarfs at all temperatures are the product of binary evolution, altering their circumstellar environments and reducing the occurrence of planetary debris (Farihi et al., 2024a).

Thirty per cent of the white dwarf population in 40 pc have He-rich atmospheres, and DZ and DQ white dwarfs independently correspond to about 18 per cent of those white dwarfs with He-rich atmospheres. If the presence of carbon and metals in white dwarfs are independent of each other, the percentage of He-rich white dwarfs in a volume-limited sample with both metal and carbon lines should be about 3 per cent. Therefore in 40 pc one would expect to find 8 ± 3 metal-polluted DQ white dwarfs.

The white dwarf WD J0916+1011 was classified as a DQZ by Kleinman et al. (2013) and is at a distance of 38.6 pc. WD J2147–4035 is a white dwarf with spectral type DZQH (Elms et al., 2022). The white dwarf Procyon B is not in the *Gaia* DR3 catalogue, however it is at a distance of ≈ 3.5 pc and was classified as a DQZ following the detection of Mg lines in its UV spectrum (Provencal et al., 2002).

Adding Procyon B, WD J0916+1011 and WD J2147–4035 to the two newly observed DQZ white dwarfs and the DZQ in this paper gives six out of 253 He-rich white dwarfs in the 40 pc sample that display both metal lines and carbon lines. There is not a notable deficit in the numbers of these white dwarfs, but I note that the numbers are too small to draw meaningful conclusions. Coutu et al. (2019) analysed a sample of SDSS spectra which have lower signal-to-noise than the X-shooter and Goodman spectra in the sample, possibly explaining why they detected less metal-pollution in DQs, or Swan bands in DZs, than I observed in 40 pc. They could have potentially missed those stars with very weak Swan bands and stronger metal features such as WD J2112–2922.

3.5.3 WDJ2140-3637: A warm DQ white dwarf

WDJ2140–3637 is a warm DQ white dwarf that was identified in Bergeron et al. (2021). Warm DQ white dwarfs have spectra dominated by C I lines in the optical, and tend to have

He-dominated atmospheres (Koester and Kepler, 2019) compared to the C/O-dominated magnetic hot DQ white dwarfs at $T_{\text{eff}} > 18\,000$ K (Dufour et al., 2007b). Bergeron et al. (2021) showed that WD J2140–3637 belongs to a massive warm DQ white dwarf sequence identified by Coutu et al. (2019) and they stated that it has the largest carbon abundance of any warm DQ.

This object was fitted using the same models as for the other DQ stars in this sample (Koester, 2010), to obtain the parameters $T_{\text{eff}} = 11\,800 \pm 200$ K and $\log(g) = 8.77 \pm 0.01$. Assuming carbon is the dominant atmospheric element, the following abundances were estimated: $\log(\text{H}/\text{C}) < -3.50$, $\log(\text{He}/\text{C}) < 1.00$, $\log(\text{N}/\text{C}) < -2.50$, $\log(\text{O}/\text{C}) = -2.10 \pm 0.10$. The limit for He due to an absence of spectral features means it could be possible that He is more abundant than C. Therefore this white dwarf is potentially the first warm non-magnetic DQ which has a carbon-dominated atmosphere.

I detected an O I triplet absorption feature at 7772, 7774, and 7775 Å, and an O I feature around 8446 Å, which are labelled in Fig. 3.6. As with atmospheric carbon, the presence of oxygen in the atmosphere of WD J2140–3637 is likely due to dredge-up by an extending convection zone in the upper helium layer of a CO-core white dwarf with small total masses of H and He. This is the first detection of oxygen in the atmosphere of WD J2140–3637.

Warm DQ white dwarfs may be the cooled down counterparts of hot DQ stars, which are thought to originate from double CO-core white dwarf mergers (Dunlap and Clemens, 2015; Williams et al., 2016; Cheng et al., 2019; Coutu et al., 2019). A mass of $1.06 \pm 0.01 M_{\odot}$ was determined for WD J2140–3637.

3.5.4 Comparison of DA spectroscopic and photometric parameters

For the homogeneous sub-sample of DA white dwarfs with X-shooter spectroscopy, Fig. 3.7 displays the differences in T_{eff} of the spectroscopic fitting method adopted in this paper compared to *Gaia* photometric parameters. There is no clear systematic differences for DA white dwarfs above 8000 K due to low number statistics. However, there is a clear systematic offset between X-shooter spectroscopic solutions and *Gaia* photometric parameters in the region $6000 < T_{\text{eff}} < 8000$ K, where *Gaia* photometric temperatures are systematically lower by 1.5 ± 0.8 per cent (see Fig. 3.7). There is a known issue with photometric fits for white dwarfs with $T_{\text{eff}} < 6000$ K (see Fig. 3.1), and these are excluded from this discussion.

In Tremblay et al. (2020), using a different spectroscopic data set from WHT for a similar sample of cool DA white dwarfs within 40 pc in the northern hemisphere, a similar offset was found between spectroscopic and photometric temperatures. Tremblay et al. (2020) concluded that *Gaia* colours are systematically too red, or the spectroscopic solutions are too warm. Radius measurements using *Gaia* photometry and astrometry

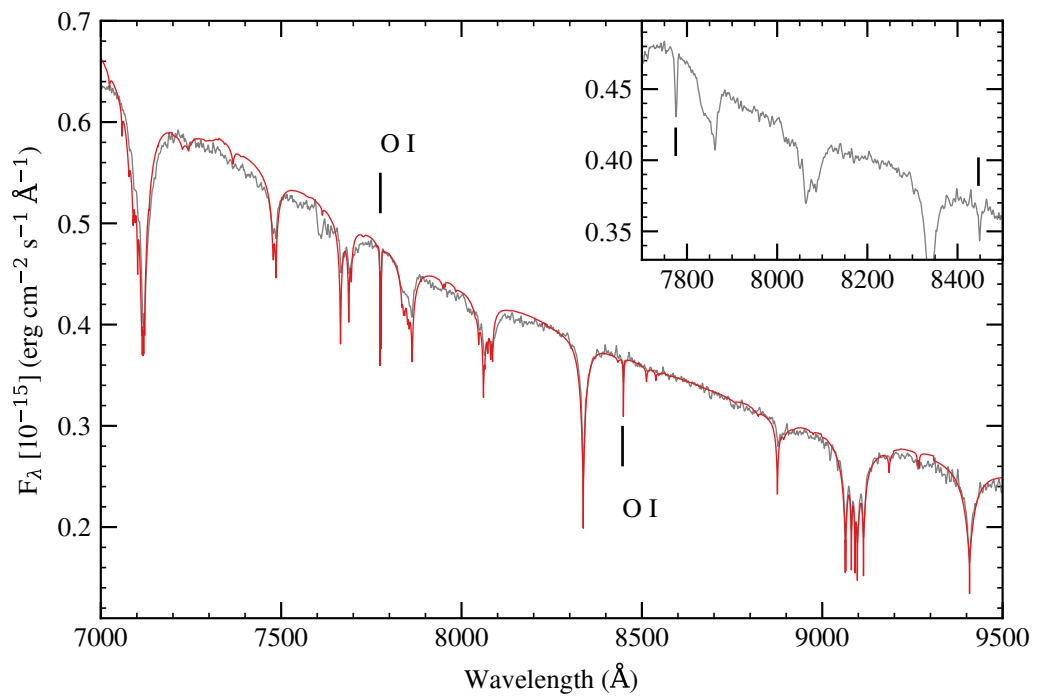


Figure 3.6: X-shooter spectrum of WD J2140–3637 plotted with the combined photometric and spectroscopic fit using Koester (2010) models. The O I absorption features around 7775 \AA and 8446 \AA are highlighted with ticks. The spectrum was convolved by a Gaussian with a FWHM of 1 \AA and shifted by 45 km/s. An inset plot shows the region around the oxygen absorption features without the overplotted model.

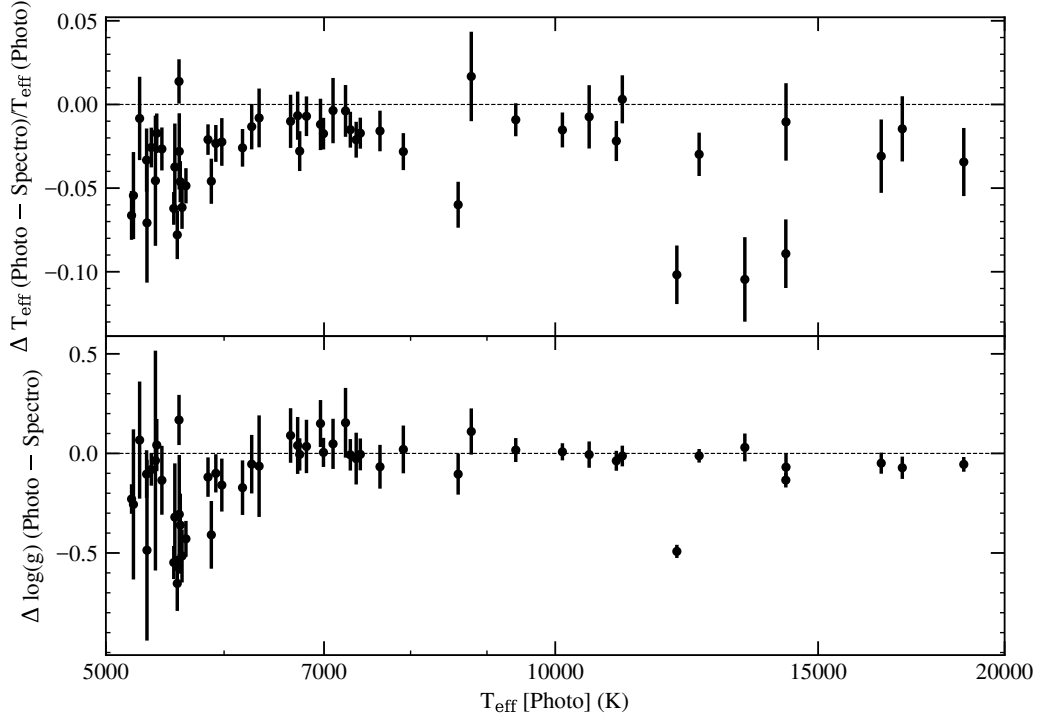


Figure 3.7: Differences between *Gaia* photometric (*Photo*) and X-shooter spectroscopic (*Spectro*) T_{eff} (top panel) and $\log(g)$ (bottom panel) for DA white dwarfs, against *Gaia* photometric T_{eff} (Gentile Fusillo et al., 2021). The spectroscopic fitting method is described in Section 3.3.2.

depend on a comparison between observed and predicted absolute magnitude, and the latter is itself a function of T_{eff} . Therefore, an under-prediction of photometric T_{eff} would result in an over-prediction of radius, and hence a systematic decrease in $\log(g)$ given the mass-radius relation. As a consequence, any systematic offset in $\log(g)$ values between both techniques is in part a consequence of the offset in T_{eff} .

In summary, from this work and the recent literature (Tremblay et al., 2020; Genest-Beaulieu and Bergeron, 2019; Tremblay et al., 2019a; Cukanovaite et al., 2021), there is a clear offset between photometric and spectroscopic T_{eff} solutions for DA white dwarfs that is present when using different homogeneous spectroscopic data sets (e.g. WHT, X-shooter, SDSS) and photometric data sets (e.g. *Gaia* DR2 and DR3, Pan-STARRS, SDSS). This offset appears to be of a similar percentage for temperatures between 6000 K and 30 000 K, where the 1.5 per cent offset value found in this work is very similar to the offset found for warm non-convective ($T_{\text{eff}} > 15\,000$ K) DA white dwarfs from SDSS in Tremblay et al. (2019a). Additionally, a similar offset is seen for DB white dwarfs (Cukanovaite et al., 2021).

3.6 Conclusions

The 20 pc sample was 86 per cent complete pre-*Gaia* (Holberg et al., 2016), and following *Gaia* DR2, it was the largest volume-limited sample of spectroscopically confirmed white dwarfs (Hollands et al., 2018b). In Tremblay et al. (2020) and McCleery et al. (2020), a sample of northern hemisphere white dwarfs within 40 pc was presented, with a high level of spectroscopic completeness. In this work, I have described the spectral types of 246 white dwarfs within $1\sigma_{\varpi}$ of 40 pc, of which 209 were previously unobserved and five have updated spectral types from higher quality spectroscopic observations. Following these new observations, the 40 pc white dwarf sample is essentially volume-complete with spectroscopic follow-up.

I have identified many new magnetic white dwarfs, some of which display complex Zeeman splitting, and have estimated their field strengths. New metal-polluted white dwarfs have been observed, including WDJ2236–5548 and WDJ0808–5300 which are polluted by five and six metals, respectively. The warm DQ white dwarf WDJ2140–3637 was re-observed, and oxygen was detected in its atmosphere for the first time. I reported three new white dwarfs which are metal-polluted and display carbon absorption lines (DQZ and DZQ spectral types). I have also presented new candidate unresolved binary systems based on their photometric over-luminosity. I have fitted DA white dwarfs spectroscopically as well as photometrically. I noted that there is a similar offset in T_{eff} for spectroscopic parameters using both southern X-shooter (this work) and northern WHT (Tremblay et al., 2020) data sets, when compared to *Gaia* photometric fitting.

The volume-limited 40 pc sample of *Gaia* white dwarfs now has a very high level of spectroscopic completeness and I have used this sample to perform a statistical analysis of the local population of white dwarfs (Cukanovaite et al., 2023). The classification of 1058 white dwarfs out of 1083 candidates from DR3 have now been confirmed. The 40 pc sample provides an eight-fold increase in volume over the previous 20 pc sample, which did not have the level of spectroscopic completeness that the 40 pc sample now has. The completeness of the *Gaia* DR3 white dwarf catalogue as well as the selection of Gentile Fusillo et al. (2021) are expected to be very high for single white dwarfs.

Creating significantly larger volume-limited samples than 40 pc requires MOS surveys such as WEAVE, 4MOST and DESI (de Jong et al., 2019; Dalton et al., 2020; Cooper et al., 2023), which may take decades to cover the whole sky. Therefore, the 40 pc sample will be the benchmark volume-limited white dwarf sample for many years to come. A full statistical analysis of the 40 pc sample will be presented in Chapter 4.

Chapter 4

The *Gaia* 40 pc white dwarf sample

In this chapter, I present a comprehensive overview of the volume-complete sample of white dwarfs located within 40 pc of the Sun, a significant proportion of which were detected in *Gaia* DR3. The final DR3 sample contains 1078 spectroscopically confirmed white dwarfs, with just two candidates within the volume remaining unconfirmed (> 99 per cent spectroscopic completeness). Additionally, 28 white dwarfs were not in the initial selection from *Gaia* DR3, most of which are in unresolved binaries. I used *Gaia* DR3 photometry and astrometry to determine a uniform set of white dwarf parameters, including mass, effective temperature, and cooling age. I then assessed the demographics of the 40 pc sample, specifically magnetic fields, binarity, space density and mass distributions.

4.1 Introduction

Following the observations presented in Chapter 3, and some additional observations presented in this chapter, the 40 pc *Gaia* sample has over 97 per cent spectroscopic completeness. In this chapter, I present a study of the full, unbiased sample of white dwarfs within 40 pc of the Sun. This work builds upon that of McCleery et al. (2020) who previously used *Gaia* DR2 to study the 40 pc northern hemisphere sample. Larger 100 pc volume samples have also been studied, including the white dwarf sample in the SDSS footprint (Kilic et al., 2020b; Caron et al., 2023; Kilic et al., 2025), and the *Gaia* DR3 sample of low resolution spectra (Jiménez-Esteban et al., 2023; García-Zamora et al., 2023; Vincent et al., 2024). However, these samples have a significantly lower volume completeness than the 40 pc sample in terms of high signal-to-noise and medium resolution spectroscopy.

White dwarf volume samples have been found to have several practical advantages for deriving astrophysical relations, despite suggestions that volume samples reflect a highly sub-optimal selection function (Rix et al., 2021). First and foremost, decades of spectroscopic and spectropolarimetric follow-up work for nearby white dwarfs allows the derivation of stellar parameters that are more precise and accurate than for white dwarfs at larger distances (Bergeron et al., 2019; McCleery et al., 2020; Bagnulo and Landstreet, 2022). Furthermore, white dwarfs with cooling ages > 5 Gyr rapidly become fainter than the *Gaia* magnitude limit at distances larger than 40–100 pc, resulting in increasingly age- and mass-biased samples. Older and heavier white dwarfs that have long cooling ages and short main-sequence lifetimes are intrinsically faint and only seen in the local volume, yet they provide a robust test of the oldest planetary systems (Hollands et al., 2018a; Kaiser et al., 2021; Hollands et al., 2021; Blouin and Xu, 2022; Elms et al., 2022) and stellar evolution models, e.g. by using wide binaries (El-Badry et al., 2021; Qiu et al., 2021; Heintz et al., 2022; Moss et al., 2022).

The star formation history of the disc of the Milky Way has been determined using white dwarfs (Fantin et al., 2019, and references therein). Recently, Cukanovaite et al. (2023) derived the star formation history of the Galactic disc using the 40 pc white dwarf sample. They found that a uniform star formation history with one galactic component provided a good fit to the *Gaia* G-magnitude distribution of the white dwarfs in this local volume. Local white dwarf samples have been used to study the evolution of magnetism in stars and the origin of magnetic white dwarfs (Ferrario et al., 2020; Bagnulo and Landstreet, 2020, 2022; Hardy et al., 2023a), the initial-final mass relation (El-Badry et al., 2018), core crystallisation (Tremblay et al., 2019b; Cheng et al., 2019; McCleery et al., 2020; Kilic et al., 2020b; Blouin et al., 2021), white dwarf spectral evolution, convective mixing and carbon dredge-up (Blouin et al., 2019b; Ourique et al., 2020; Cunningham et al., 2020;

López-Sanjuan et al., 2022a; Blouin et al., 2023a,b; Camisassa et al., 2023), and binary evolution and gravitational wave background predictions (Toonen et al., 2017; Hollands et al., 2018b; Rebassa-Mansergas et al., 2021; Torres et al., 2022; Korol et al., 2022; Kupfer et al., 2024).

Tremblay et al. (2020) used the *Gaia* DR2 white dwarf catalogue from Gentile Fusillo et al. (2019) to confirm 179 new white dwarfs within 40 pc, mostly in the northern hemisphere. O’Brien et al. (2023) (Chapter 3 of this work) used the updated *Gaia* DR3 white dwarf catalogue from Gentile Fusillo et al. (2021) to confirm 203 new white dwarfs within 40 pc, mostly in the southern hemisphere. With the additional 21 new observations presented in this work, the nature of 1081 *Gaia* white dwarf candidates out of the 1083 from the Gentile Fusillo et al. (2021) white dwarf catalogue have now been spectroscopically confirmed within 40 pc. Just three of these are main-sequence contaminants and the other 1078 are white dwarfs. Therefore, the *Gaia* DR3 40 pc white dwarf sample now has 99.8 per cent spectroscopic completeness. In addition, the completeness of the *Gaia* DR3 white dwarf selection from Gentile Fusillo et al. (2021) at 40 pc is estimated to be ≈ 97 per cent based on pre-*Gaia* surveys and population synthesis (Toonen et al., 2017; Hollands et al., 2018b; McCleery et al., 2020, and this work). The 40 pc white dwarf sample is the largest ever volume-complete sample of white dwarfs with complete medium-resolution optical spectroscopic follow-up. As noted by Gentile Fusillo et al. (2021), reddening effects for white dwarfs closer than 40 pc are essentially negligible, and therefore no correction was made for reddening in this work.

Section 4.2 describes the 40 pc white dwarf sample, considering the *Gaia*-identified white dwarfs as well as those that are not in the Gentile Fusillo et al. (2021) *Gaia*-based catalogue. Section 4.3 discusses aspects of the 40 pc white dwarf sample, including binarity, magnetism, pollution from planetary debris, and space density. I conclude in Section 4.4.

4.2 The 40 pc sample

The 40 pc white dwarf sample, as discussed in this work, refers to all white dwarf candidates from the Gentile Fusillo et al. (2021) catalogue, selected from *Gaia* DR3, within 40 pc of the Sun that have been spectroscopically confirmed. The *Gaia* 40 pc white dwarf sample, with 1078 members, is accessible online at: <https://cygnus.astro.warwick.ac.uk/phrtxn/>. A description of the contents of the online material is in Table 4.1. The tables follow a similar format to table A1 from McCleery et al. (2020). Unless specified, the analysis in this work only considered the white dwarfs in this main *Gaia*-identified sample (Gentile Fusillo et al., 2021).

A noise cut in *Gaia* DR3 identifies $\approx 18\,000$ total sources within 40 pc. In this cut, I

selected sources with `parallax_over_error > 1` and outside the Galactic plane `astrometric_excess_noise < 1.5`, but within the Galactic plane `astrometric_excess_noise < 1`. Given the 1078 white dwarfs in this volume, approximately 6 per cent of stars within 40 pc are white dwarfs. This result is consistent with the volume-complete RECONS 10 pc sample, for which 6 per cent of stars are white dwarfs (19 out of 316) (Henry et al., 2018).

There are two sources which are white dwarf candidates without spectroscopic follow-up within 40 pc; these are listed in Table 4.2. There are 15 confirmed and candidate white dwarfs within $1\sigma_{\varpi}$ of 40 pc, listed in Table 4.3. There are 28 known white dwarfs that did not make the cut of Gentile Fusillo et al. (2021), mostly due to photometric contamination from nearby bright stars, which are listed in Table 4.4. In Sections 4.3.3 and 4.3.4, it is specified that all white dwarfs and candidates from these tables will be included along with the main 40 pc white dwarf sample, for completeness in the analysis. There are issues with the *Gaia* photometric parameters caused by the low-mass issue for low- T_{eff} white dwarfs, which are corrected for and discussed in Section 4.2.1. For the main *Gaia*-defined 40 pc sample, there are some white dwarfs which are very cool or have contaminated photometry, and therefore their T_{eff} and $\log(g)$ values determined from fitting *Gaia* photometry were not included. These white dwarfs are listed in Table 4.5, and I discuss the reasons for these issues in Section 4.2.2. Fig. 4.1 shows a *Gaia* HR diagram of the full 40 pc sample, including evolution models, where candidate white dwarfs and those with unreliable *Gaia* parameters are highlighted. I also provide a wide binary catalogue online at this link: <https://cygnus.astro.warwick.ac.uk/phrtxn/>, which includes all 40 pc wide multiple-star systems where at least one component is a white dwarf. The methods used to determine common proper motion pairs using *Gaia* are discussed in Section 4.3.3.

Every white dwarf in the sample has been classified into a spectral type with a published reference which, coupled with a careful inspection of prior spectral modelling (see, e.g., Limoges et al., 2015; Tremblay et al., 2020; O’Brien et al., 2023) and a comparison with *Gaia* photometric parameters (Gentile Fusillo et al., 2021), informed the atmospheric composition (H- or He-rich). I used this composition to identify the appropriate set of *Gaia* photometric parameters determined by Gentile Fusillo et al. (2021). Table 4.6 shows the adopted atmospheric composition for every spectral type in the 40 pc white dwarf sample.

An atmospheric composition of $\log(\text{H}/\text{He}) = -5$ (in number of atoms) was adopted for $T_{\text{eff}} > 7000$ K white dwarfs with He-dominated atmospheres, as a pure-He composition does not reproduce the B-branch bifurcation seen in the *Gaia* HR diagram for white dwarfs above this T_{eff} (Bergeron et al., 2019). The amount of H in this composition is typically below the optical spectroscopic detection limit. However, Blouin et al. (2023a) and Camisassa et al. (2023) have demonstrated that an atmospheric composition of He with trace C below the optical detection limit better reproduces the *Gaia* HR diagram bifurcation. Both trace

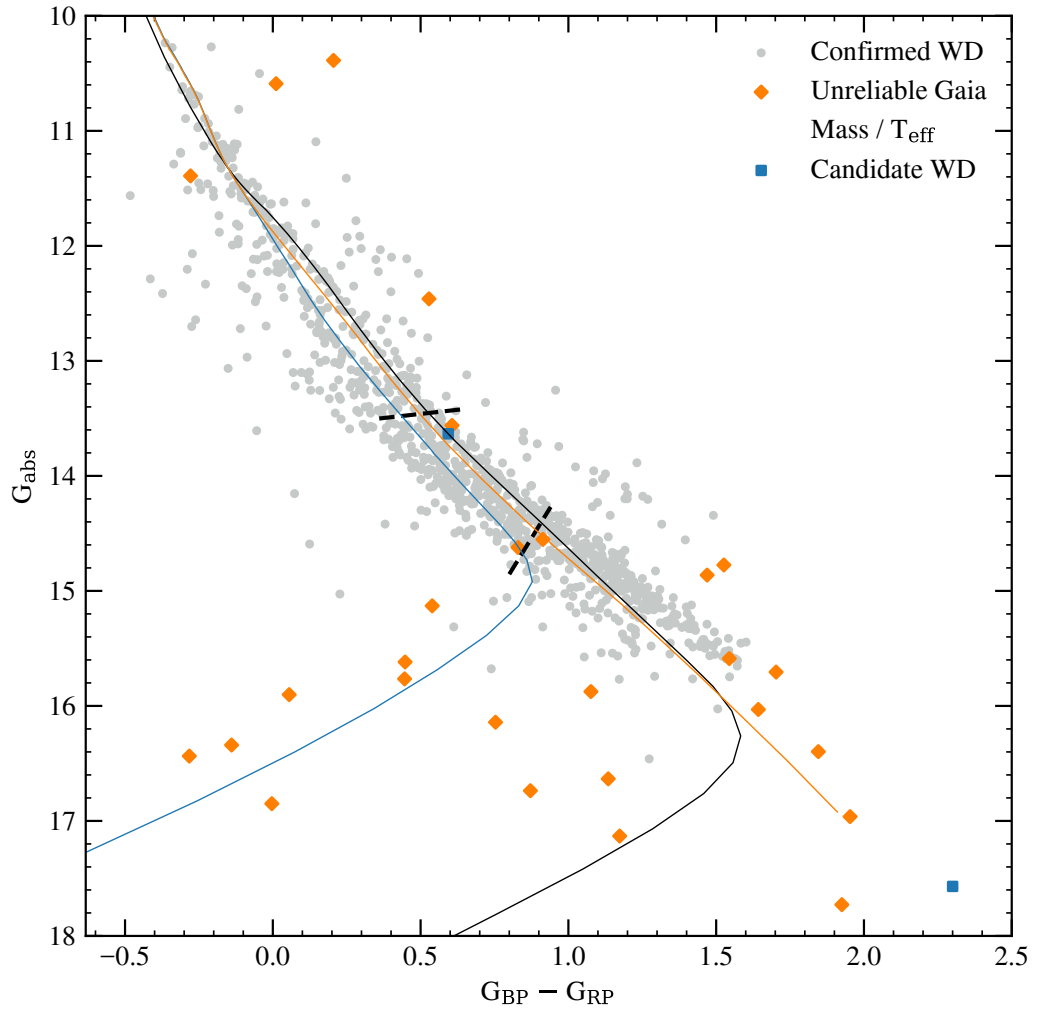


Figure 4.1: A *Gaia* HR diagram showing all spectroscopically confirmed white dwarfs within 40 pc that are in the Gentile Fusillo et al. (2021) catalogue. Confirmed white dwarfs that have unreliable masses determined from *Gaia* photometry and astrometry are shown as orange diamonds. The remaining unobserved candidates from Gentile Fusillo et al. (2021) are shown as blue squares. The orange line indicates pure-He cooling tracks, the black line indicates pure-H cooling tracks and the blue line indicates mixed H/He = 10^{-5} cooling tracks for a $0.6 M_{\odot}$ white dwarf. The black dashed lines indicate where 7000 K (upper line) and 5000 K (lower line) white dwarfs sit on the cooling tracks.

C and H contribute to increase the number of free electrons, and hence the strength of the He^- free-free opacity at optical wavelengths (e.g. Provencal et al. 2002). Therefore, the effects of C and H are fully degenerate for individual white dwarfs, unless detailed abundances are available, e.g. C/He for DQ stars, or H/He for a handful of He-rich DA or DZA. As a consequence, I continued to adopt the H/He mixed model atmospheres (McCleery et al., 2020) to account for the effect of both H and C in He-rich atmospheres, where $\log(\text{H}/\text{He}) = -5$ reproduces the median position of the B-branch. I opted not to use models with tailored atmospheric compositions for DZ and DQ white dwarfs, for the reasons explained above and for homogeneity, as these models change the T_{eff} and mass by less than 3% and $0.05 M_{\odot}$, respectively, in the majority of cases. See Blouin and Dufour (2019), Coutu et al. (2019) and Caron et al. (2023) for abundances and parameters of DQ and DZ white dwarfs calculated using tailored models, some of which overlap with the 40 pc sample presented in this work.

Below ≈ 7000 K, models with $\log(\text{H}/\text{He}) = -5$ composition start to develop bluer colours (Gentile Fusillo et al., 2020; Bergeron et al., 2022) due to collision-induced absorption (CIA), which was not observed in the large majority of white dwarfs in the local sample. This could be a consequence of using H as a proxy for C in the model atmospheres, as carbon is not predicted to contribute to any IR opacity. The spectral evolution of trace H and C abundances in He-rich atmospheres at cool temperatures remains only partially understood (Blouin and Dufour, 2019; Bergeron et al., 2022). Hydrogen would need to be almost fully removed from He-rich models to fit most *Gaia* observations, which is at odds with the current understanding of spectral evolution (Blouin et al., 2023a), or H_2 -He CIA opacity could be modified to match the observations (Bergeron et al., 2022). Instead of using ad-hoc corrections in this case, pure-helium models for He-rich atmospheres below 7000 K were used, which fitted reasonably well to the *Gaia* white dwarf cooling track (Fig. 4.1).

Below 5200 K, the large majority of white dwarfs are of the DC spectral type, and their atmospheric composition is unconstrained from spectroscopy alone. Optical and IR photometry demonstrates a single, homogeneous cool white dwarf population (Gentile Fusillo et al., 2020), not enabling the separation of H- and He-rich atmospheres from photometry alone. This might be evidence for spectral evolution to H-rich composition for the vast majority of cool white dwarfs (Caron et al., 2023), although there is no direct evidence nor models that predict that spectral evolution takes place in this temperature range. Rather, evidence from the cool DZ population, where the broadening of metal lines depends on atmospheric composition, suggests that both H- and He-rich atmospheres are frequent below 5200 K (Dufour et al., 2007b; Blouin et al., 2018b; Hollands et al., 2021; Kaiser et al., 2021; Elms et al., 2022), plausibly at the He-rich/H-rich frequency of ≈ 30 per cent seen in the warmer range $7000 \gtrsim T_{\text{eff}} \gtrsim 5000$ K (Blouin et al., 2019b; McCleery et al., 2020; López-

Sanjuan et al., 2022a). For simplicity, pure-H models were used for all DC white dwarfs with $T_{\text{eff}} < 5200$ K, since both pure-H and pure-He models predict similar *Gaia* fluxes in this range (Fig. 4.1).

4.2.1 Correction to mass and effective temperature

A population of white dwarfs evolved from single stars are expected to have an essentially constant median mass, independent of temperature (Tremblay et al., 2016). This is in contrast with atmosphere-modelled observations, where there is a low-mass issue found when fitting white dwarf optical photometry. White dwarfs with H-rich and with He-rich atmospheres that are cooler than ≈ 6000 K are found to have significantly lower masses than the canonical $\approx 0.6 M_{\odot}$ value (Hollands et al., 2018b; Bergeron et al., 2019; Blouin et al., 2019b; McCleery et al., 2020; Hollands et al., 2021), most likely due to inaccurate opacities in the atmospheric models (Caron et al., 2023), for example a problem with the red wing of Ly α .

The low-mass issue is demonstrated in Fig. 4.2, where the 40 pc mass distribution determined from *Gaia* photometry is compared with synthetic white dwarf masses from Cunningham et al. (2024). The synthetic mass distribution was formed from a Monte Carlo simulation of a Galactic disc population of main-sequence stars put through an initial-final mass relation based on the 40 pc sample. *The synthetic mass distribution was produced by T. Cunningham.* There is only a small difference between the synthetic masses for cool and warm white dwarfs, however, in the atmosphere-modelled observations there is a strong excess of lower-mass white dwarfs below 6000 K.

It could be the case that the low-mass cool white dwarfs are actually unresolved double degenerates. In this case, the implication of a trend to lower masses as a function of age is that many double white dwarfs and few single white dwarfs formed more than 3 Gyr ago, compared to the population that formed more recently. This is not consistent with binary evolution theory, and therefore it is more likely that the low-mass trend is caused by incorrect opacities.

Effect of changing the Ly α opacity

I tested the effect of correcting opacities in the atmosphere models on the masses determined from *Gaia* photometry. The dominant opacities at optical wavelengths ($0.3 - 1.0 \mu\text{m}$) for a pure-H atmosphere at ≈ 4000 K (see Figure 17 of Saumon et al., 2022) are the red wing of Ly α (Kowalski and Saumon, 2006; Rohrmann et al., 2011) and H⁻ bound-free. CIA opacity is dominant in the IR, and hence can also indirectly influence the overall optical flux by energy redistribution.

Table 4.1: Format of the online 40 pc catalogue, which is accessible at: <https://cygnus.astro.warwick.ac.uk/phrtxn/>

| Index | Column Name | Units | Description |
|-------|----------------|--------------------|-------------------------------------------------------------------------------|
| 1 | WDJ_name | – | WDJ (RA) hhmss.ss ± (Dec) ddmss.ss, equinox and epoch 2000 |
| 2 | DR3_source_id | – | <i>Gaia</i> DR3 source identifier |
| 3 | parallax | mas | <i>Gaia</i> DR3 parallax |
| 4 | parallax_error | mas | <i>Gaia</i> DR3 parallax standard error |
| 5 | ra | deg | Right ascension (J2015.5) |
| 6 | ra_error | deg | Standard error of right ascension |
| 7 | dec | deg | Declination (J2015.5) |
| 8 | dec_error | deg | Standard error of declination |
| 9 | absG | magnitude | Absolute <i>Gaia</i> DR3 G magnitude |
| 10 | bp_rp | magnitude | <i>Gaia</i> DR3 BP minus <i>Gaia</i> DR3 RP colour index |
| 11 | SpT | – | Spectral type |
| 12 | comp | – | Atmospheric composition (H for hydrogen-dominated or He for helium-dominated) |
| 13 | gaia_teff | K | Adopted <i>Gaia</i> DR3 effective temperature |
| 14 | gaia_teff_err | K | Standard error on adopted <i>Gaia</i> DR3 effective temperature |
| 15 | gaia_logg | cm s ⁻² | Adopted <i>Gaia</i> DR3 surface gravity |
| 16 | gaia_logg_err | cm s ⁻² | Standard error on adopted <i>Gaia</i> DR3 surface gravity |
| 17 | gaia_mass | M _⊙ | Adopted <i>Gaia</i> DR3 mass |
| 18 | gaia_mass_err | M _⊙ | Standard error on adopted <i>Gaia</i> DR3 mass |
| 19 | corrected_teff | K | Effective temperature after low-mass correction (see Section 4.2.1) |
| 20 | corrected_mass | M _⊙ | Mass after low-mass correction (see Section 4.2.1) |
| 21 | corrected_age | Gyr | Cooling age after low-mass correction (see Section 4.2.1) |
| 22 | bibcode | – | Reference paper for spectral type |
| 23 | comment | – | Additional comment |

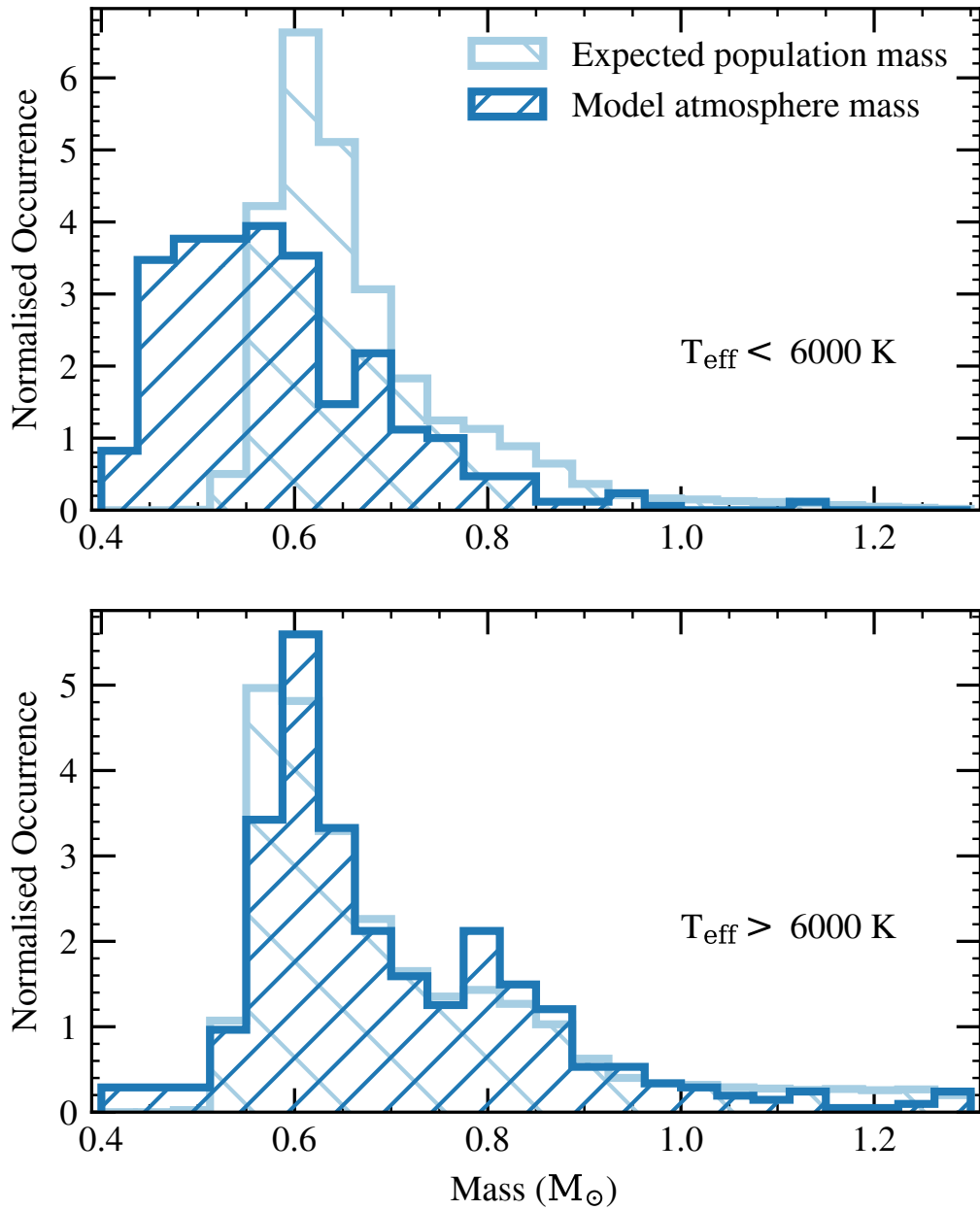


Figure 4.2: The mass distribution of white dwarfs in the 40 pc sample determined from *Gaia* photometry. Also shown is the mass distribution of simulated white dwarfs, with estimated observational errors drawn from a normal distribution with $\mu = 0$ and $\sigma = 0.02 M_{\odot}$, taken from Cunningham et al. (2024). Double-degenerate candidates have been removed from the observational distribution. Upper panel: white dwarfs with T_{eff} below 6000 K; lower panel: white dwarfs with T_{eff} above 6000 K.

Table 4.2: White dwarf candidates within 40 pc in the Gentile Fusillo et al. (2021) DR3 catalogue that do not have spectroscopic follow-up.

| WDJ Name | DR3 Source ID | Parallax | P_{WD} |
|----------------------|---------------------|--------------|----------|
| 095953.92–502717.75 | 5405389966089801984 | 26.57 (0.04) | 1.00 |
| *224600.88–060947.02 | 2611515835965491968 | 27 (1) | 0.79 |

*: This system is likely to be a brown dwarf (see Section 4.2.4 for details).

The grids of pure-H model atmospheres and spectra were recomputed by multiplying the overall Ly α H-H₂ opacity of Kowalski and Saumon (2006) by an illustrative factor of 5. This factor of 5 is arbitrary, but was chosen because Ly α \times 5 cooling tracks follow the shape of the *Gaia* HR diagram well. *The recomputed model atmosphere grids were generated by P.-E. Tremblay.* The resulting *Gaia* parameters for white dwarfs with $T_{\text{eff}} < 10\,000$ K are shown in Fig. 4.3. The results of this change in the Ly α opacity demonstrate that a possible uncertainty in the strength of this opacity at visible wavelengths is a plausible explanation for the low-mass issue observed in cool white dwarfs in the optical. However, the median mass following this correction, as shown in Fig. 4.3 is not exactly constant for cooling white dwarfs and therefore would need further tweaking if it were adopted.

Ad-hoc correction

Missing and incorrect opacities in low- T_{eff} and high-pressure white dwarf atmospheres is a major challenge for the research area (Saumon et al., 2022), and it is out of the scope of this work to attempt to solve these issues. Therefore, in order to obtain the expected constant median mass for cooling white dwarfs, I chose to apply an ad-hoc *Gaia* mass and T_{eff} correction to all the white dwarfs in the 40 pc sample with an initial *Gaia* T_{eff} less than 6000 K, the effect of which is shown in Fig. 4.4. Correcting the mass and T_{eff} in this way enabled meaningful analysis of the volume-complete sample, for which 45 per cent of white dwarfs have $T_{\text{eff}} < 6000$ K and would otherwise have unreliable masses from photometry.

For this ad-hoc correction, I first fitted a function to the median mass distribution of white dwarfs with T_{eff} values below 6000 K (shown by the black dashed line in Fig. 4.4). When calculating median masses as discussed here, double degenerate candidates and white dwarfs on the crystallisation sequence were removed, to ensure the correction was set to the canonical $\approx 0.6 M_{\odot}$ value. I then fitted a correction function so that the median mass as a function of T_{eff} tended towards the canonical mass, which is the median mass in the stable range of $8000 < T_{\text{eff}} < 13\,000$ K (shown by the solid blue line in Fig. 4.4). I applied this mass correction to all 40 pc white dwarfs with $T_{\text{eff}} < 6000$ K.

Once the mass had been corrected, the corresponding T_{eff} had to be corrected according to the white dwarf mass-radius relation (Bédard et al., 2020) and the Stefan-

Table 4.3: Confirmed white dwarfs and candidates in the Gentile Fusillo et al. (2021) DR3 catalogue that are within $1\sigma_{\varpi}$ of 40 pc.

| WD J Name | DR3 Source ID | Parallax | P _{WD} | SPT | Reference |
|----------------------|---------------------|----------------|-----------------|------|-------------------------|
| 014240.09-171410.85 | 5142336825646176256 | 24.97 (0.09) | 1.00 | DAH | O'Brien et al. (2023) |
| 054858.25-750745.20 | 4648527839871194880 | 24.97 (0.09) | - | DZH | O'Brien et al. (2023) |
| 055231.03+164250.27 | 3349849778193723008 | 24.97 (0.04) | 1.00 | DBA | Tremblay et al. (2020) |
| 080247.02+564640.62 | 1081514379072280320 | 24.9 (0.2) | 0.99 | DC | Tremblay et al. (2020) |
| 100819.19+121813.94 | 3881550619014086912 | 23 (3) | 1.00 | - | - |
| *102834.88-000029.39 | 3831059120921201280 | 24.997 (0.026) | 0.03 | DA+M | Gianninas et al. (2011) |
| 122257.77-742707.70 | 5838312052354944256 | 24.97 (0.07) | 0.99 | DA | O'Brien et al. (2023) |
| 133340.50-370550.65 | 6162813873991704960 | 24.99 (0.07) | 0.99 | - | - |
| 134118.69+022737.01 | 3713218786120541824 | 24.96 (0.09) | 0.99 | DQ | Kilic et al. (2010) |
| 180218.60+135405.46 | 4496751667093478016 | 25.00 (0.04) | 0.99 | DAZ | Tremblay et al. (2020) |
| 183010.48-244209.53 | 4077104740685645056 | 24 (1) | 1.00 | - | - |
| 193500.68-172443.11 | 4180014832789446400 | 25.0 (0.2) | 1.00 | DC | Tremblay et al. (2020) |
| 193501.33-072527.42 | 4207055367062840320 | 24.9 (0.2) | 0.96 | DC | This work |
| 214810.74-562613.14 | 6460523071166427392 | 24.98 (0.08) | 1.00 | DAH | O'Brien et al. (2023) |
| 222919.46-444138.86 | 6520516480027596288 | 24.97 (0.03) | 1.00 | DA | Beers et al. (1992) |

*: This system has a low P_{WD} due to the M-dwarf companion.

Table 4.4: White dwarfs within 40 pc that are not in the Gentile Fusillo et al. (2021) DR3 catalogue.

| DR3 Source ID | WD Name | Parallax | SpT | SpT Reference | Note |
|---------------------|----------------|--------------|-------|---------------------------------|------|
| – | Procyon B | 285 (1) | DQZ+F | Limoges et al. (2015) | (1) |
| 1355264565043431040 | WD 1708+437 | 131.6 (0.4) | WD+M | Delfosse et al. (1999) | (2) |
| 4937000898856154624 | WD 0210–510 | 92.6 (0.1) | DQ | Farihi et al. (2013) | (3) |
| 975968340910692608 | WD 0727+482B | 88.72 (0.03) | DA | Limoges et al. (2015) | (4) |
| 975968340912517248 | WD 0727+482A | 88.72 (0.03) | DA | Limoges et al. (2015) | (4) |
| 3223516063958808064 | GJ 207.1 | 63.36 (0.05) | WD+M | Baroch et al. (2021) | (2) |
| 1005873614080407296 | LHS 1817 | 61.43 (0.05) | WD+M | Winters et al. (2020) | (2) |
| 2185710338703934976 | WD 2003+542 | 60.30 (0.03) | WD+M | Gizis (1998) | (2) |
| 4788741548375134336 | WD 0419–487 | 47.2 (0.02) | DA+M | Gianninas et al. (2011) | (2) |
| 1362295082910131200 | HD 159062B | 46.19 (0.01) | WD+G | Hirsch et al. (2019) | (4) |
| 2274076301516712704 | WD 2126+734B | 44.91 (0.07) | DC | Zuckerman et al. (1997) | (3) |
| 6431977687725247104 | SCR J1848–6855 | 43.9 (0.1) | WD+M | Jao et al. (2014) | (2) |
| 3701290326205270528 | WD 1214+032 | 42.77 (0.04) | DA | Limoges et al. (2015) | (3) |
| 2983256662868370048 | GJ 3346 B | 42.24 (0.04) | WD+K | Bonavita et al. (2020) | (3) |
| – | Regulus B | 41.1 (0.4) | WD+B | Gies et al. (2020) | (1) |
| 3729017810434416128 | HD 114174 B | 37.87 (0.02) | WD+G | Crepp et al. (2013) | (2) |
| 1548104507825815296 | WD 1213+528 | 34.95 (0.02) | DA+M | Limoges et al. (2015) | (2) |
| 1550299304833675392 | WD 1324+458 | 32.77 (0.02) | DA+M | van den Besselaar et al. (2007) | (2) |
| 5389590533737966208 | WD 1108–408 | 32.5 (0.2) | DC | Monteiro et al. (2006) | (3) |
| 6665685378201412992 | CD–53 8345B | 31.3 (0.08) | DA | O’Brien et al. (2023) | (3) |
| 4478524169500496000 | HD 169889 | 28.27 (0.03) | WD+G | Crepp et al. (2018) | (2) |
| – | WD 1634–573 | 27.9 (0.2) | DOA+K | Dreizler and Werner (1996) | (1) |
| 1962707287281651712 | PM J22105+4532 | 27.76 (0.09) | DC | Limoges et al. (2013) | (3) |
| 2643862402903084544 | 12 Psc B | 27.53 (0.02) | WD+G | Bowler et al. (2021) | (2) |
| 3845263368043086080 | WD 0911+023 | 27.1 (0.6) | WD+B | Holberg et al. (2013) | (2) |
| 3817534337626005632 | WD 1120+073 | 27.0 (0.5) | DC | Limoges et al. (2015) | (4) |
| 759601941671398272 | WD 1133+358 | 25.91 (0.06) | DC+M | Putney (1997) | (2) |
| 3000597125173673088 | PM J06157–1247 | 25.8 (0.1) | WD+M | Fajardo-Acosta et al. (2016) | (2) |

Notes: (1) Missing entirely from *Gaia* DR3, (2) Unresolved white dwarf plus main sequence binary, (3) Missing or incorrect colours, (4) Missing five-parameter astrometry. For many binaries, parallaxes are for the companion. Where no *Gaia* ID is available, parallaxes are from *Hipparcos* (van Leeuwen, 2007). A white dwarf that has not been spectroscopically confirmed is denoted as WD.

Table 4.5: White dwarfs within 40 pc with unreliable *Gaia* parameters. Best-fit parameters are instead taken from literature.

| WDJ Name | Parallax [mas] | SpT | T_{eff} [K] | Mass [M_{\odot}] | Description | Reference |
|---------------------|-------------------|--------|-------------------------|-------------------------|-------------|---------------------------|
| 021348.83-334530.03 | 53.33 (0.06) | DAZ | 5150 (150) | 0.4 (0.1) | (1) | This work |
| 023538.55-303225.52 | 30.6 (0.2) | DC | - | - | (2) | This work |
| 022432.27-285459.46 | 34.5 (0.1) | DC | 4880 (160) | 1.071 (0.003) | (2) | Bergeron et al. (2022) |
| 034646.52+245602.67 | 25.3 (0.2) | DC | 3640 (60) | 0.423 (0.007) | (2) | Bergeron et al. (2022) |
| 041359.12-212222.67 | 27.87 (0.08) | DC | - | - | (3) | This work |
| 050600.41+590326.89 | 27.7 (0.3) | DC | - | - | (2) | This work |
| 063038.60-020550.49 | 46.72 (0.03) | DA+M | 6910 (140) | 0.53 (0.1) | (1) | Gianninas et al. (2011) |
| 064509.30-164300.72 | 374.5 (0.2) | DA | 25 970 (380) | 0.98 (0.03) | (1) | Giammichele et al. (2012) |
| 075508.95-144550.95 | 25.55 (0.02) | DA+M | 19 440 (290) | 0.58 (0.02) | (1) | Gianninas et al. (2011) |
| 085357.69-244656.23 | 38.8 (0.1) | DC | 3740 (40) | 0.672 (0.003) | (2) | Bergeron et al. (2022) |
| 090208.37+201051.57 | 26.1 (0.1) | DQ | 5500 (110) | 0.71 (0.01) | (4) | Blouin and Dufour (2019) |
| 101141.58+284559.07 | 67.88 (0.06) | DQpecH | 4340 (170) | 0.70 (0.06) | (4) | Blouin and Dufour (2019) |
| 104410.24-691818.08 | 34.18 (0.02) | DA+M | 22 570 (330) | 0.54 (0.02) | (1) | Gianninas et al. (2011) |
| 110217.52+411321.18 | 28.7 (0.3) | DC | 3790 (20) | 0.56 (0.01) | (2) | Caron et al. (2023) |
| 115007.08+240403.54 | 33.2 (0.3) | DC | - | - | (5) | This work |
| 122048.70+091413.08 | 26.7 (0.3) | DC | 3890 (60) | 1.081 (0.008) | (2) | Bergeron et al. (2022) |
| 130503.44+702243.05 | 28.9 (0.2) | DC | - | - | (2) | Tremblay et al. (2020) |
| 140324.75+453333.02 | 29.1 (0.2) | DC | 4820 (20) | 1.184 (0.003) | (2) | Bergeron et al. (2022) |
| 155647.51-080601.24 | 30.6 (0.2) | DC | 4880 (110) | 1.054 (0.004) | (2) | Bergeron et al. (2022) |
| 165401.26+625354.91 | 32.5 (0.1) | DC | 4990 (30) | 1.049 (0.002) | (2) | Bergeron et al. (2022) |
| 192206.20+023313.29 | 25.4 (0.3) | DZ | 3340 (50) | 0.57 (0.03) | (2) | Elms et al. (2022) |
| 195211.78-732235.48 | 31.2 (0.3) | DC | - | - | (2) | O'Brien et al. (2023) |
| 201231.78-595651.67 | 60.80 (0.03) | DC | 4910 (210) | 0.44 (0.01) | (2) | Giammichele et al. (2012) |
| 214756.59-403527.79 | 35.8 (0.5) | DZQH | 3050 (40) | 0.69 (0.02) | (5) | Elms et al. (2022) |
| 215406.45-011709.55 | 39.2 (0.1) | DA+M | 9190 (130) | 0.58 (0.03) | (1) | Giammichele et al. (2012) |
| 230550.09+392232.88 | 27.9 (0.1) | DC | 4550 (30) | 0.698 (0.004) | (2) | Bergeron et al. (2022) |
| 231732.63-460816.77 | 26.0 (0.3) | DQpec | 4080 (100) | 0.70 (0.01) | (1) | This work |

Notes: (1) *Gaia* photometry contaminated by nearby main-sequence star or unresolved main-sequence companion, (2) IR-faint white dwarf with no unique *Gaia* fit solution, (3) Candidate double-degenerate, (4) Strong C₂ molecular features affect *Gaia* photometry, (5) Ultra-cool white dwarf.

Table 4.6: All white dwarf spectral types listed in the 40 pc sample, where photometric model composition refers to composition-selected Gentile Fusillo et al. (2021) parameters. Spectral types ending with H (Zeeman splitting) or P (polarised) imply magnetism, which does not impact atmospheric composition. In all cases other than for DA and DAH/P, (H/P) were added to spectral types to note that some white dwarfs in that group are magnetic. The lowercase ‘e’ indicates the presence of emission features.

| Spectral type (SpT) | Number in 40 pc | Photometric model composition |
|---------------------|-----------------|--------------------------------------------------------------------------------------|
| DA | 538 | pure-H (except for 2 He-rich DA) |
| DAH or DAP | 64 | pure-H |
| DA(H)e | 4 | pure-H |
| DAZ(H/P) | 53 | pure-H |
| DB(H/P) | 9 | $\log(\text{H}/\text{He}) = -5$ |
| DBA(H/P) | 6 | $\log(\text{H}/\text{He}) = -5$ |
| DBQA | 1 | $\log(\text{H}/\text{He}) = -5$ |
| DBZA | 1 | $\log(\text{H}/\text{He}) = -5$ |
| DC(H/P) | 287 | $\log(\text{H}/\text{He}) = -5$, pure-He below 7000 K, assumed pure-H below 5200 K |
| DQ(H/P) | 34 | $\log(\text{H}/\text{He}) = -5$, pure-He below 7000 K |
| warm DQ | 2 | pure-He |
| DQpec(H/P) | 8 | $\log(\text{H}/\text{He}) = -5$, pure-He below 7000 K |
| DQZ | 3 | $\log(\text{H}/\text{He}) = -5$, pure-He below 7000 K |
| DX(H/P) | 4 | dependent on individual atmospheric analysis |
| DZ(H/P) | 45 | $\log(\text{H}/\text{He}) = -5$, pure-He below 7000 K, except pure-H for H-rich DZ |
| DZA(H/P) | 14 | $\log(\text{H}/\text{He}) = -5$, pure-He below 7000 K, except pure-H for H-rich DZA |
| DZAB | 1 | $\log(\text{H}/\text{He}) = -5$, pure-He below 7000 K |
| DZQ(H/P) | 2 | $\log(\text{H}/\text{He}) = -5$, pure-He below 7000 K |

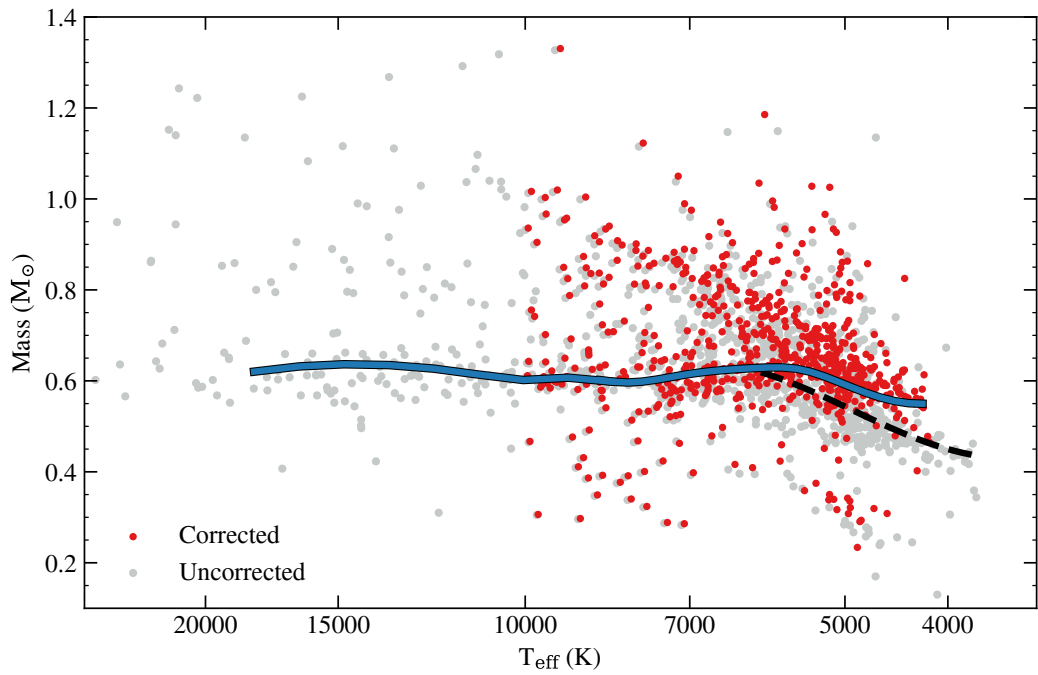


Figure 4.3: The effect of using pure-H atmosphere models where the Ly α red wing opacity of Kowalski and Saumon (2006) has been multiplied by a factor of 5, on the resulting white dwarf *Gaia* mass and T_{eff} , for objects with $T_{\text{eff}} < 10\,000$ K. The dashed black line shows the median mass before the model corrections, and the solid blue line shows the median mass after these corrections. The corrections were only applied to white dwarfs with H-rich or assumed H-rich compositions.

Boltzmann law to reproduce the known luminosity of each white dwarf. For all analysis in this paper, *Gaia* mass and T_{eff} were corrected using this method. Given a mass correction, the radius correction will be roughly the same at all masses up to $1.1 M_{\odot}$, which includes every white dwarf with $T_{\text{eff}} < 6000$ K in the sample, hence I did not include a mass dependence in the correction.

The function for correcting the *Gaia* masses for $T_{\text{eff}} < 6000$ K is a fifth-order polynomial:

$$\Delta M(T_{\text{eff},i}) = -4.613 \times 10^{-19} T_{\text{eff},i}^5 + 1.726 \times 10^{-14} T_{\text{eff},i}^4 - 2.486 \times 10^{-10} T_{\text{eff},i}^3 + 1.706 \times 10^{-6} T_{\text{eff},i}^2 - 0.005487 T_{\text{eff},i} + 7.068, \quad (4.1)$$

where $T_{\text{eff},i}$ is the initial uncorrected T_{eff} . The corrected mass is:

$$M_c = M_i + M_{\text{med}} - \Delta M(T_{\text{eff},i}), \quad (4.2)$$

where M_i is the initial uncorrected mass, M_{med} is the median of the canonical mass in the stable mass range ($0.63 M_{\odot}$ for this sample), and M_c is the final corrected mass.

After applying Equations 4.1 and 4.2, the T_{eff} is corrected by combining the white dwarf mass-radius relation and the Stefan-Boltzmann law:

$$\frac{T_{\text{eff},c}}{T_{\text{eff},i}} = \left(\frac{M_c}{M_i} \right)^{1/6}, \quad (4.3)$$

where $T_{\text{eff},c}$ is the corrected T_{eff} .

Following the ad-hoc correction, the median mass for standard single white dwarfs (solid blue line in Fig. 4.4) is relatively constant as T_{eff} decreases, which is expected. There is a small increase around 7000 K due to the overlap of the crystallisation sequence with the canonical-mass white dwarfs.

Due to the ad-hoc nature, these corrections are only applicable to masses determined from *Gaia* photometry. Columns 19 and 20 of Table 4.1 correspond to these corrected mass and T_{eff} values respectively, where the statistical uncertainties should be taken to be the same as those without corrections. Mass and T_{eff} values that have not been corrected are also provided in Table 4.1. Ad-hoc mass corrections have been used in previous white dwarf studies, e.g. Bergeron et al. (1994); Giammichele et al. (2012), for other issues that have now been largely resolved with better models (Tremblay and Bergeron, 2009; Tremblay et al., 2013a).

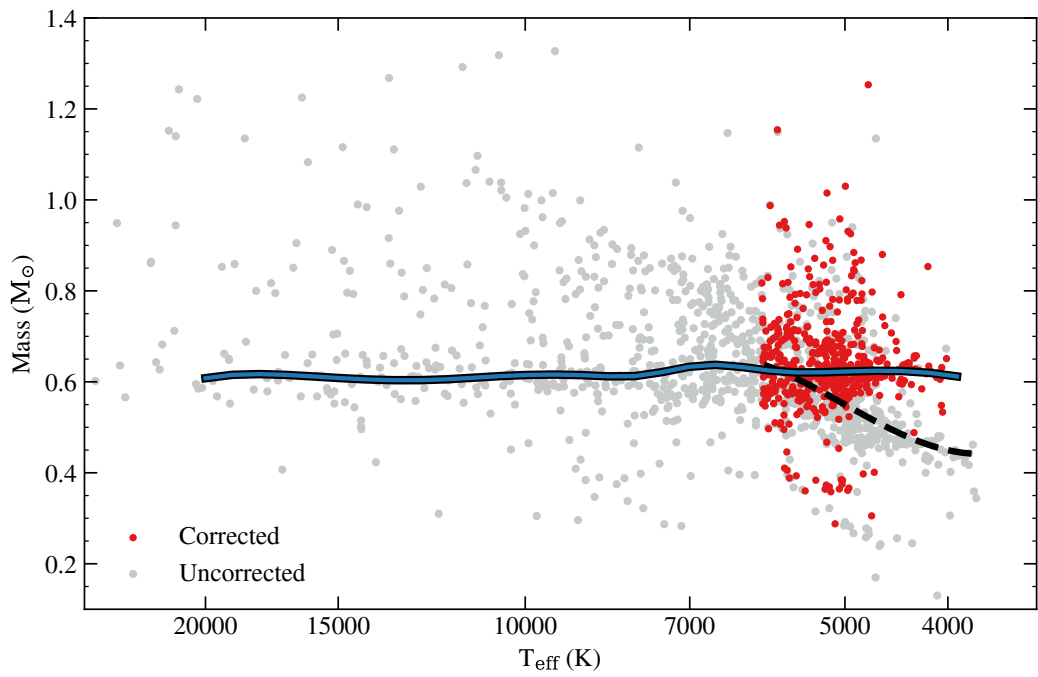


Figure 4.4: Corrected *Gaia* mass and T_{eff} for all 40 pc white dwarfs below 6000 K (red points) with the ad-hoc mass correction presented in this work, compared to the original mass distribution (grey points). The dashed black line shows the median mass before the mass and T_{eff} corrections, and the solid blue line shows the median mass after these corrections. The median mass in the stable range of $13\,000 > T_{\text{eff}} > 8000$ K was used as a reference for the correction.

4.2.2 White dwarfs with unreliable *Gaia* masses and temperatures

Gaia T_{eff} , $\log(g)$ and masses are not provided for 27 white dwarfs in the 40 pc sample. These white dwarfs are listed in Table 4.5 and correspond to the orange diamond points in Fig. 4.1. For some, their *Gaia* photometry has been contaminated by a bright main-sequence star which is either a companion or a background object.

Many of the white dwarfs in Table 4.5 display signs of CIA which greatly affects the shape of their spectral energy distributions. White dwarfs displaying strong CIA opacity are classified as IR-faint (Kilic et al., 2020b; Bergeron et al., 2022; Elms et al., 2022). The parameters of these IR-faint white dwarfs listed in Table 4.5 are heavily dependent on the atmosphere models used to fit them, since different codes use different microphysics to account for the extremely dense atmospheres of these stars. Due to their positions on the *Gaia* HR diagram, these white dwarfs are potentially ultra-cool ($T_{\text{eff}} < 4000$ K). However, Bergeron et al. (2022) suggested that many IR-faint white dwarfs are warmer than 4000 K (see parameters in Table 4.5). Spectral features caused by metal pollution enable a more accurate determination of parameters in these white dwarfs displaying CIA (Elms et al., 2022), but in most cases IR-faint spectra are featureless. There are also two white dwarfs in Table 4.5 for which strong molecular carbon absorption bands dramatically affect the *Gaia* colours of the white dwarf. Therefore, the parameters from *Gaia* photometric fitting of these white dwarfs are not considered to be reliable.

4.2.3 New spectroscopic observations

In this section, 21 new white dwarfs within 40 pc are presented, for which there are no previous spectroscopic observations at medium resolution or higher. Their parameters are given in Table 4.7. Observations from the following spectroscopic instruments were used to confirm these new candidates: the High Resolution Echelle Spectrometer (HIRES) on the Keck 10-m telescope (Vogt et al., 1994), the Kast Double Spectrograph on the 3-m Shane telescope, the Magellan Echelle (MagE) and Magellan Inamori Kyocera Echelle (MIKE) instruments on the 6.5-m Magellan telescopes (Marshall et al., 2008), and the X-shooter spectrograph on the VLT (Vernet et al., 2011). New spectra of stars previously confirmed as white dwarfs are also shown, where spectral types have been updated following higher-resolution or wider wavelength coverage of the new spectra.

Following the addition of 21 new white dwarfs, the *Gaia* 40 pc sample has 1078 confirmed white dwarfs out of 1083 candidates from Gentile Fusillo et al. (2021). There are three confirmed main-sequence star contaminants in the sample (O’Brien et al., 2023), designated as WD J081219.58–261639.46, WD J092424.45–181859.87, and WD J173230.79–171033.14 in Gentile Fusillo et al. (2021), which leaves just two candidates

remaining without spectroscopic follow-up (see Section 4.2.4 for details).

WD J0413–2122 has a P_{WD} of 0.657 in Gentile Fusillo et al. (2021) and a low *Gaia* $\log(g)$ and T_{eff} . Fitting unresolved double degenerate systems as if they are single stars causes their $\log(g)$ and mass to be underestimated, so this star is likely an unresolved double degenerate.

I determined equivalent widths of the Ca II K lines in WD J0213–3345 and WD J1154–6239 to be 450 mÅ and 220 mÅ respectively. Best-fit results from the combined spectra and available photometry alongside metal abundances for these new DAZ white dwarfs are shown in Table 4.10. These Ca II lines are not likely to be interstellar in origin, given that in both spectra the radial velocities of the lines are in agreement with the photospheric velocity as best as it can be determined from H α .

WD J0213–3345 had moved to within 1.1 arcsec of an equally bright star during the epoch of the *Gaia* observations (Hollands et al., 2018b). In *Gaia* DR3, this star has a renormalised unit weight error (RUWE) of 1.8. Therefore, the *Gaia* photometry is likely to be contaminated. In the combined fit, APASS photometry from 2012 and 2MASS photometry from 2003 were incorporated, which are likely to be less contaminated given the 0.4 arcsec/year proper motion of the star.

WD J2236–0140 was theorised to be a highly magnetic DAH white dwarf in O’Brien et al. (2023), but due to the limited resolution and coverage of the available spectrum, its field strength could not be constrained. The new Kast spectrum confirmed that this white dwarf is indeed a high-field DAH.

WD J2317–4608 is a DQpec white dwarf with strong carbon features. It has a wide main-sequence companion separated by 330 au (6 arcsec on-sky separation), which has contaminated the IR photometry of the white dwarf, and the *Gaia* RP colour is also potentially affected by the companion. For this reason, the $\log(g)$ was fixed for the fit (see Table 4.10). The models do not account for the distortions of the carbon Swan bands, which is associated with the DQpec class. Therefore the best-fit model does not accurately trace the carbon features. With an absolute *Gaia* G value of 16.40, this white dwarf is significantly fainter than any DQ in the Montreal White Dwarf Database (Dufour et al., 2017), and therefore is potentially the coolest confirmed DQ white dwarf with a calculated carbon abundance.

WD J0235–3032 is an IR-faint DC white dwarf that displays strong signs of CIA. Only *Gaia* and Pan-STARRS photometry are available for this white dwarf, so its T_{eff} , mass and atmospheric composition could not be accurately constrained without near-IR photometry. Similarly, WD J0506+5903 is also a very blue, IR-faint white dwarf.

WD J2141–3300 and WD J1927–0355 are highly metal-polluted white dwarfs with He-dominated atmospheres. The *Gaia* photometry of these stars indicates $T_{\text{eff}} \approx 7000$ K

Table 4.7: White dwarfs within 40 pc confirmed in this work with spectroscopic follow-up.

| WDJ Name | Parallax [mas] | SpT | <i>Gaia</i> T_{eff} [K] | <i>Gaia</i> $\log(g)$ | Instrument | Date of Observation |
|----------------------|--------------------------------|-------|-------------------------------------|-----------------------|---------------|------------------------|
| 011103.67-722741.26 | 34.78 (0.07) | DC | 4160 (130) | 7.72 (0.09) | Magellan/MIKE | 2023/09/21 |
| *021348.83-334530.03 | 53.33 (0.06) | DAZ | - | - | Magellan/MIKE | 2021/12/19 |
| 023538.55-303225.52 | 30.6 (0.2) | DC | - | - | VLT/X-shooter | 2023/08/09 |
| 031330.78-424243.22 | 25.73 (0.09) | DC | 4990 (60) | 7.96 (0.05) | Magellan/MIKE | 2023/09/21 |
| 041359.12-212222.67 | 27.87 (0.08) | DC | - | - | Shane/Kast | 2023/12/11; 2024/01/06 |
| 050600.41+590326.89 | 27.7 (0.3) | DC | - | - | Shane/Kast | 2023/10/20 |
| 055602.01+135446.71 | 36.53 (0.08) | DA | 5020 (70) | 7.92 (0.05) | Shane/Kast | 2021/09/27 |
| 090834.39+172148.53 | 30.68 (0.06) | DC | 4950 (60) | 7.32 (0.05) | Shane/Kast | 2021/11/13 |
| 102926.67+125733.40 | 27.8 (0.2) | DZH | 5496 (100) | 8.18 (0.07) | Shane/Kast | 2023/05/15 |
| 110143.04+172139.39 | 34.67 (0.05) | DA | 7710 (210) | 8.39 (0.06) | Shane/Kast | 2023/05/15 |
| 115007.08+240403.54 | 33.2 (0.3) | DC | - | - | Shane/Kast | 2023/12/11; 2024/01/06 |
| *115454.07-623919.42 | 44.54 (0.05) | DAZ | 4950 (160) | 7.8 (0.1) | Magellan/MagE | 2022/03/23 |
| 115954.88-601625.45 | 38.50 (0.06) | DA | 4780 (50) | 7.79 (0.03) | Magellan/MagE | 2022/03/23 |
| 151358.72-201445.94 | 36.26 (0.02) | DA | 10900 (110) | 7.98 (0.02) | Keck/HIRES | 2018/05/18 |
| 171409.55-053419.96 | 38.20 (0.03) | DA | 9630 (80) | 8.16 (0.02) | Keck/HIRES | 2018/05/18 |
| 171955.76+363936.32 | 28.54 (0.05) | DQpec | 6730 (390) | 8.4 (0.2) | Shane/Kast | 2023/06/25 |
| 174512.54-215309.25 | 25.5 (0.3) | DC | 3980 (240) | 7.6 (0.2) | Shane/Kast | 2023/06/25 |
| 184700.42+181107.49 | 34.49 (0.04) | DA | 8540 (230) | 8.19 (0.06) | Shane/Kast | 2023/05/15 |
| *192743.10-035555.23 | 41.93 (0.04) | DZA | 6850 (50) | 8.07 (0.02) | Keck/HIRES | 2019/07/07; 2019/09/07 |
| 193501.33-072527.42 | 24.9 (0.2) [$1\sigma_{\pi}$] | DC | 4150 (170) | 7.5 (0.1) | Shane/Kast | 2018/08/02; 2019/07/26 |
| *231732.63-460816.77 | 26.0 (0.3) | DQpec | - | - | Magellan/MIKE | 2023/09/21 |
| | | | | | VLT/X-shooter | 2023/06/20 |

*: Spectroscopic T_{eff} and $\log(g)$ are presented in Table 4.10.

Table 4.8: Known white dwarfs within 40 pc with new spectroscopic follow-up and updated spectral types.

| WDJ Name | Parallax [mas] | Old SpT (Reference) | Updated SpT | <i>Gaia</i> T _{eff} [K] | <i>Gaia</i> log(<i>g</i>) | Instrument | Date of Observation |
|----------------------|-------------------|------------------------|-------------|-------------------------------------|-----------------------------|------------|---------------------------------------|
| 031907.61+423045.45 | 32.71 (0.03) | DC (1) | DBA | 10 970 (130) | 8.22 (0.02) | Shane/Kast | 2016/09/23 |
| 131830.01+735318.25 | 27.4 (0.1) | DC: (2) | DA | 5000 (40) | 7.35 (0.04) | Shane/Kast | 2022/04/09 |
| 191936.23+452743.55 | 35.70 (0.04) | DC: (2) | DA | 4780 (20) | 7.31 (0.02) | Shane/Kast | 2021/11/14 |
| *214157.57-330029.80 | 62.07 (0.02) | DZH (3) | DZAH | 7110 (50) | 8.00 (0.02) | Keck/HIRES | 2008/08/06; 2008/08/07; 2008/11/14 |
| 223607.66-014059.65 | 25.63 (0.04) | DAH: (2) | DAH | 10 020 (160) | 8.37 (0.03) | Shane/Kast | 2018/07/16; 2016/09/22 |

Notes: (1) Tremblay et al. (2020), (2) O’Brien et al. (2023), (3) Bagnulo and Landstreet (2019). *: Spectroscopic T_{eff} and log(*g*) are presented in Table 4.10.

and $\log(g) = 8$ for both objects, assuming no metals. However, the spectra show very strong features that influence the photometry. WD J2141–3300 is commonly known as WD 2138–332 and was discovered as a polluted white dwarf by Subasavage et al. (2007). WD J1927–0355 was first identified as polluted by the Kast spectrograph, and was followed up with the HIRES instrument. A detailed analysis of the accreted material observed in the atmospheres of these two white dwarfs is presented Chapter 5.

WD J1719+3639 was observed with the Kast spectrograph. It appears to show features resembling carbon Swan bands. The spectrum of WD J1719+3639 is similar to that of SDSS J161847.38+061155.2, which was designated as a problematic DQpec object by Blouin and Dufour (2019). I therefore tentatively classified this white dwarf as a DQpec. WD J1029+1257 was also observed with the Kast spectrograph. This star has distorted Ca II H+K-lines that are indicative of a magnetic field, and therefore I classified this star as a DZH.

Three new cool DC white dwarfs were observed, which have high-resolution echelle spectra from the MIKE instrument on the Magellan telescope. One of these is a newly confirmed white dwarf that lies within $1\sigma_w$ of 40 pc, WD J1935–0725. These white dwarfs have the spectral type DC because there is no indication of an H α feature even with such high resolution data.

4.2.4 White dwarfs missing from the 40 pc spectroscopic sample

There are two candidate white dwarfs in the catalogue of Gentile Fusillo et al. (2021) that are within 40 pc but do not have medium or high-resolution spectroscopic observations to confirm their classification. These are presented in Table 4.2. Medium-resolution spectroscopy with a higher signal-to-noise is still required to confirm these candidates. The SDSS $g - z$ colour for WD J2246–0609 of almost 6.0 is consistent with an isolated brown dwarf, and as such it is likely to be a contaminant in the white dwarf sample. WD J0959–5027 is likely to be a standard 7000 K white dwarf, but is in front of the Galactic plane, so is challenging to observe spectroscopically without strong contamination.

There are 15 known white dwarfs within $1\sigma_w$ of 40 pc, 12 of which have been spectroscopically confirmed. These white dwarfs are listed in Table 4.3. All white dwarfs were taken from the catalogue of Gentile Fusillo et al. (2021), except WD J0548–7507 (see O’Brien et al. 2023 for details). These stars were included in the statistical analysis of the space density of white dwarfs, for completeness (see Section 4.3.4).

There are 28 known white dwarfs within 40 pc that are not in the catalogue of Gentile Fusillo et al. (2021). These objects are presented in Table 4.4. Not all white dwarfs in this list are spectroscopically confirmed, as some were detected from radial velocity variations in main-sequence stars, rendering spectral classification difficult. Binaries are discussed

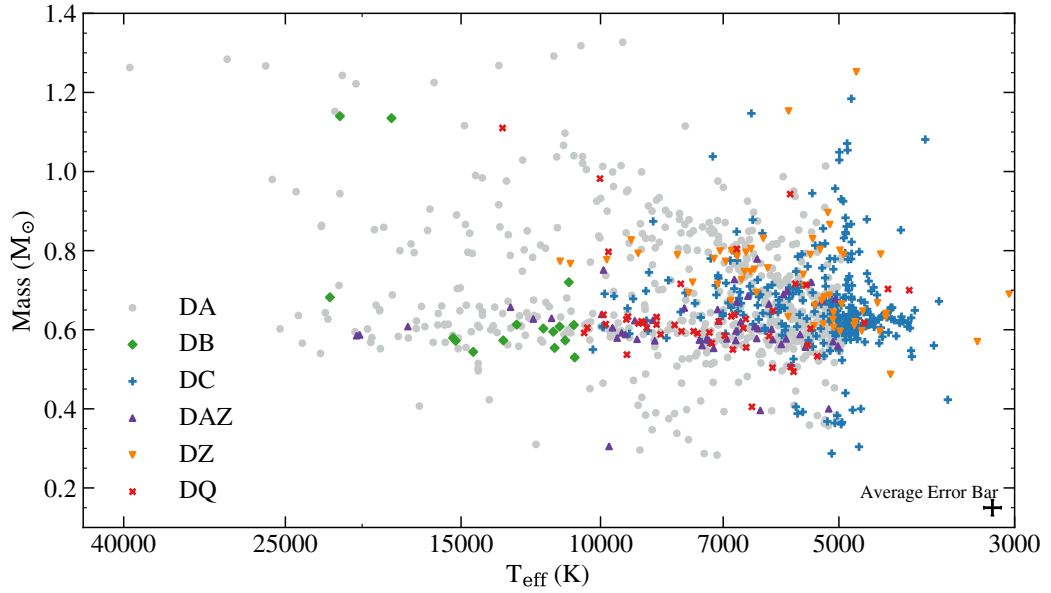


Figure 4.5: Corrected *Gaia* mass and T_{eff} for all 40 pc white dwarfs, where spectral type is indicated by the shape and colour of points. For white dwarfs with unreliable *Gaia* atmospheric parameters, parameters from Table 4.5 were plotted instead. The average statistical error is shown by the black point on the lower right. More complex spectral types have been simplified to only their most prominent features.

further in Section 4.3.3.

The star WISE 1028–6327 was tentatively classified as a DAZ white dwarf by Kirkpatrick et al. (2016), but is missing from the Gentile Fusillo et al. (2021) catalogue. Its very faint absolute magnitude of $G_{\text{abs}} = 18.5$ is not consistent with a DA white dwarf and the *JHK* flux is consistent with an M dwarf or brown dwarf. The spectrum shown in Kirkpatrick et al. (2016) and the *Gaia* colours are not consistent with a binary (white dwarf + M dwarf). Therefore this object was removed from the 40 pc sample.

4.2.5 Spectroscopic biases

Fig. 4.5 shows the full *Gaia* 40 pc white dwarf sample with spectral types indicated. For those with unreliable *Gaia* atmospheric parameters, parameters were instead taken from the literature, for completeness (See Table 4.5). However, for the remainder of the analysis in this work relating to white dwarf mass and T_{eff} , only white dwarfs that have reliable parameters determined from *Gaia* photometry were considered, in order to keep the sample parameters homogeneous.

The 40 pc *Gaia* white dwarf sample is spectroscopically heterogeneous – spectra confirming the white dwarfs in the sample have been collected from a wide range of

instruments with varying resolution and wavelength coverage. In almost all cases, spectral types were decided based on optical medium-resolution ($R > 1000$) spectroscopy at signal-to-noise > 30 . In many cases, a white dwarf has been observed multiple times at different facilities, and not all observations found in public archives are published. Therefore, it is outside of the scope of this work to list the average or best-achieved signal-to-noise, instrumental resolution and wavelength coverage for the white dwarfs in the sample.

There are inherent issues with using a spectroscopically heterogeneous sample. Not every white dwarf has been observed with the resolution required to identify very weak signatures of metal pollution in the Ca II H+K lines, like the kind seen in the high-resolution survey of DA white dwarfs from Zuckerman et al. (2003). Similarly, not every white dwarf has spectropolarimetric observations or has observations at the resolution required to see faint Zeeman splitting of the spectral features, meaning the magnetic sub-sample is currently incomplete. Some DC, DB, and DZ white dwarfs may display a weak $H\alpha$ feature which would not be detected without coverage of the $H\alpha$ region.

4.3 Discussion

4.3.1 Spectral evolution

The atmospheric composition of a white dwarf can change with time due to physical processes including convection, atomic diffusion and accretion. Fig. 4.6 demonstrates the evolution of the fraction of He-rich atmosphere white dwarfs as a function of T_{eff} . The vertical error bars on the binned data in Fig. 4.6 were calculated by assuming that the fraction of He-atmosphere white dwarfs, $\frac{N_{\text{He}}}{N_{\text{WD}}}$, follows Poisson statistics, and therefore the vertical error $\sigma_{\frac{N_{\text{He}}}{N_{\text{WD}}}}$ is as follows,

$$\sigma_{\frac{N_{\text{He}}}{N_{\text{WD}}}} = \frac{N_{\text{He}}}{N_{\text{WD}}} \sqrt{\frac{1}{N_{\text{He}}} + \frac{1}{N_{\text{WD}}}}. \quad (4.4)$$

This same equation was used to calculate the errors in Fig. 4.13.

There are few very young and hot white dwarfs in the 40 pc sample, so I did not extend the spectral evolution analysis to T_{eff} above 15 000 K. Below 5000 K there will be no visible $H\alpha$ line in the white dwarf spectrum, so the atmospheric composition cannot be directly constrained. Therefore Fig. 4.6 also does not extend to T_{eff} below 5000 K. The full 40 pc observations of spectral evolution are consistent with earlier results for the 40 pc northern hemisphere sample (McCleery et al., 2020). The increase in He-atmosphere incidence between 17 000 K and 9000 K, which is marginal in the 40 pc sample, has previously been attributed to convective mixing using larger samples (Tremblay and Bergeron, 2008; Ourique et al., 2020; Cunningham et al., 2020; López-Sanjuan et al., 2022a; Bédard et al., 2022b).

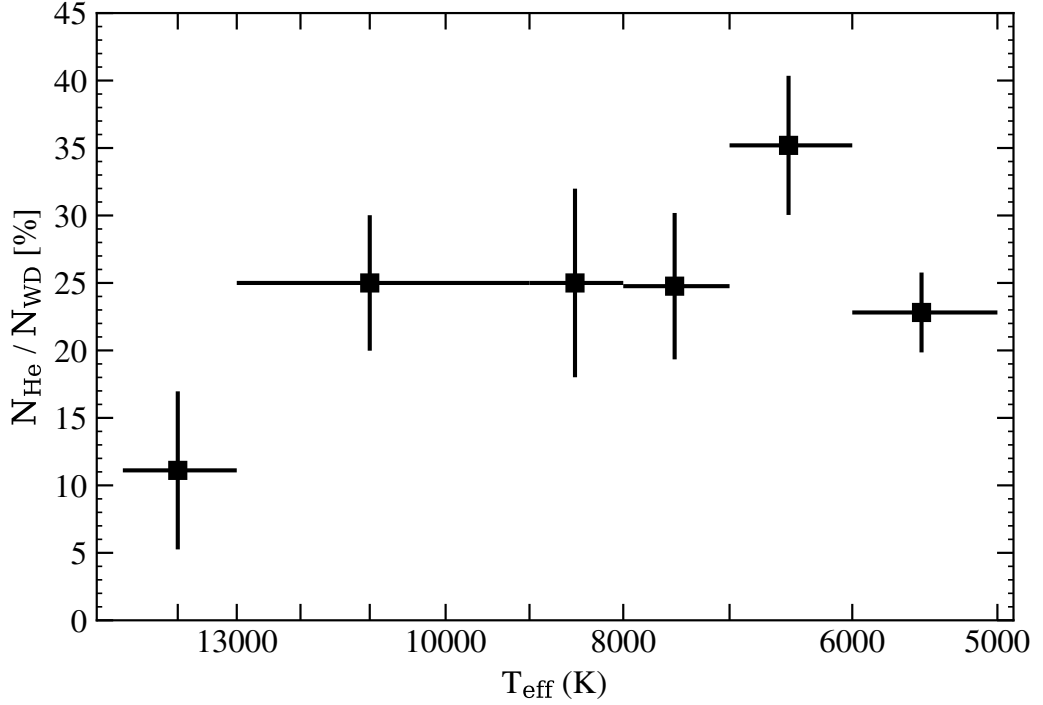


Figure 4.6: The fractional distribution of He-atmosphere white dwarfs compared to the full 40 pc white dwarf sample. Horizontal error bars represent T_{eff} bins and vertical error bars show the uncertainty of the frequency of the occurrence of He-atmosphere white dwarfs within each bin.

Fig. 4.6 suggests an increase in the fraction of He-atmosphere white dwarfs in the range $7000 > T_{\text{eff}} > 6000$ K, although only at 1σ . This excess could be a consequence of model atmospheres with incorrect trace fractions of C and H (see Section 4.2), which in turn would result in an incorrect temperature scale. The temperature range $5000 - 6000$ K has been referred to as the “non-DA gap”, where a decrease in the fraction of He-rich atmosphere white dwarfs was initially identified by Bergeron et al. (1997, 2001). However, there is no clear evidence of spectral evolution in the 40 pc observations at the 2σ level.

4.3.2 Mass distributions

Kilic et al. (2020b) produced a volume-like sample of DA white dwarfs within 100 pc in the SDSS footprint, with $T_{\text{eff}} > 6000$ K. Fig. 4.7 shows that the peak of the mass distribution of the 40 pc sample with corrected photometric *Gaia* masses is in a similar position to that of the 100 pc SDSS sample, in which photometric masses were derived from SDSS u , Pan-STARRS *grizy* and *Gaia* DR2 parallaxes (Kilic et al., 2020b).

Kilic et al. (2020b) observed a peak in the 100 pc DA mass distribution at $0.59 M_{\odot}$,

and a ‘shoulder’ at $0.7 M_{\odot} - 0.9 M_{\odot}$. In Fig. 4.7, I similarly fitted two Gaussian curves, one to the main peak and one to the prominent shoulder of the 40 pc mass distribution, the cause of which remains elusive. The main peak in this distribution sits at $0.61 M_{\odot}$ with a standard deviation of $0.04 M_{\odot}$, with a similar shoulder at $0.7 M_{\odot} - 0.9 M_{\odot}$. Fig. 4.5 displays that same distinct branch of $0.8-0.9 M_{\odot}$ white dwarfs at $10\,000-25\,000$ K, separated from the main distribution at $0.6 M_{\odot}$, and the crystallisation branch at higher masses.

Kilic et al. (2020b) demonstrated, based on binary population synthesis models (Temmink et al., 2020), that the single white dwarfs formed from mergers cannot be the dominant explanation for a shoulder in the white dwarf mass distribution, and instead suggested that the shoulder could be attributed to white dwarf core crystallisation. The 40 pc sample is volume complete and crystallisation cooling delays should not influence the mass distribution, as all white dwarfs at all T_{eff} values were considered. Furthermore, samples of warm, non-crystallised white dwarfs show this shoulder (Tremblay et al., 2016; Sahu et al., 2023). Another explanation given by Tremblay et al. (2016, 2019a) and El-Badry et al. (2018) is that the shoulder is caused by a flattening of the initial-final mass relation at initial masses $3.5 \leq M/M_{\odot} \leq 4.5$ (Cummings et al., 2018), leading to an accumulation of white dwarfs with masses $\sim 0.8 M_{\odot}$. This is possibly linked to the the onset of the second dredge-up in asymptotic giant branch stars (Marigo and Girardi, 2007; Cummings et al., 2015).

The photometric *Gaia* masses for white dwarfs with $T_{\text{eff}} < 6000$ K have been artificially corrected (see Section 4.2.1). The mean *Gaia* mass for white dwarfs with $T_{\text{eff}} > 6000$ K is $0.69 \pm 0.01 M_{\odot}$. The mean mass of the 40 pc northern sample from McCleery et al. (2020) for $T_{\text{eff}} > 5000$ K is slightly lower, $0.66 M_{\odot}$, however in the full 40 pc sample the masses were corrected for $T_{\text{eff}} < 6000$ K so these mean values cannot be directly compared.

There are 33 white dwarfs in the 40 pc sample with masses $> 1 M_{\odot}$ (3 per cent of the sample). Just over a third of these are magnetic, the impact of which is discussed in Section 4.3.6. Of these, 79 per cent have H-dominated atmospheres, which is comparable to the 72 per cent of the full sample with T_{eff} above 5000 K which have H-dominated atmospheres.

4.3.3 Multiple-star systems containing white dwarfs

Considering all known and candidate white dwarfs within 40 pc (see Section 4.3.4 for details), and considering all double degenerate candidates, I determined that there are 209 multiple-star systems containing at least one white dwarf within 40 pc. Based on binary population synthesis models, when considering a constant stellar formation history as was found for the 40 pc sample by Cukanovaite et al. (2023), it was predicted using Toonen et al. (2017) models that there should be 318–458 binary systems containing a white dwarf within

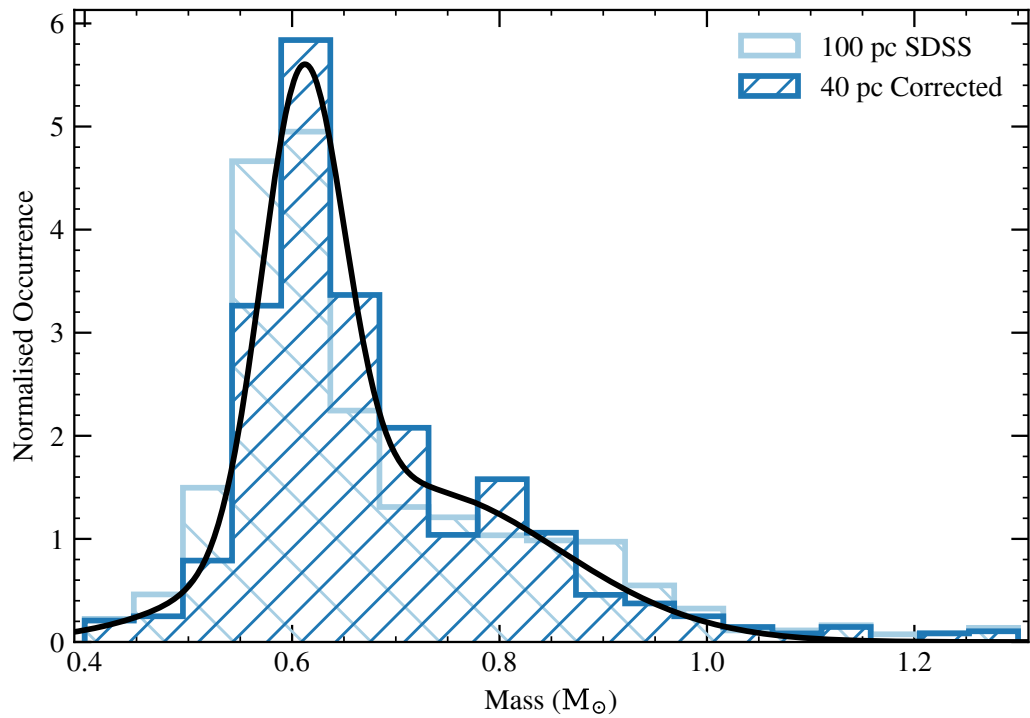


Figure 4.7: The mass distribution of white dwarfs in the 40 pc sample compared to the published masses from the 100 pc SDSS sample of Kilic et al. (2020b). The mass correction outlined in Section 4.2.1 was applied to the 40 pc parameters. The solid black line represents the bimodal best-fitting Gaussians to the 40 pc mass distribution.

40 pc. This discrepancy partially originates from the lack of wide double white dwarfs which will be discussed in Section 4.3.3.

Wide binaries

Wide and unresolved binaries are distinguished in this work based on whether they were resolved as separate sources in *Gaia* DR3 or not, where the *Gaia* on-sky resolution is 0.4 arcsec. In this section, WD denotes a white dwarf, MS denotes a main-sequence star, and BD denotes a brown dwarf.

To search for resolved *Gaia* common proper motion companions to the white dwarfs within 40 pc, I used a similar strategy as described in Hollands et al. (2018b) and McCleery et al. (2020). In short, I performed a cone-search for each white dwarf with a *Gaia* parallax greater than 25 mas, scaled by distance, for a projected separation of 1 pc and radial distance within 1 pc of the white dwarf. The tangential velocity difference was obtained using the difference in proper motion for the two stars as given in *Gaia* DR3. I recovered 121 wide binaries and higher-order systems from this search, which are displayed in Fig. 4.8. I also recovered 33 contaminant pairs, which were subsequently removed. These sources either have large parallax errors, are in crowded regions of the Galaxy, or have unphysical separations in velocity-separation space. The dashed line on Fig. 4.8 indicates the maximum difference in tangential velocity for a WD+MS binary system with component masses $1.4 M_{\odot}$ and $2.5 M_{\odot}$ respectively (Torres et al., 2022). Some triple systems were also identified, in which at least one component is resolved in *Gaia*.

A few systems that are above the dashed line in Fig. 4.8 are known to be genuine wide systems, where their inconsistent separation and velocity difference is caused by higher-order multiplicity. WD J2101–4906 has a main-sequence companion that is itself an unresolved binary (Hollands et al., 2018b), and WD J1702–5314 also has an unresolved binary as a companion. WD J2004+0109 is a wide companion to a spectroscopic triple main-sequence system (Venner et al., 2023). WD J0103+0504 is an unresolved double white dwarf with a double main-sequence binary companion. I inspected systems lying near the dashed line in Fig. 4.8, and kept three such systems in the final wide binary catalogue, for completeness. The dashed line assumes an upper limit on companion mass and orbital geometry that might not always be applicable, and is therefore not an absolute cut.

There are six WD(+MS)+BD systems in the sample, for which the brown dwarf is not in *Gaia* DR3 (Leggett et al., 2015; Mace et al., 2018; Meisner et al., 2020; Zhang et al., 2020; Gonzales et al., 2022). There are three known quadruple systems in the sample: one of which comprises of WD J0103+0504 which is a double degenerate, plus the K-type stars HD 6101 A+B (McCleery et al., 2020); and another which has two resolved white dwarfs from Limoges et al. (2015) that are not in Gentile Fusillo et al. (2021) (WD 0727+482A and B)

combined with an unresolved pair of M-dwarfs. WD J2004+0109 is also part of a quadruple system as mentioned above. Adding these systems as well as other known systems missing from *Gaia* finalised the list at 132 wide binaries, triples, and quadruples in total within 40 pc. These systems are classified as follows: 97 WD+MS, 15 WD+WD, 9 WD+MS+MS, 1 WD+WD+MS, 1 WD+WD+WD, 2 WD+WD+MS+MS, 1 WD+MS+MS+MS, 5 WD+BD, 1 WD+MS+BD. For 8 of these systems, the white dwarf is missing from the catalogue of Gentile Fusillo et al. (2021), because the bright main-sequence companion affects the white dwarf colours or astrometry. These systems are shown as cross symbols in Fig. 4.8, where proper motions are available.

El-Badry et al. (2021) searched for wide binaries in *Gaia* DR3, and intentionally removed triple and quadruple systems. They did not recover seven WD+MS systems that I found in the cone search, for which *Gaia* proper motions were available for both stars. These are shown as plus symbols in Fig. 4.8. Five of these missing systems have a white dwarf that is in Gentile Fusillo et al. (2021). For one of these systems, the main-sequence star has a candidate close brown dwarf companion, which would make this system a triple (Díaz et al., 2012). Another missing system, ϵ Reticuli A+B, also has a close gas giant planet orbiting the main-sequence component (Butler et al., 2001).

Toonen et al. (2017) predicted 169–228 resolved WD+MS systems within 40 pc, compared to the 97 that were observed, and 119–167 resolved WD+WD systems compared to the 15 that were observed. The notable lack of wide WD+WD systems in volume-limited samples compared to predictions from binary population models is discussed in detail in Toonen et al. (2017); El-Badry et al. (2018); McCleery et al. (2020).

Two polluted white dwarfs out of 90 (2 per cent) were found to be in wide binaries with projected separations between 120 and 2500 au, and two polluted white dwarfs out of 22 (10 per cent) were in wide binaries with projected separations greater than 2500 au. The overall fraction of white dwarfs displaying signs of pollution within 40 pc is 11 per cent. Therefore the 40 pc findings are in line with predictions made by Zuckerman (2014), indicating that a close secondary star can suppress the formation or retention of a planetary system (see also Wilson et al. (2019) for further discussion).

Unresolved binaries

There are five unresolved WD+MS systems in the *Gaia* 40 pc sample that have white dwarfs in the Gentile Fusillo et al. (2021) catalogue. There are also 19 unresolved WD+MS systems that are not in the main sample (see Table 4.4), and one extra unresolved WD+MS within $1\sigma_{\varpi}$ of 40 pc. Many of these systems that are missing from Gentile Fusillo et al. (2021) consist of cool white dwarfs with main-sequence companions, such that their *Gaia* photometry places them on or close to the main sequence (see Fig. 4.9). These systems have

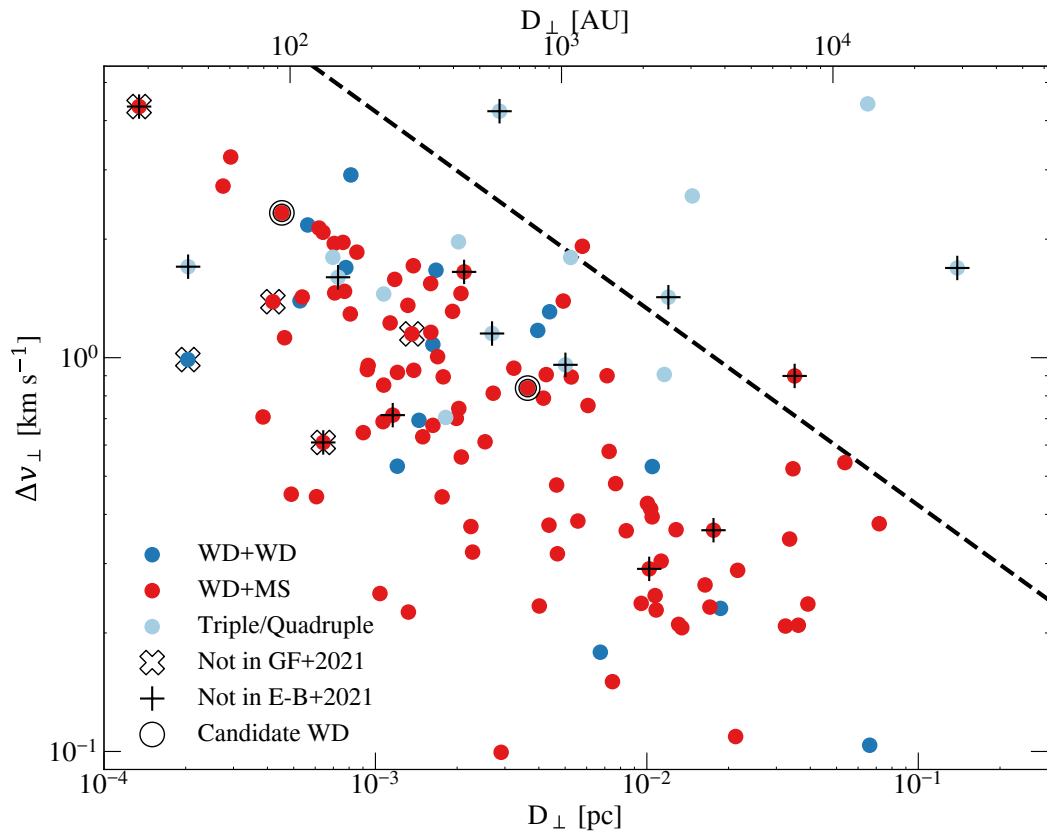


Figure 4.8: Tangential velocity differences as a function of projected separation for *Gaia* DR3 sources that are common proper motion companions to white dwarfs in the 40 pc sample. The black dashed line indicates the maximum tangential velocity difference for a binary with $1.4 M_{\odot} + 2.5 M_{\odot}$ stars on a circular orbit. WD+WD systems are shown in dark blue, WD+MS systems are shown in red, and any type of triple or quadruple system containing at least one white dwarf is shown in light blue.

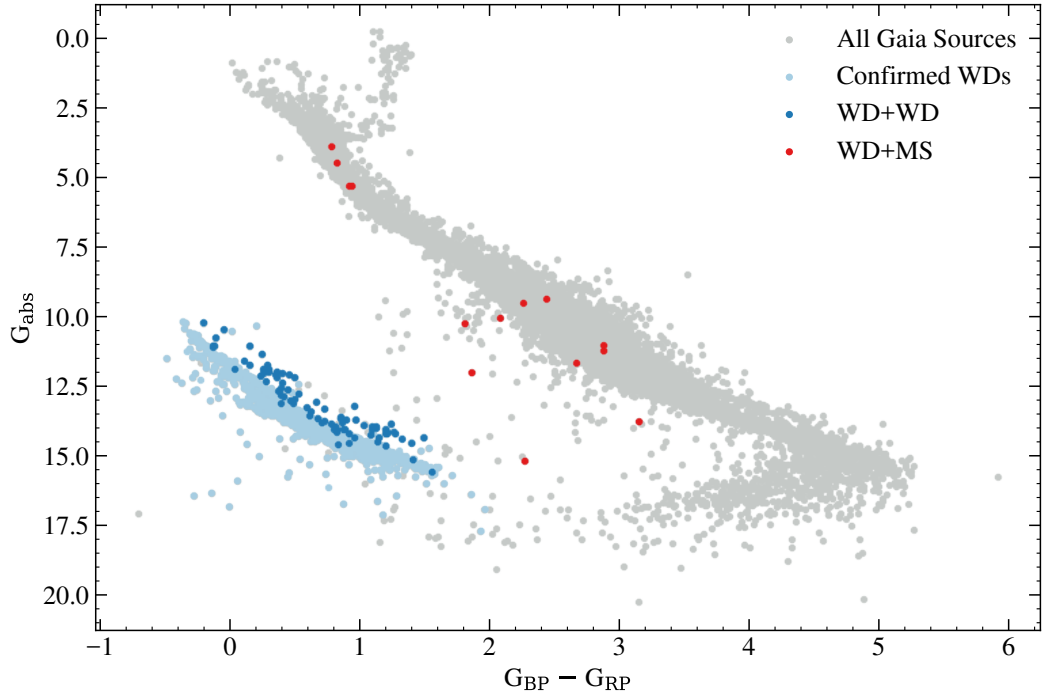


Figure 4.9: A *Gaia* HR diagram showing all spectroscopically confirmed white dwarfs within 40 pc as light blue points, alongside all other *Gaia* sources in the same volume which have `parallax_over_error > 1` and `astrometric_excess_noise < 1.5` from *Gaia* DR3 as grey points. White dwarfs in unresolved binaries with main-sequence companions that are not in the Gentile Fusillo et al. (2021) catalogue are shown as red points. Candidate double white dwarfs are in dark blue.

been serendipitously detected in the literature due to a UV excess from the white dwarf, photometric variability or radial velocity measurements. Regulus A+B, Procyon A+B and HD 149499 A+B are known WD+MS binaries, but the white dwarf is not in *Gaia* at all. The binary sample is likely to be incomplete until systematic spectroscopic, photometric and astrometric variability searches are performed for all $\approx 20\,000$ main-sequence stars within 40 pc.

The Cummings et al. (2018) initial-final mass relation breaks down for single-star evolution at $0.53M_{\odot}$. White dwarfs below this mass cannot be produced in isolation within the lifetime of the Milky Way (Marsh et al., 1995). If the photometry of unresolved WD+WD (double-degenerate) systems is fitted as if they were single stars, their masses will be underestimated (and radii overestimated) and they will lie below the median mass sequence. There are 54 white dwarfs within 40 pc that have corrected *Gaia* masses less than $0.49M_{\odot}$, which is 2σ below the mass limit for single-star evolution assuming an average photometric mass error of $0.02M_{\odot}$, and these stars are therefore highly likely to be double

Table 4.9: Double white dwarf binaries with *Gaia* astrometric periods.

| WDJ Name | <i>Gaia</i> Orbital Period [days] |
|---------------------|-----------------------------------|
| 023117.04+285939.88 | 103.89 (0.08) |
| 092943.17–173250.68 | 238.0 (0.3) |
| 142054.81–090508.76 | 87.53 (0.06) |
| 200654.88+614310.27 | 77.1 (0.1) |
| 211345.93+262133.27 | 219.7 (0.2) |
| 232519.87+140339.61 | 249 (1) |

degenerate systems. All candidate and confirmed unresolved WD+WD systems are flagged in the comment column of the main 40 pc tables online, and shown in Fig. 4.9. Fourteen of these systems within 40 pc are confirmed as unresolved WD+WD binaries from radial velocity measurements (Napiwotzki et al., 2020; Kilic et al., 2020a, 2021). Two of these binaries also have a third wide companion.

If one of the white dwarfs in a double degenerate system is a low-mass white dwarf, formed through mass transfer in the binary evolution process, only the bright low-mass component may be detectable in both the spectrum and photometry of the system. For a featureless double degenerate spectrum, there is no way of determining the individual white dwarf masses in the binary. However, this is possible for DA spectral types. The mass for WD J0946+4354 determined from spectroscopy is $0.45 M_{\odot}$ (Limoges et al., 2015) compared to a photometric mass of $0.42 M_{\odot}$, indicating that this system contains a genuine low-mass white dwarf. Similarly, WD J0841–3256 has a photometric mass of $0.47 M_{\odot}$ and a spectroscopic mass of $0.45 M_{\odot}$ (Bédard et al., 2017). Due to the heterogeneous nature of the 40 pc sample, not all white dwarfs have parameters determined from fitting spectroscopy, and therefore all WD+WD candidates should be followed up for further study to search for more low-mass white dwarfs.

Eleven of the candidate double degenerate systems additionally have a *Gaia* renormalised unit weight error (RUWE) value above 1.4, indicating poor quality astrometric solutions and a high probability of binarity. Six white dwarfs within 40 pc have non-single-star astrometric periods from *Gaia* ranging from 77 – 249 days, and these are shown in Table 4.9. Five of these six systems are also over-luminous double degenerate candidates.

WD J0948+2421 has a larger than average *Gaia* mass of $0.80 \pm 0.01 M_{\odot}$, but is a known DA+DAH system comprised of two more massive white dwarfs (Liebert et al., 1993; McCleery et al., 2020). Similarly, WD J0138–1954 is a double-lined DA+DA binary observed by Napiwotzki et al. (2020) with a large *Gaia* mass of $0.93 \pm 0.01 M_{\odot}$, and its combined low luminosity suggests a pair of ultra-massive white dwarfs.

Based on binary population synthesis models with a constant stellar formation history within 40 pc, Toonen et al. (2017) predicted 6–12 unresolved WD+MS systems

compared to our 25, and 24–51 unresolved WD+WD systems compared to our upper limit of 54. Furthermore, extrapolating from the Hollands et al. (2018b) 20 pc white dwarf sample predicted the number of unresolved binaries expected in 40 pc relatively well: 16 unresolved WD+MS and 56 unresolved WD+WD systems. The Toonen et al. (2017) models under-predicted the fraction of unresolved WD+MS within 40 pc – however the numbers of these systems are not well constrained by observations as they are difficult to detect.

4.3.4 Space density

Fig. 4.10 shows the results of a Galactic simulation of a single white dwarf population, carried out with the same initial conditions as described in Cukanovaite et al. (2023), with a million white dwarfs simulated within 40 pc. *The simulation discussed in this work was created by E. Cukanovaite.* The vertical position of the Sun was set to 20 pc above the Galactic plane in the simulation. The absolute value of the vertical scale height of the Galactic disc was fixed at 75 pc for 1 Gyr because it is difficult to constrain this quantity directly from faint white dwarfs. The vertical scale height varied according to the observed white dwarf velocity dispersion after 1 Gyr.

In the simulation, white dwarfs were only formed with *Gaia* masses above $0.54 M_{\odot}$, as in Cukanovaite et al. (2023). Therefore, white dwarfs below this mass were removed from the data when comparing to the simulation, resulting in 1010 white dwarfs within 40 pc including those not in the Gentile Fusillo et al. (2021) catalogue. The simulation was normalised to the data both at 20 pc and separately at 40 pc. The simulation over-predicted the number of white dwarfs expected at 30–40 pc by up to 2σ . This discrepancy could indicate that the assumed Galactic scale height in the simulation was incorrect, that the assumed vertical position of the Sun above the Galactic plane was incorrect, or that there are ≈ 50 missing white dwarfs, possibly hidden in close binaries with bright main-sequence companions.

Gentile Fusillo et al. (2021) used the *Gaia* DR3 catalogue of white dwarfs within 20 pc to infer a local space density of $4.47 \pm 0.37 \times 10^{-3} \text{ pc}^{-3}$ including those missing from *Gaia*. Unresolved double degenerates were counted as one system in the calculation of space density (see Hollands et al., 2018b). Extrapolating by volume to 40 pc, there would be 1198 ± 99 white dwarfs. Considering all confirmed DR3 white dwarfs (1078), confirmed white dwarfs within $1\sigma_{\varpi}$ of 40 pc (15), remaining DR3 candidates (2), and known white dwarfs missing from Gentile Fusillo et al. (2021) (28), I counted 1123 possible white dwarfs within 40 pc. Extrapolating from the 20 pc sample, 1198 ± 99 white dwarfs are expected to be within 40 pc, which is within 1σ of the measured number of white dwarfs.

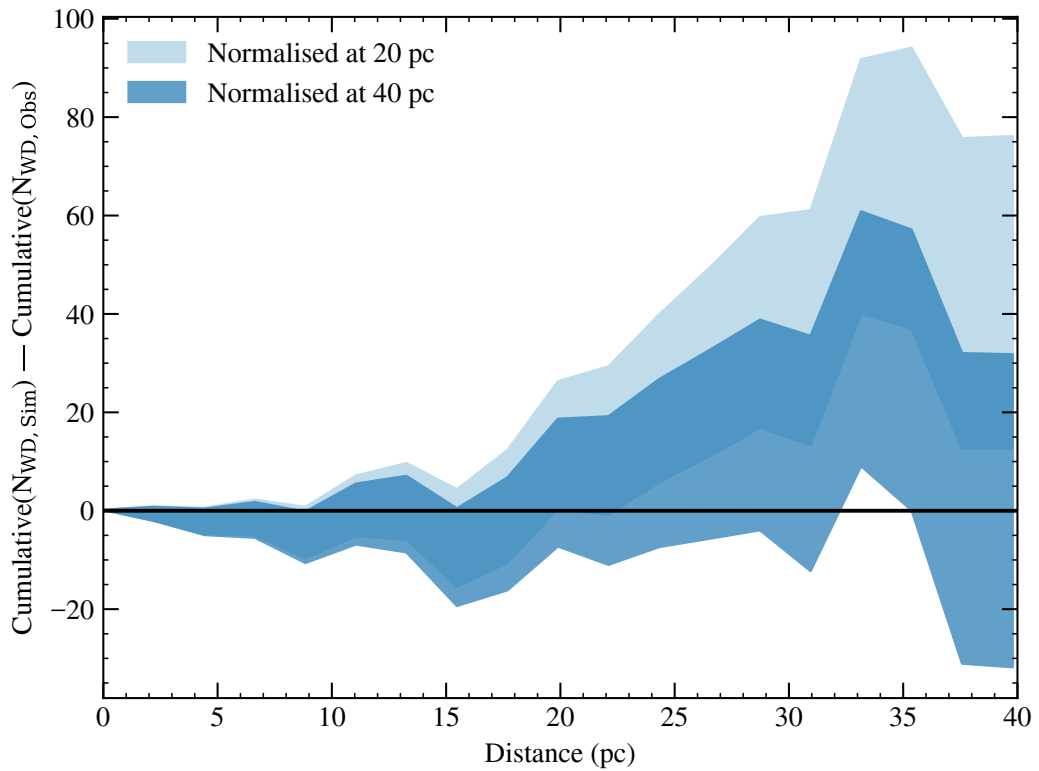


Figure 4.10: The space density of white dwarfs according to the Galactic simulation presented in this work, as a function of the distance to the Sun, compared to the observed space density from the 40 pc sample. The simulation has been normalised at both 20 pc and 40 pc separately. The filled regions represent an error of 1σ on the numbers of white dwarfs. $N_{\text{WD,Sim}}$ is the number of simulated white dwarfs, and $N_{\text{WD,Obs}}$ is the number of observed white dwarfs.

4.3.5 Multi-wavelength analysis

In Fig. 4.11 WISE (Wright et al., 2010), *Gaia*, and GALEX (Martin et al., 2005) photometry were used to study the positions of white dwarfs with H and He atmospheres (top panels) on HR diagrams. The DQ and DZ spectral types were separated out for visual clarity (middle and bottom panels). A linearity correction was applied to the GALEX near-UV photometry, provided by Wall et al. (2019). Cool DC white dwarfs are shown in the top panels of Fig. 4.11 as green points; they are assumed to have pure-H atmospheres for the purpose of deriving atmospheric parameters, but a lack of spectral features means that their composition cannot be constrained.

There is a bifurcation observed between H and He atmosphere white dwarfs in the *Gaia* HR diagram (Gaia Collaboration et al., 2018; Gentile Fusillo et al., 2019; Bergeron et al., 2019; Blouin et al., 2023a; Camisassa et al., 2023), commonly described as DA (H-rich atmosphere) white dwarfs following the A-branch and He-rich atmosphere white dwarfs following the B-branch (Gaia Collaboration et al., 2018). It is clear from Fig. 4.11 that DB, DC, DQ, and DZ white dwarfs indeed follow the B branch. In this work and previous papers in the 40 pc series, He-rich models with additional H, with a composition of $\log(\text{H}/\text{He}) = -5$, were used to fit DC white dwarfs (McCleery et al., 2020; Gentile Fusillo et al., 2021; O’Brien et al., 2023). In Fig. 4.11, the white dwarfs with He-dominated atmospheres (DB, DC, DQ and DZ) follow this model sequence closely, but deviate from it as they cool (e.g. $G_{\text{BP}} - G_{\text{RP}} < 0.8$). It is noted that the bifurcation and its agreement with models are very similar at optical and IR wavelengths, which is expected since He^- free-free opacity, which is sensitive to free electrons from trace hydrogen or carbon, dominates at both wavelengths. At cool temperatures, CIA opacity from hydrogen sets in, which explains why mixed H/He models turn bluer.

As discussed in Section 4.2, He-rich models with trace C below the optical detection limit better reproduce the *Gaia* HR diagram bifurcation (Blouin et al., 2023a,b; Camisassa et al., 2023). Fig. 4.11 shows mixed C/He cooling tracks with three different initial C mass fractions in the envelope of the PG 1159 star progenitor to the white dwarf: 0.2, 0.4 and 0.6 (Blouin et al., 2023a). The C abundance was not fixed in these models, but instead followed the evolutionary predictions of Bédard et al. (2022a). For $T_{\text{eff}} < 7000$ K, the C abundance is so low in these models that pure-He models are equally appropriate, and therefore pure-He models from Blouin et al. (2018b) were used at these cool T_{eff} values. C/He (pure-He) cooling tracks provided a better fit to the *Gaia* HR diagram than H/He tracks for faint white dwarfs ($G_{\text{abs}} \gtrsim 15$). However, both cooling tracks fitted poorly in the IR for the same regime, suggesting that additional physical issues need to be solved in the models (Saumon et al., 2022) before spectral evolution of trace H and C can be studied in low temperature (< 7000 K) He-atmosphere white dwarfs.

In the UV, cool DA white dwarfs lie below the pure-H sequence for $G_{\text{abs}} \gtrsim 13.5$ whereas in the optical they lie above the pure-H sequence for $G_{\text{abs}} \gtrsim 15$, corresponding to the *Gaia* low-mass problem at low temperatures (< 6000 K) discussed in Section 4.2.1. Re-scaling the Ly α opacity in the models improves the fit to the optical HR diagram but worsens the fit to the UV HR diagram, indicating that a simple multiplication factor of the Ly α opacity is an incomplete solution to the opacity problem of cool white dwarfs.

DZ white dwarfs appear redder than expected in the bottom right panel of Fig. 4.11, the *Gaia*–GALEX HR diagram, when compared to H/He cooling tracks. UV flux suppression in DZ white dwarfs compared to He-atmosphere white dwarfs is expected because of the large number of UV metal absorption lines (Wolff et al., 2002). Flux is therefore emitted at redder wavelengths to produce the same overall flux corresponding to the white dwarf T_{eff} .

4.3.6 Magnetic white dwarfs

A fraction of local white dwarfs have been observed to host magnetic fields, ranging in strength from 30 kG to several hundreds of MG (Kawka and Vennes, 2012; Bagnulo and Landstreet, 2021, 2022; Hardy et al., 2023a,b); and the origin of these fields is not currently well constrained. These fields are usually detected through direct observations of the Zeeman splitting of white dwarf spectral features, although dedicated searches using spectropolarimetry have also discovered many of these magnetic stars (e.g. Bagnulo and Landstreet 2018, 2021). Current ideas to explain magnetic fields in isolated white dwarfs include: the field was generated by a dynamo in the core of the white dwarf during the crystallisation process or the merger of two white dwarfs, the field has been generated by a dynamo in the core of the giant or main-sequence progenitors (possibly with binary/planet interaction), or a fossil field has persisted since stellar formation (Briggs et al., 2015, 2018; Cantiello et al., 2016; Ferrario et al., 2020; Schreiber et al., 2021; Bagnulo and Landstreet, 2021; Ginzburg et al., 2022; Bagnulo and Landstreet, 2022).

With the 40 pc northern hemisphere sample, McCleery et al. (2020) demonstrated using UV and IR photometry that *Gaia* temperatures and masses are similarly accurate for cool ($T_{\text{eff}} \lesssim 12\,000$ K) magnetic white dwarfs as they are for non-magnetic white dwarfs. Hardy et al. (2023a) found a similar result for cool magnetic white dwarfs. This is also supported by the observation that most of the massive DAHs in 40 pc lie on the *Gaia* crystallisation branch (Q-branch; that extends from the upper left corner to about $0.8 M_{\odot}$ and $T_{\text{eff}} = 7000$ K in Fig. 4.5). This would be an unlikely coincidence if the *Gaia*-derived atmospheric parameters were inaccurate.

McCleery et al. (2020) observed in the northern 40 pc sample that magnetic white dwarfs have, on average, a higher mass than non-magnetic white dwarfs. The mass distri-

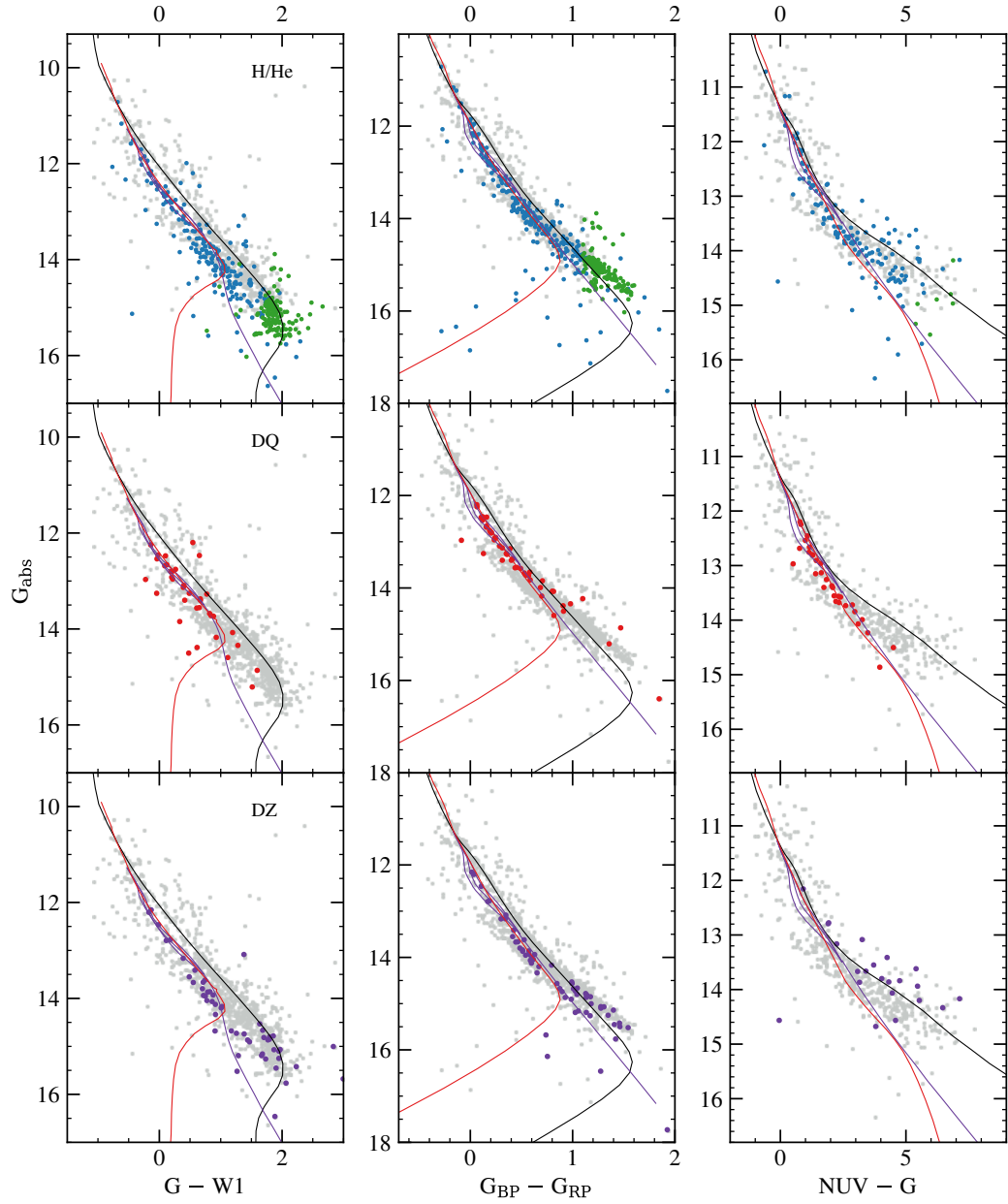


Figure 4.11: HR diagrams for the 40 pc white dwarf sample. Top: H-atmosphere white dwarfs are in grey, He-atmosphere white dwarfs are in blue, and cool DC white dwarfs with unconstrained composition are in green. Middle: DQ white dwarfs are in red and the rest of the sample is in grey. Bottom: DZ white dwarfs are in purple and the rest of the sample is in grey. In all panels, the black lines indicate pure-H cooling tracks, the red lines indicate mixed $H/He = 10^{-5}$, and the purple lines indicate mixed C/He cooling tracks with varying initial C mass fractions in the envelope of the PG 1159 star (0.2, 0.4 and 0.6; see Blouin et al. 2023a). In all cases, tracks are for a $0.6 M_{\odot}$ white dwarf.

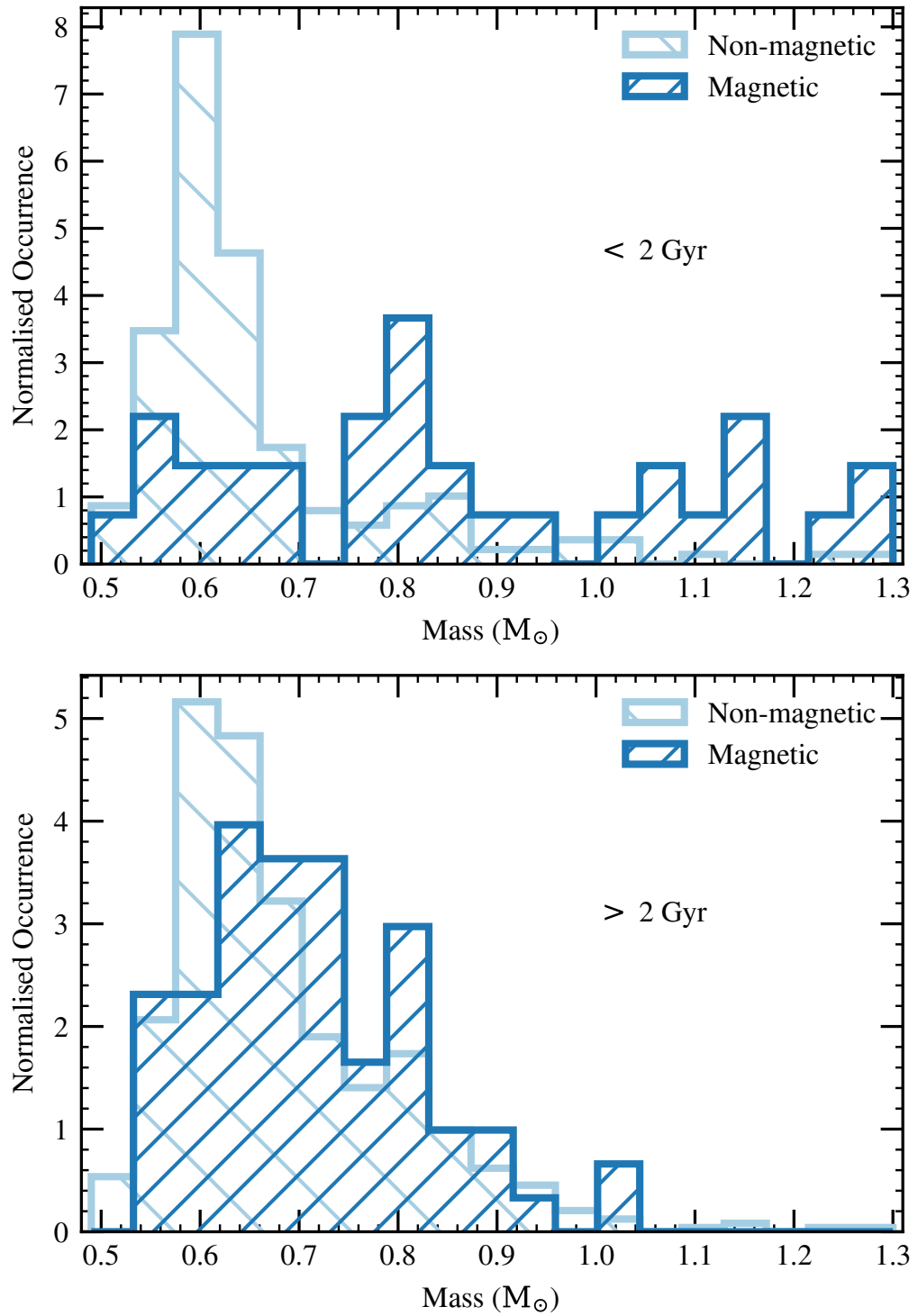


Figure 4.12: The mass distribution of magnetic (dark blue) and non-magnetic (light blue) white dwarfs within 40 pc. Top: White dwarfs younger than 2 Gyr. Bottom: White dwarfs older than 2 Gyr.

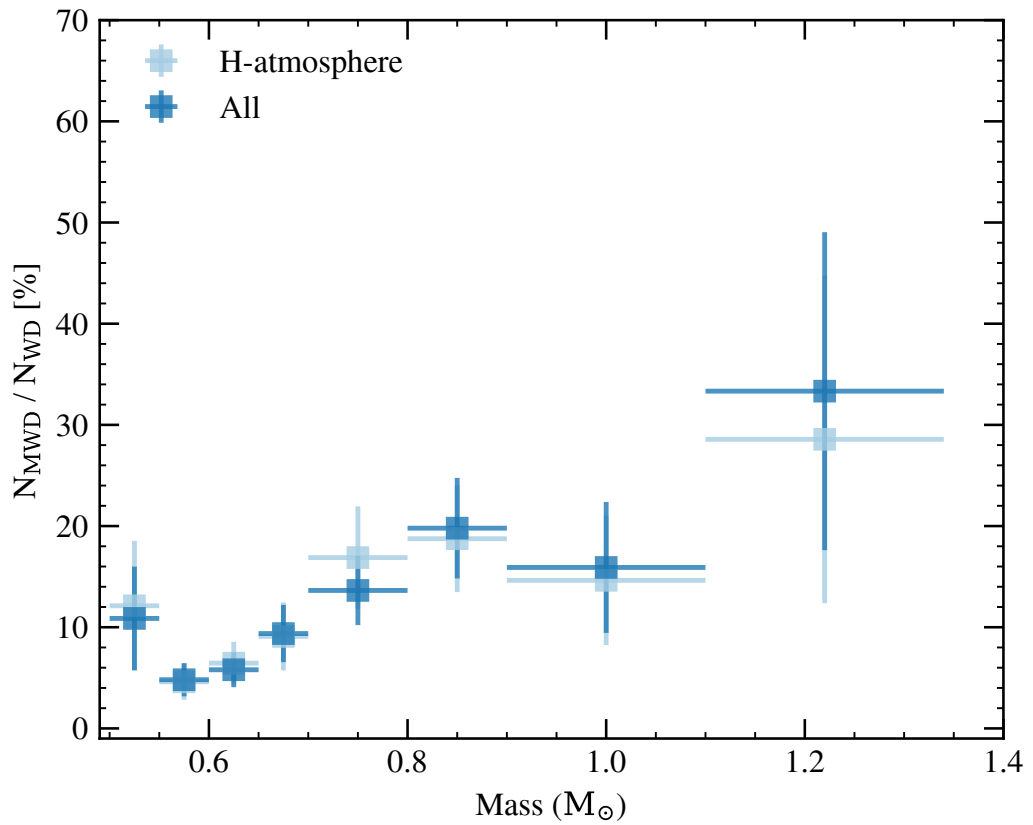


Figure 4.13: Frequency of magnetic white dwarfs as a function of mass for white dwarfs within 40 pc with $T_{\text{eff}} > 5000$ K, for H-dominated atmospheres (light blue) and for all spectral types (dark blue). Horizontal error bars represent mass bins and vertical error bars show the uncertainty of the frequency of the occurrence of magnetic fields within each bin.

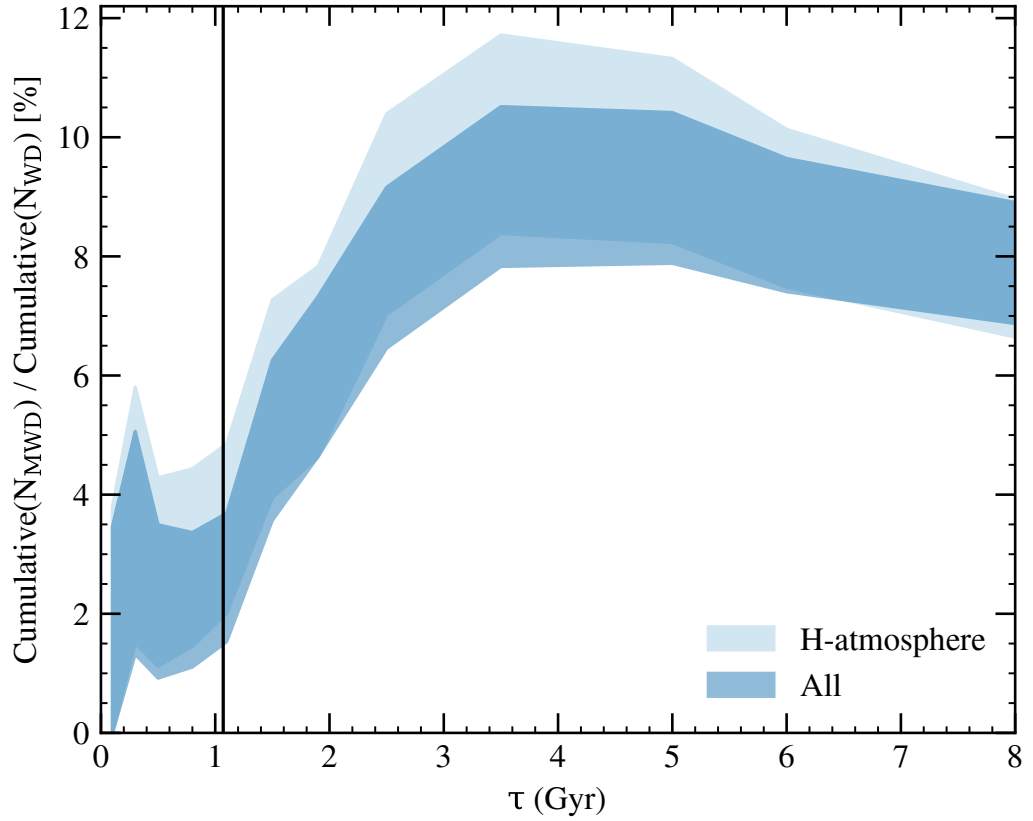


Figure 4.14: Fractional cumulative frequency of magnetic white dwarfs as a function of cooling age for corrected masses between $0.49 M_{\odot}$ and $0.8 M_{\odot}$, for all white dwarfs within 40 pc that have H-dominated atmospheres (light blue) and all white dwarfs within 40 pc (dark blue). τ indicates the cooling age of the white dwarf. Cooling ages were derived using updated STELUM evolutionary models (Bédard et al., 2022b; Elms et al., 2023), and the filled regions cover 1σ uncertainty. The black line indicates the cooling age of the onset of crystallisation for core oxygen mass fraction $X(\text{O}) = 0.8$ for a white dwarf with a mass of $0.8 M_{\odot}$.

butions in Fig. 4.12 show that non-magnetic white dwarfs have a narrow peak around the canonical mass of $0.6 M_{\odot}$, whereas young magnetic white dwarfs have a less prominent peak and a larger dispersion, leading to a larger average mass. The older magnetic white dwarfs have a similar mass distribution to non-magnetic white dwarfs. The resulting magnetic to non-magnetic ratio as a function of mass is demonstrated in Fig. 4.13. Magnetism is much easier to detect in pure-H DA white dwarfs as they have visible spectral features down to $T_{\text{eff}} \approx 5000$ K. Therefore I chose to focus on just DA white dwarfs above this temperature in the following discussion, but note that the same trends are observed in the full sample. For this analysis, only white dwarfs with corrected *Gaia* masses greater than $0.49 M_{\odot}$ were considered, to remove contamination from double degenerates (see Section 4.3.3 for details).

Bagnulo and Landstreet (2022) inferred that there are two populations of magnetic white dwarfs with very different typical masses. They searched for magnetism using spectropolarimetry for all white dwarfs within 20 pc and white dwarfs younger than 0.6 Gyr within 40 pc. For the most massive white dwarfs, they found magnetic fields to be common at short cooling ages. For lower-mass white dwarfs, they found that magnetic fields are rare, but their incidence grows with cooling age. These two populations of magnetic white dwarfs are hinted in 4.13. There is a peak in the fraction of magnetic white dwarfs at around $0.8 M_{\odot}$, but there is also a tentative peak at higher masses ($>1.1 M_{\odot}$). However, not enough of these massive magnetic white dwarfs have been observed out to 40 pc to constrain the significance of this second peak.

Fig. 4.14 indicates that for white dwarfs with masses $<0.8 M_{\odot}$, magnetic fields emerge 1 – 3 Gyr after the star becomes a white dwarf, similar to the observations of Bagnulo and Landstreet (2022). This result was missed by McCleery et al. (2020) due to their smaller sample size and lack of mass cut-off. This 1 – 3 Gyr cooling age is around the time at which white dwarfs begin to crystallise.

I determined the age of the onset of crystallisation for all 40 pc magnetic white dwarfs with masses $0.5 M_{\odot} < M < 0.8 M_{\odot}$, and tested the effect of changing the assumed core oxygen mass fraction, $X(\text{O})$, on the predicted onset of crystallisation, using updated crystallisation models from the STELUM code (Bédard et al., 2022b; Elms et al., 2023). For $X(\text{O}) = 0.60$, it was found that $55 (\pm 4)$ out of 69 systems have already begun crystallising, while for $X(\text{O}) = 0.8$, $61 (\pm 2)$ out of 69 have begun crystallising, where errors indicate those that are within 3σ of the age of the onset of crystallisation. The earliest possible age at which crystallisation could begin according to these models, with $X(\text{O}) = 0.80$ and $0.8 M_{\odot}$, is shown by the black line in in Fig. 4.14. It is clear that some magnetic systems lie to the left of that line. $X(\text{O}) = 0.60$ is a more standard abundance based on pre-white dwarf evolution models, however even with more lenient conditions, some white dwarfs that have not begun crystallising have clearly been observed to harbour a magnetic field.

The drop-off in magnetic frequency towards larger cooling ages in Fig. 4.14 is largely due to detection biases – Zeeman splitting of spectral features is harder to detect at lower T_{eff} . The continuing effort to search for magnetism in DC white dwarfs using broadband filter polarimetry (e.g. Berdyugin et al. 2022, 2023, 2024) provides vital information on whether the drop-off in magnetism as a function of cooling age at late ages is genuine. There may be an elusive population of very highly magnetic DA white dwarfs that have been misclassified due to their spectral features being so broadened and distorted that they resemble featureless DCs, which may further bias our results. There are also observational biases in the population of He-atmosphere white dwarfs, as those with metal lines enable sensitive detections of magnetic fields (Hollands et al., 2017; Bagnulo and Landstreet, 2020).

4.3.7 Metal-polluted white dwarfs

The pollution of white dwarf atmospheres by heavy elements is indicative of the accretion of planetary debris (Zuckerman et al., 2007; Farihi, 2016; Veras, 2021). Around 11 per cent of white dwarfs in the 40 pc sample are polluted. This fraction is dependent on spectroscopic resolution (O’Brien et al., 2023), as well as both the T_{eff} range considered and the wavelength coverage (Zuckerman et al., 2003; Koester et al., 2014). Almost all metal-polluted white dwarfs in the 40 pc sample have only been observed spectroscopically at optical wavelengths. For far-ultraviolet (FUV) spectroscopy, Si II and C II lines are prominent (Koester et al., 2014), and for near-ultraviolet (NUV) spectroscopy, Mg I and Mg II lines dominate (Allard et al., 2018). For cooler white dwarfs with $T_{\text{eff}} < 8000$ K, Ca generally has the greatest equivalent width for metals and in many cases is the only metal detected in optical spectra (see Fig. 4.15). Therefore targeted high-resolution spectroscopic follow-up around the Ca II H+K lines for 40 pc white dwarfs should be carried out to improve completeness. High-resolution observations do not always reveal more metals, many white dwarfs observed at very high resolution still only display Ca absorption features (Zuckerman et al., 2003).

4.3.8 Gaia XP spectra

There are low-resolution *Gaia* BP/RP (commonly abbreviated to XP) spectra available for 99 per cent of the 40 pc white dwarf sample, which were released as part of *Gaia* DR3 (Gaia Collaboration et al., 2023). By integrating under a *Gaia* XP spectrum convolved with the transmission function of a desired photometric band, photometry can be generated in any arbitrary band that is within the wavelength coverage of *Gaia* (Torres et al., 2023).

The $u - g$ colour from SDSS is well known to be sensitive to the Balmer jump for warm white dwarfs, which by its nature is only observed in white dwarfs with H-atmospheres. Therefore, an HR diagram using the $u - g$ colour allows for the separation

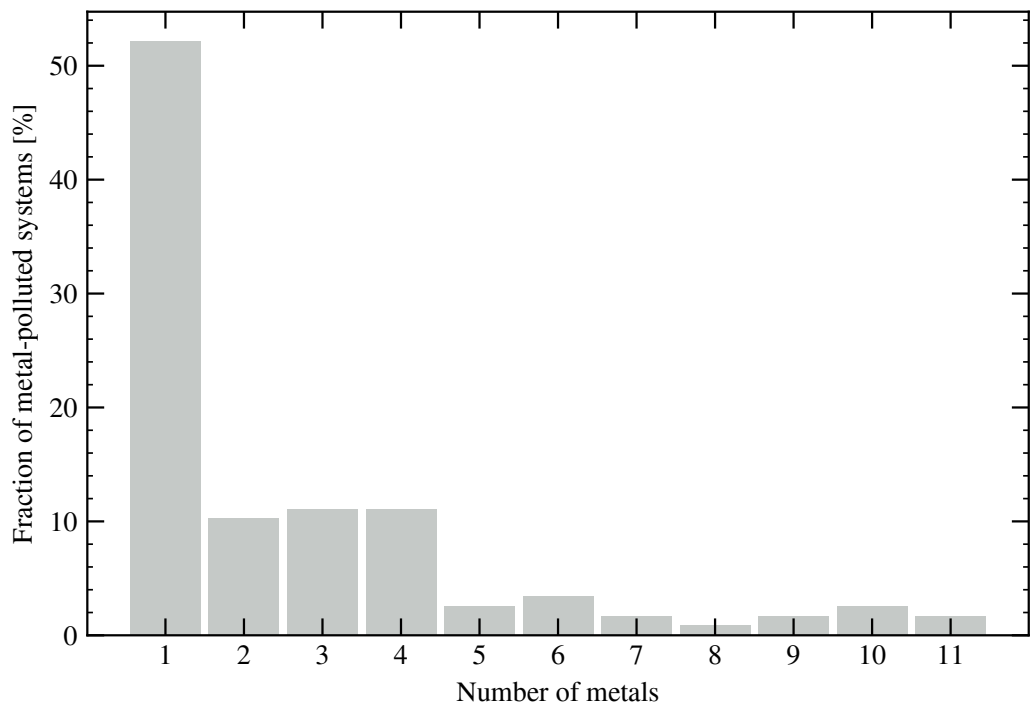


Figure 4.15: The fraction of metal-polluted white dwarfs in the 40 pc sample with different numbers of polluting metals. Data for this figure have been compiled from Williams et al. (2024).

of H- and He-atmosphere white dwarfs without the need for spectroscopy. I determined magnitudes from *Gaia* XP spectra using the system defined in Holberg and Bergeron (2006) for SDSS. The calculated magnitudes are differentiated from catalogue SDSS magnitudes by the prime symbol (').

Fig. 4.16 demonstrates that integrating under *Gaia* XP spectra in u' and g' bands separates H- and He-atmospheres from the Balmer jump for bright white dwarfs ($M_{g'} \lesssim 13$) within 40 pc, as was previously found using catalogue SDSS photometry (see, e.g., Caron et al., 2023). However, Fig. 4.16 becomes noisy for fainter ($M_{g'} \gtrsim 14$) white dwarfs, as the average signal-to-noise of the XP spectra becomes low, resulting in narrow-band u' and g' photometry becoming much less reliable than broadband G_{BP} and G_{RP} photometry.

Most *Gaia* XP spectra are presented in the form of Gauss-Hermite polynomials. A truncation to the number of coefficients in these polynomials is often applied to fainter sources, as higher-order polynomials may attempt to fit noise (Montegriffo et al., 2022). There is a non-negligible effect in the resulting calculated magnitudes when applying a truncation, as some signal is removed. This effect is particularly strong in the SDSS u -band, as cool white dwarfs are fainter in this wavelength region (see also López-Sanjuan et al., 2022b). Therefore, I did not apply a truncation to any of the *Gaia* XP spectra when calculating photometry.

Fig. 4.17 demonstrates that *Gaia* XP spectra can accurately recreate SDSS g colours down to faint absolute magnitudes, but the SDSS u colour determination is problematic, and gets worse for fainter sources, which was also demonstrated by Vincent et al. (2024) for a much larger sample of white dwarfs. As a consequence, I did not attempt to test *Gaia* capabilities in identifying cool and faint DZ or DQ white dwarfs from u' , g' or other ad-hoc narrow band filters. However, we note that recent work from García-Zamora et al. (2023); Vincent et al. (2024); Kao et al. (2024) have successfully used machine learning methods to classify white dwarfs into spectral types using *Gaia* XP spectra, which does not rely on the creation of narrow-band photometry.

4.4 Conclusions

This chapter presented the sample of white dwarfs within 40 pc of the Sun, selected primarily from *Gaia* DR3, complete with spectroscopic follow-up. The 40 pc sample contains 1078 spectroscopically confirmed white dwarfs selected from the *Gaia* DR3 catalogue of Gentile Fusillo et al. (2021). White dwarfs were found to make up ≈ 6 per cent of stars in the local volume as observed by *Gaia*. Only 2 candidates from Gentile Fusillo et al. (2021) within 40 pc remain without spectroscopic follow-up. Spectroscopic observations have enabled the determination of the atmospheric composition of each white dwarf with $T_{\text{eff}} > 5000$ K

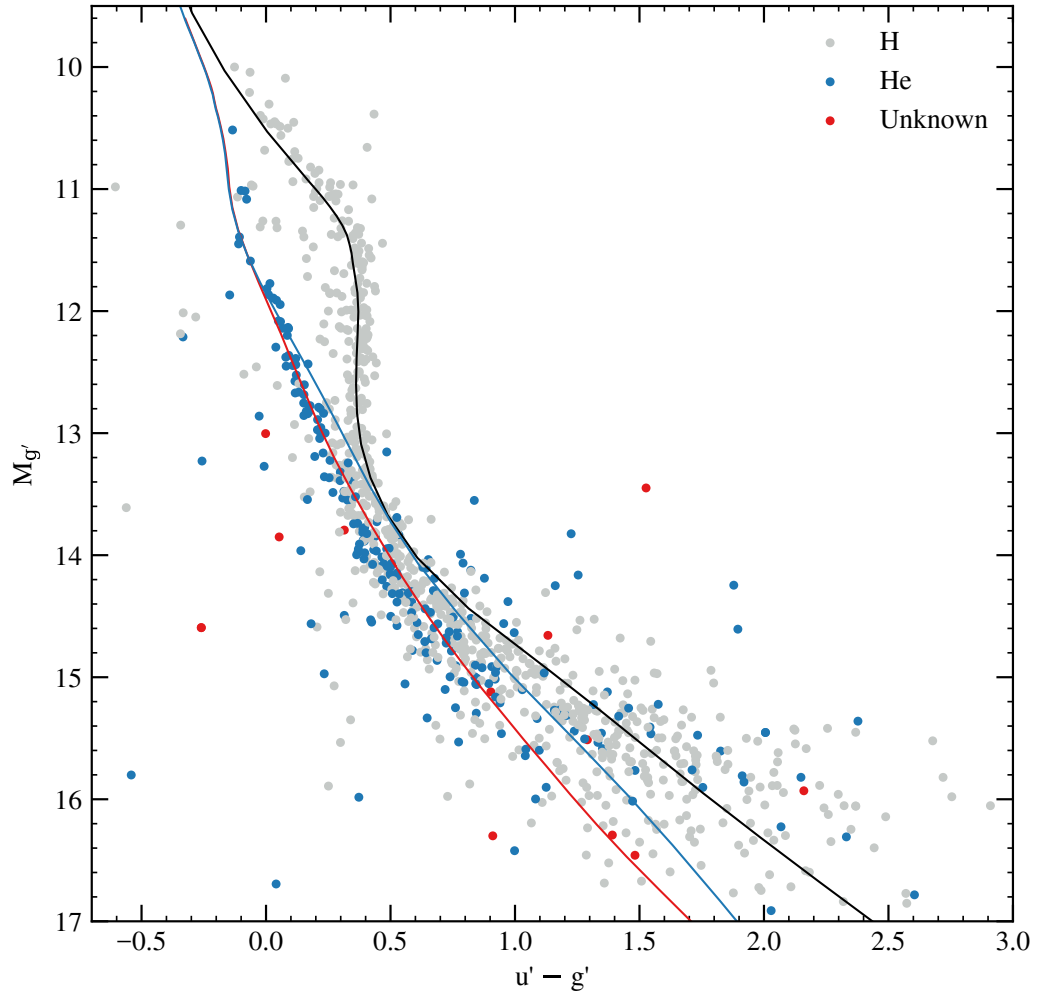


Figure 4.16: Photometry calculated using *Gaia* XP spectrophotometry in SDSS u and g bands, which we distinguish from catalogue SDSS photometry with a prime symbol. H-atmosphere white dwarfs are shown in grey, and He-atmosphere white dwarfs are in blue. Unconfirmed candidates are in red. The blue line indicates pure-He cooling tracks, the black line indicates pure-H cooling tracks and the red line indicates mixed H/He = 10^{-5} cooling tracks for a $0.6 M_{\odot}$ white dwarf.

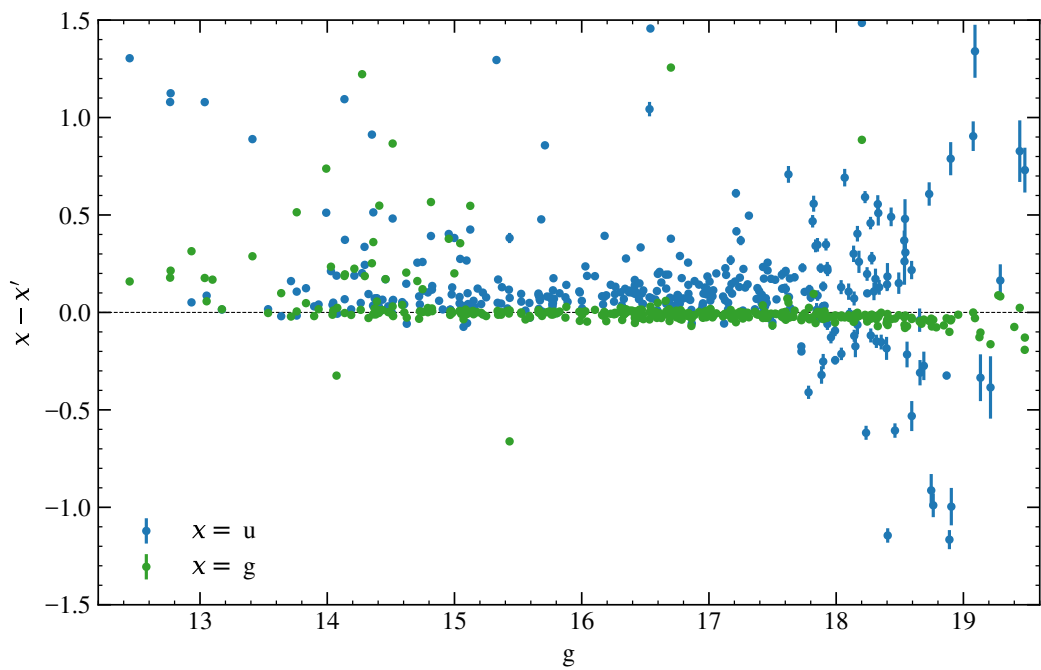


Figure 4.17: Comparison of catalogue SDSS photometry (u and g) to photometry calculated using *Gaia* XP spectra in SDSS bands (u' and g'). The difference is shown as a function of apparent SDSS g -magnitude.

(90 per cent of the sample); therefore providing accurate T_{eff} and $\log(g)$ from broadband *Gaia* photometric fitting.

A correction was performed on the *Gaia* T_{eff} and masses of the sample to remove the effects of the low-mass issue in white dwarfs (Hollands et al., 2018b; McCleery et al., 2020; Bergeron et al., 2019; Cukanovaite et al., 2023). The mass distribution of the sample revealed a main peak with a median mass of $0.61 M_{\odot}$, with a shoulder (or secondary peak) of higher mass white dwarfs in the range $0.7\text{--}0.9 M_{\odot}$. The spectroscopic heterogeneity of the sample prevented complete unbiased analyses based on spectral sub-types, such as metal polluted or magnetic white dwarfs. No clear evidence of spectral evolution was observed between H- and He-atmospheres at cool temperatures ($T_{\text{eff}} < 9000$ K).

There are 28 suspected or confirmed white dwarfs within 40 pc that did not make the cut of the Gentile Fusillo et al. (2021) *Gaia* white dwarf catalogue. These are mostly in close binaries with main-sequence companions, such that their *Gaia* colours are blended. Constraining the numbers of these white dwarfs missing from the main selection will improve volume-completeness and inform future binary population models.

Comparison of the 40 pc sample with the binary population models of Toonen et al. (2017) has demonstrated a distinct lack of wide double white dwarf binaries – models predict almost a factor of ten more systems than was recovered from the search within 40 pc. This deficit was observed in smaller volume-limited samples, but becomes more apparent within the 40 pc volume. The numbers of other types of binary star systems agree well with models. The space density of white dwarfs within 40 pc of the Sun generally agreed with simulations from Cukanovaite et al. (2023), but predictions from simulations depend on the vertical position of the Sun with respect to the Galactic plane and vertical scale height of the Galactic disc.

It was found that the mass distribution of 40 pc magnetic white dwarfs has a primary peak centred at $0.7 M_{\odot}$, which is larger than the canonical non-magnetic white dwarf mass, and there is a hint of a secondary peak at very high masses ($M > 1.1 M_{\odot}$). For white dwarfs with $M < 0.8 M_{\odot}$, the incidence of magnetism was found to increase with cooling age, as was observed by Bagnulo and Landstreet (2022). Even the most relaxed constraints on core composition did not produce a good agreement between the increased incidence of magnetism and the onset of core crystallisation. Therefore, a dynamo generated by core crystallisation might not explain magnetic field generation in a significant fraction of magnetic white dwarfs.

The 40 pc sample is the largest volume-complete white dwarf sample to date, it is unaffected by reddening, and it will be the benchmark white dwarf sample for many years to come, until the era of multi-object spectroscopic surveys such as DESI (Cooper et al., 2023), SDSS-V (Ahumada et al., 2020), 4MOST (de Jong et al., 2019), and WEAVE (Dalton et al.,

2020).

Table 4.10: Abundances and upper limits of elements determined from combined fitting of spectra and photometry of newly observed DAZ, DZ, and DQ white dwarfs with Koester (2010) models.

| Parameter | WD J0213–3345 | WD J1154–6239 | WD J1927–0355 | WD J2141–3300 | WD J2317–4608 |
|----------------------------------|---------------|---------------|---------------|---------------|---------------|
| T_{eff} [K] | 5150 (150) | 5100 (100) | 6540 (150) | 6870 (150) | 4075 (100) |
| $\log(g)$ [cm s^{-2}] | 7.6 (0.2) | 7.97 (0.05) | 7.99 (0.04) | 7.96 (0.04) | 8.2 (0.2) |
| Composition, X | H | H | He | He | He |
| $\log(\text{H}/\text{X})$ | – | – | –3.5 | –3.5 | – |
| $\log(\text{C}/\text{X})$ | – | – | – | – | –8.3 (1.0) |
| $\log(\text{Na}/\text{X})$ | – | – | < –9.4 | –9.2 (0.2) | – |
| $\log(\text{Mg}/\text{X})$ | – | – | –7.00 (0.15) | –7.50 (0.15) | – |
| $\log(\text{Al}/\text{X})$ | – | – | < –8.6 | –8.5 (0.3) | – |
| $\log(\text{Si}/\text{X})$ | – | – | < –7.6 | –7.2 (0.2) | – |
| $\log(\text{Ca}/\text{X})$ | –10.9 (0.1) | –11.1 (0.2) | –9.1 (0.11) | –8.9 (0.1) | – |
| $\log(\text{Sc}/\text{X})$ | – | – | < –11.7 | < –11.7 | – |
| $\log(\text{Ti}/\text{X})$ | – | – | –10.7 (0.1) | –10.0 (0.1) | – |
| $\log(\text{V}/\text{X})$ | – | – | < –10.5 | < –10.4 | – |
| $\log(\text{Cr}/\text{X})$ | – | – | –10.2 (0.2) | –10.0 (0.2) | – |
| $\log(\text{Mn}/\text{X})$ | – | – | < –9.2 | < –9.3 | – |
| $\log(\text{Fe}/\text{X})$ | – | – | –8.0 (0.1) | –8.2 (0.1) | – |
| $\log(\text{Co}/\text{X})$ | – | – | < –11.0 | < –10.7 | – |
| $\log(\text{Ni}/\text{X})$ | – | – | –9.3 (0.2) | –9.2 (0.2) | – |
| $\log(\text{Cu}/\text{X})$ | – | – | < –11.7 | < –11.7 | – |
| $\log(\text{Sr}/\text{X})$ | – | – | < –12.3 | –12.1 (0.3) | – |
| $\log(\text{Ba}/\text{X})$ | – | – | < –12.2 | < –12.2 | – |

Chapter 5

Characterising planetary material accreted by cool helium atmosphere white dwarfs using an exponentially decaying disc model

In this chapter, I present a spectroscopic and compositional analysis of two heavily metal-polluted white dwarfs, WD J1927–0355 and WD J2141–3300. Both spectra were published as part of the 40 pc sample (see Chapter 4; Section 4.2.3), and required dedicated follow-up. I adopted a model in which a disc of planetary material exponentially decays onto the white dwarf, which was first proposed by Jura et al. (2009). I compared the abundances of the polluting material, propagated through the Jura et al. (2009) disc model with two free parameters, with typical solar system abundances including chondritic, achondritic, and stony-iron meteorites. The two free parameters: the time elapsed since the accretion event began and the characteristic disc lifetime, were somewhat degenerate, and therefore many combinations provided adequate comparisons with solar system material. I found that in both cases the white dwarfs were most likely to be accreting rocky, bulk planetary material with a similar composition to bulk Earth, and that the accretion event in both cases began at least a few Myr ago. The mass of the parent body accreting onto each white dwarf was at least the mass of a small moon, and could be as large as a dwarf planet. I also did the same analysis procedure but with the constant accretion rate model, and found a similar composition but with less reliable comparisons. The work presented in this chapter was published in O’Brien et al. (2025). The spectroscopic observations from Keck HIRES presented in this chapter were obtained by PI M. Jura (2008) and PI C. Melis (2019). The echelle spectra were merged and aligned by B. Klein and were fitted by D. Koester.

5.1 Introduction

When a white dwarf accretes planetary material, metals appear in its otherwise pristine H or He spectrum. These metals will sink through the white dwarf atmosphere on timescales which vary as a function of atmospheric composition and temperature. In the atmosphere of a metal polluted helium-rich atmosphere white dwarf (typically spectral type DZ or DBZ), metals can have settling timescales of the order of Myrs, such that metals remain visible in the atmosphere long after an accretion event has ceased (Paquette et al. 1986; Dufour et al. 2007a; Koester et al. 2011; Hollands et al. 2017, 2018a; Swan et al. 2023). Each metal sinks out of the underlying convection zone at a different rate, and therefore the relative fractions of elements observed in the atmosphere may not reflect the composition of the accreted parent body, depending on the phase of accretion at the time of observation (Koester, 2009). The settling timescales of metals in cool DZ and DBZ white dwarfs are comparable to the lifetime of dust discs, which are expected to last on the order of Myrs before becoming depleted (Girven et al., 2012; Veras and Heng, 2020; Cunningham et al., 2021).

White dwarf discs are often assumed to accrete at a constant accretion rate until the disc is depleted, at which point accretion ceases (Koester, 2009). The theory behind the balance between accretion and diffusion is described in detail in Dupuis et al. (1993). Jura et al. (2009) instead considered an exponentially decaying accretion rate where the disc lifetime is the characteristic e -folding timescale. Lodato (2008) motivates such a choice as they considered the physics of a disc for which viscosity was proportional to radius, accreting onto a star, and found that the mass accretion rate decayed exponentially as a function of time, and that the disc evolved over a viscous timescale. Following a tidal disruption event, planetary debris is expected to spread and evolve dynamically and the accretion rate should decrease over time as material is depleted from the disc. In contrast, the constant accretion rate model assumes that a steady supply of material is being accreted over an arbitrarily long time.

In this work, I present analysis of optical Keck HIRES (Vogt et al., 1994) spectra of two DZ white dwarfs that were published as part of the volume-limited 40 pc white dwarf sample (O’Brien et al., 2024): WD J192743.10–035555.23 and WD J214157.57–330029.80 (WD 2138–332). Throughout this chapter, I refer to these white dwarfs by their shorthand WD Jhhmm ± ddmm names: WD J1927–0355 and WD J2141–3300. At distances of 24 pc and 16 pc respectively, these white dwarfs are some of the most heavily polluted within the local solar neighbourhood, with six metals detected in the atmosphere of WD J1927–0355 and ten in the atmosphere of WD J2141–3300. I applied an exponentially decaying disc model from Jura et al. (2009) to the metal abundances of these white dwarfs in order to constrain the composition of the parent bodies that were accreted by both white dwarfs. The

Jura et al. (2009) disc model has been adopted in only a handful of white dwarf studies (Jura and Xu, 2010; Doyle et al., 2020, 2021; Trierweiler et al., 2022), and this work is the first to treat the disc lifetime as a free parameter when determining the composition of accreted material in observed white dwarfs with this model.

5.2 Observations and stellar modelling

Hundreds of thousands of new white dwarf candidates were identified in *Gaia* DR2, including WD J1927–0355 (Gentile Fusillo et al., 2019). The Kast spectrograph on the Shane 3 m telescope at the Lick Observatory confirmed its white dwarf status and enabled a DZ classification (PI C. Melis), and the star was then followed up at higher resolution with HIRES in order to identify extra metal species and hydrogen. WD J2141–3300 was identified as a DZ white dwarf by Subasavage et al. (2007). Bagnulo and Landstreet (2019) confirmed that WD J2141–3300 harbours a weak magnetic field via spectropolarimetric measurements, and Bagnulo et al. (2024a) observed that the equivalent widths of each of its spectral features vary over its rotation period.

Details of the observations analysed in this work are presented in Table 5.1. Reduced and merged HIRES spectra for both white dwarfs are presented in Fig. 5.1. The HIRES data of WD J1927–0355 were reduced using the MAKEE pipeline. The HIRES data of WD J2141–3300 were reduced using PyRAF (Science Software Branch at STScI, 2012), following Klein et al. (2010). Continuum fits of the calibration stars BD+28 4211, G191–B2B, and EGGR 131 were used to model and divide out the instrumental response function. Procedures described in Klein et al. (2011) were used to align, trim, and merge the echelle orders in order to generate the spectra. *The reduction and merging of the echelle spectra were done by B. Klein.*

The HIRES spectra extend to the very blue end of the optical ($\approx 3100 \text{ \AA}$) at high signal to noise, enabling the detection of many metal lines. In the spectra of WD J1927–0355, lines originating from six individual elements were identified: Mg, Ca, Ti, Cr, Fe, and Ni. In the spectra of WD J2141–3300, Na, Mg, Al, Si, Ca, Ti, Cr, Fe, Ni, and Sr lines were identified. More than one line was detected for each element, aside from Si I in WD J2141–3300, for which there was only one line at 3905.65 \AA . $H\alpha$ and weak $H\beta$ features were identified in the spectra of both white dwarfs. *The identification of metal lines was done by A. Doyle and B. Klein.*

Synthetic spectra for the two white dwarfs were computed using white dwarf atmosphere models. The basic input data and methods are described in Koester (2010), but the code has been considerably improved regarding the equation of state, absorption coefficients, and line broadening theories (see e.g. Hollands et al. 2017; Gänsicke et al. 2018; Wilson

| WDJ Name | WDJ Name (shortened) | <i>Gaia</i> DR3 ID | Observation Date (UT) | Collimator | Wavelength Range (Å) | Nominal Resolution | Exposure (s) |
|---------------------|-------------------------|---------------------|--------------------------|------------|-------------------------|-----------------------|-----------------|
| 192743.10-035555.23 | 1927-0355 | 4213409341688406912 | 2019 July 07 | Blue | 3050-5940 | 35 800 | 3000 |
| | | | 2019 July 07 | Blue | 3130-5940 | 35 800 | 3000 |
| | | | 2019 September 07 | Red | 4690-9140 | 35 800 | 2100 |
| 214157.57-330029.80 | 2141-3300 | 6592315723192176896 | 2008 August 06 | Blue | 3050-5940 | 23 800 | 1500 × 2 |
| | | | 2008 August 07 | Blue | 3130-5940 | 35 800 | 1500 × 2 |
| | | | 2008 November 14 | Red | 4690-9150 | 35 800 | 1800 × 2 |

Table 5.1: Keck HIRES observation details.

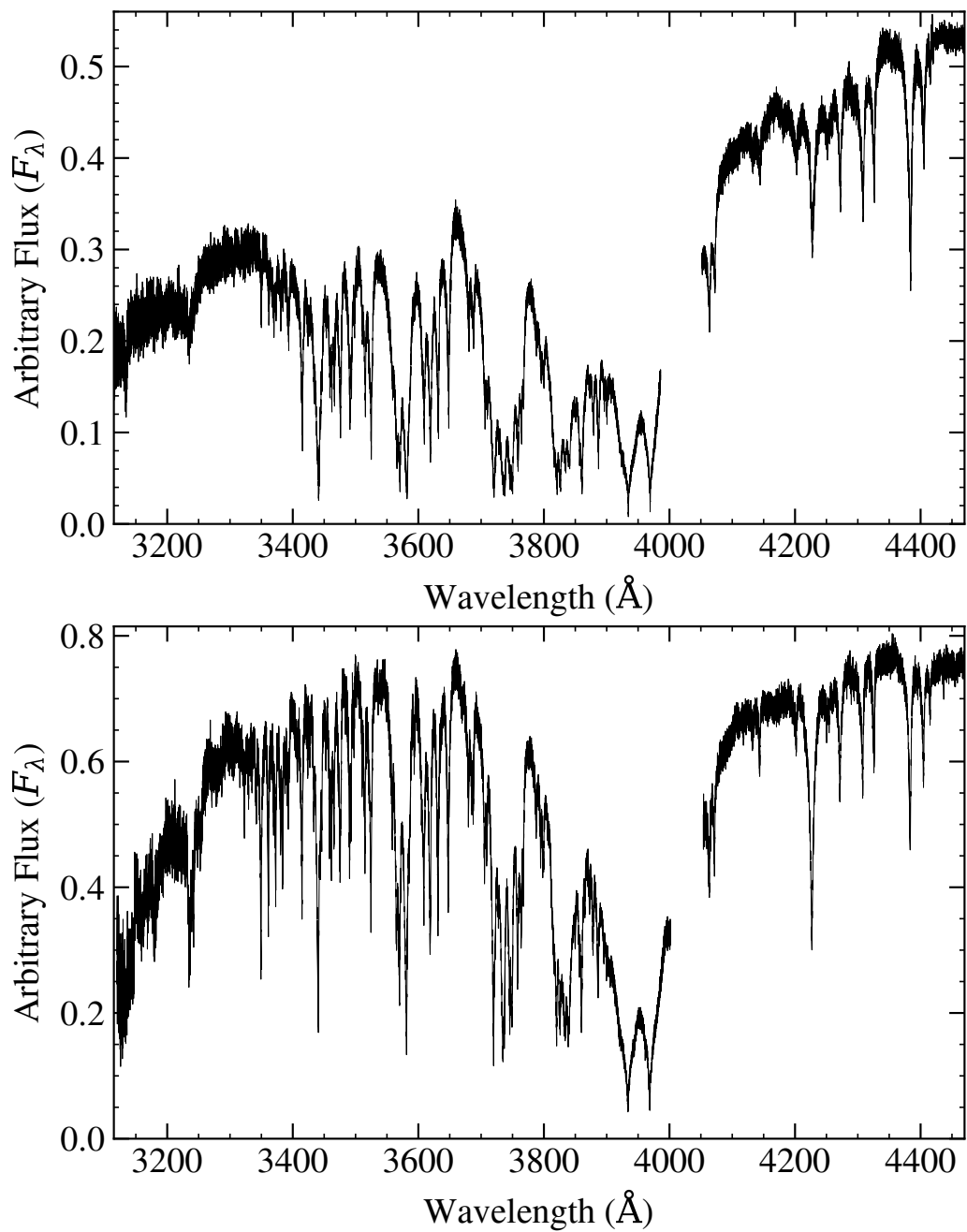


Figure 5.1: Combined, echelle-order-merged, blue portions of the HRES spectra of WDJ1927–0355 (top) and WDJ2141–3300 (bottom). The continua and slopes of the spectra are not well flux calibrated, and therefore the spectra do not accurately depict the true spectral shape for each star.

et al. 2019; Elms et al. 2022). In the subsequent envelope modelling, there were two options: one where convective overshoot was switched on (Kupka et al., 2018; Cunningham et al., 2019), meaning its pressure scale height was set equal to one, and a second option with no convective overshoot. I chose to use the output where convective overshoot was switched on. If convective overshoot is not considered, then there must be a discontinuity between the convective layer and the non-convective layer, which is not physical (Spiegel, 1963). The convective overshoot process overcomes this discontinuity, and mixes material in white dwarf atmospheres. Incorporating overshoot into the models does not affect the number abundances, but does impact the settling timescales, which alters the inferred composition and mass of the parent body.

A hybrid fit of spectroscopy and photometry was used to determine the best-fit parameters of these stars. Metal abundances were changed until all strong features were reasonably well reproduced by models. With these abundances a small model grid was calculated, alongside a table with theoretical absolute magnitudes for all available observed photometry. Fitting to the photometry resulted in new values for the best-fit parameters, and this iteration process was repeated three times to provide a final converged T_{eff} and $\log(g)$ as well as metal abundances. *The spectra were fitted by D. Koester.*

The best-fit parameters for both white dwarfs are presented in Table 5.2. The uncertainties on the number abundances quoted in Table 5.2 are estimates of the uncertainties derived from spectroscopic fitting, and the uncertainties of T_{eff} and $\log(g)$ were not incorporated in their determination. The influence of these additional sources of uncertainty on the relative abundances is minor. In O’Brien et al. (2024), a typographical error resulted in an incorrect value being reported for $\log(\text{Mg}/\text{He})$ for WD J1927–0355. The correct abundance is -7.80 , as shown in Table 5.2, and this correction does not impact any conclusions or analysis in O’Brien et al. (2024). I have also updated the upper limits of copper and cobalt for both white dwarfs in Table 5.2, providing less stringent values in order to prevent over-interpretation of these limits. The settling timescales and masses of all elements in the convection zone at the time of observation are presented in Table 5.3.

In Fig. 5.2, the best-fit models are plotted alongside GALEX *NUV* (Martin et al., 2005), 2MASS *JHK_s* (Skrutskie et al., 2006) and WISE *W1, W2* photometry (Wright et al., 2010), plus Pan-STARRS *grizy* (Chambers et al., 2016) for WD J1927–0355 and SkyMapper *uvgriz* (Keller et al., 2007) for WD J2141–3300. In Table 5.2, I assumed that the distance is the inverse of the *Gaia* DR3 parallax, which is appropriate for these stars since their parallax error is less than 0.2 per cent. I used these distances to scale the model spectra to the photometry. Fig. 5.2 shows that neither white dwarf displays an excess indicative of a dust disc above the white dwarf flux in their 2MASS and WISE IR photometry. Girven et al. (2012) presented *Spitzer* IRS peak-up imaging of WD J2141–3300, detecting a 3σ flux

excess at $15.6\ \mu\text{m}$, but mentioned that this excess could be caused by a background galaxy. They noted that a dust disc emitting at such long wavelengths must be cool and probably outside of the region where material would be accreted by the star, meaning it might not be the cause of the currently observed pollution.

Fits to individual metal lines are shown in Fig. 5.3 for WD J1927–0355 and Fig. 5.4 for WD J2141–3300. The data in these plots were smoothed with a five-point boxcar average and the model spectra were convolved with a Gaussian function according to the resolution of the observations listed in Table 5.1. The wavelengths of the models were shifted to match the best-fit radial velocity shift of the data in the heliocentric frame of rest. The spectra and models were normalised to the continuum level and detrended for improved visual clarity. The reduction of echelle spectra is notoriously challenging, and there were substantial issues with the shapes and slopes of the spectra following reduction. The blue parts of the spectra for both white dwarfs have few points which can be considered as ‘continuum’, and therefore normalising the spectrum to match the model was not straightforward. Less than optimal visual fits to some lines in the spectrum of WD J2141–3300 are due to weak Zeeman splitting that was not accounted for in the models. The continuum mismatch near Sr II in Fig. 5.4 is an artifact of the normalisation procedure, and the strontium abundance was determined with a continuum range that was local to the line. To date, strontium has been detected in the atmosphere of just three other white dwarfs: GD 362 (Zuckerman et al., 2007), WD 0446–255 (Swan et al., 2019), and 2MASS J0916–4215 (Vennes et al., 2024). Plots showing the full fits to the HIRES spectra can be found in Fig. A2 of the supplementary data of O’Brien et al. (2024).

Figure 5.5 shows $H\alpha$ detections with non-local thermodynamic equilibrium line cores for both white dwarfs. The equivalent widths of the $H\alpha$ lines are $170\ \text{m}\text{\AA}$ for WD J1927–0355 and $30\ \text{m}\text{\AA}$ for WD J2141–3300, the latter of which also shows Zeeman splitting of the line core. The temperature of a hydrogen-rich atmosphere white dwarf model required to match the $H\alpha$ equivalent widths in Fig. 5.5 would be $< 5000\ \text{K}$, which is discrepant with the photometric effective temperatures for both white dwarfs, which are $6500 - 7000\ \text{K}$. Therefore, both white dwarfs must have helium-rich atmospheres with some hydrogen. It was not possible to match both the $H\alpha$ features and the shapes of the metal lines using current helium-rich atmosphere white dwarf models. Therefore, a standard ratio of $\log(\text{H}/\text{He}) = -3.5$ was adopted for the models of both white dwarfs, in accordance with measured hydrogen abundances in similar DZA white dwarfs (Hollands et al., 2017; Coutu et al., 2019). Models with this composition fit the metal line shapes well, but produce a very broad and shallow $H\alpha$ feature compared to the narrow, sharp $H\alpha$ lines observed in the spectra. Unexpectedly sharp and narrow $H\alpha$ features have also been observed in other cool DZA white dwarfs (O’Brien et al., 2023).

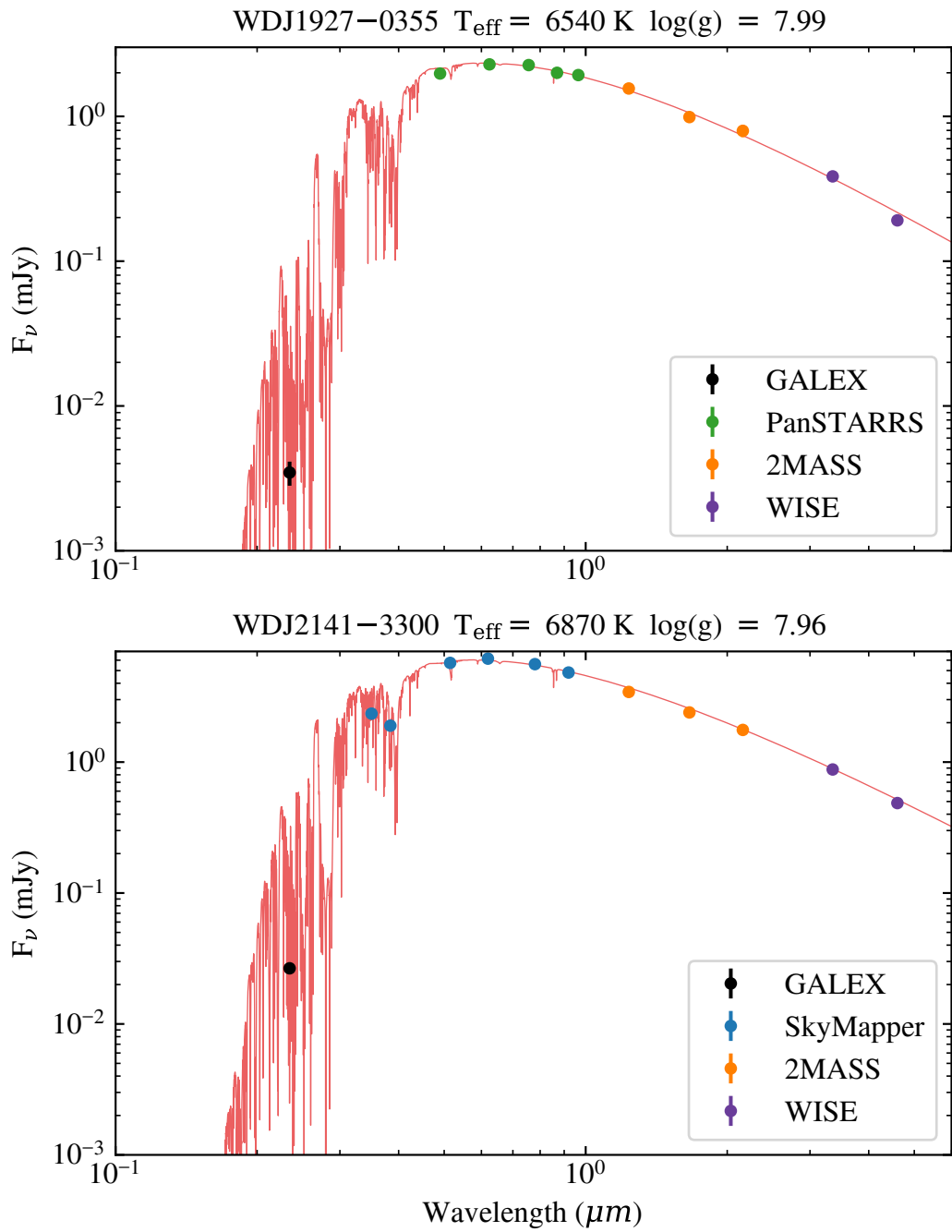


Figure 5.2: Best-fit model to the metal lines in the HIRES spectra and catalogue photometry for both WDJ1927-0355 (top) and WDJ2141-3300 (bottom). The model was calculated using code from Koester (2010).

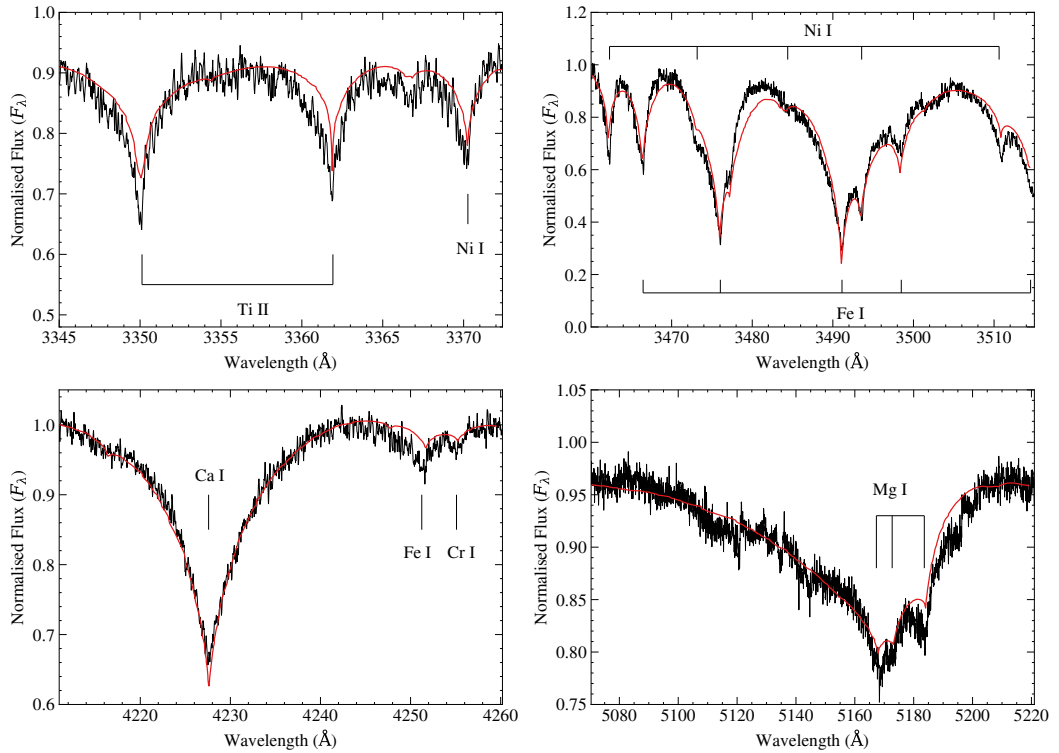


Figure 5.3: A selection of Ti II, Cr I, Ca I, Mg I, Ni I and Fe I lines in the HIRES spectrum of WDJ1927–0355, with the best-fit model overplotted in red. The data were smoothed with a five-point boxcar average and the model spectra were convolved with a Gaussian function. The wavelengths of the models were shifted to match the best-fit radial velocity shift of the data. The spectra and models were normalised to the continuum level and detrended for improved visual clarity. There are many lines of each metal throughout the spectrum.

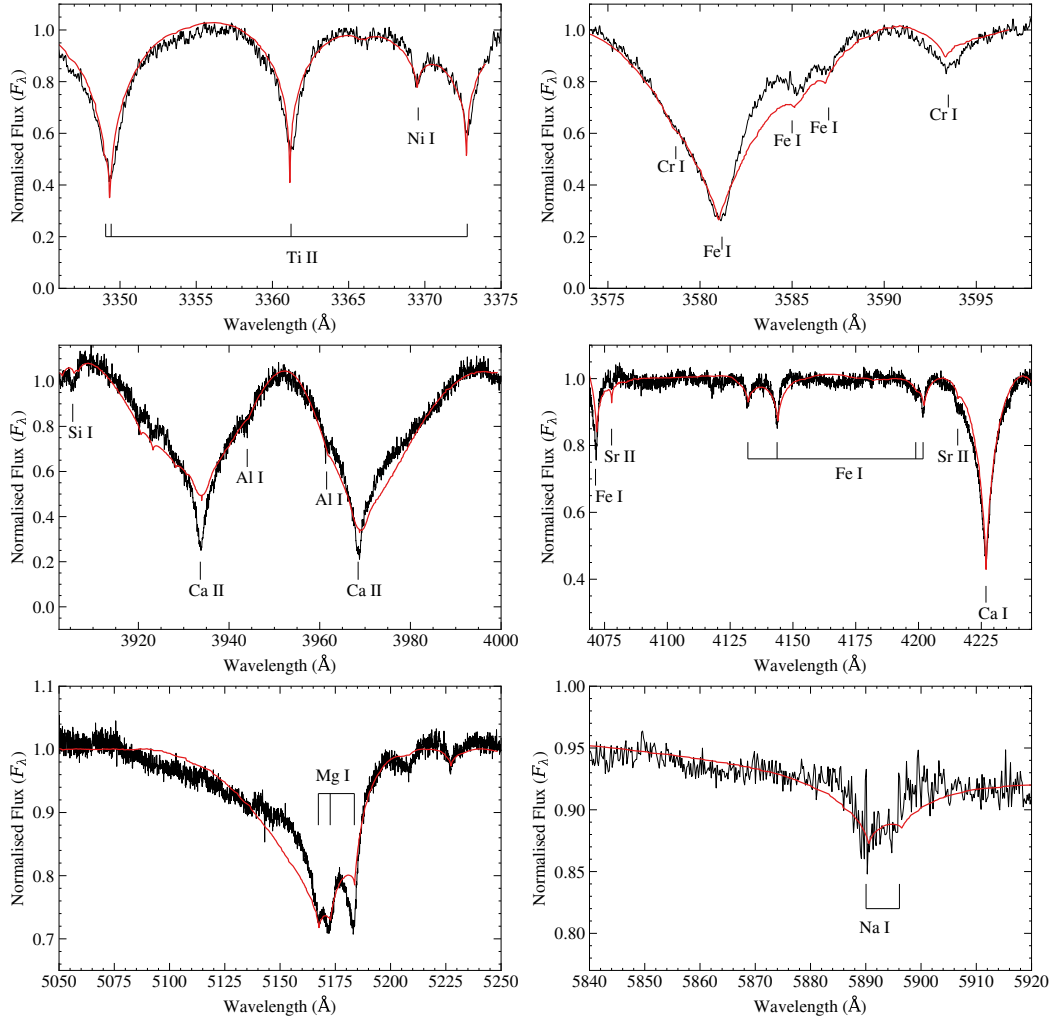


Figure 5.4: A selection of Ti II, Cr I, Ca I, Ca II, Mg I, Na I, Si I, Al I, Sr II, and Fe I lines in the HIRES spectrum of WDJ2141–3300, with the best-fit model overplotted in red. The data were smoothed with a five-point boxcar average and the model spectra were convolved with a Gaussian function. The wavelengths of the models were shifted to match the best-fit radial velocity shift of the data. The spectra and models were normalised to the continuum level and detrended for improved visual clarity. There are many lines of each metal throughout the spectrum. Some portions of the spectrum are poorly calibrated despite normalisation and detrending. Some fits are also poor due to Zeeman splitting of metal lines caused by the magnetic field at WDJ2141–3300, which was not incorporated into the models.

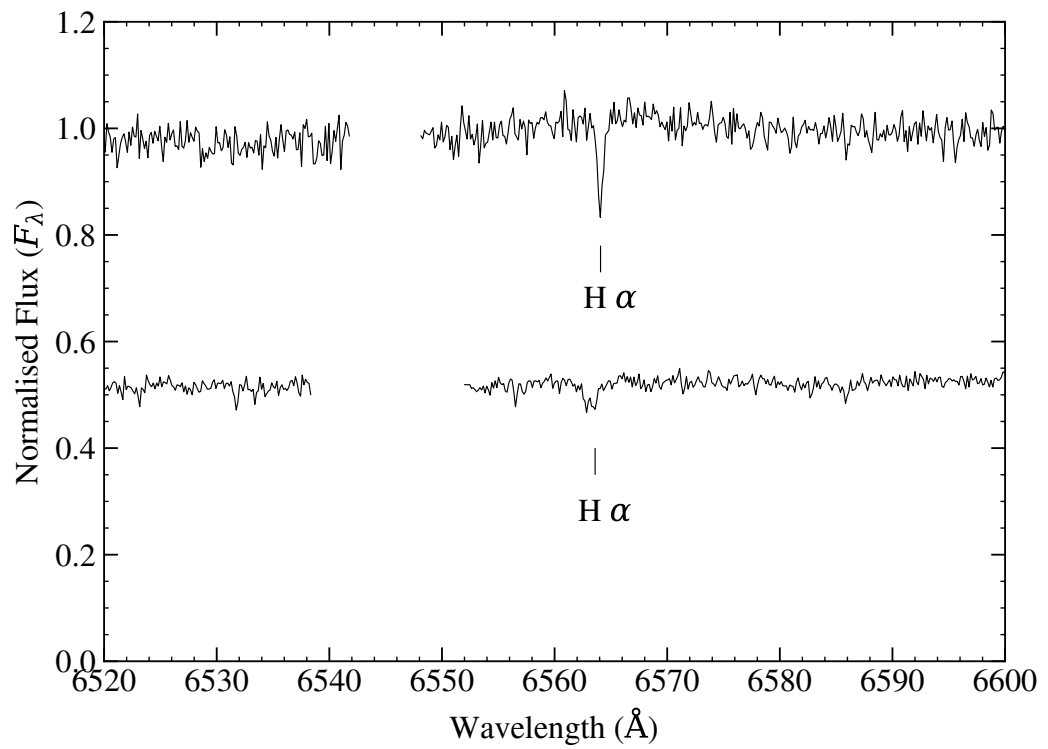


Figure 5.5: Normalised and binned HIRES spectra of WD J1927–0355 (top) and WD J2141–3300 (bottom) in the region around the H α line. A constant offset has been applied to the flux of WD J2141–3300, for visual clarity.

| Parameter | WD J1927–0355 | WD J2141–3300 |
|----------------------------------|---------------|----------------|
| Spectral Type | DZA | DZAH |
| T_{eff} [K] | 6540 (150) | 6870 (150) |
| $\log(g)$ [cm s^{-2}] | 7.99 (0.04) | 7.96 (0.04) |
| Distance [pc] | 23.85 (0.04) | 16.111 (0.006) |
| * $\log(\text{H}/\text{He})$ | –3.5 | –3.5 |
| $\log(\text{Na}/\text{He})$ | < –9.4 | –9.2 (0.2) |
| $\log(\text{Mg}/\text{He})$ | –7.80 (0.15) | –7.50 (0.15) |
| $\log(\text{Al}/\text{He})$ | < –8.6 | –8.5 (0.3) |
| $\log(\text{Si}/\text{He})$ | < –7.6 | –7.2 (0.2) |
| $\log(\text{Ca}/\text{He})$ | –9.1 (0.1) | –8.9 (0.1) |
| $\log(\text{Sc}/\text{He})$ | < –11.7 | < –11.7 |
| $\log(\text{Ti}/\text{He})$ | –10.7 (0.1) | –10.0 (0.1) |
| $\log(\text{V}/\text{He})$ | < –10.5 | < –10.4 |
| $\log(\text{Cr}/\text{He})$ | –10.2 (0.2) | –10.0 (0.2) |
| $\log(\text{Mn}/\text{He})$ | < –9.2 | < –9.3 |
| $\log(\text{Fe}/\text{He})$ | –8.0 (0.1) | –8.2 (0.1) |
| $\log(\text{Co}/\text{He})$ | < –9.8 | < –10.0 |
| $\log(\text{Ni}/\text{He})$ | –9.3 (0.2) | –9.2 (0.2) |
| $\log(\text{Cu}/\text{He})$ | < –11.5 | < –11.2 |
| $\log(\text{Sr}/\text{He})$ | < –12.3 | –12.1 (0.3) |
| $\log(\text{Ba}/\text{He})$ | < –12.2 | < –12.2 |

Table 5.2: Abundances and upper limits of elements determined from combined fitting of the spectra and photometry of the two DZA white dwarfs with Koester (2010) models. * indicates that the abundance was fixed, not measured. Distances were determined from inverting *Gaia* DR3 parallaxes, and distance errors incorporated the *Gaia* astrometric excess noise.

| Atomic Number | Element | $\log(t_{\text{set}}/\text{yr})$ | | $M_{\text{CVZ}} / 10^{21} \text{ g}$ | | $\log(t_{\text{set}}/\text{yr})$ | | $M_{\text{CVZ}} / 10^{21} \text{ g}$ | |
|---------------|---------|----------------------------------|------------------------------|--------------------------------------|------------------------------|----------------------------------|------------------------------|--------------------------------------|------------------------------|
| | | WD J1927-0355 | WD J1927-0355 | WD J1927-0355 | WD J1927-0355 | WD J2141-3300 | WD J2141-3300 | WD J2141-3300 | WD J2141-3300 |
| 1 | * H | - | 1071 | - | 1259 | - | - | - | - |
| 11 | Na | 6.55 | < 0.03 | 6.62 | $0.06^{+0.03}_{-0.02}$ | 6.62 | $0.06^{+0.03}_{-0.02}$ | 6.62 | $0.06^{+0.03}_{-0.02}$ |
| 12 | Mg | 6.55 | $1.3^{+0.5}_{-0.4}$ | 6.62 | 3^{+1}_{-1} | 6.62 | 3^{+1}_{-1} | 6.62 | 3^{+1}_{-1} |
| 13 | Al | 6.50 | < 0.23 | 6.57 | $0.3^{+0.3}_{-0.2}$ | 6.57 | $0.3^{+0.3}_{-0.2}$ | 6.57 | $0.3^{+0.3}_{-0.2}$ |
| 14 | Si | 6.51 | < 2.37 | 6.58 | 7^{+4}_{-3} | 6.58 | 7^{+4}_{-3} | 6.58 | 7^{+4}_{-3} |
| 20 | Ca | 6.37 | $0.11^{+0.03}_{-0.02}$ | 6.45 | $0.20^{+0.05}_{-0.04}$ | 6.45 | $0.20^{+0.05}_{-0.04}$ | 6.45 | $0.20^{+0.05}_{-0.04}$ |
| 21 | Sc | 6.31 | < 0.0003 | 6.38 | < 0.0004 | 6.38 | < 0.0004 | 6.38 | < 0.0004 |
| 22 | Ti | 6.28 | $0.0032^{+0.0008}_{-0.0007}$ | 6.35 | $0.019^{+0.005}_{-0.004}$ | 6.35 | $0.019^{+0.005}_{-0.004}$ | 6.35 | $0.019^{+0.005}_{-0.004}$ |
| 23 | V | 6.25 | < 0.005 | 6.33 | < 0.008 | 6.33 | < 0.008 | 6.33 | < 0.008 |
| 24 | Cr | 6.25 | $0.011^{+0.006}_{-0.004}$ | 6.33 | $0.021^{+0.012}_{-0.008}$ | 6.33 | $0.021^{+0.012}_{-0.008}$ | 6.33 | $0.021^{+0.012}_{-0.008}$ |
| 25 | Mn | 6.22 | < 0.12 | 6.30 | < 0.11 | 6.30 | < 0.11 | 6.30 | < 0.11 |
| 26 | Fe | 6.23 | $1.9^{+0.5}_{-0.4}$ | 6.30 | $1.4^{+0.4}_{-0.3}$ | 6.30 | $1.4^{+0.4}_{-0.3}$ | 6.30 | $1.4^{+0.4}_{-0.3}$ |
| 27 | Co | 6.20 | < 0.003 | 6.28 | < 0.02 | 6.28 | < 0.02 | 6.28 | < 0.02 |
| 28 | Ni | 6.22 | $0.10^{+0.06}_{-0.04}$ | 6.29 | $0.15^{+0.09}_{-0.05}$ | 6.29 | $0.15^{+0.09}_{-0.05}$ | 6.29 | $0.15^{+0.09}_{-0.05}$ |
| 29 | Cu | 6.17 | < 0.0007 | 6.25 | < 0.0015 | 6.25 | < 0.0015 | 6.25 | < 0.0015 |
| 38 | Sr | 6.04 | < 0.0001 | 6.12 | $0.0003^{+0.0003}_{-0.0001}$ | 6.12 | $0.0003^{+0.0003}_{-0.0001}$ | 6.12 | $0.0003^{+0.0003}_{-0.0001}$ |
| 56 | Ba | 5.87 | < 0.0003 | 5.95 | < 0.0003 | 5.95 | < 0.0003 | 5.95 | < 0.0003 |

Table 5.3: Gravitational settling times and masses of heavy elements in the convection zone for WD J1927-0355 and WD J2141-3300, for the models with overshoot. The total mass of heavy elements (i.e. excluding hydrogen) detected in the convection zone is $6.15 \times 10^{21} \text{ g}$ for WD J1927-0355 and $1.23 \times 10^{22} \text{ g}$ for WD J2141-3300. The * indicates that the hydrogen abundance was fixed at $\log(\text{H}/\text{He}) = -3.5$.

WD J2141–3300 has an average mean magnetic field modulus of 50 ± 10 kG (Bagnulo et al., 2024b) and rotates with a period of 6.2 hours (Hernandez et al., 2024; Farihi et al., 2024b). WD J2141–3300 was observed to have varying equivalent widths of metal lines within its rotation period (Bagnulo et al., 2024b). A hypothesis for this variation is that there is an inhomogeneous chemical composition at the white dwarf photosphere which changes in visibility as the star rotates (Bagnulo et al., 2024b,a). Bagnulo et al. (2024b) found that the measured metal abundances varied over the rotation period of the white dwarf, but that all the abundances varied in phase. Therefore, the ratios of metal abundances should remain roughly constant with time. The analysis presented in this work relies only on abundance ratios and the variation in line strength should not significantly affect any results.

5.3 Methods

5.3.1 Exponentially decaying disc model

For the analysis of the composition of the material accreted by these two white dwarfs, I employed the model of Jura et al. (2009), which considers a disc for which the accretion rate decays exponentially with a characteristic e -folding timescale t_{disc} . This model is appropriate for a disc in which viscosity is inversely proportional to radius (Lodato, 2008), and for a disc which is not replenished and decays over time. Cool helium-atmosphere white dwarfs are the systems for which the choice of disc model has the most substantial effect, since the disc lifetime and settling timescales in these systems are similar orders of magnitude.

In the Jura et al. (2009) model, the mass accretion rate decays according to

$$\dot{M}_{\text{acc}}(t) = \frac{M_{\text{PB}}}{t_{\text{disc}}} e^{-t/t_{\text{disc}}}, \quad (5.1)$$

where $\dot{M}_{\text{acc}}(t)$ is the mass accretion rate as a function of time t , and M_{PB} is the total mass of the parent body. In this context, parent body refers to the total planetary body that gets accreted within the duration of the overall accretion event.

The mass of a particular element Z observed at time t in the convection zone of the white dwarf, is given by

$$M_{\text{CVZ}}(Z, t) = \frac{M_{\text{PB}}(Z)t_{\text{set}}(Z)}{t_{\text{disc}} - t_{\text{set}}(Z)} \left(e^{-t/t_{\text{disc}}} - e^{-t/t_{\text{set}}(Z)} \right), \quad (5.2)$$

in the Jura et al. (2009) model, where $M_{\text{CVZ}}(Z, t)$ is the mass of element Z in the convection zone of the white dwarf at time t , $t_{\text{set}}(Z)$ is the settling timescale for element Z , and $M_{\text{PB}}(Z)$ is the mass of element Z in the parent body.

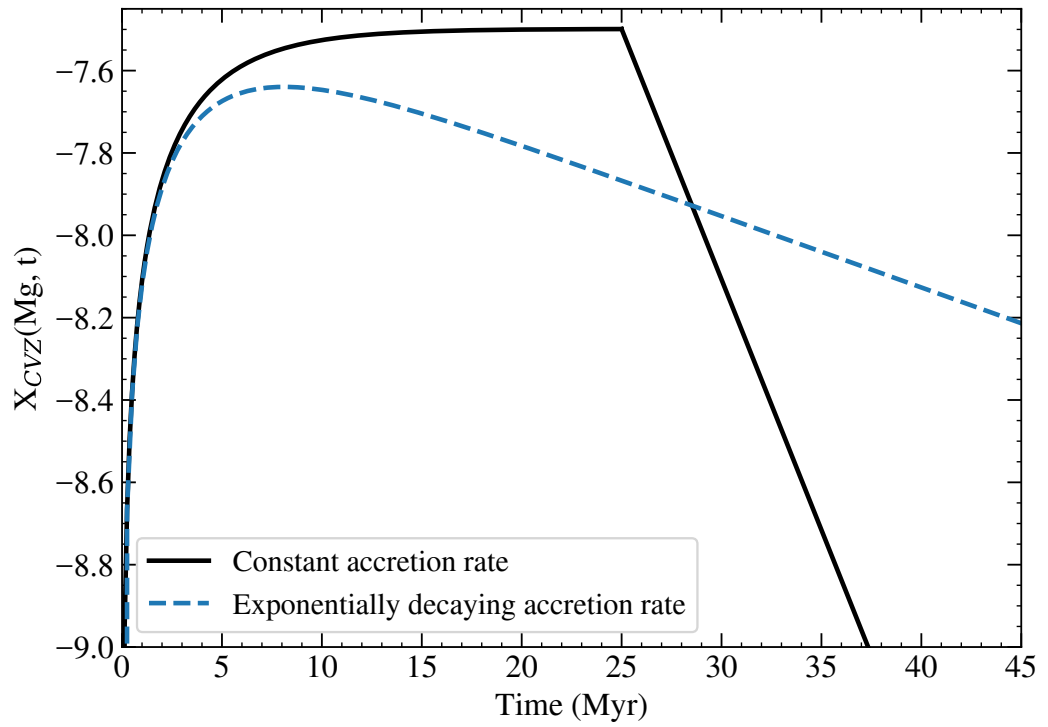


Figure 5.6: A demonstration of the mass abundance (X_{CVZ}) of Mg in the convection zone of WD J1927–0355 for the constant accretion rate model (Dupuis et al., 1993; Koester, 2009) and for the Jura et al. (2009) exponentially decaying model with a 25 Myr disc e -folding characteristic timescale. The accretion was switched off at 25 Myr for the constant accretion rate model scenario, for illustrative purposes. $\dot{M}_{\text{acc}}(t = 0)$ for the exponentially decaying accretion rate model was set equal to \dot{M}_{acc} for the constant accretion rate model.

The characteristic e -folding timescale of the disc affects the inferred composition and mass of material accreted, but is poorly constrained. Girven et al. (2012) inferred from IR observations that disc lifetimes could range from 0.03 Myr to 5 Myr. With updated models and a larger sample of white dwarfs with IR excesses from Farihi (2016), Cunningham et al. (2021) derived a characteristic lifetime range for white dwarf discs of $\log(t_{\text{disc}} / \text{yr}) = 6.1 \pm 1.4$, which corresponds to a range of 0.05 Myr to 32 Myr, and which I adopt as bounds in this work. Wyatt et al. (2014) inferred that disc lifetimes could be as low as 20 yr, however they mention that pollution could be sustained for longer if there were multiple consecutive accretion events of this duration. For simplicity, however, in this work, I have assumed that the accretion of a single object, that I refer to as the parent body, has produced the pollution.

Figure 5.6 demonstrates the difference between the exponentially decaying accretion rate model (Jura et al., 2009) and the constant accretion rate model (Dupuis et al., 1993; Koester, 2009). A steady state is never reached in the exponentially decaying model under the conditions demonstrated in Fig. 5.6, due to the settling timescales of WD J1927–0355 being of the order of a typical disc lifetime (see Table 5.3). For the cool DZ(A) white dwarfs discussed in this work, a steady state solution cannot be reached for a typical disc lifetime, as $t_{\text{disc}} \approx t_{\text{set}}$ or $t_{\text{disc}} \ll t_{\text{set}}$, depending on the disc lifetime. However, as noted by Koester (2009), if $t_{\text{disc}} \gg t_{\text{set}}$, as is the case for hot hydrogen-atmosphere and hot helium-atmosphere white dwarfs, a steady state-like solution can be recovered in the exponentially decaying disc model.

I rearranged equation 5.2 to incorporate the observed mass of each element in the convection zone, as in equation 3 of Trierweiler et al. (2022)

$$M_{\text{PB}}(Z, t_{\text{elapse}}) = \frac{M_{\text{CVZ}}(Z)(t_{\text{disc}} - t_{\text{set}}(Z))}{t_{\text{set}}(Z)(e^{-t_{\text{elapse}}/t_{\text{disc}}} - e^{-t_{\text{elapse}}/t_{\text{set}}(Z)})}, \quad (5.3)$$

where t_{elapse} is the time elapsed since the start of the accretion event. This rearranged equation and re-labelling of t_{elapse} enables it to be set as a free parameter, and represents the phase of accretion that we are observing the system to be in. In Section 5.4, I use equation 5.3 to infer the parent body composition, given the observed number abundances and therefore convection zone masses at the time of observation, with t_{elapse} and t_{disc} set as free parameters. The two-dimensional parameter space of disc lifetime and time of observation provides constraints on both the phase of accretion and the total mass of the accreted material.

5.3.2 Comparisons to solar system compositions

To learn more about the accreted material and the phase of accretion, I compared the composition of the material inferred at different phases of accretion with compositions of different types of solar system objects, such as meteorites and the bulk Earth composition. The best-matching compositions imply that the white dwarf was likely to have accreted material of a particular composition, observed at a particular time after the accretion event began.

Number abundances $n(Z)$ in a white dwarf atmosphere can be converted from mass abundances via:

$$\log\left(\frac{n(Z_1)}{n(Z_2)}\right) = \log\left(\frac{X(Z_1) m(Z_2)}{X(Z_2) m(Z_1)}\right), \quad (5.4)$$

where $X(Z)$ is the mass fraction of element Z compared to the total mass, and $m(Z)$ is the atomic mass of element Z .

In the context of solar system abundances, the mass fraction is the percentage composition by mass of element Z in that object. To find the best compositional match to the material accreted by each white dwarf, I used equation 5.3 to calculate the masses of each element in the parent body, and by extension the number abundances in the parent body, for all combinations of t_{elapse} and t_{disc} within the parameter space. I then calculated reduced χ^2 values for number abundances propagated through equation 5.3, ratioed to a reference element, and compared them with various solar system compositions. The total inferred parent body mass was not important for the calculations, as it cancelled out in the ratios between each element and the reference element.

The reduced χ^2 (χ_ν^2) is defined as

$$\chi_\nu^2 = \frac{1}{\nu} \sum_{i=1}^N \frac{(Y_{\text{WD}} - Y_{\text{SS}})^2}{\sigma_{\text{WD}}^2(Z_i) + \sigma_{\text{WD}}^2(Z_{\text{ref}})} + \frac{1 - S(Y_{\text{WD}})}{\sigma_i}, \quad (5.5)$$

where ν is the number of degrees of freedom (the total number of elements detected in the white dwarf atmosphere, N , minus the number of free parameters, t_{disc} and t_{elapse}), $Y = \log\left(\frac{n(Z_i)}{n(Z_{\text{ref}})}\right)$ for the white dwarf or comparison solar system composition, ‘WD’ and ‘SS’ represent the white dwarf and the comparison solar system composition respectively, $n(Z_{\text{ref}})$ is the abundance of the reference element, which I chose to be magnesium, and $\sigma_{\text{WD}}(Z_i)$ is the error on the white dwarf number abundance. The choice of reference element was somewhat arbitrary, but checks showed that other reference elements did not substantially change the regions of parameter space that best matched the meteorite compositions. The bounds on the input free parameters were set at 0.05 – 32 Myr for the disc lifetime from Cunningham et al. (2021), and 0 – 100 Myr for the time since the accretion event began.

For any upper limit measurements in the white dwarf for which abundances of a given meteorite class were available, I did not directly use the limit in the χ_v^2 calculation, but applied a survival function $S(Y_{\text{WD}})$ to the χ_v^2 value. The survival function was adapted from Swan et al. (2023) and references therein, and is of the form,

$$S(Y_{\text{WD}}) = \frac{1}{2} \left[1 - \operatorname{erf} \left(\frac{Y_{\text{WD}} - Y_{\text{SS}}}{\sqrt{2}\sigma_i} \right) \right], \quad (5.6)$$

where the function *erf* is the Gauss error function. Since this function is being used for upper limits, the uncertainty σ_i is set at a standard value of 0.3 dex, as in Swan et al. (2023), which corresponds to the largest error on an abundance measurement in Table 5.2. For each upper limit, the term $\frac{1 - S(Y_{\text{WD}})}{\sigma_i}$ is applied to the upper limits to incorporate a penalty to the χ_v^2 value if the upper limit lies below the meteorite abundance.

The method for determining the most likely composition of the parent body as well as t_{elapse} and t_{disc} proceeds as follows:

1. Select a meteorite class and determine the number abundances of all elements in ratio with magnesium.
2. Create a 500×500 log-spaced grid of values of t_{disc} (0.05 – 32 Myr) and t_{elapse} (0 – 100 Myr), which are both free parameters in the disc model.
3. For all combinations of t_{disc} and t_{elapse} in the grid, convert each number abundance observed in the white dwarf convection zone, as well as each upper limit, into a mass in the convection zone.
4. Propagate the mass of each element in the convection zone through equation 5.3 to determine the mass of each element in the parent body at each pair of t_{disc} and t_{elapse} . Convert these masses back to number abundances, and ratio with magnesium.
5. Use equation 5.5 to determine the χ_v^2 comparing: the number abundances of all detected elements in the parent body for a combination of t_{disc} and t_{elapse} , and the number abundances of all elements in the chosen meteorite class. Treat upper limits slightly differently: instead of calculating χ_v^2 , use a survival function to add a penalty to the total χ_v^2 .
6. Produce a χ_v^2 contour plot for all combinations of t_{disc} and t_{elapse} to determine if there are degeneracies in the two parameters, i.e. if many combinations provide an almost equally good comparison.
7. Repeat this process for all meteorite classes or other solar system compositions, e.g. bulk Earth.

| Composition | | Minimum χ_v^2 WDJ1927–0355 | Minimum χ_v^2 WDJ2141–3300 |
|-------------|---------------|------------------------------------|------------------------------------|
| Bulk Earth | | 0.8 | 1.8 |
| Earth Crust | | 65.2 | 31.0 |
| Chondrites | C | 1.9 | 1.3 |
| | E | 2.8 | 2.7 |
| | H | 2.0 | 2.3 |
| | L | 2.8 | 1.9 |
| | LL | 3.2 | 1.8 |
| Achondrites | Aubrites | 51.9 | 20.7 |
| | Brachinites | 3.9 | 2.3 |
| | Diogenites | 32.1 | 16.8 |
| | Eucrites | 63.2 | 24.6 |
| | Howardites | 31.5 | 10.8 |
| | Urelites | 9.9 | 8.3 |
| Stony-iron | Mesosiderites | 9.4 | 1.6 |
| | Pallasites | 18.3 | 42.8 |

Table 5.4: Minimum χ_v^2 for solar system abundances compared to the abundances and upper limits of elements in WDJ1927–0355 and WDJ2141–3300 propagated through the Jura et al. (2009) model.

I determined χ_v^2 values as described above for abundances of both white dwarfs compared to the median composition of each major meteorite class provided in the Nittler et al. (2004) database: carbonaceous (C) chondrites, L chondrites, LL chondrites, H chondrites, E chondrites, aubrites, brachinites, eucrites, diogenites, howardites, urelites, mesosiderites, and pallasites. I also compared the white dwarf abundances to the bulk Earth composition (Allègre et al., 2001) and Earth’s crust (Rudnick and Gao, 2003).

5.4 Results

All major meteorite classes were compared to the abundances and upper limits of elements in WDJ1927–0355 and WDJ2141–3300, propagated through equation 5.3 with t_{disc} and t_{elapse} as free parameters. The results for the minimum χ_v^2 are shown in Table 5.4. The two free parameters are degenerate, and therefore the minimum χ_v^2 corresponds to a range of parameter space, as explained below. The current sample size of white dwarfs with abundance measurements of the trace elements scandium, vanadium, cobalt, copper, strontium and barium is too small to assess consistency, and their abundance ratios often show variability. As such, these elements were not used for determining constraints on the phase of accretion, even when they were available in datasets including the Allègre et al. (2001) bulk Earth composition.

The best matching solar system composition for WD J1927–0355 was bulk Earth. The minimum χ_v^2 for bulk Earth was 0.8, at $t_{\text{disc}} = 32$ Myr and $t_{\text{elapse}} = 5.3$ Myr. The minimum χ_v^2 for bulk Earth is below 1, implying the error bars on the abundances are somewhat overestimated. The abundances of each element in a parent body accreted 5.3 Myr ago, with a disc lifetime of 32 Myr, normalised to magnesium and CI chondrites, are shown in Fig. 5.7. The black horizontal line at zero in Fig. 5.7 corresponds to the CI chondrite composition from Lodders (2019). The abundances of C chondrites are also shown, highlighting that both chondrite and bulk Earth compositions provide a good comparison to the material accreted by WD J1927–0355. Fig. 5.7 is an example of one set of well-matching t_{disc} and t_{elapse} , but many other combinations create almost equally good matches because the two free parameters are degenerate, as shown by the χ_v^2 contour plot in Fig. 5.8. Therefore, the disc lifetime of this system cannot be constrained, however the accretion event is most likely to have occurred between 1 Myr ago and 10 Myr ago, depending on the disc lifetime. Table 5.4 shows that C and H chondrites were also good matches to the composition of WD J1927–0355, but the white dwarf abundances did not match well to achondrites, stony-iron meteorites, or the Earth’s crust composition.

The best-matching meteorite compositions to WD J2141–3300 were C chondrites. The minimum χ_v^2 for C chondrites was 1.3, for $t_{\text{disc}} = 0.09$ Myr and $t_{\text{elapse}} = 3.5$ Myr. The corresponding compositions for this combination of t_{disc} and t_{elapse} are shown in Fig. 5.9. The inferred titanium and silicon abundances are slightly enhanced compared to C chondrites but remain within 2σ , suggesting no strong deviation from a C chondrite composition. Both the titanium and silicon ratios could be explained by variations of a similar order of magnitude seen in nearby stars. As with WD J1927–0355, the two free parameters t_{disc} and t_{elapse} are degenerate, as shown by the χ_v^2 contour plot in Fig. 5.10. However, the minimum χ_v^2 values constrain the time since accretion began to be between 1 Myr and 6 Myr ago for shorter disc lifetimes. For the longest disc lifetimes t_{elapse} is more likely to be greater than 10 Myr. Fig. 5.9 demonstrates that the bulk Earth abundances compare well to the WD J2141–3300 abundances. Table 5.4 also shows that L chondrites, LL chondrites, and mesosiderites were also good matches to the composition of WD J2141–3300. The mesosiderite composition is very different to bulk Earth and chondrites, with a iron and nickel-rich composition, and it is only a good comparison for a narrow region of parameter space: at elapsed times greater than 12 Myr for 4–6 Myr disc lifetimes. Achondrites, the Earth’s crust composition, and the stony-iron pallasites were poor matches.

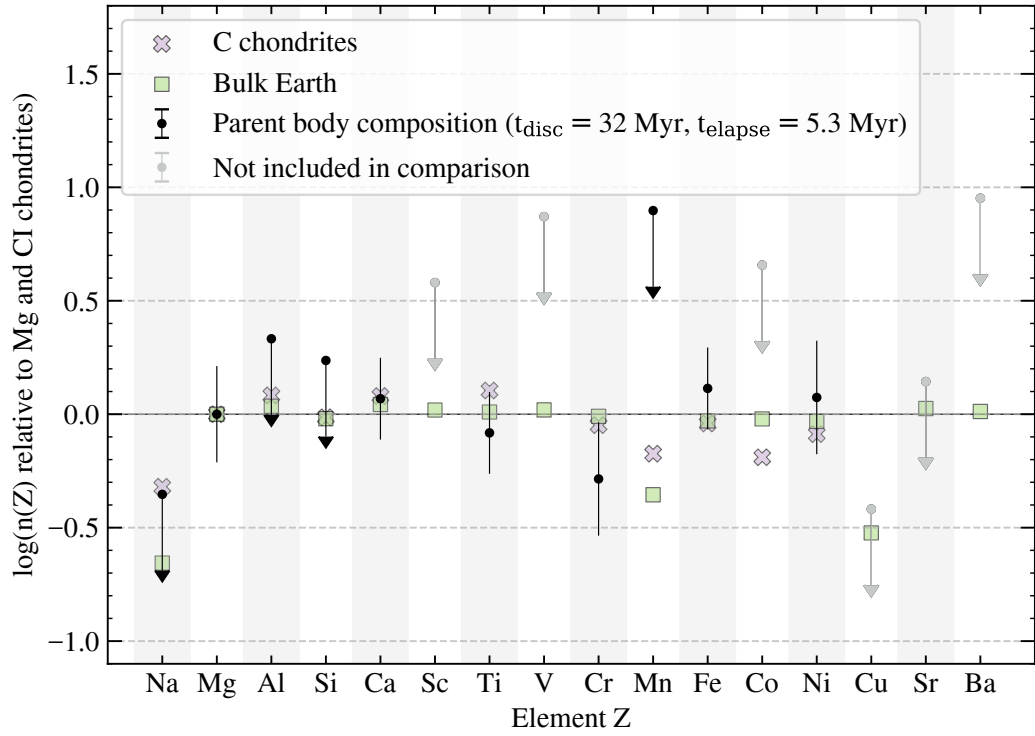


Figure 5.7: Element abundances for WD J1927–0355, propagated through the Jura et al. (2009) model for the values of t_{disc} and t_{elapse} corresponding to the minimum χ^2_{ν} , normalised to Mg and CI chondrites, are shown in black. Elements are ordered from left to right in order of increasing atomic weight. Bulk Earth abundances normalised to Mg and CI chondrites are shown by square symbols (Allègre et al., 2001). C chondrite abundances normalised to Mg and CI chondrites are shown by cross symbols (Nittler et al., 2004). Upper limits are denoted with a downwards arrow. CI chondrite abundances are from Lodders (2019). Error bars are propagated using the errors on abundances from Table 5.2. Faded (grey) points represent elements that were not considered in the comparison.

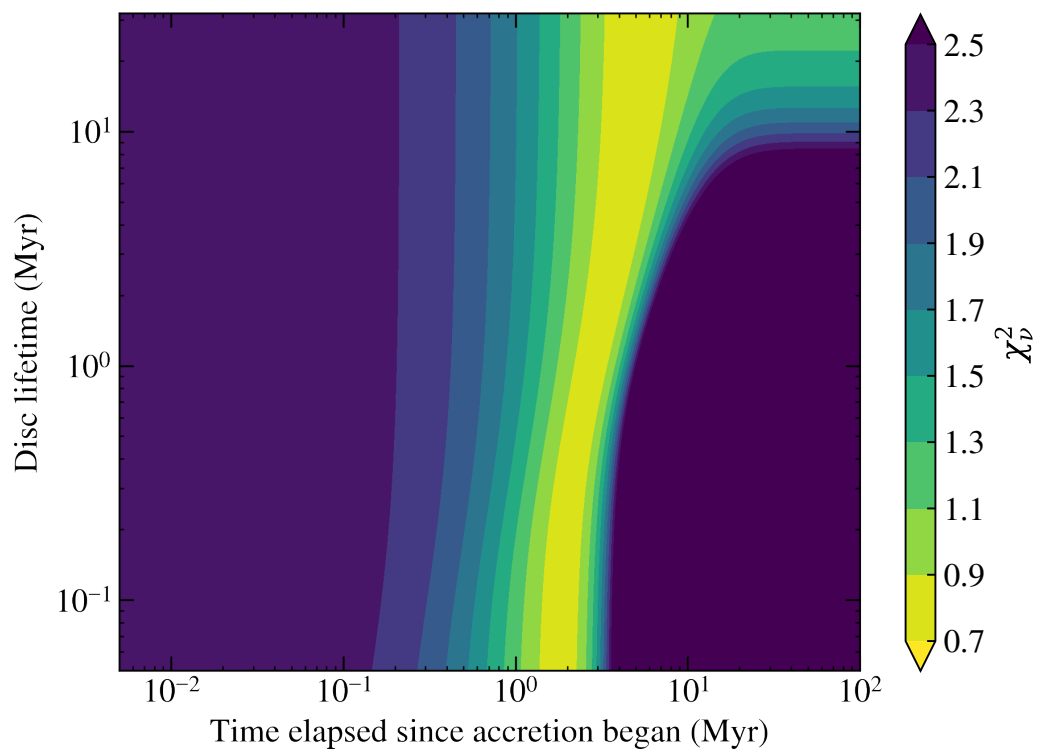


Figure 5.8: χ^2_ν contour plot for the abundances in WDJ1927–0355 compared with bulk Earth abundances (relative to magnesium).

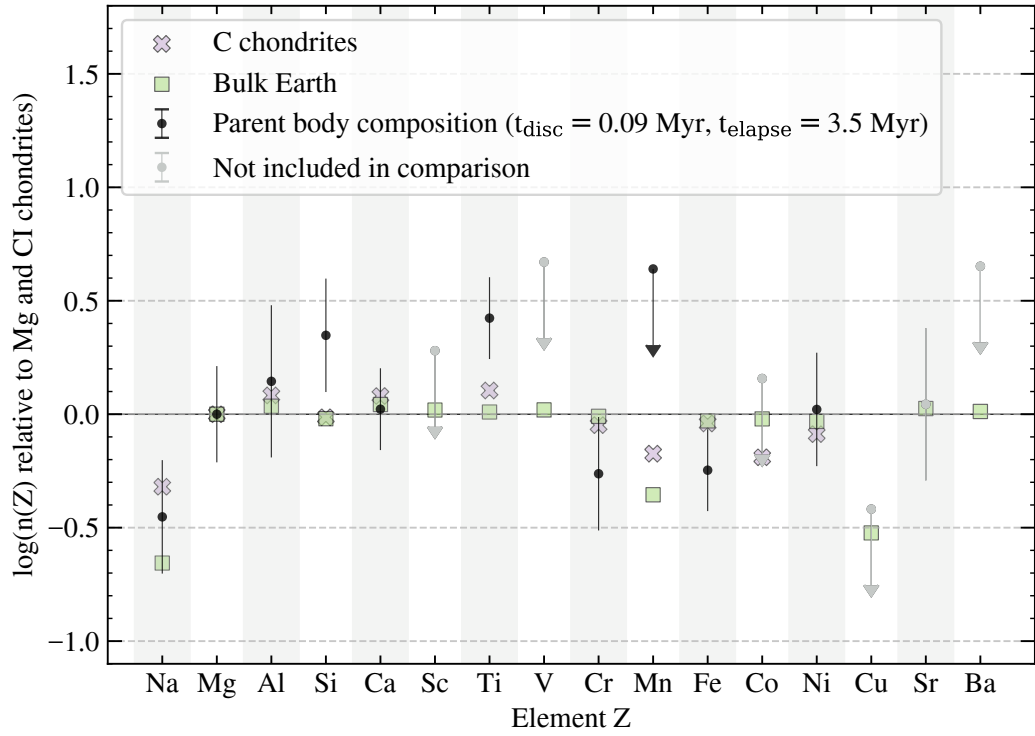


Figure 5.9: Element abundances for WD J2141–3300, propagated through the Jura et al. (2009) model for the values of t_{disc} and t_{elapse} corresponding to the minimum χ^2_{ν} , normalised to Mg and CI chondrites, are shown in black. Elements are ordered from left to right in order of increasing atomic weight. Bulk Earth abundances normalised to Mg and CI chondrites are shown by square symbols (Allègre et al., 2001). C chondrite abundances normalised to Mg and CI chondrites are shown by cross symbols (Nittler et al., 2004). Upper limits are denoted with a downwards arrow. CI chondrite abundances are from Lodders (2019). Error bars are propagated using the errors on abundances from Table 5.2. Faded (grey) points represent elements that were not considered in the comparison.

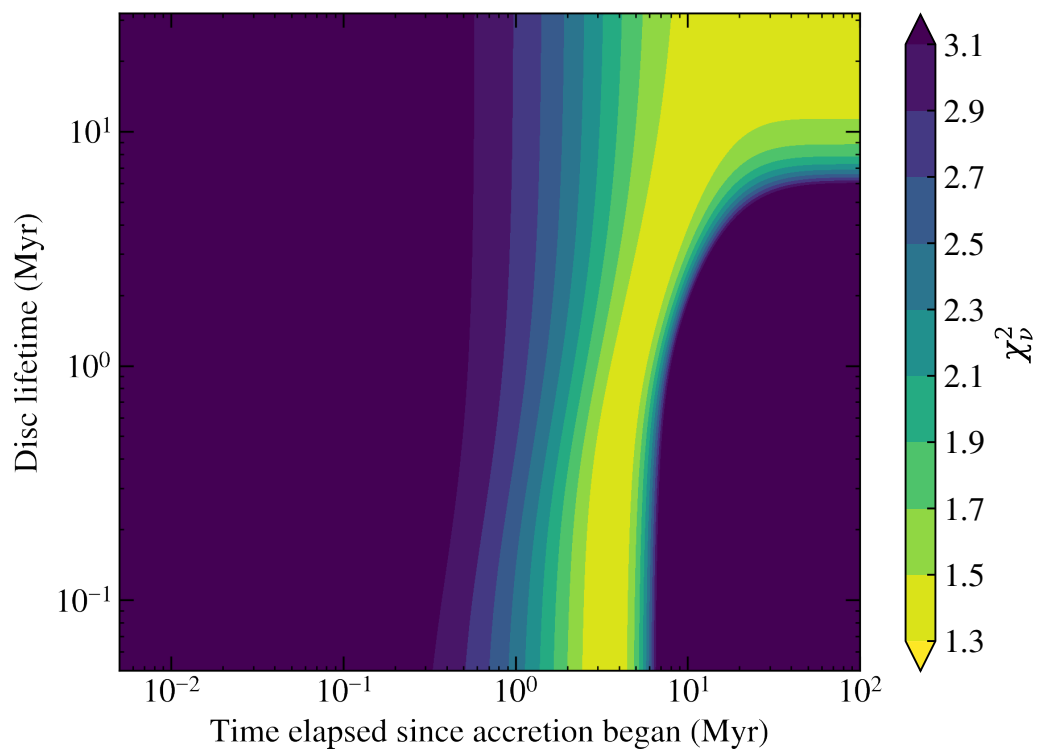


Figure 5.10: χ^2_{ν} contour plot for the abundances in WDJ2141–3300 compared with C chondrite abundances (relative to magnesium).

5.5 Discussion

5.5.1 Interpretation of WDJ1927-0355 results

I determined an estimate of the mass of the parent body at a given t_{disc} and t_{elapse} by calculating the mass of all detected elements in the parent body using equation 5.3, plus an assumed mass of oxygen in the parent body. Oxygen is a major component of rock-forming elements, yet is challenging to detect in optical spectra. There are no detections of oxygen absorption lines in either white dwarf, so I adopted an assumed oxygen abundance of $\log(\text{O}/\text{He}) = -6.55$ for both white dwarfs, based on the amount required to achieve a stoichiometric balance with detected rock-forming elements, assuming they were present in the parent body as the following rocky oxides: NaO_2 , MgO , Al_2O_3 , SiO_2 , CaO , TiO_2 , Cr_2O_3 , FeO , and NiO . The total mass of heavy elements detected in the convection zone is 6.15×10^{21} g, and including the assumed oxygen abundance this mass goes up to 2.13×10^{22} g. This mass sets a lower limit on the mass of the parent body, and therefore the inferred parent body mass, including the assumed amount of oxygen, ranges from $10^{22} - 10^{24}$ g. The uncertainty in this measurement is dominated by the uncertainty in t_{elapse} . This mass range spans from roughly the mass of a small moon such as Proteus, a moon of Neptune, up to the mass of a dwarf planet such as Ceres.

Fig. 5.11 shows the mass ratio profile in the parent body accreted by WD J1927–0355, as a function of t_{elapse} , with an illustrative disc lifetime of 0.05 Myr. Fig. 5.11 was normalised to 100 per cent for the parent body mass as a function of time since the accretion event began. However, the initial parent body mass required to explain the present day abundances varies depending on the choice of t_{elapse} , as shown in the lower panel. The shaded region indicates the range of t_{elapse} that best matches with the bulk Earth.

Given the lack of volatile detections, it is challenging to determine if the parent body is volatile-rich or not, or if the composition is more like bulk Earth or chondrites. Sodium can be considered as a semi-volatile element, however only an upper limit is available. This upper limit indicates that the accreted material is unlikely to be solar or stellar in origin. For non-volatile elements, chondritic and bulk Earth element ratios are very similar, but chondrites have much higher levels of volatiles, hence why some chondrites provide a good match to the accreted material as well as bulk Earth. The sodium upper limit provides a good comparison both to bulk Earth and C chondrites, and therefore both solutions are equally reliable. If the parent body were differentiated, the white dwarf would have still accreted bulk planetary material as opposed to parts of the crust or core of the object, given the best-matching compositions.

I conclude that WDJ1927–0355 is likely to have accreted bulk material from a rocky planetary body which is the mass of a small moon or dwarf planet. The composition

of the parent body is equally likely to be bulk Earth or chondritic. The conclusion that this system begun accreting material Myrs ago is broadly consistent with many cool DZ systems analysed by Harrison et al. (2021).

5.5.2 Interpretation of WDJ2141-3300 results

The best-matching composition to the material accreted by WDJ2141–3300 was C chondrites, but L and LL chondrites were also good matches, as well as bulk Earth (Table 5.4). The mass of heavy elements in the convection zone is 1.23×10^{22} g, excluding the oxygen assumption, and reaches 3.02×10^{22} g including it. The parent body mass, assuming that the only elements present are all the detected elements and upper limits plus oxygen from rocky oxides, ranges from $10^{22} - 10^{24}$ g. As with WDJ1927–0355, the parent body mass for WDJ2141–3300 corresponds to a small moon or dwarf planet.

Fig. 5.12 shows the mass ratio profile in the parent body accreted by WDJ2141–3300, as a function of t_{elapse} , normalised to 100 per cent for the parent body mass as a function of time since the accretion event began, with an assumed oxygen abundance of $\log(\text{O}/\text{He}) = -6.55$, and a disc lifetime of 0.05 Myr. The shaded region indicates the range of t_{elapse} that best matches with the C chondrites, corresponding to the region where the sinking of the material is beginning to dominate over the disc accretion.

Similarly to WDJ1927–0355, the lack of volatile detections means we cannot reliably determine if the accreted material is rich in volatile elements. There is a detection of the semi-volatile element sodium, which shows that WDJ2141–3300 is not accreting solar or stellar material, and matches with the C chondrite composition as well as the bulk Earth composition, within errors, as shown in Fig. 5.9. More volatile detections are required for a robust conclusion to be drawn, however cool DZ white dwarfs show extreme line blanketing in the blue end of the optical (see Fig. 5.2), and therefore produce minimal flux in the UV, making the detection of other volatiles challenging. Therefore, I conclude that WDJ2141–3300 has accreted bulk planetary material with a rocky composition, which could be bulk Earth or chondritic in composition.

5.5.3 Comparison with constant accretion rate model

Throughout this work, I have been using the Jura et al. (2009) model, in which the accretion rate decays exponentially with time after the start of the accretion event. However, a much more commonly used disc model in white dwarf pollution studies assumes instead that the accretion rate is constant until the disc is depleted, after which point it becomes zero (Dupuis et al., 1993; Koester, 2009). In this model, the accretion of planetary material onto white dwarfs is separated into three somewhat distinct phases: the increasing phase

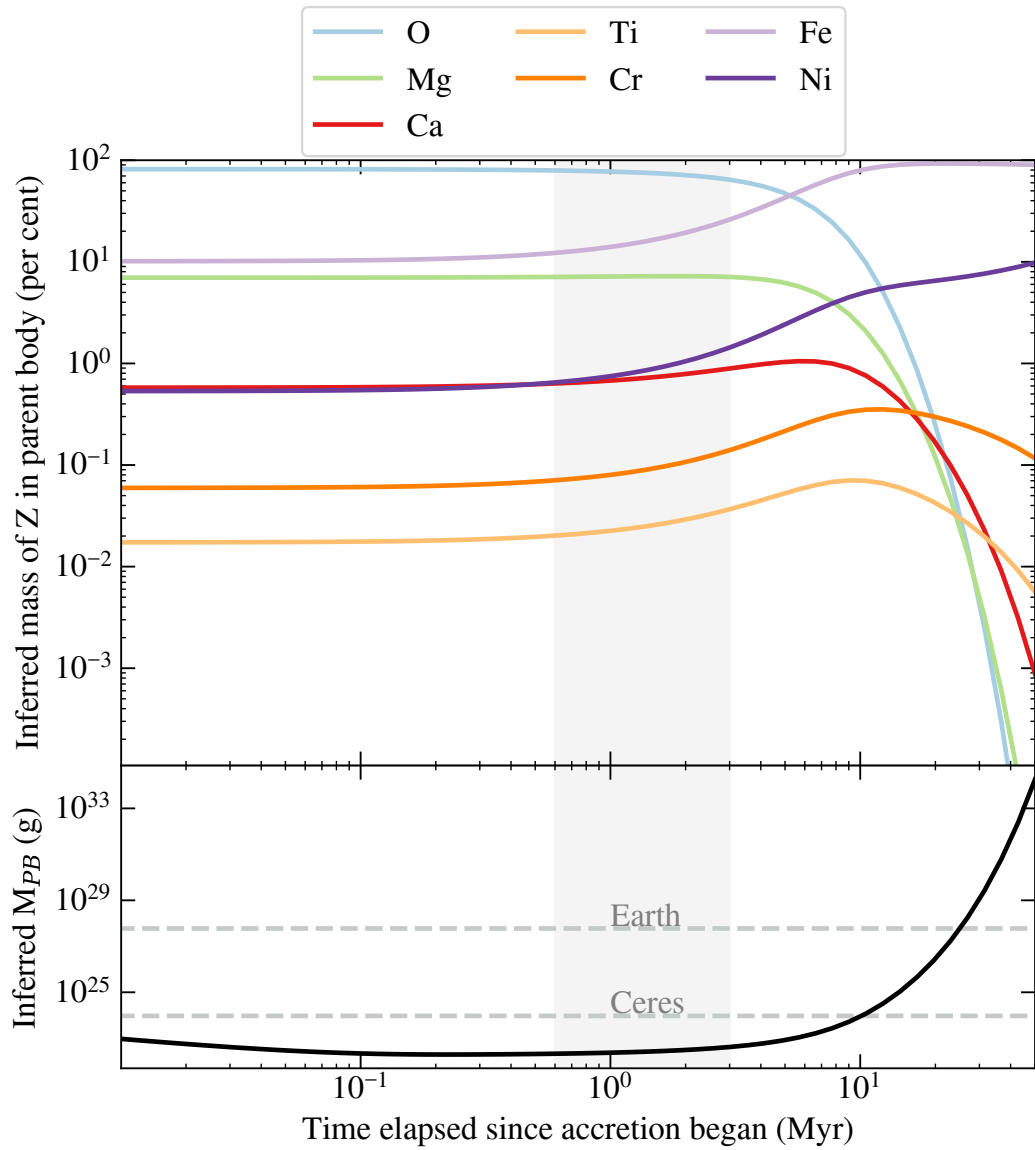


Figure 5.11: **Top:** The percentage by mass of all observed elements inferred to be in the parent body accreted by WD J1927–0355, as well as oxygen, as a function of the time since the accretion event began. The disc lifetime is assumed to be 0.05 Myr. At $t_{\text{elapse}} = 0$, the order of elements on the plot from top to bottom is: O, Fe, Mg, Ca, Ni, Cr, Ti. **Bottom:** The inferred total parent body mass (M_{PB}) as a function of the time since the accretion event began. The grey horizontal dashed lines indicate the mass of the dwarf planet Ceres, and the Earth. The grey vertical shaded region is the most likely elapsed time for WD J1927–0355 since accretion began.

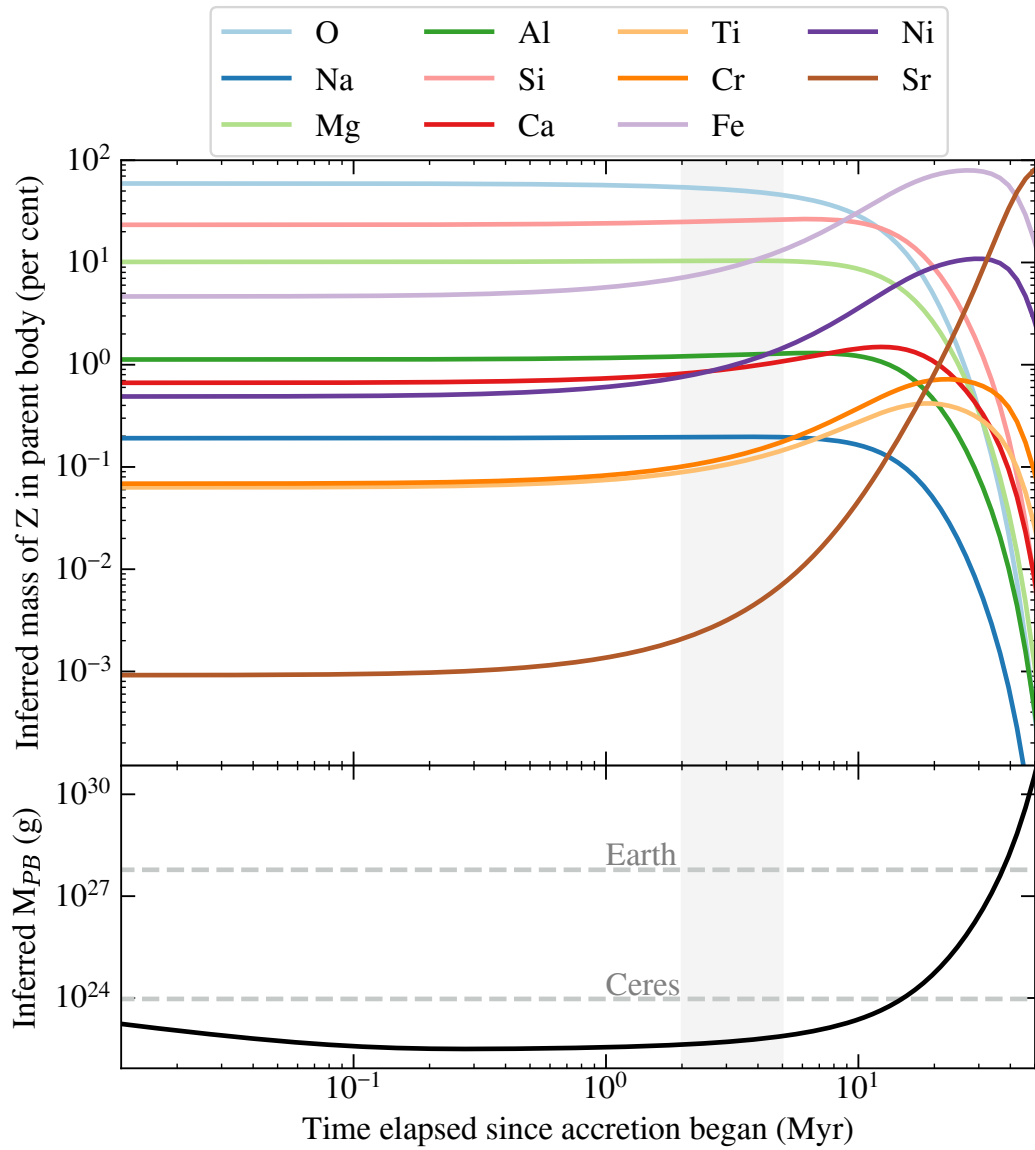


Figure 5.12: **Top:** The percentage by mass of all observed elements inferred to be in the parent body accreted by WD J2141–3300, as well as oxygen, as a function of the time since the accretion event began. The disc lifetime is assumed to be 0.05 Myr. At $t_{\text{elapse}} = 0$, the order of elements on the plot from top to bottom is: O, Si, Mg, Fe, Al, Ca, Ni, Na, Cr, Ti, Sr. **Bottom:** The inferred total parent body mass (M_{PB}) as a function of the time since the accretion event began. The grey horizontal dashed lines indicate the mass of the dwarf planet Ceres, and the Earth. The grey vertical shaded region is the most likely elapsed time for WD J2141–3300 since accretion began.

where material is building up onto the surface, the steady state where material is sinking out of the convection zone at roughly the same rate as it is being accreted, and the declining phase where the disc has been depleted and material is sinking out of the atmosphere. The accretion rate is constant in the increasing and steady state phases, and is zero in the declining phase.

I calculated the minimised χ_v^2 for the constant accretion rate model, comparing the WDJ1927–0355 abundances to the solar system compositions in Table 5.4. To calculate χ_v^2 , I used a similar method to that outlined in Section 5.3, but with equations from Koester (2009) to model the constant accretion rate. The best-matching composition was again bulk Earth, with a minimised χ_v^2 of 2.5 which corresponded to steady state accretion. The abundances of the individual elements used in this calculation compared to bulk Earth are shown in Fig. 5.13. The best-matching composition under the constant accretion rate model for WDJ2141–3300 abundances was LL chondrites, with the minimum χ_v^2 being 2.4, also when the system was in a steady state. The abundances of the individual elements used in this calculation compared to LL chondrites are shown in Fig. 5.14. These results are independent of the disc lifetime, since theoretically the disc lifetime could have any duration if both white dwarfs are accreting in the steady state.

Figures 5.13 and 5.14 highlight that the error bars on the abundances are sufficiently large that the choice of disc model, constant accretion rate or exponentially decaying accretion rate, does not affect the best-matching compositions. Both white dwarfs were best matched by a steady state accretion scenario under the constant accretion rate model. Metals remain in the atmosphere of cool helium-atmosphere white dwarfs for Myrs, and therefore steady state accretion requires a sustained source of accretion over a period much longer than the settling timescales. This could be possible if many smaller parent bodies are being consistently accreted onto the white dwarf over long timescales, therefore replenishing the disc. However, the exponentially decaying model assumes that the disc is not replenished, and provides a solution of which there is no analogue in the constant accretion rate model: that the metals are sinking slightly faster than the rate at which they are being accreted, but accretion has not ceased entirely.

5.5.4 Future work

The results of applying the exponentially decaying disc model to WDJ1927–0355 and WDJ2141–3300 demonstrate the importance of considering disc lifetimes in the analysis of polluted white dwarfs. To date, 62 helium-atmosphere white dwarfs have been observed to contain six or more metals in their atmosphere originating from the accretion of planetary debris (Hollands et al., 2017; Williams et al., 2024). Applying the Jura et al. (2009) disc model to this large group of white dwarfs would enable further constraints on the masses

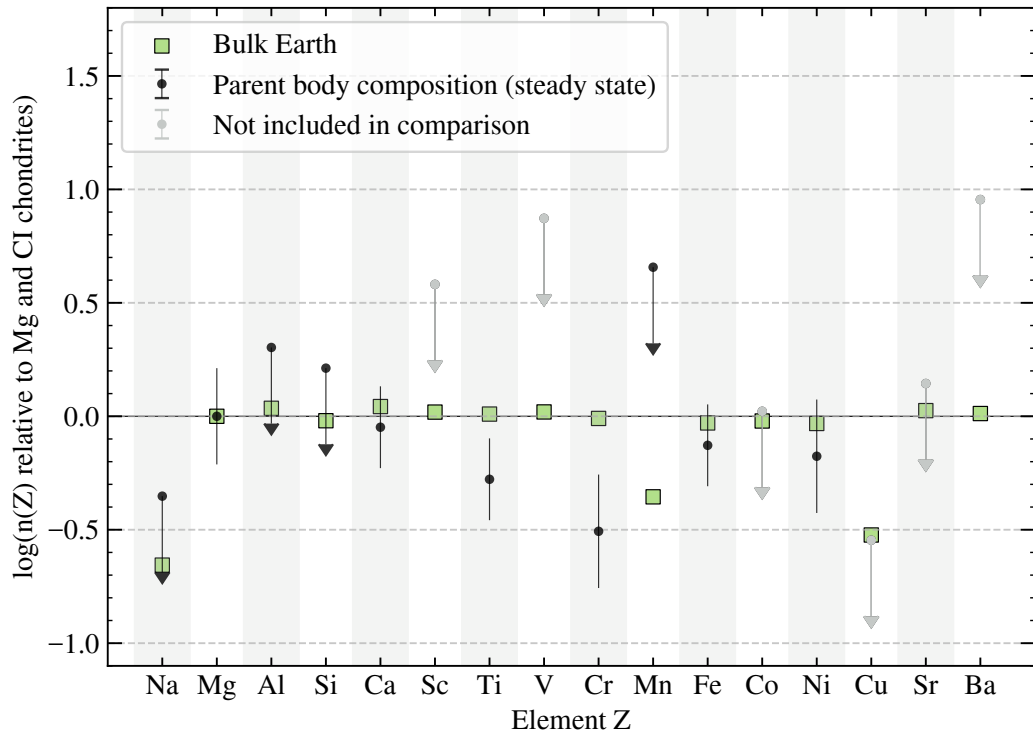


Figure 5.13: Element abundances for WD J1927–0355, propagated through the constant accretion rate model for steady state accretion, normalised to Mg and CI chondrites, are shown in black. Elements are ordered from left to right in order of increasing atomic weight. Bulk Earth abundances normalised to Mg and CI chondrites are shown by square symbols (Nittler et al., 2004). Upper limits are denoted with a downwards arrow. Error bars are propagated using the errors on abundances from Table 5.2. CI chondrite abundances are from Lodders (2019). Faded (grey) points represent elements that were not considered in the comparison.

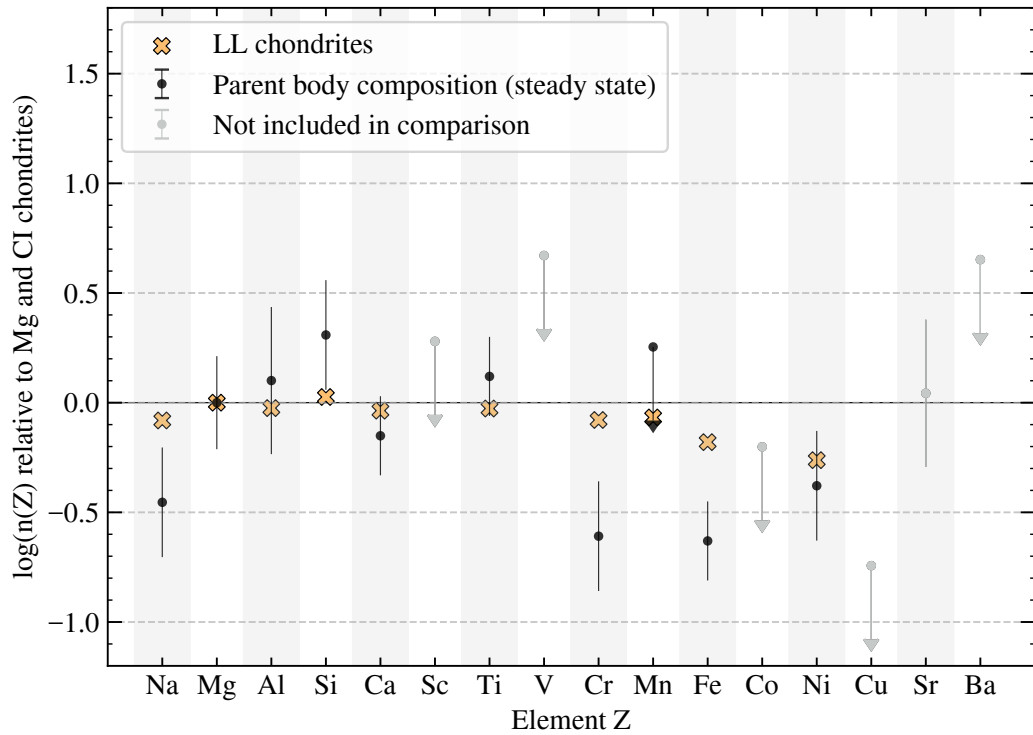


Figure 5.14: Element abundances for WD J2141–3300, propagated through the constant accretion rate model for steady state accretion, normalised to Mg and CI chondrites, are shown in black. Elements are ordered from left to right in order of increasing atomic weight. LL chondrite abundances normalised to Mg and CI chondrites are shown by cross symbols (Nittler et al., 2004). Upper limits are denoted with a downwards arrow. Error bars are propagated using the errors on abundances from Table 5.2. CI chondrite abundances are from Lodders (2019). Faded (grey) points represent elements that were not considered in the comparison.

and types of parent bodies providing the pollution.

The exponentially decaying disc model is not necessarily a physical improvement on the constant accretion rate model, as there is no way to know without a direct disc detection whether the disc is being replenished or not. Both stars should be followed up with IR facilities such as *JWST*, which has the capability to detect faint white dwarf dust discs (Farihi et al., 2025), and can further constrain the phase of accretion of these systems. The exponentially decaying disc model assumes that no further material is being added to the disc, whereas a model assuming steady state accretion could imply that material is continuously being added to the disc, similar to the scenarios described in e.g. Wyatt et al. (2014). However, the exponentially decaying disc model provides a wider range of parameter space in order to compare observations with solar system compositions, and a scenario in which material is decaying slightly faster than it is being accreted matches better with both white dwarf observations than any part of the constant accretion model.

A larger sample of observations of white dwarf debris discs are required in order to reduce the uncertainty on the characteristic disc lifetime. A set of observations of cool helium-atmosphere white dwarfs with many photospheric metals should additionally be analysed using the framework outlined in this work, in order to begin distinguishing if the exponentially decaying disc model makes a systematic difference on the analysis, and whether it should be used going forward in the analysis of these systems.

5.6 Conclusions

An exponentially decaying disc model from Jura et al. (2009) was adopted in the analysis of the planetary material accreted by two cool helium-atmosphere white dwarfs: WD J1927–0355 and WD J2141–3300. These stars have detections of six and ten metals in their atmosphere respectively. Optical spectra of these two white dwarfs, taken from the HIRES instrument on the Keck telescope, were fitted with tailored white dwarf atmosphere models incorporating detected elements plus upper limits (Koester, 2010). The white dwarf atmosphere models struggled to fit the narrow $H\alpha$ features in both spectra. Similarly narrow $H\alpha$ features have been observed in other cool, polluted helium-atmosphere white dwarfs, and further improvements to model atmosphere codes are needed to obtain accurate H/He ratios. The Jura et al. (2009) model was applied to the abundances from the spectroscopic fits in order to constrain the type of accreted material and the phase of accretion.

The Jura et al. (2009) model considers a disc for which accretion rates decay exponentially, which is physically motivated by derivations from Lodato (2008) for a disc in which viscosity is proportional to radius. The time since the accretion event began and the

characteristic lifetime of the disc were set as free parameters, and χ^2_{ν} contour plots constrained the mass and type of the accreted material. This approach considers disc lifetime as a free parameter in the Jura et al. (2009) disc model in order to constrain the composition of the material accreted by the white dwarfs, and motivates further observations and theory in order to constrain white dwarf disc lifetimes.

It was found that WD J1927–0355 and WD J2141–3300 are likely to be experiencing accretion of material similar to bulk Earth or C chondrites in composition. The only available element to distinguish between these compositions is sodium, and in both cases the sodium detection or upper limit matches with both bulk Earth and chondrites within errors. These compositions are typical for white dwarf planetary systems (Hollands et al., 2018a). The best matches to the observations of both stars implied that they are being observed Myrs into an accretion event, and their discs must therefore be slightly depleted. The masses of the parent bodies accreted onto both systems span a range from 10^{22} – 10^{24} g, which means both systems are likely to be accreting bulk planetary material with a parent body roughly the mass of a large asteroid or dwarf planet. The two-dimensional parameter space of disc lifetime and time since the accretion event began provided constraints on both the phase of accretion and the total mass of the accreted material, but could not constrain the duration of the accretion event. As a comparison, the constant accretion rate model places both of these white dwarfs in the steady state phase.

These two white dwarfs add to the growing number of polluted white dwarfs that have been analysed in detail, and they provide further evidence that typical white dwarf planetary systems contain rocky planetesimals with composition ratios similar to bulk Earth and chondritic compositions. A larger sample of cool white dwarfs with multiple photospheric metals should be analysed with this same method in the future, in order to identify targets for IR follow-up. Additionally, more robust measurements of disc lifetimes would help to further constrain the masses of the accreted parent bodies.

Chapter 6

Ultraviolet and optical spectroscopy of white dwarfs within 13 pc

This chapter presents ongoing work on the analysis of a volume-limited sample of white dwarfs observed spectroscopically in the UV by *HST* STIS. The sample of 36 white dwarfs within 13 pc of the Sun covers all major spectral types, and due to their proximity almost all members also have optical and infrared photometry available from *Gaia*, 2MASS, and WISE. This dataset has been supplemented with medium-resolution optical spectroscopy, which enables precise identification of atmospheric compositions, alongside UV-to-IR flux-calibrated spectral energy distributions for the full sample. The aim of the 13 pc project is to identify new characteristics of white dwarfs in the UV that would not be known from just analysing optical data. This includes identifying additional absorption features in the UV, and using the UV spectra to constrain fundamental parameters further. In this chapter, I present an analysis of the hydrogen-atmosphere white dwarfs within 13 pc. I fit the flux-calibrated STIS spectra plus optical and infrared photometry, as well as just optical and infrared photometry, and compare the parameters and quality of the fits when including and excluding the UV data. I find that there is a systematic discrepancy between fits to UV data of pure-H white dwarfs compared to fits to optical and infrared data.

6.1 Introduction

Despite the recent discoveries of hundreds of thousands of white dwarfs from the *Gaia* mission (Gentile Fusillo et al., 2019, 2021), and the full optical characterisation of white dwarfs within 40 pc (Chapters 3 and 4), even the white dwarfs that are located just a few parsecs away in our stellar backyard have still not been fully characterised across all wavelengths. Optical spectroscopy of white dwarfs is commonplace, and enables an initial characterisation of the atmospheric composition, but additional UV observations provide new insights into a star. Some photospheric or interstellar metal absorption lines that are not visible in the optical appear in the UV. Extra continuum flux and absorption lines in the UV enable models to be fitted over a larger wavelength range to better constrain white dwarf parameters such as mass, age and relative abundances of heavy elements.

The determination of fundamental white dwarf parameters including effective temperature (T_{eff}) and surface gravity ($\log(g)$) has historically relied on optical observations, but additional UV observations provide an independent dataset to test white dwarf model atmosphere codes on a population, and have so far revealed systematic offsets in parameters for hotter white dwarfs (Sahu et al., 2023). Hot H-atmosphere white dwarfs show a strong Ly α line in the UV, but cool and old white dwarfs emit flux only in the very near-UV, and as such have not been studied extensively in that wavelength range. The accurate modelling of cool white dwarf atmospheres is a significant issue that affects most of the local white dwarf population, as over half of white dwarfs are cooler than 6000 K (O’Brien et al., 2024). The high-density atmospheres of the coolest white dwarfs are notoriously challenging to model (Blouin et al., 2017; Elms et al., 2022; Bergeron et al., 2022). Improved Ly α broadening profiles from Kowalski and Saumon (2006), Allard and Kielkopf (2009), and Saumon et al. (2014) showed that the Ly α line can be collision-broadened into the blue part of the optical, and that this broadening is caused mostly by H₂ molecular collisions. However, there are still discrepancies between the modelling of Ly α plus the rest of the white dwarf continuum compared to observations (see Chapter 4, Section 4.2.1).

In this chapter, I present the results of my ongoing analysis of UV spectroscopy from the STIS and COS (Cosmic Origins Spectrograph) spectrographs onboard *HST* of white dwarfs within 13 pc of the Sun; some of our nearest stellar neighbours. Given their proximity, white dwarfs within 13 pc are the brightest members of their spectral types, providing uniquely high-quality data for atmospheric modelling. The coolest and oldest white dwarfs are faint in the UV, and therefore the closest white dwarfs to the Sun are the only white dwarfs for which UV spectroscopy can be reliably obtained. These UV observations have been supplemented with medium-resolution optical spectroscopy from two VLT spectrographs: X-shooter and the UV and Visual Echelle Spectrograph (UVES),

as well as the ISIS spectrograph on the WHT. I combined the STIS data, which is flux-calibrated up to the 1 per cent level (Bohlin et al., 2019), with optical and IR photometry from *Gaia* DR3 (Gaia Collaboration et al., 2021a), 2MASS (Skrutskie et al., 2006) and WISE (Wright et al., 2010). I then performed spectrophotometric fits from the UV to the IR incorporating the STIS spectra plus the photometry. By fitting multi-wavelength flux-calibrated data across these wavelengths, there is an immediate visual and statistical insight into discrepancies and offsets between the fits to different regions of the white dwarf continuum. The white dwarfs observed with STIS as part of this 13 pc study span a T_{eff} range of 4500 K to 24 000 K, making them some of the coolest white dwarfs that have been fitted spectroscopically in the UV (Saumon et al., 2014). I also performed separate fits to the Balmer lines in the optical spectra to determine independent parameters.

This chapter presents ongoing work, and therefore the full 13 pc sample has not been analysed at the time of writing. All observations are presented in Section 6.2, but only H-atmosphere white dwarf models, fitting and analysis are presented in Sections 6.3–6.5. For the H-atmosphere white dwarfs, I determined two sets of T_{eff} and $\log(g)$ by fitting the optical and IR photometry with and without the inclusion of the STIS spectra, as well as a third set of parameters from fits to the Balmer lines in the optical spectra. I then compared the parameters and visual fits with and without the incorporation of STIS data. The remainder of the ongoing 13 pc work will be discussed in Section 6.6.

6.2 Observations

HST observations of 36 white dwarfs within 13 pc were conducted during Cycle 23 (program 14076; PI Gänsicke), the details of which are displayed in Table 6.1. Twenty-nine targets were observed with the STIS NUV-MAMA G230L grating with the 52x2" aperture, which is optimised for spectrophotometry. Four of the brightest and hottest targets were instead observed with the STIS NUV-MAMA E140M or E230M gratings with the 0.2"x0.2" aperture. Additionally, nine targets were sufficiently hot to be observed with the COS FUV-MAMA G140L, G130M, or G160M gratings. All *HST* spectra were taken between November 2015 and January 2017.

Three of the STIS G230L observations were taken with different setups to limit contamination from a nearby companion star. WD 0208–501 has a 2.1 arcsec separation from a K dwarf GJ86A, and was observed with the 52x0.2" aperture. WD 0426+588 has a 9.0 arcsec separation from an M dwarf (Stein 2051A), and was observed with the 52x0.5" aperture. WD 1132–325 has a 15 arcsec separation from a K dwarf (GJ432A), and was also observed with the 52x0.5" aperture. WD 0727+073 A+B is a white dwarf – white dwarf binary with a separation of 0.66 arcsec. Both stars were positioned along the 52x2" long-

slit, and were later extracted individually. The cool DZ white dwarf WD 2251–070 was not detected with the STIS G230L setup in 3 orbits, which is expected given its properties. Sirius B was observed with the STIS NUV-MAMA E140H and E230H gratings with the 0.2"x0.09" aperture, as part of Cycle 20 in March 2014 (program 12981; PI Lehner). It was also observed with the optical STIS gratings G430L and G750M with the 52x2" aperture in Cycle 19 in January 2013 (program 12606; PI Barstow). Procyon B was observed in Cycle 7 with the STIS CCD G230LB grating (program 7398; PI Shipman), and the spectrum, along with optical *HST* spectra were analysed in Provencal et al. (2002).

Eighteen white dwarfs within 13 pc were observed with the X-Shooter spectrograph on the VLT (Vernet et al., 2011). I reduced the data using the REFLEX pipeline (Freudling et al., 2013), and performed telluric corrections using MOLECFIT (Kausch et al., 2015; Smette et al., 2015). Three white dwarfs were observed with the UVES instrument, also on the VLT, and reduction was carried out using the same procedure. Six white dwarfs within 13 pc were observed with the ISIS instrument on the WHT. All of the WHT ISIS observations were taken on 2016 September 04. *The ISIS spectra were reduced by M. Hollands using a tailored pipeline.*

13 pc white dwarfs without HST UV observations

A handful of white dwarfs within the 13 pc volume were not observed as part of the *HST* program – in part because the STIS observations pre-date *Gaia* DR2, and following the *Gaia* data releases there were some newly discovered nearby white dwarfs, or parallaxes were improved and updated. Additionally some white dwarfs in unfavourable binary configurations were not observed with *HST*. These are listed alongside the other 13 pc white dwarfs in binary systems in Table 6.2.

G203–47 – 7.60 pc: This system is a post-common envelope binary (PCEB) with an M-dwarf and white dwarf in a 15-day orbit (Delfosse et al., 1999). It has the second longest orbital period for a PCEB candidate with an M dwarf. The system will be observed by *HST* STIS in my upcoming program (program 17778; PI O’Brien).

WD J215140.11+591734.85 – 8.46 pc: This white dwarf was discovered by *Gaia* and has not yet been observed in the UV with *HST*.

WD 0738–172 – 9.15 pc: This white dwarf has a late-M dwarf companion at 27 arcsec separation. An International Ultraviolet Explorer (IUE) spectrum was analysed by Zeidler-K. T. et al. (1986).

WDJ 081227.07–352943.32 – 11.17 pc: This white dwarf was discovered by *Gaia* and has not yet been observed in the UV with *HST*.

WD 1630+089 – 12.93 pc: The pre-*Gaia* parallax placed this DA white dwarf outside of 13 pc, but it is actually just within that volume, and has not yet been observed in the UV.

| WD name | Alt. name | Distance (pc) | STIS UV Grating | COS UV Grating | Optical Observation or SpT Citation |
|----------|------------------------|---------------|-----------------|----------------|-------------------------------------|
| 0642-166 | Sirius B | 2.67 | E230H/E140H | - | Barstow et al. (2015) |
| 0736+053 | Procyon B | 3.51 | G230LB | - | Provencal et al. (2002) |
| 0046+051 | van Maanen 2 | 4.31 | G230L | - | VLT/X-shooter |
| 1142-645 | LAWD 37 | 4.64 | G230L | G140L | VLT/X-shooter |
| 0413-077 | 40 Eri B | 5.01 | E230M/E140M | - | VLT/X-shooter |
| 0426+588 | Stein 2051 B | 5.52 | G230L | G140L | Giammichele et al. (2012) |
| 1748+708 | G 240-72 | 6.21 | G230L | - | WHT/ISIS |
| 0552-041 | LP 658-2 | 6.44 | G230L | - | VLT/X-shooter |
| 0553+053 | G 99-47 | 8.12 | G230L | - | VLT/X-shooter |
| 0752-676 | L 97-12 | 8.17 | G230L | - | VLT/X-shooter |
| 2359-434 | GJ 915 | 8.33 | G230L | - | VLT/X-shooter |
| 1334+039 | Wolf 489 | 8.35 | G230L | - | VLT/X-shooter |
| 2150+591 | WDJ215140.11+591734.85 | 8.46 | - | - | Tremblay et al. (2020) |
| 0839-327 | GJ 318 | 8.52 | G230L | G140L | VLT/X-shooter |
| 2251-070 | LP 701-29 | 8.54 | - | - | VLT/X-shooter |
| 0038-226 | LHS 1126 | 9.10 | G230L | - | VLT/X-shooter |
| 0738-172 | LAWD 25 | 9.15 | - | - | Giammichele et al. (2012) |
| 0435-088 | LHS 194 | 9.40 | G230L | - | VLT/X-shooter |
| 1132-325 | 20 Crt B | 9.56 | G230L | - | Giammichele et al. (2012) |
| 0141-675 | L 88-59 | 9.72 | G230L | - | VLT/X-shooter |
| 0912+536 | G 195-19 | 10.27 | G230L | G140L | Giammichele et al. (2012) |
| 0310-688 | LB 3303 | 10.40 | E230M/E140M | - | VLT/X-shooter |
| 1202-232 | LP 852-7 | 10.43 | G230L | G140L | VLT/X-shooter |
| 1917-077 | LDS 678 A | 10.51 | E230M | G130M/G160M | VLT/X-shooter |

Table 6.1: Details of all spectroscopic observations of white dwarfs within 13 pc that have been analysed in this work. Optical spectroscopy used for fitting in this work is also listed. Distances were determined using *Gaia* parallaxes in all cases except where indicated by ‡, which were instead taken from van Alena et al. (1995).

| WD name | Alt. name | Distance (pc) | STIS UV Grating | COS UV Grating | Optical Observation or SpT Citation |
|--------------|------------------------|---------------|-----------------|----------------|-------------------------------------|
| 0821-669 | SCR 0821-6703 | 10.68 | G230L | - | Subasavage et al. (2007) |
| 0208-510 | HD 13445B | 10.80 | G230L | - | Farihi et al. (2013) |
| 0245+541 | LHS 1446 | 10.87 | G230L | - | Zuckerman et al. (2003) |
| 0009+501 | LHS 1038 | 10.87 | G230L | - | WHT/ISIS |
| 1647+591 | G 226-29 | 10.95 | - | G130M/G160M | WHT/ISIS |
| 2140+207 | LHS 3703 | 11.04 | G230L | G140L | Koester et al. (2001) |
| ‡ 0727+482 A | G 107-70A | 11.10 | G230L | - | Bergeron et al. (2001) |
| ‡ 0727+482 B | G 107-70B | 11.10 | G230L | - | Bergeron et al. (2001) |
| 0810-353 | WDJ081227.07-352943.32 | 11.17 | - | - | Landstreet et al. (2023) |
| 0548-001 | G 99-37 | 11.22 | G230L | - | VLT/X-shooter |
| 1953-011 | LHS 3501 | 11.57 | G230L | - | VLT/UVES |
| 1345+238 | LP 380-5 | 11.86 | G230L | - | Koester et al. (2001) |
| 1917+386 | G 125-3 | 11.87 | G230L | - | WHT/ISIS |
| 1055-072 | LHS 2333 | 12.27 | G230L | - | VLT/X-shooter |
| 0135-052 | L 870-2 | 12.62 | G230L | - | VLT/UVES |
| 1900+705 | GW+70 8247 | 12.88 | G230L | G140L | WHT/ISIS |
| 1620-391 | CD-38 10980 | 12.91 | E230M/E140M | - | VLT/UVES |
| 1630+089 | WDJ163233.17+085122.67 | 12.93 | - | - | Subasavage et al. (2007) |

Table 6.1: (continued). Details of all spectroscopic observations of white dwarfs within 13 pc that have been analysed in this work. Optical spectroscopy used for fitting in this work is also listed. Distances were determined using *Gaia* parallaxes in all cases except where indicated by ‡, which were instead taken from van Alstena et al. (1995).

| Star 1 | Star 1 | Star 2 | Star 2 | Star 3 | Star 3 | Star 4 | Star 4 | Star 4 | Projected |
|-----------------|--------|--------------|--------|------------|--------|------------|--------|--------------|-----------------|
| Name | SpT | Name | SpT | Name | SpT | Name | SpT | Name | Separation [au] |
| Sirius A | A0 | Sirius B | DA | - | - | - | - | - | 20 |
| Procyon A | F5 | Procyon B | DQZ | - | - | - | - | - | 15 |
| 40 Eri A | K1 | 40 Eri B | DA | 40 Eri C | M4.5 | - | - | - | 42; 417 |
| Stein 2051 A | M4 | Stein 2051 B | DC | - | - | - | - | - | 57 |
| G 203-47 A | M3.5 | G 203-47 B | WD: | - | - | - | - | - | 0.05 |
| WD0839-327 A | DA | WD0839-327 B | WD: | - | - | - | - | - | - |
| IRAS 21500+5903 | M3 | WD2150+591 | DAH | - | - | - | - | - | 124 |
| LP 783-2 | M6.5 | WD0738-172 | DZA | - | - | - | - | - | 186 |
| GJ 432 A | K0 | GJ 432 B | DC | - | - | - | - | - | 146 |
| L 923-22 | M5 | WD 1917-077 | DBQA | - | - | - | - | - | 285 |
| GJ 86 A | K1.5 | GJ 86 B | DQ | - | - | - | - | - | 28 |
| WD0727+482 A | DA | WD0727+482 A | DA | G 107-69 A | M4.5 | G 107-69 B | dM/BD: | 0.5; 8; 1161 | |
| GJ 1179 A | M5 | GJ 1179 B | DC | - | - | - | - | - | 2231 |
| WD0135-052 A | DA | WD0135-052 B | DA | - | - | - | - | - | 0.03 |
| HD 147513 | G5 | WD1620-391 | DA | - | - | - | - | - | 4454 |

Table 6.2: Details of all white dwarfs within 13 pc of the Sun that are part of a multiple-star system. Projected separations were calculated in most cases using *Gaia* DR3 data, aside from those binaries that are unresolved in *Gaia*. A colon symbol indicates that the spectral type of the star has not been confirmed. For higher-order systems (triple or quadruple) the periods separated by semicolons are the innermost to outermost periods for the hierarchical system.

6.3 Model atmospheres and fitting

The coolest white dwarfs within 13 pc have almost no flux in the STIS G230L band except for at the reddest end. When fitted in isolation with atmosphere models, these cool STIS spectra do not provide meaningful white dwarf parameters. Additional optical and IR photometry is required to constrain their parameters. For this reason, I decided to employ a universal hybrid fitting method, where STIS spectra, together with *Gaia* DR3 G , G_{BP} , G_{RP} , 2MASS J , H , K_s and WISE $W1$, $W2$ photometry were combined into a hybrid spectrophotometric fit to obtain atmospheric parameters including T_{eff} and $\log(g)$. This method constrains the parameters of the coolest members of the sample well, and the fit was not weighted in favour of any particular dataset. The STIS spectra are flux-calibrated at the 1–2 per cent level (Elms et al., 2024), and *Gaia* DR3 G , G_{BP} , G_{RP} , and 2MASS J , H , K_s and WISE $W1$, $W2$ photometry are also well flux-calibrated. This flux calibration enables a precise full continuum fit. I elected not to incorporate Pan-STARRS *grizy* and SDSS *ugriz* optical photometry in the fits, because many of the 13 pc white dwarfs were bright enough to saturate in some of the Pan-STARRS and SDSS filters. Additionally, *Gaia* has proven to be as precise as Pan-STARRS and SDSS for local white dwarfs (O’Brien et al., 2024).

I expanded on the fitting routine presented in Sahu et al. (2023). The STIS E140M and E230M observations initially suffered from echelle order ripples, which I corrected using the STISBLAZEFIX package from Baer et al. (2018) before fitting. Prior to fitting, I also convolved the STIS spectrum with the appropriate line spread function for a given grating, using LINETOOLS. Reddening was fixed at zero, due to the proximity of all white dwarfs in this sample. To obtain the radius and mass, I applied the evolutionary sequences of Bédard et al. (2020), for white dwarfs with thick or thin layers of hydrogen in their atmosphere, depending on the individual composition of each star. The parallax of each star was fixed to the *Gaia* DR3 parallax value during the fit. I assumed distance to be the inverse of the parallax, which is appropriate for these sources as their *Gaia* `parallax_over_error` > 1800, and therefore they have a negligible measurement error (Bailer-Jones, 2015). Reduced χ^2 least-squares fitting was applied to return the best solution for the white dwarf parameters T_{eff} and $\log(g)$, where the data were compared to a variety of state-of-the-art model spectra (Koester, 2010; Tremblay et al., 2013a). Filter response functions and zeropoint fluxes for fitting photometry were taken from the Spanish Virtual Observatory (SVO) Filter Profile Service (Rodrigo et al., 2012; Rodrigo and Solano, 2020). The SVO zeropoints were derived using `alpha_lyr_stis_010.fits`¹ as the Vega reference spectrum for $\lambda < 1\mu\text{m}$, and `alpha_lyr_stis_011.fits`² for $\lambda > 1\mu\text{m}$.

An interstellar dust cloud along the line of sight of the white dwarf produces narrow

¹https://archive.stsci.edu/hlsps/reference-atlases/cdb/calspec/alpha_lyr_stis_010.fits

²https://archive.stsci.edu/hlsps/reference-atlases/cdb/calspec/alpha_lyr_stis_011.fits

absorption lines. The STIS E140M/H and E230M/H gratings have a high enough resolution that the narrow photospheric and interstellar lines are resolved. Some common photospheric metal lines such as Si II at 1265 Å cannot be interstellar in origin, so all lines with the same radial velocity as the Si II 1265 Å line must be photospheric in origin, whereas all other metal lines have a different radial velocity, which is that of the interstellar cloud in the line of sight of the star. Before continuum and photospheric absorption lines can be fitted, any interstellar lines must be identified and masked. Interstellar lines and their corresponding radial velocities for the five white dwarfs with high-resolution STIS spectra are shown in Table 6.3. The lines were identified and then fitted with a Gaussian using a least squares fitting method, or in the case of the two dust cloud components in WD0642–166 (Sirius B), two Gaussians. The regions around the ISM lines were then masked from the spectra.

I used updated 3D local thermodynamic equilibrium (LTE) H-atmosphere model spectra from Tremblay et al. (2013a, 2015), with line profiles from Tremblay and Bergeron (2009) and additional H₂ molecular lines, to fit Ly α and the continuum from the UV spectra and optical and IR photometry of pure-H atmosphere white dwarfs. H₂ molecular lines have only been incorporated in the models below 1800 Å, and therefore were only used when fitting high-resolution COS spectra. These grids of model spectra span $T_{\text{eff}} = 1500 - 40\,000$ K, and $\log(g) = 7.0 - 9.0$ in steps of 0.5 dex. LTE models are appropriate for fitting the white dwarfs in this sample because they are below 40 000 K, and non-LTE effects only become significant above that temperature. For the mass-radius relation, I used the thick H-layer option from Bédard et al. (2020), $q_{\text{H}} = M_{\text{H}}/M_{\text{WD}} = 10^{-4}$. For the spectrophotometric fits, I masked any photospheric metal lines in the H-atmosphere white dwarfs because they were sufficiently narrow enough not to affect the shape of the continuum.

Where more than one Balmer line was visible in the optical spectrum, these were independently fitted using a PYTHON implementation of a fitting code that was created as part of the 4MOST white dwarf fitting pipeline 4MOST_WDpipe³. For these fits, I used pure-H 1D LTE models from Tremblay et al. (2011a) with 3D corrections from Tremblay et al. (2013a). I did not fit the Balmer lines and photometry simultaneously, as there is a well-known offset of ≈ 2 per cent between photometric and spectroscopic T_{eff} solutions for DA white dwarfs that is present when fitting different homogeneous spectroscopic data sets and photometric data sets (Genest-Beaulieu and Bergeron, 2019; Tremblay et al., 2019a, 2020; Cukanovaite et al., 2021; O’Brien et al., 2023). For the two unresolved double white dwarf systems in the 13 pc sample, I fitted Balmer lines from UVES spectroscopy from the SPY survey (Napiwotzki et al., 2020) to determine the parameters of both components of the system. I used the code WD-BASS⁴ to fit the Balmer lines (Munday et al., 2024), where

³https://github.com/NPGFusillo/4MOST_WDpipe

⁴<https://zenodo.org/records/11188044>

the same updated Tremblay et al. (2013a, 2015) models were used for fitting.

6.4 Results

The best-fit parameters for the H-atmosphere 13 pc white dwarfs, determined using the fitting methods outlined in Section 6.3, are presented in Table 6.4. I fitted STIS spectra alongside *Gaia* DR3 G , G_{BP} , G_{RP} , 2MASS J , H , K_s and WISE $W1$, $W2$ photometry, where available. I fitted the data twice for most white dwarfs, once including the STIS spectrum, labelled as ‘with UV’ in Table 6.4, and once without it, labelled as ‘without UV’ in Table 6.4. Additional independent parameters determined from fits to the Balmer lines of DA white dwarfs are also presented in Table 6.4.

6.4.1 Spectrophotometric fits incorporating UV

Figures 6.1 and 6.2 show the best-fit models for two different fits of H-atmosphere white dwarfs: one including STIS spectra plus optical and IR photometry (blue models), and another for just optical and IR photometry (red models). The STIS spectra and photometry are shown in Fig. 6.1 in grey, and low-resolution *Gaia* XP spectra are also displayed on all plots in grey. *Gaia* XP spectra are well-flux calibrated so provide a visual insight into the performance of the models, but are noisy at the bluest and reddest ends, and as such I chose to fit *Gaia* photometry instead (which is partially derived from *Gaia* XP spectra), and therefore the *Gaia* XP spectra were not incorporated into the hybrid fit. In almost all cases, there is a visual discrepancy between the two best-fit models. For some of the coolest spectra, the best-fit models with and without STIS appear practically on top of each other, as the STIS flux is minimal and does not significantly affect the overall fit to the SED.

Hybrid fits to the components of the resolved binary WD 0727+482 A+B are shown in Fig. 6.3. This system has no *Gaia* photometry, but Bergeron et al. (2001) observed the system in *BVRI* bands, which I incorporated into the fits. Three 13 pc H-atmosphere white dwarfs did not have STIS spectra available, so I fitted just their photometry, which is shown in Fig. 6.4. For WD 0642–166 (Sirius B), all photometry was at least partially contaminated, so the fit presented in Fig. 6.5 is just to the suboptimally flux-calibrated STIS E140H spectra. The fit to the COS spectrum of the DAV WD 1647+591 is shown in Fig. 6.6. This star was not observed with STIS so I did not attempt a hybrid fitting method, and instead fitted the detailed molecular hydrogen lines visible in the high-resolution COS spectrum.

| WD name | Metal species | Vacuum wavelengths (\AA) | ISM line velocities (km s^{-1}) |
|-----------------------|-----------------------|------------------------------------------------|------------------------------------------------|
| WD0310–688 | Si II | 1260.42, 1526.71 | 6.898, 6.877 |
| | O I | 1302.17 | 6.677 |
| | Fe II | 2344.21, 2382.76, 2600.17 | 4.588, 5.628, 5.115 |
| | Mg II | 2796.35, 2803.53 | 6.823, 6.778 |
| WD0413–077 | Si II | 1260.42, 1304.37, 1526.71 | 16.102, 18.847, 18.659 |
| | O I | 1302.17 | 17.497 |
| | C II | 1334.53 | 15.882 |
| | Fe II | 2382.76, 2586.67, 2600.17 | 18.336, 20.471, 17.336 |
| | Mg II | 2796.35, 2803.53 | 16.257, 17.044 |
| WD0642–166 Cloud 1 | Si II | 1190.42, 1193.29, 1260.42, 1304.37, 1526.71 | 14.355, 12.813, 12.535 14.250, 14.339 |
| | N I | 1199.55, 1200.22 | 15.245, 12.739 |
| | O I | 1302.17 | 12.202 |
| | C II | 1334.53 | 12.063 |
| | Mg II | 2796.35, 2803.53 | 13.148, 13.515 |
| | WD0642–166 Cloud 2 | Si II | 1190.42, 1193.29, 1260.42, 1304.37, 1526.71 |
| N I | | 1199.55, 1200.22, 1200.71 | 19.994, 19.233 |
| O I | | 1302.17 | 19.109 |
| C II | | 1334.53 | 20.600 |
| Mg II | | 2796.35, 2803.53 | 19.473, 19.503 |
| WD1620–391 | Si II | 1190.42, 1193.29, 1260.42, 1304.37, 1526.71 | –28.206, –28.138, –27.900, –25.972, –26.702 |
| | N I | 1199.55, 1200.22 | –28.241, –28.225, –27.465 |
| | S II | 1253.81, 1259.52 | –25.823, –25.944 |
| | O I | 1302.17 | –26.476 |
| | C II | 1334.53 | –27.249 |
| | Fe II | 2344.21, 2374.46, 2382.76, 2586.67, 2600.17 | –28.023, –28.344, –28.342, –28.786, –28.091 |
| | Mg II | 2796.35, 2803.53 | –28.342, –27.227 |
| WD1917–077 | Si II | 1526.71 | –31.344, –30.435 |
| | Fe II | 2344.21, 2374.46, 2382.76, 2586.67, 2600.17 | –31.476, –29.859, –30.607 –29.829, –30.858 |
| | Mg II | 2796.35, 2803.53 | –31.344, –30.435 |

Table 6.3: Radial velocities of interstellar lines observed in high-resolution *HST* spectra of 13 pc white dwarfs.

| WD name | SpT | T_{eff} [K] (with UV) | $\log(g)$ (with UV) | T_{eff} [K] (without UV) | $\log(g)$ (without UV) | T_{eff} [K] (Balmer) | $\log(g)$ (Balmer) |
|--------------|------------|--------------------------------|---------------------|-----------------------------------|------------------------|-------------------------------|-----------------------------|
| 0009+501 | DAH | 6837 (5) | 8.365 (0.004) | 6704 (34) | 8.326 (0.013) | 6529 (62) | 8.35 (0.08) |
| 0135-052.1 | DA (DD) | - | - | - | - | 7422 ($^{+966}_{-392}$) | 7.65 ($^{+0.76}_{-0.09}$) |
| 0135-052.2 | DA (DD) | - | - | - | - | 7204 ($^{+127}_{-5486}$) | 7.88 ($^{+0.40}_{-0.18}$) |
| 0141-675 | DAZ | 6704 (2) | 8.145 (0.003) | 6444 (25) | 8.021 (0.010) | 6414 (8) | 7.877 (0.018) |
| 0245+541 | DAZ | 5026 (2) | 8.102 (0.003) | 5070 (46) | 8.133 (0.032) | - | - |
| 0310-688 | DAZ | 15 683 (4) | 8.031 (0.004) | 16 449 (160) | 8.135 (0.011) | 16 205 (12) | 8.12 (0.003) |
| * 0413-077 | DA | 16 328 (8) | 7.900 (0.001) | 16 697 (339) | 7.964 (0.026) | 16 959 (10) | 7.981 (0.002) |
| 0553+053 | DAH | 6111 (3) | 8.346 (0.004) | 5826 (31) | 8.213 (0.014) | - | - |
| § 0642-166 | DA | 25 599 (21) | 8.960 (0.006) | - | - | 25 762 (106) | 8.723 (0.025) |
| ‡ 0727+482 A | DA | 52001(111) | 8.2 (0.2) | 4870 (60) | 7.89 (0.05) | - | - |
| ‡ 0727+482 B | DA | 4863 (84) | 8.1 (0.2) | 4850 (60) | 8.10 (0.04) | - | - |
| 0752-676 | DA | 5750 (2) | 8.028 (0.002) | 5690 (16) | 8.000 (0.009) | 5763 (7) | 8.33 (0.01) |
| 0810-353 | DAH | - | - | 6502 (46) | 8.285 (0.020) | - | - |
| * 0821-669 | DA | 4865 (6) | 7.982 (0.005) | 4831 (31) | 7.957 (0.025) | - | - |
| 0839-327.1 | DA (DD) | - | - | - | - | 9853 ($^{+49}_{-59}$) | 7.89 ($^{+0.02}_{-0.04}$) |
| 0839-327.2 | DC(?) (DD) | - | - | - | - | 5019 ($^{+107}_{-16}$) | 8 (fixed) |
| 1202-232 | DAZ | 9009 (4) | 8.146 (0.002) | 8539 (70) | 7.972 (0.022) | 8637 (4) | 7.911 (0.006) |
| * 1334+039 | DA | 4908 (4) | 7.886 (0.004) | 4896 (20) | 7.876 (0.020) | - | - |
| 1345+238 | DC | 4693 (10) | 7.874 (0.008) | 4697 (67) | 7.877 (0.051) | - | - |
| 1620-391 | DAZ | 23 238 (25) | 7.935 (0.003) | 25 011 (528) | 8.071 (0.032) | 24 651 (26) | 8.2 (0.1) |
| 1630+089 | DA | - | - | 5650 (16) | 8.065 (0.009) | - | - |
| § 1647+591 | DAV | 12 410 (20) | 8.32 (0.02) | - | - | 12 283 (35) | 8.324 (0.009) |
| 1953-011 | DAH | 8380 (8) | 8.399 (0.004) | 8000 (74) | 8.242 (0.021) | 7688 (28) | 8.2 (0.1) |
| * 2150+591 | DAH | - | - | 5128 (22) | 8.024 (0.016) | - | - |
| 2359-434 | DA | 8939 (7) | 8.529 (0.003) | 8682 (70) | 8.429 (0.016) | 8383 (5) | 8.265 (0.005) |

Table 6.4: Best-fit parameters for H-atmosphere white dwarfs within 13 pc of the Sun. A fit with UV refers to hybrid spectrophotometric parameters for white dwarfs observed with *HST* STIS or COS. DD indicates unresolved double degenerate. Symbols indicate the photometry used for the fit. No symbol indicates *Gaia*, 2MASS and WISE. * indicates *Gaia* and 2MASS. † indicates *Gaia* only. ‡ indicates *BVRI* + 2MASS photometry. § indicates no photometry was used in the fit. Any metal features were masked for these fits.

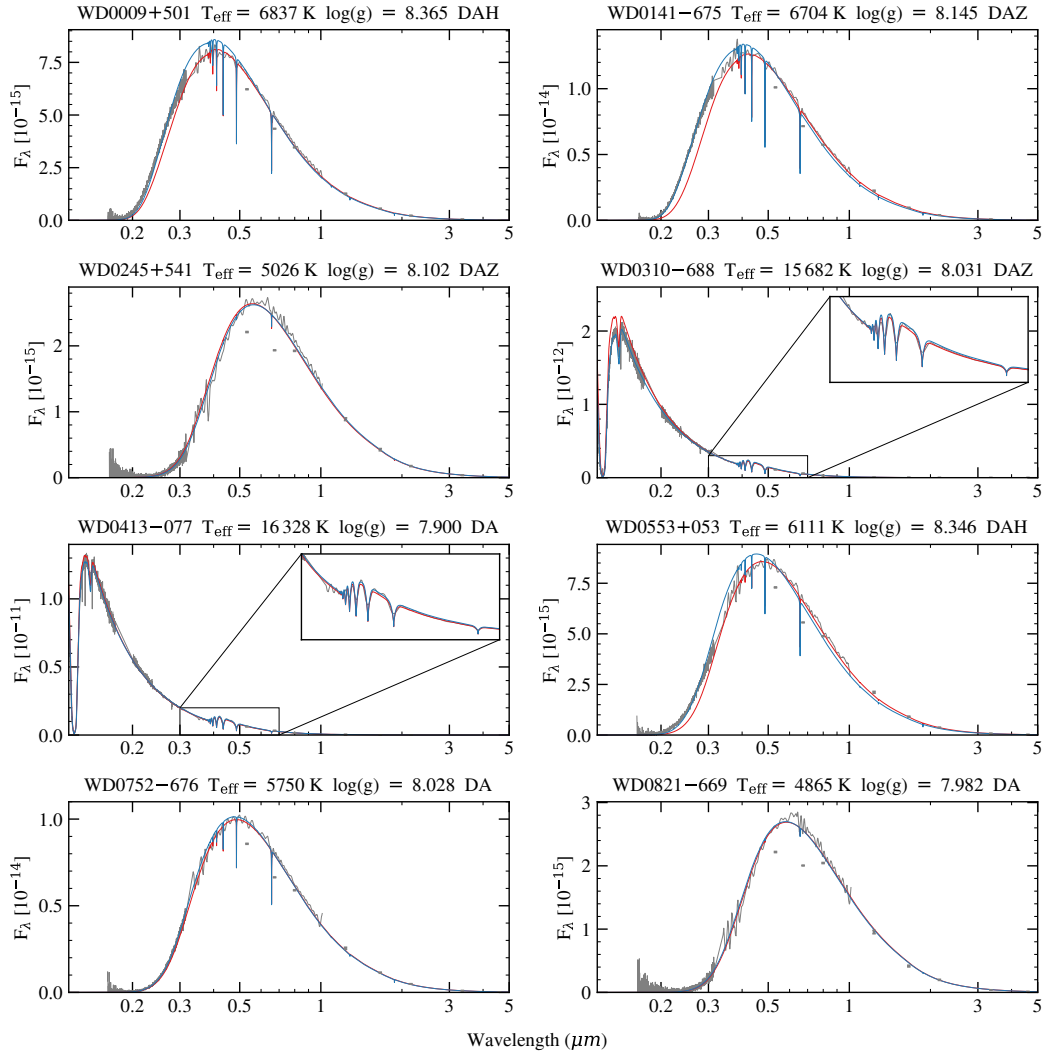


Figure 6.1: Hybrid spectrophotometric fits of H-atmosphere white dwarfs in the 13 pc sample. Flux is given in units of $\text{erg cm}^{-2} \text{s}^{-1} \text{\AA}^{-1}$. The blue models are best fits to STIS spectra plus *Gaia*, 2MASS, and WISE photometry, where available. The red models are the fits to just the *Gaia*, 2MASS, and WISE photometry, where available. All parameters in this figure are from the fits to STIS plus photometry (blue models).

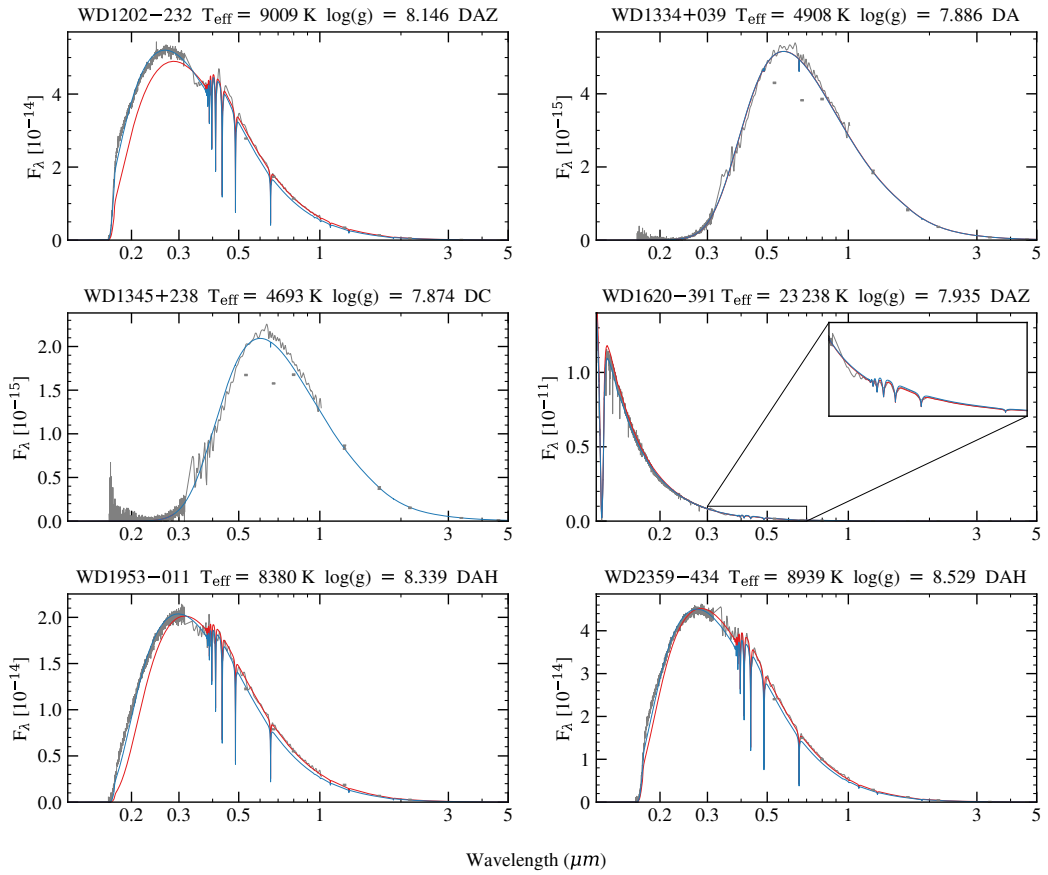


Figure 6.2: Hybrid spectrophotometric fits of H-atmosphere white dwarfs in the 13 pc sample. Flux is given in units of $\text{erg cm}^{-2} \text{s}^{-1} \text{\AA}^{-1}$. The blue models are best fits to STIS spectra plus *Gaia*, 2MASS, and WISE photometry, where available. The red models are the fits to just the *Gaia*, 2MASS, and WISE photometry, where available. All parameters in this figure are from the fits to STIS plus photometry (blue models).

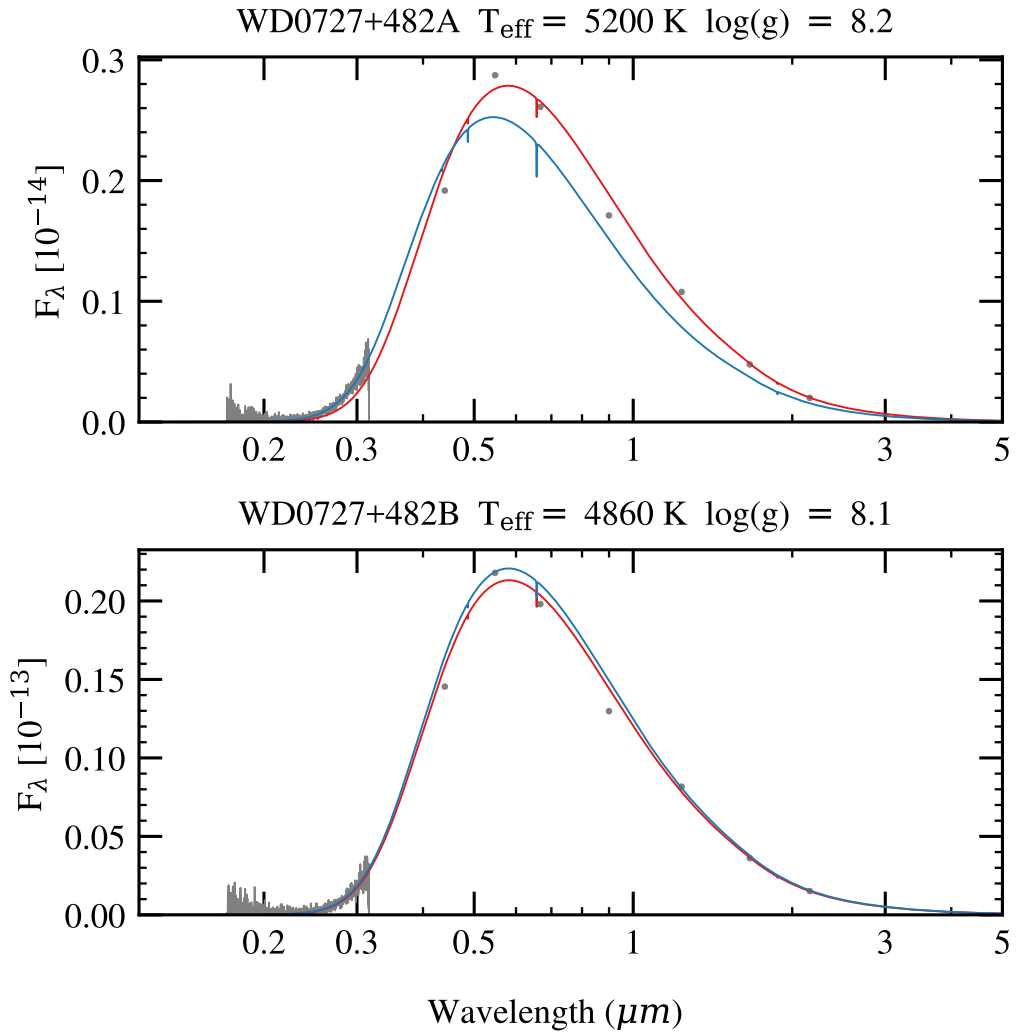


Figure 6.3: Hybrid spectrophotometric fits to spectra and photometry of the wide DA + DA system WD 0727+482 A+B. Flux is given in units of $\text{erg cm}^{-2} \text{s}^{-1} \text{\AA}^{-1}$. Reliable *Gaia* photometry is not available for these stars so archive *BVRI* optical photometry are used in the fit instead. The blue models are best fits to STIS spectra plus *BVRI* and 2MASS photometry. The red models are the fits to just the photometry. All parameters in this figure are from the fits to STIS plus photometry (blue models).

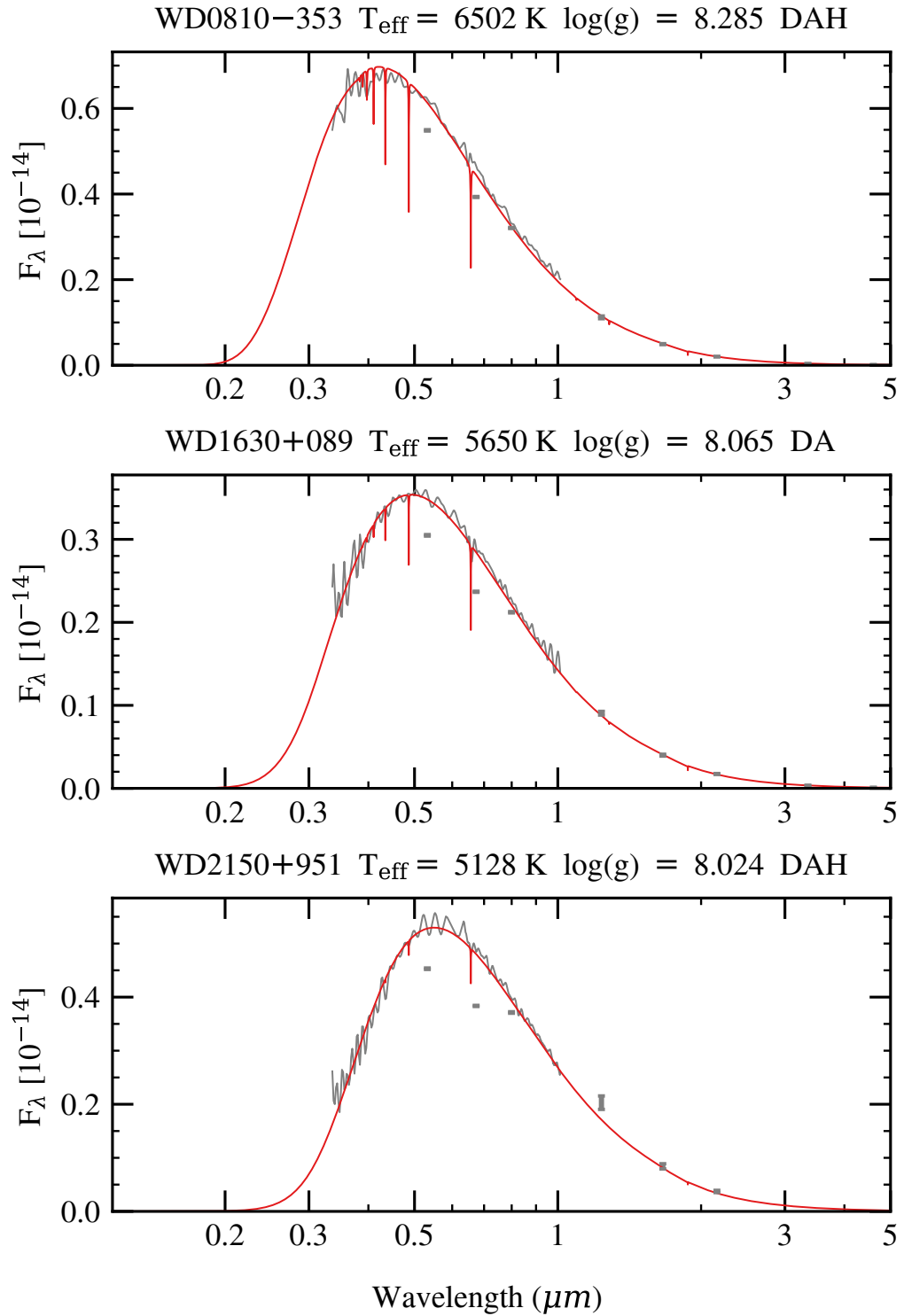


Figure 6.4: Fits to photometry DA white dwarfs within 13 pc for which no STIS spectra are available. Flux is given in units of $\text{erg cm}^{-2} \text{s}^{-1} \text{\AA}^{-1}$. The red models show the fits to the photometry.

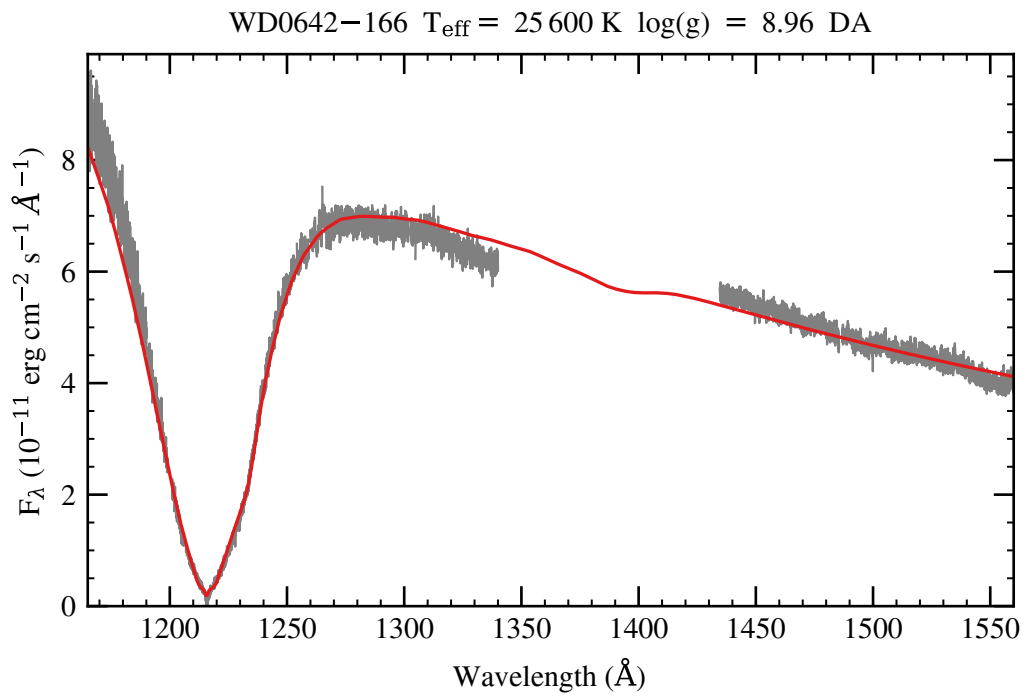


Figure 6.5: Fit of the STIS E140H spectra of WD 0642-166 with Tremblay et al. (2013a) models, no additional photometry is available to further constrain the fit. All interstellar lines were masked in the fit and are not shown in the plot. An instrumental defect at 1486 \AA was also masked.

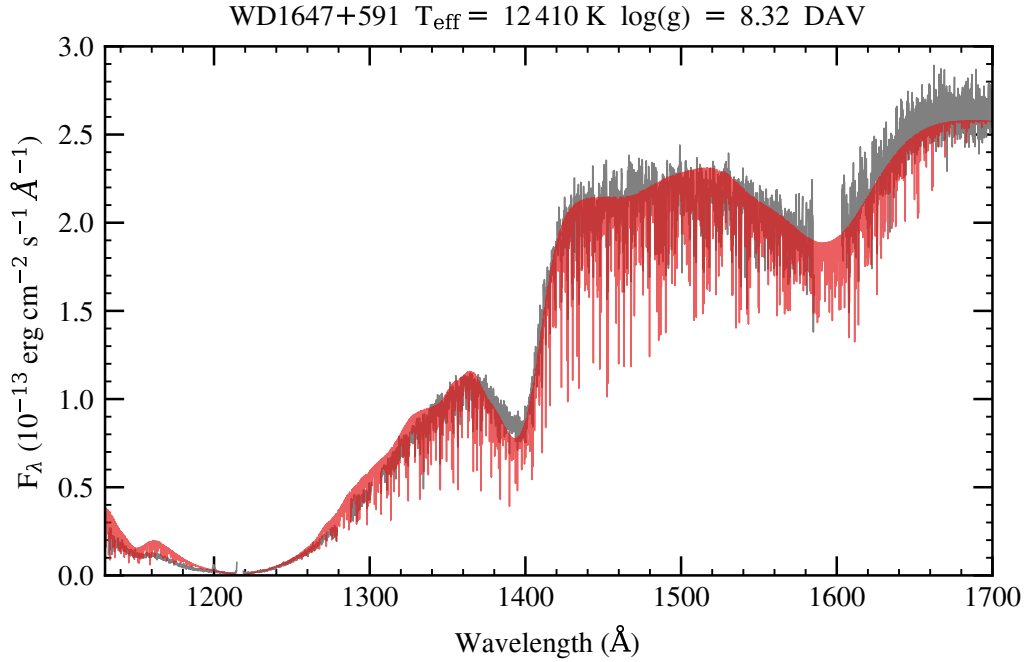


Figure 6.6: Fit of the COS G130M and G160M spectra of WD 1647+591 with Tremblay et al. (2013a) models with additional H_2 molecular lines.

6.4.2 Fits to Balmer lines

Fits to the Balmer lines of single DA white dwarfs from optical spectroscopy are shown in Figs. 6.7 and 6.8. These fits provide an extra set of parameters for single DA white dwarfs in Table 6.4. There are known discrepancies between photometric and spectroscopic fits of DA white dwarfs (see Chapter 3; Section 3.5.4), and this issue will therefore not be discussed further in this chapter.

Fits to the Balmer lines of unresolved double white dwarfs are shown in Fig. 6.9. Typically, photometry is incorporated into Balmer line fits of unresolved double-degenerates in order to reduce the degeneracy of the fit. For the double-lined system, WD 0135–052, the fit with photometry incorporated was very poor, so I chose instead to adopt a purely spectroscopic fit for the parameters in Table 6.4 and the fits in Fig. 6.9, therefore increasing the uncertainty on the best-fit parameters. Napiwotzki et al. (2020) were unable to fit WD 0135–052 and obtain reliable parameters. The best-fit parameters for WD 0135–052 were determined from the combined fits to both UVES spectra shown in Fig. 6.9.

I determined a $\log(g)$ of 7.526 ± 0.002 when the Balmer lines of the single-lined system WD 0839–327 were fitted with a single DA white dwarf model, suggesting an unseen degenerate companion. Therefore I fitted the spectra with a two white dwarf model,

both DA+DA and DA+DC since the composition of the companion is not determinable. I incorporated 2MASS photometry into the fit, and fixed the $\log(g)$ of the unseen companion at 8. Both DA+DA and DA+DC model fits are shown in Fig. 6.9. In Table 6.4, I provide the best-fit parameters of both components of the double-degenerate systems. Table 6.4 shows the DA+DC solution for WD 0839–327. The DA+DA solution is less well-constraining: $T_{\text{eff}} = 10\,228 \left(\begin{smallmatrix} +29 \\ -3189 \end{smallmatrix} \right)$ K and $\log(g) = 7.62 \left(\begin{smallmatrix} +0.01 \\ -0.07 \end{smallmatrix} \right)$ for the visible component, and $T_{\text{eff}} = 8302 \left(\begin{smallmatrix} +3689 \\ -51 \end{smallmatrix} \right)$ K with $\log(g)$ fixed at 8 for the secondary.

6.5 Discussion

Saumon et al. (2014) analysed white dwarfs cooler than 6000 K with STIS observations to test the effect of the Ly α red wing opacity in white dwarf models. They generated photometric-style datapoints by binning the STIS spectra, before fitting them in combination with optical and IR photometry. They compared optical and IR photometric fits to STIS, optical and IR fits, and concluded that their parameters agreed within uncertainties and there was no systematic offset. They also found that incorporating STIS data into their fits halved the T_{eff} uncertainty. The parallaxes used by Saumon et al. (2014) were ten times less precise than the more recent *Gaia* parallaxes.

The analysis of Saumon et al. (2014) differs to my analysis due to their binning of the STIS spectra. This binning meant that the weight of the STIS spectra was similar to the weight of the photometry in their overall fit. I chose not to bin the 13 pc STIS spectra prior to fitting, as my goal is different to that of Saumon et al. (2014). Rather than trying to get the best unbiased parameters from a full UV-to-IR fit, as they have done, I am comparing UV fits to optical plus IR fits. However, I needed to include the optical and IR photometry in the STIS fit in order to constrain the shape of the spectral energy distribution for the coolest white dwarfs with minimal STIS flux, so I adopted this approach universally, for consistency. Therefore, the two fits I provide in this work are largely independent, as the hybrid STIS plus optical plus IR fit is highly dominated by the fit to the hundreds of precise STIS flux points.

Table 6.4 indicates a discrepancy between the fundamental parameters T_{eff} and $\log(g)$ determined by hybrid fitting incorporating STIS UV data compared to fitting solely optical and IR data. This discrepancy is displayed in Fig. 6.10 for both T_{eff} and $\log(g)$. For $T_{\text{eff}} < 10\,000$ K, the hybrid T_{eff} and $\log(g)$ values are systematically larger than the photometric T_{eff} and $\log(g)$ values by up to 6 per cent. This discrepancy is smaller for the lowest T_{eff} members of the sample, because at these temperatures the STIS spectrum has minimal flux and therefore does not provide much new information for the fit. Figs. 6.1 and 6.2 demonstrate that neither the UV-dominated fits nor the optical plus IR fits are a

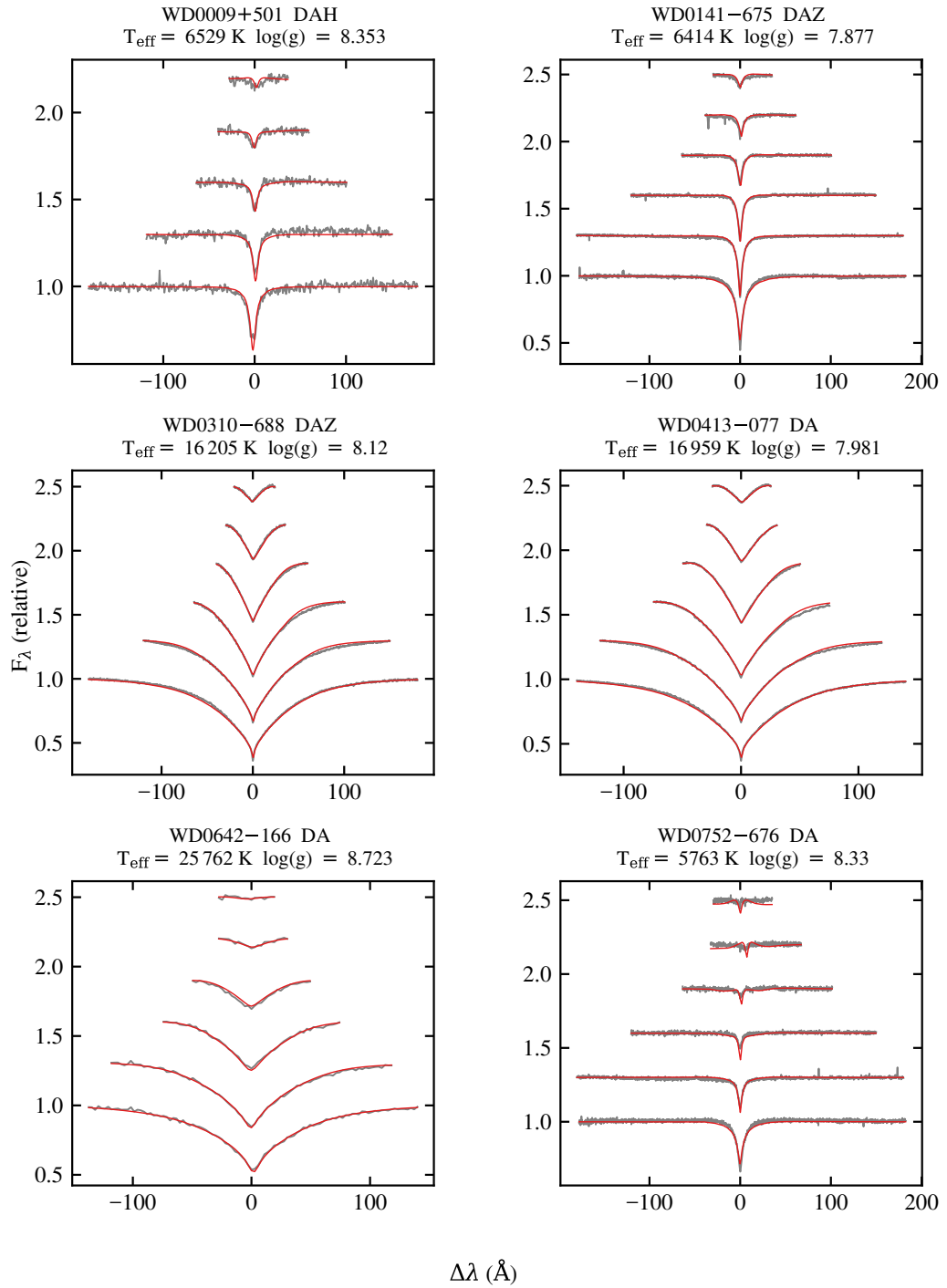


Figure 6.7: Fits of Balmer lines for white dwarfs the 13 pc sample. Flux is given in units of $\text{erg cm}^{-2} \text{s}^{-1} \text{\AA}^{-1}$.

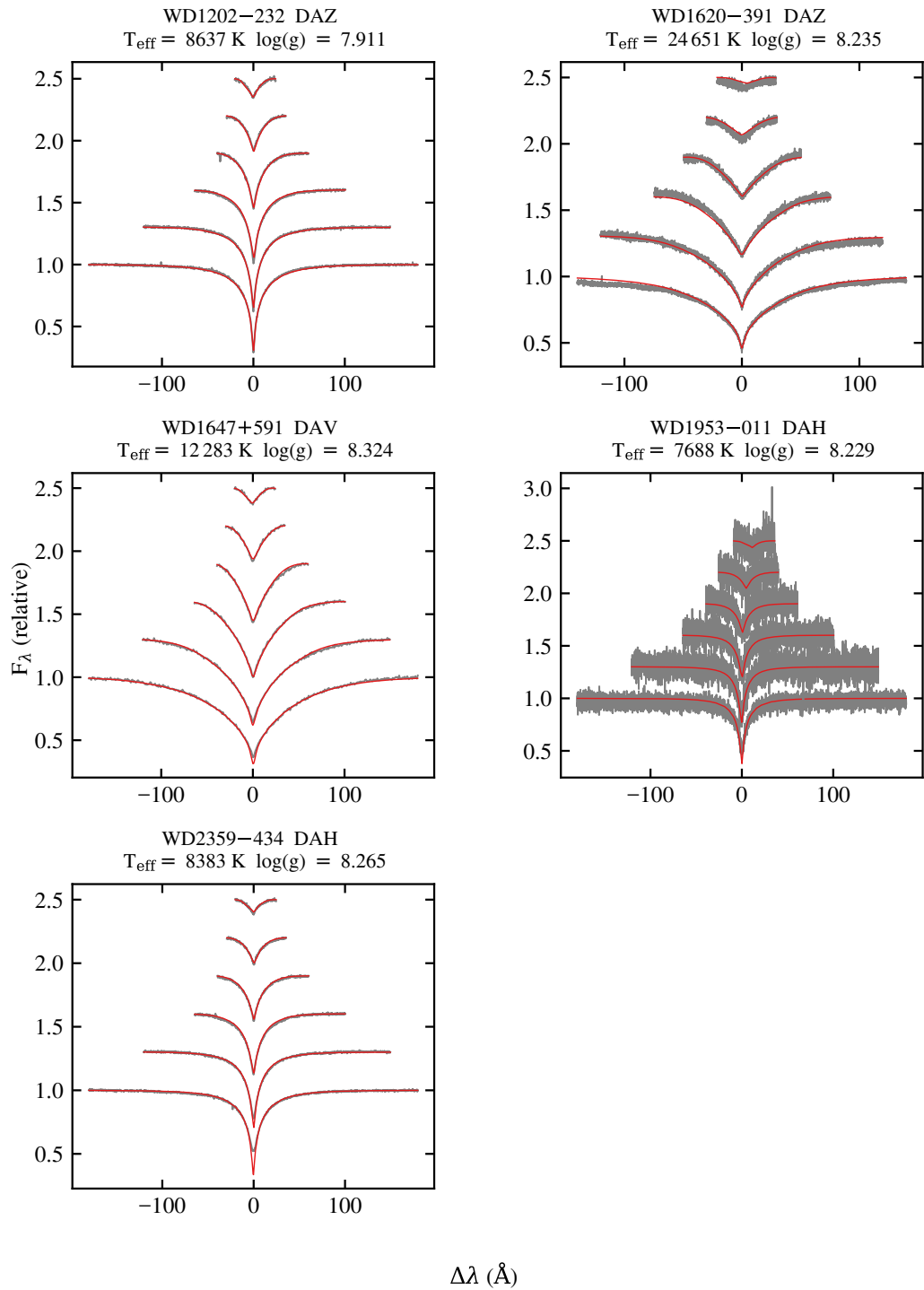


Figure 6.8: Fits of Balmer lines for white dwarfs the 13 pc sample. Flux is given in units of $\text{erg cm}^{-2} \text{s}^{-1} \text{\AA}^{-1}$.

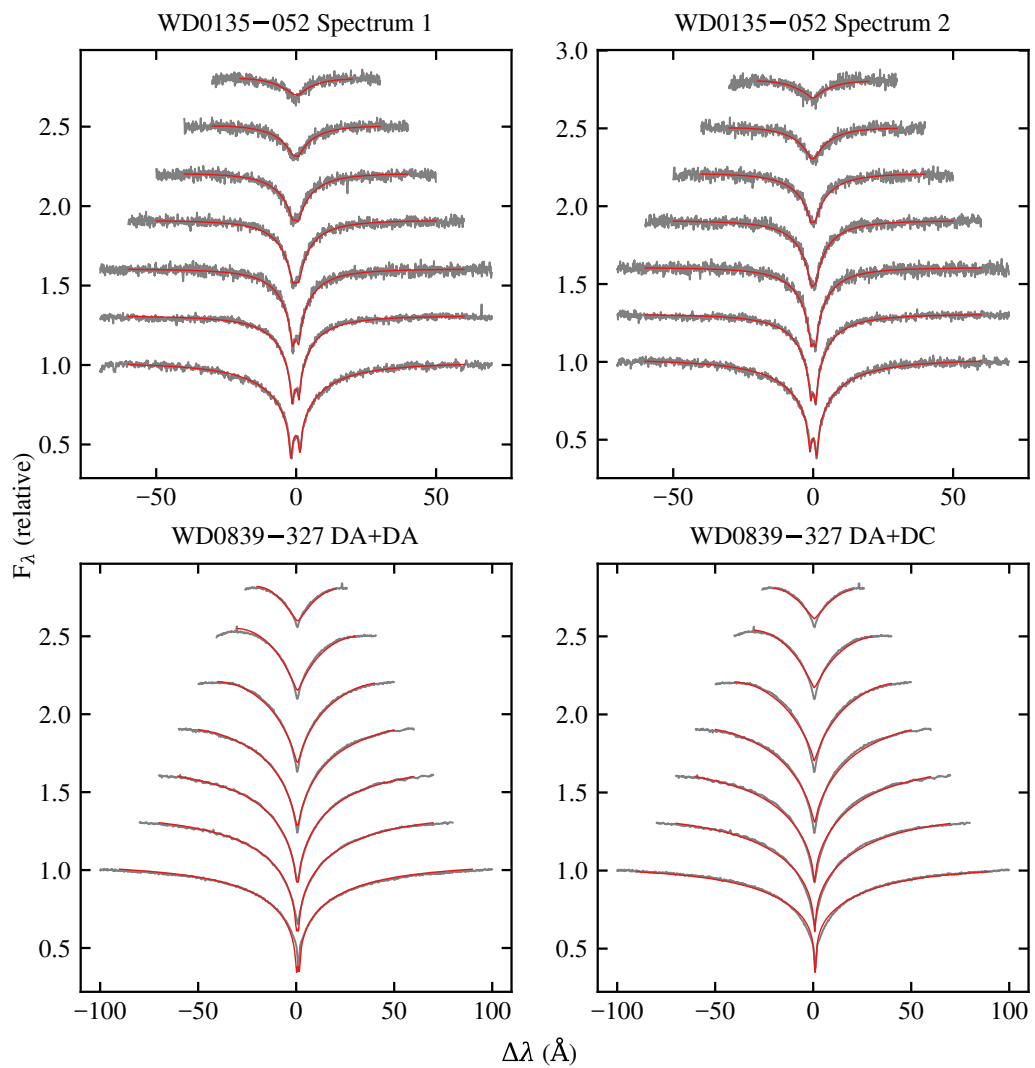


Figure 6.9: Fits of Balmer lines for unresolved double white dwarfs in the 13 pc sample. Flux is given in units of $\text{erg cm}^{-2} \text{s}^{-1} \text{\AA}^{-1}$.

good visual match across all wavelengths. The additional precision of *Gaia* photometry has enabled further reductions to the magnitudes of the T_{eff} and $\log(g)$ uncertainties compared to those presented in Saumon et al. (2014). The three hottest DA white dwarfs in the sample have smaller hybrid T_{eff} values than photometric, which is not a systematic effect and is likely due to their high-resolution STIS echelle spectra not being reliably flux-calibrated.

When models are fitted to optical and IR photometry of cool white dwarfs, their masses tend to be under-predicted, in what is known as the low-mass problem (see Chapter 4; Section 4.2.1). The T_{eff} dependence of the discrepancies between the fits with and without STIS data does not correlate with the T_{eff} dependence of the low-mass problem, and therefore the UV vs optical discrepancy is likely not to be linked to the low-mass issue. Therefore this discrepancy is a separate issue that warrants further investigation.

6.6 Future work

Completing the remainder of the 13 pc project requires generating tailored models for white dwarfs of many different spectral types. The primary goal of the project is to uncover discrepancies in fits to optical and UV data, therefore identifying improvements that need to be made to atmosphere models. Additionally, the STIS spectra show metal features in some of the white dwarfs that seemingly had pure H or He atmospheres given their optical spectra alone, enabling more precise modelling of their atmospheres.

DC white dwarfs have featureless spectra across all wavelengths, so constraining their atmospheric composition is challenging. Many DC white dwarfs have He-dominated atmospheres, and adding trace hydrogen or carbon to the models may improve the fit to the data. Adding trace H at a composition of $\log(\text{H}/\text{He}) = -5$ reproduces the *Gaia* HR diagram B branch well (Bergeron et al., 2019). Likewise, trace C can also reproduce the B branch (Camisassa et al., 2023; Blouin et al., 2023a). With the full UV-to-IR spectral energy distribution of 13 pc DC white dwarfs, I will test the impact of adding these trace elements to the models and see whether they produce a significantly better fit.

To fit DQ white dwarfs with detectable carbon features in their atmospheres, He-rich models with C must be used. To do this, I have written a code that is based on a fitting method for DQs that has been used for many decades (Bergeron et al., 1997; Dufour et al., 2005; Blouin and Dufour, 2019; Coutu et al., 2019). In brief, the photometry and spectral features are fitted independently in order to constrain the three free parameters, T_{eff} , $\log(g)$, and $\log(\text{C}/\text{He})$. The procedure is as follows:

1. Fix to a starting $\log(\text{C}/\text{He})$, and perform a hybrid fit to the STIS spectrum plus the optical and IR photometry. Mask any strong carbon lines in the STIS spectrum prior to

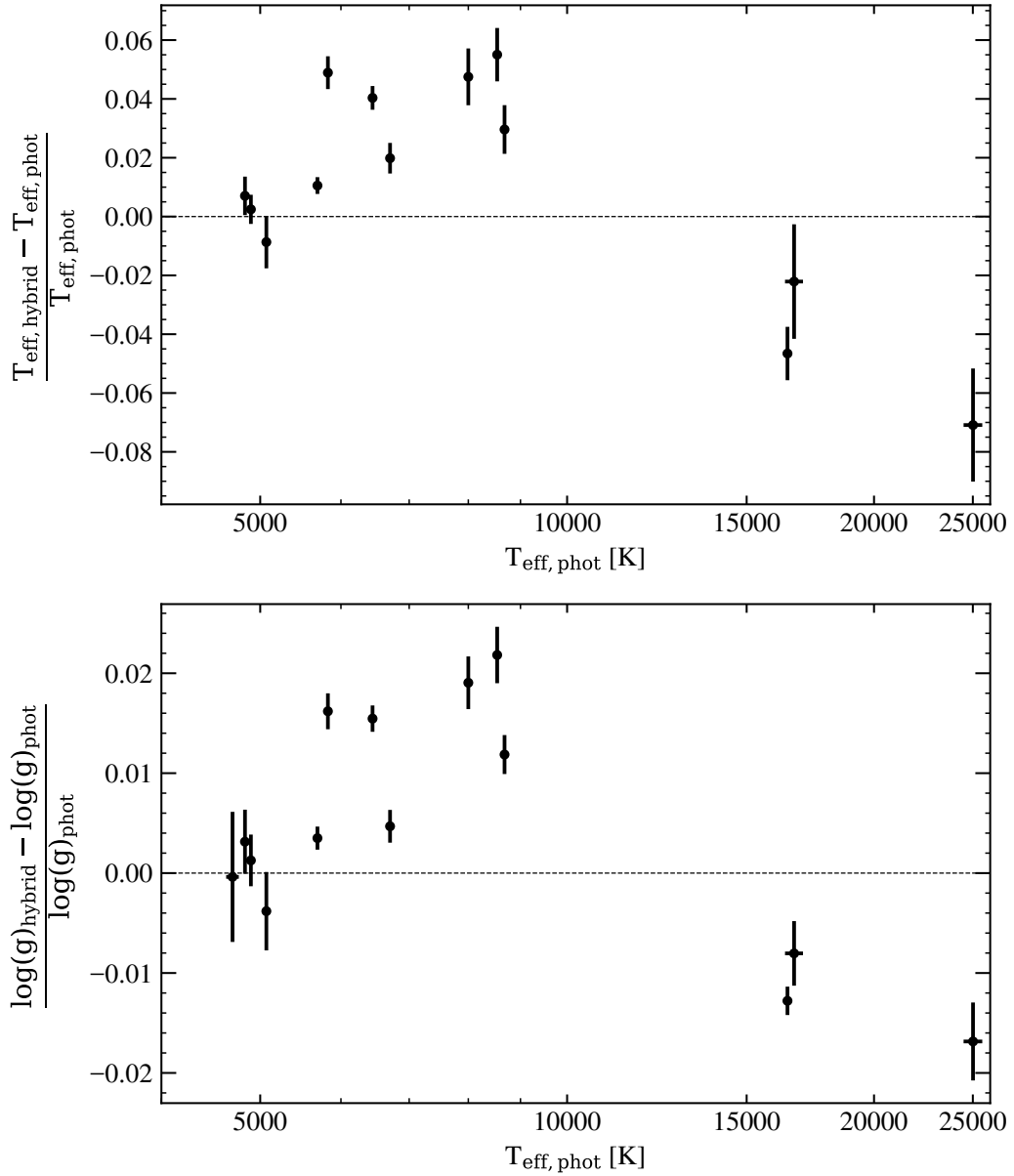


Figure 6.10: Comparisons of parameters for H-atmosphere white dwarfs. Top panel: The T_{eff} derived from the photometric (phot) optical and IR only fit, compared to the T_{eff} derived from the hybrid STIS, optical and IR fit. Bottom panel: The $\log(g)$ derived from the photometric optical and IR only fit, compared to the $\log(g)$ derived from the hybrid STIS, optical and IR fit.

fitting, instead using the STIS spectrum to constrain the shape of the SED. Determine T_{eff} and $\log(g)$ from this fit.

2. Fix the T_{eff} and $\log(g)$ from the initial fit, and fit the carbon lines in the optical spectrum to determine $\log(\text{C}/\text{He})$.
3. Generate new models with the new $\log(\text{C}/\text{He})$ and again fit the spectrophotometric data to determine T_{eff} and $\log(g)$.
4. Repeat these steps until convergence.

Additional atomic carbon features in the STIS spectra will be fitted independently because preliminary tests show that the models cannot reproduce both the optical molecular carbon features and the UV atomic carbon features. I will use DQ models with trace H to determine whether the fit to carbon lines can be improved, which adds another free parameter to the models. Additionally, there is a DBQA white dwarf within 13 pc that I will also fit with He + C + H models.

The metal lines in both H-rich and He-rich white dwarfs will be fitted in order to constrain the composition of the planetary material that was accreted by the white dwarfs. Metal lines in H-rich white dwarf spectra do not substantially alter the shape of the SED, meaning they could be masked for fitting with pure H models. Fitting the individual lines is more simple in the H-rich case. In He-rich atmospheres, metal lines drastically change the shape of the spectral energy distribution, and therefore an iterative procedure is required in order to constrain the T_{eff} , $\log(g)$, and metal abundances. This procedure works similarly to the DQ procedure, but is more complex as more elements must be incorporated into the models.

Two of the white dwarfs in the 13 pc sample, WD1748+708 and WD1900+705, are very strongly magnetic, with fields of 300 and 200 MG respectively. The strong magnetic fields cause the spectral features of both white dwarfs to become distorted and blended, therefore making it challenging not only to fit the spectra but to identify the atmospheric composition of the stars. With state-of-the-art magnetic models, Hardy et al. (2023b) could not fit the spectrum of WD1900+705. The spectral type of WD1748+708 has not been constrained beyond possibly being a magnetic DB or DQ. With the models I have available, there is limited meaningful analysis that can be done on these spectra.

Chapter 7

Summary and Outlook

7.1 Conclusions

In this thesis, I have presented observations and analysis of white dwarfs in the local stellar neighbourhood. These white dwarfs are the brightest members of their spectral classes, and many have only recently been identified by the *Gaia* satellite. This thesis is primarily focused on volume-limited samples of white dwarfs, namely the *Gaia*-identified 40 pc and 13 pc samples. The 40 pc sample (Chapters 3 and 4) is the largest volume-complete sample of white dwarfs with optical medium-resolution spectroscopic follow-up. The 13 pc sample (Chapter 6) is the largest volume-complete sample of white dwarfs with UV spectroscopic follow-up from *HST*. The individual characterisation of interesting systems in these samples is also important, and as such, I present a detailed analysis of two highly metal-polluted white dwarfs in Chapter 5 that were identified as part of the 40 pc sample.

Gaia DR3 provided reliable parallaxes for stars, therefore enabling the creation of catalogues of hundreds of thousands of white dwarf candidates (Gentile Fusillo et al., 2021), just over a thousand of which are within 40 pc of the Sun. Many of these 40 pc candidates in the northern hemisphere were followed up spectroscopically by Tremblay et al. (2020), and in Chapter 3 I led the analysis of a similar follow-up program of 40 pc white dwarf candidates in the southern hemisphere. These 248 new white dwarfs drastically improved the spectroscopic completeness of the 40 pc sample to > 97 per cent. In Chapter 3 I classified the spectral types of these 248 white dwarfs, and determined their atmospheric compositions and parameters including effective temperature and surface gravity. I showed, using our sub-sample of VLT X-shooter spectra that a higher spectral resolution reveals a greater fraction of magnetic, polluted, and carbon-atmosphere white dwarfs. I also identified a systematic difference in effective temperatures determined by fitting photometry and spectroscopy of pure-hydrogen atmosphere white dwarfs. I identified in this new sample a warm DQ with

a carbon-dominated atmosphere and oxygen features, three rare DQZ white dwarfs, and a highly-magnetic DZH white dwarf which has since been followed up and analysed by Vennes et al. (2024).

Following the classification and analysis of the new 40 pc white dwarf spectra in Chapter 3, I analysed the full, complete, 40 pc sample in Chapter 4. The sample, following a few additional spectroscopic observations, contains 1078 confirmed white dwarfs out of the 1083 candidates from Gentile Fusillo et al. (2021), with three confirmed main sequence stars contaminating the sample, meaning only two candidates remain unobserved due to unfavourable configurations with nearby bright stars. The rapid early cooling of white dwarfs means that most of the white dwarfs within 40 pc are cool, and therefore their parameters are affected by the now well-known low-mass issue where models under-predict cool white dwarf masses. In order to perform meaningful statistics on the parameters of the sample, I designed an ad-hoc correction to the masses and effective temperatures of cool white dwarfs, such that their median mass remained constant as they cooled. I found that there is no clear evidence of spectral evolution in the 40 pc observations of cool white dwarfs, contrary to prior studies such as Bergeron et al. (1997, 2001). I performed a comprehensive search for stellar companions to all the 40 pc white dwarfs, and found that 209 multiple-star systems containing at least one white dwarf were within 40 pc. Most of these systems were identified by *Gaia* proper motions, but some were also found to be candidate spectroscopic binaries or white dwarfs with low enough masses that they must be part of binary systems. All results agreed with Toonen et al. (2017) simulations aside from the number of wide (resolved by *Gaia*) double white dwarf systems, of which I found a factor of ten fewer than predicted: 119–167 predicted compared to 15 observed. Additionally, similarly to Bagnulo and Landstreet (2022), I found that the typical-mass magnetic white dwarfs in 40 pc seem to become magnetic as they age, and that there is a separate population of massive magnetic white dwarfs.

Chapter 5 presents a detailed analysis of two helium-atmosphere white dwarfs with high levels of metal pollution. These are some of the most polluted white dwarfs within 40 pc, but there had not yet been dedicated studies to infer the composition of the planetary material that was accreted by them. The helium-dominated composition of their atmospheres and cool temperatures made it challenging to disentangle what sort of material was accreted and if accretion was ongoing. A lack of IR excess at both systems did not rule out ongoing accretion, as currently available data from 2MASS, WISE and *Spitzer* was not sensitive enough to detect an accretion disc. I chose to adopt an accretion model in which a single disruption event produces a disc that is not replenished and decays over time as material is accreted onto the white dwarf surface (Jura et al., 2009). Using this model, I devised a method to compare the composition of the accreted material to that of typical solar system

bodies including chondrites, stony-iron meteorites, and the Earth’s crust. I allowed the time since the accretion event began and the characteristic disc lifetime to vary as two free parameters in the Jura et al. (2009) model and produced reduced χ^2 contour plots with the two free parameters. I found that the parameters were somewhat degenerate, but that the best-matching scenario for both white dwarfs is that they are each accreting a body with a chondritic or bulk-Earth composition, with a mass between that of a small moon or dwarf planet, and the accretion event in both cases was likely to have begun a few Myr ago. This newly-developed analysis method should be applied to a wider range of systems to test if the exponentially decaying disc model provides different or better conclusions than the standard constant accretion rate model.

Optical spectroscopy of white dwarfs provides many vital insights into atmospheric compositions and parameters. However, additional UV spectroscopy can unveil new characteristics including extra metal lines, carbon bands, and other unexpected features. In Chapter 6, I presented some ongoing work on the analysis of a volume-complete sample of white dwarfs within 13 pc which have both UV spectra and medium-resolution optical spectra. Despite the mere tens of stars in this small sample, it is the largest volume-complete white dwarf sample with UV spectroscopic follow-up. Most of the UV spectra were taken with the *HST* STIS G230L grating, which is well flux-calibrated. I adopted a ‘hybrid’ fitting method for the H-atmosphere white dwarfs within 13 pc, which involved fitting the STIS spectrum plus *Gaia*, 2MASS and WISE photometry together. I identified that there was an offset in the parameters from fitting cool white dwarfs with and without UV data, and that no current models can reliably fit the entire UV-to-IR spectral energy distribution.

7.2 Future work

***HST* observations of local white dwarf + M dwarf close binaries**

When a white dwarf and a main sequence star are in a binary system with separations less than ≈ 0.07 au, they will have undergone a common envelope phase during the evolution of the white dwarf progenitor (Zorotovic et al., 2011). Systems like these are therefore known as post-common envelope binaries (PCEBs). The only missing members of the large and complete volume samples of white dwarfs are the white dwarfs that are hidden in PCEBs. These white dwarfs are difficult to identify, even when they are nearby, as the main-sequence star completely outshines the white dwarf in optical photometry. Most PCEBs are not eclipsing systems, and the identification of a white dwarf companion is therefore challenging; white dwarfs with effective $T_{\text{eff}} < 6500$ K would be invisible in the optical. However, flux from the cool white dwarf in a PCEB begins to dominate over its companion at UV wavelengths.

PCEB systems containing M dwarfs, which make up the majority of main-sequence stars, should produce a UV excess in their photometry compared to single M dwarfs, however significant numbers of M dwarfs display a photometric near-UV excess resulting from chromospheric activity of the M dwarf or even from background galaxies (Lagos et al., 2022), and therefore UV photometry alone cannot be used to identify hidden white dwarf companions to M dwarfs in PCEBs. Fitting just one or two UV photometry points also cannot constrain parameters of any white dwarf companion. Bar et al. (2017) demonstrated that the combination of UV photometry and optical spectroscopy also struggles to successfully identify white dwarfs in PCEBs with M dwarfs. Candidate non-eclipsing PCEBs have been discovered serendipitously through radial velocity surveys searching for M dwarfs hosting exoplanets (e.g. Baroch et al. 2021). When a high-mass companion to an M dwarf is detected that is not observable in the optical, a white dwarf is theorised to be the companion. However, the companion mass is not well constrained from the radial velocity measurements, as the inclinations of the systems are not known. PCEBs have orbital periods on the order of hours or a few days, which are too short to be resolved using *Gaia* astrometry.

Based on limited observational data of binary systems, and using population models, Toonen et al. (2017) predict that there should only be 0.5–1.6 white dwarf plus M dwarf (WD + dM) binaries within 20 pc that have separations less than ≈ 5 au. However, these models are calibrated against the limited currently observed population, and previous estimates predict larger numbers within this volume (Holberg et al., 2013). I am leading an upcoming *HST* Cycle 32 program which will observe the white dwarfs in the three most nearby candidate PCEBs using near-UV STIS gratings (program 17778; PI O’Brien). These observations will be taken in late 2025 – mid-2026. Confirming the existence of these three local ‘missing’ white dwarfs will result in a more complete 20 pc white dwarf sample, which currently has 147 confirmed single and binary white dwarfs. These detections will also provide a vital constraint on the numbers of these systems within larger volumes, i.e. within the benchmark 40 pc white dwarf sample. If four close WD + dM systems are confirmed to be within 20 pc (the Cycle 32 targets plus Wolf 1130), this would scale with volume such that ≈ 30 close WD + dM systems should be within 40 pc. Studies of the 40 pc volume indicate that there are of the order 50 white dwarfs missing compared to simulations, and our observations would disentangle if this discrepancy is caused by missing close WD + dM binaries or issues with predicting Galactic scale height or the Sun’s position above the Galactic plane in simulations (O’Brien et al., 2024).

The ages of the PCEB systems determined from these observations will provide better constraints for population models on stellar formation history and initial mass ratios in binaries (Toonen et al., 2017). Constraining the space density of white dwarfs in compact binaries also impacts the gravitational wave background predictions for LISA (Korol et al.,

2022). Additionally, determining the fraction of binaries in the local volume that have undergone a common envelope phase will put constraints on the outcome of close binary evolution, given that the common envelope phase is usually approximated in models as it is not well understood (Ivanova et al., 2013).

MOS surveys and volume samples

The recent advances led by *Gaia* have provided many answers in the field of white dwarf physics, but the tremendous amounts of data have also provided many new questions that need to be answered. Multi-object spectroscopic (MOS) data releases are on the horizon, providing many tens of thousands of new optical white dwarf spectra to classify, analyse, and interpret. The advantages of both *Gaia* data and MOS surveys are twofold: they provide us with large samples to determine meaningful statistics of white dwarfs, and uncover new and interesting individual objects that require detailed analytical follow-up. The MOS surveys that will observe white dwarfs include WEAVE (Dalton et al., 2020), 4MOST (de Jong et al., 2019), SDSS-V (Kollmeier et al., 2017), and DESI (Cooper et al., 2023).

The DESI Early Data Release has already identified over 1500 new white dwarfs which had no previous spectroscopic classification, and it was found that DESI is less skewed to blue and hot white dwarfs, enabling its larger data releases to be more complete than SDSS (Manser et al., 2024). Such large surveys will enable us to identify new white dwarf classifications where previously only a prototype or a few members of that class were known. For example, a group of 21 DAHe white dwarfs which show emission features in their Zeeman-split Balmer lines have been identified in the DESI data (Manser et al., 2023).

The 100 pc *Gaia* white dwarf sample is the next milestone post-40 pc, and Kilic et al. (2020b, 2025) have already obtained spectroscopic follow-up for 86 per cent of 100 pc white dwarfs hotter than 5000 K that are within the SDSS footprint. The completeness of the 100 pc sample will grow following the data releases of DESI, WEAVE and 4MOST. At 100 pc, some of the very coolest and faintest white dwarfs may be too faint and therefore missed. Given the time it will take for MOS surveys to cover the whole sky, and that some of the oldest white dwarfs will be missed beyond 40 pc, the 40 pc sample will remain as a benchmark sample for statistical analysis of white dwarfs despite the advances of the MOS surveys. However, the 40 pc cutoff does remove some key white dwarf systems such as the closest cataclysmic variable system at 45 pc, and the closest super-Chandrasekhar double white dwarf system at 49 pc (Munday et al., 2025).

With *HST* recently celebrating its 35th birthday, the amount of time left to obtain high-quality UV spectra of white dwarfs is limited, until a replacement flagship UV instrument is launched. Therefore the currently available UV spectra of white dwarfs are limited in quantity, and as such the 13 pc UV sample is a valuable and important tool for studying optical and UV white dwarf parameters across all ages and spectral types. The MOS surveys

will not cover UV wavelengths so the small 13 pc sample provides vital constraints on cool white dwarf models.

Bibliography

- W. S. Adams. *PASP*, 26(155):198, 1914.
- R. Ahumada, C. A. Prieto, A. Almeida, F. Anders, S. F. Anderson, et al. *ApJ, Supplement*, 249(1):3, 2020.
- N. F. Allard and J. F. Kielkopf. *A&A*, 493(3):1155–1160, 2009.
- N. F. Allard, J. F. Kielkopf, S. Blouin, P. Dufour, F. X. Gadéa, T. Leininger, and G. Guillon. *A&A*, 619:A152, 2018.
- C. Allègre, G. Manhès, and E. Lewin. *Earth and Planetary Science Letters*, 185(1-2):49–69, 2001.
- L. G. Althaus and O. G. Benvenuto. *ApJ*, 477(1):313–334, 1997.
- L. G. Althaus, M. M. Miller Bertolami, and A. H. Córscico. *A&A*, 557:A19, 2013.
- J. J. Andrews, M. A. Agüeros, A. Gianninas, M. Kilic, S. Dhital, and S. F. Anderson. *ApJ*, 815(1):63, 2015.
- K. Apps, R. L. Smart, and R. Silvotti. *Research Notes of the American Astronomical Society*, 5(10):229, 2021.
- M Baer, C. R. Proffitt, and S. A. Lockwood. Instrument Science Report STIS 2018-1, 13 pages, 2018.
- S. Bagnulo and J. D. Landstreet. *A&A*, 618:A113, 2018.
- S. Bagnulo and J. D. Landstreet. *A&A*, 630:A65, 2019.
- S. Bagnulo and J. D. Landstreet. *A&A*, 643:A134, 2020.
- S. Bagnulo and J. D. Landstreet. *MNRAS*, 507(4):5902–5951, 2021.
- S. Bagnulo and J. D. Landstreet. *ApJ, Letters*, 935(1):L12, 2022.

- S. Bagnulo, J. Farihi, J. D. Landstreet, and C. P. Folsom. *ApJ Letters*, 963(1):L22, 2024a.
- S. Bagnulo, J. D. Landstreet, J. Farihi, C. P. Folsom, M. A. Hollands, and L. Fossati. *A&A*, 688:L14, 2024b.
- C. A. L. Bailer-Jones. *PASP*, 127(956):994, 2015.
- I. Bar, P. Vreeswijk, A. Gal-Yam, E. O. Ofek, and G. Nelemans. *ApJ*, 850(1):34, 2017.
- D. Baroch, J. C. Morales, I. Ribas, V. J. S. Béjar, S. Reffert, et al. *A&A*, 653:A49, 2021.
- M. A. Barstow, S. Jordan, D. O’Donoghue, M. R. Burleigh, R. Napiwotzki, and M. K. Harrop-Allin. *MNRAS*, 277(3):971–985, 1995.
- M. A. Barstow, H. E. Bond, M. R. Burleigh, S. L. Casewell, J. Farihi, J. B. Holberg, and I. Hubeny. In P. Dufour, P. Bergeron, and G. Fontaine, editors, *19th European Workshop on White Dwarfs*, volume 493 of *Astronomical Society of the Pacific Conference Series*, page 307, 2015.
- A. Bédard. *Astrophysics and Space Science*, 369(4):43, 2024.
- A. Bédard, P. Bergeron, and G. Fontaine. *AJ*, 848(1):11, 2017.
- A. Bédard, P. Bergeron, P. Brassard, and G. Fontaine. *AJ*, 901(2):93, 2020.
- A. Bédard, P. Bergeron, and P. Brassard. *AJ*, 930(1):8, 2022a.
- A. Bédard, P. Brassard, P. Bergeron, and S. Blouin. *AJ*, 927(1):128, 2022b.
- A. Bédard, S. Blouin, and S. Cheng. *Nature*, 627(8003):286–288, 2024.
- T. C. Beers, G. W. Preston, S. A. Shectman, S. P. Doinidis, and K. E. Griffin. *AJ*, 103:267, 1992.
- V. Belokurov, Z. Penoyre, S. Oh, G. Iorio, S. Hodgkin, et al. *MNRAS*, 496(2):1922–1940, 2020.
- A. Berdyugin, J. D. Landstreet, S. Bagnulo, V. Piirola, and S. V. Berdyugina. *A&A*, 690:A10, 2024.
- A. V. Berdyugin, V. Piirola, S. Bagnulo, J. D. Landstreet, and S. V. Berdyugina. *A&A*, 657:A105, 2022.
- A. V. Berdyugin, V. Piirola, S. Bagnulo, J. D. Landstreet, and S. V. Berdyugina. *A&A*, 670:A2, 2023.

- P. Bergeron, F. Wesemael, A. Beauchamp, M. A. Wood, R. Lamontagne, G. Fontaine, and J. Liebert. *AJ*, 432:305, 1994.
- P. Bergeron, M. T. Ruiz, and S. K. Leggett. *ApJ, Supplement*, 108(1):339–387, 1997.
- P. Bergeron, S. K. Leggett, and M. T. Ruiz. *ApJ, Supplement*, 133(2):413–449, 2001.
- P. Bergeron, F. Wesemael, Pierre Dufour, A. Beauchamp, C. Hunter, et al. *AJ*, 737(1):28, 2011.
- P. Bergeron, P. Dufour, G. Fontaine, S. Coutu, S. Blouin, C. Genest-Beaulieu, A. Bédard, and B. Rolland. *AJ*, 876(1):67, 2019.
- P. Bergeron, F. Wesemael, G. Fontaine, R. Lamontagne, S. Demers, et al. *AJ*, 162(5):188, 2021.
- P. Bergeron, M. Kilic, S. Blouin, A. Bédard, S. K. Leggett, and W. R. Brown. *AJ*, 934(1):36, 2022.
- F. W. Bessel. *MNRAS*, 6:136–141, 1844.
- S. Blouin. *A&A*, 666:L7, 2022.
- S. Blouin and P. Dufour. *MNRAS*, 490(3):4166–4174, 2019.
- S. Blouin and S. Xu. *MNRAS*, 510(1):1059–1067, 2022.
- S. Blouin, P. M. Kowalski, and P. Dufour. *AJ*, 848(1):36, 2017.
- S. Blouin, P. Dufour, and N. F. Allard. *ApJ*, 863(2):184, 2018a.
- S. Blouin, P. Dufour, N. F. Allard, and M. Kilic. *AJ*, 867(2):161, 2018b.
- S. Blouin, P. Dufour, N. F. Allard, S. Salim, R. M. Rich, and L. V. E. Koopmans. *AJ*, 872(2):188, 2019a.
- S. Blouin, P. Dufour, C. Thibeault, and N. F. Allard. *AJ*, 878(1):63, 2019b.
- S. Blouin, J. Daligault, and D. Saumon. *ApJ, Letters*, 911(1):L5, 2021.
- S. Blouin, A. Bédard, and P.-E. Tremblay. *MNRAS*, 523(3):3363–3375, 2023a.
- S. Blouin, M. Kilic, A. Bédard, and P.-E. Tremblay. *MNRAS*, 525(1):L112–L116, 2023b.
- R. C. Bohlin, S. E. Deustua, and G. de Rosa. *AJ*, 158(5):211, 2019.

- M. Bonavita, C. Fontanive, S. Desidera, V. D’Orazi, A. Zadsurlo, K. Mužić, B. Biller, R. Gratton, D. Mesa, and A. Sozzetti. *MNRAS*, 494(3):3481–3490, 2020.
- A. Bonsor, A. J. Mustill, and M. C. Wyatt. *MNRAS*, 414(2):930–939, 2011.
- B. P. Bowler, W. D. Cochran, M. Endl, K. Franson, T. D. Brandt, et al. *AJ*, 161(3):106, 2021.
- G. P. Briggs, L. Ferrario, C. A. Tout, D. T. Wickramasinghe, and J. R. Hurley. *MNRAS*, 447(2):1713–1723, 2015.
- G. P. Briggs, L. Ferrario, C. A. Tout, and D. T. Wickramasinghe. *MNRAS*, 478(1):899–905, 2018.
- A. Bruch and M. P. Diaz. *AJ*, 116(2):908–916, 1998.
- A. M. Buchan, A. Bonsor, O. Shorttle, J. Wade, J. Harrison, L. Noack, and D. Koester. *MNRAS*, 510(3):3512–3530, 2022.
- R. P. Butler, C. G. Tinney, G. W. Marcy, H. R. A. Jones, A. J. Penny, and K. Apps. *AJ*, 555(1):410–417, 2001.
- M. Camisassa, S. Torres, M. Hollands, D. Koester, R. Raddi, L. G. Althaus, and A. Rebassa-Mansergas. *A&A*, 674:A213, 2023.
- M. Cantiello, J. Fuller, and L. Bildsten. *AJ*, 824(1):14, 2016.
- A. Caron, P. Bergeron, S. Blouin, and S. K. Leggett. *MNRAS*, 519(3):4529–4549, 2023.
- B. W. Carroll and D. A. Ostlie. Cambridge University Press, 2017.
- P. W. Cauley, J. Farihi, S. Redfield, S. Bachman, S. G. Parsons, and B. T. Gänsicke. *ApJ Letters*, 852(2):L22, 2018.
- J. Cepa, M. Aguiar, V. G. Escalera, I. Gonzalez-Serrano, E. Joven-Alvarez, et al. In Masanori Iye and Alan F. Moorwood, editors, *Optical and IR Telescope Instrumentation and Detectors*, volume 4008 of *Society of Photo-Optical Instrumentation Engineers (SPIE) Conference Series*, pages 623–631, 2000.
- J. Cepa, M. Aguiar-Gonzalez, J. Bland-Hawthorn, H. Castaneda, F. J. Cobos, et al. In Masanori Iye and Alan F. M. Moorwood, editors, *Instrument Design and Performance for Optical/Infrared Ground-based Telescopes*, volume 4841 of *Society of Photo-Optical Instrumentation Engineers (SPIE) Conference Series*, pages 1739–1749, 2003.

- K. C. Chambers, E. A. Magnier, N. Metcalfe, H. A. Flewelling, M. E. Huber, et al. *arXiv e-prints*, art. arXiv:1612.05560, 2016.
- S. Chandrasekhar. *ApJ*, 74:81, 1931.
- P. Chayer, G. Fontaine, and F. Wesemael. *ApJ Supplement*, 99:189, 1995.
- S. Cheng, J. D. Cummings, and B. Ménard. *AJ*, 886(2):100, 2019.
- C. Chiappini, I. Minchev, E. Starkenburg, F. Anders, N. Gentile Fusillo, et al. *The Messenger*, 175:30–34, 2019.
- J. Choi, A. Dotter, C. Conroy, M. Cantiello, B. Paxton, and B. D. Johnson. *ApJ*, 823(2):102, 2016.
- J. C. Clemens, J. A. Crain, and R. Anderson. In Alan F. M. Moorwood and Masanori Iye, editors, *Ground-based Instrumentation for Astronomy*, volume 5492 of *Society of Photo-Optical Instrumentation Engineers (SPIE) Conference Series*, pages 331–340, 2004.
- A. P. Cooper, S. E. Koposov, C. Allende Prieto, C. J. Manser, N. Kizhuprakkat, et al. *AJ*, 947(1):37, 2023.
- A. H. Córscico, L. G. Althaus, M. M. Miller Bertolami, and S. O. Kepler. *The A&A Review*, 27(1):7, 2019.
- S. Coutu, P. Dufour, P. Bergeron, S. Blouin, E. Loranger, N. F. Allard, and B. H. Dunlap. *AJ*, 885(1):74, 2019.
- J. R. Crepp, J. A. Johnson, A. W. Howard, G. W. Marcy, A. Gianninas, M. Kilic, and J. T. Wright. *AJ*, 774(1):1, 2013.
- J. R. Crepp, E. J. Gonzales, B. P. Bowler, F. Morales, J. Stone, et al. *AJ*, 864(1):42, 2018.
- E. Cukanovaite, P.-E. Tremblay, P. Bergeron, B. Freytag, H.-G. Ludwig, and M. Steffen. *MNRAS*, 501(4):5274–5293, 2021.
- E. Cukanovaite, P.-E. Tremblay, S. Toonen, K. D. Temmink, C. J. Manser, M. W. O’Brien, and J. McCleery. *MNRAS*, 522(2):1643–1661, 2023.
- J. D. Cummings, J. S. Kalirai, P.-E. Tremblay, and E. Ramirez-Ruiz. *AJ*, 807(1):90, 2015.
- J. D. Cummings, J. S. Kalirai, P.-E. Tremblay, E. Ramirez-Ruiz, and J. Choi. *AJ*, 866(1):21, 2018.

- T. Cunningham, P.-E. Tremblay, B. Freytag, H.-G. Ludwig, and D. Koester. *MNRAS*, 488 (2):2503–2522, 2019.
- T. Cunningham, P.-E. Tremblay, N. P. Gentile Fusillo, M. Hollands, and E. Cukanovaite. *MNRAS*, 492(3):3540–3552, 2020.
- T. Cunningham, P.-E. Tremblay, E. B. Bauer, O. Toloza, E. Cukanovaite, D. Koester, J. Farihi, B. Freytag, B. T. Gänsicke, H.-G. Ludwig, and D. Veras. *MNRAS*, 503(2): 1646–1667, 2021.
- T. Cunningham, P. J. Wheatley, P.-E. Tremblay, B. T. Gänsicke, G. W. King, O. Toloza, and D. Veras. *Nature*, 602(7896):219–222, 2022.
- T. Cunningham, P.-E. Tremblay, and M. W. O’Brien. *MNRAS*, 527(2):3602–3611, 2024.
- G. Dalton, S. Trager, D. C. Abrams, P. Bonifacio, J. A. L. Aguerri, et al. In *Society of Photo-Optical Instrumentation Engineers (SPIE) Conference Series*, volume 11447 of *Society of Photo-Optical Instrumentation Engineers (SPIE) Conference Series*, page 1144714, 2020.
- F. D’Antona and I. Mazzitelli. *Annual Rev. Astron. Astrophys.*, 28:139–181, 1990.
- R. S. de Jong, O. Agertz, A. A. Berbel, J. Aird, D. A. Alexander, et al. *The Messenger*, 175: 3–11, 2019.
- J. H. Debes and S. Sigurdsson. *ApJ*, 572(1):556–565, 2002.
- P. Debye. *Annalen der Physik*, 344(14):789–839, 1912.
- X. Delfosse, T. Forveille, J. L. Beuzit, S. Udry, M. Mayor, and C. Perrier. *A&A*, 344: 897–910, 1999.
- R. F. Díaz, A. Santerne, J. Sahlmann, G. Hébrard, A. Eggenberger, et al. *A&A*, 538:A113, 2012.
- T. Döhning. In Manuel Filipe P. C. M. Martins Costa, editor, *Society of Photo-Optical Instrumentation Engineers (SPIE) Conference Series*, volume 10453 of *Society of Photo-Optical Instrumentation Engineers (SPIE) Conference Series*, page 104530I, 2017.
- A. Dotter. *ApJ Supplement Series*, 222(1):8, 2016.
- A. E. Doyle, B. Klein, H. E. Schlichting, and E. D. Young. *ApJ*, 901(1):10, 2020.
- A. E. Doyle, S. J. Desch, and E. D. Young. *ApJ, Letters*, 907(2):L35, 2021.

- A. E. Doyle, B. L. Klein, P. Dufour, C. Melis, B. Zuckerman, et al. *AJ*, 950(2):93, 2023.
- S. Dreizler and K. Werner. *A&A*, 314:217–232, 1996.
- P. Dufour, P. Bergeron, and G. Fontaine. *AJ*, 627(1):404–417, 2005.
- P. Dufour, P. Bergeron, J. Liebert, H. C. Harris, G. R. Knapp, S. F. Anderson, P. B. Hall, M. A. Strauss, M. J. Collinge, and M. C. Edwards. *ApJ*, 663(2):1291–1308, 2007a.
- P. Dufour, J. Liebert, G. Fontaine, and N. Behara. *Nature*, 450(7169):522–524, 2007b.
- P. Dufour, S. Blouin, S. Coutu, M. Fortin-Archambault, C. Thibeault, P. Bergeron, and G. Fontaine. In P.-E. Tremblay, B. Gänsicke, and T. Marsh, editors, *20th European White Dwarf Workshop*, volume 509 of *Astronomical Society of the Pacific Conference Series*, page 3, 2017.
- B. H. Dunlap and J. C. Clemens. In P. Dufour, P. Bergeron, and G. Fontaine, editors, *19th European Workshop on White Dwarfs*, volume 493 of *Astronomical Society of the Pacific Conference Series*, page 547, 2015.
- J. Dupuis, G. Fontaine, C. Pelletier, and F. Wesemael. *ApJ Supplement*, 84:73, 1993.
- J. Dupuis, S. Vennes, S. Bowyer, A. K. Pradhan, and P. Thejll. In *American Astronomical Society Meeting Abstracts #184*, volume 184 of *American Astronomical Society Meeting Abstracts*, page 29.01, 1994.
- K. El-Badry. *New Astronomy Reviews*, 98:101694, 2024.
- K. El-Badry, H.-W. Rix, and D. R. Weisz. *ApJ, Letters*, 860(2):L17, 2018.
- K. El-Badry, H.-W. Rix, and T. M. Heintz. *MNRAS*, 506(2):2269–2295, 2021.
- A. K. Elms, P.-E. Tremblay, B. T. Gänsicke, D. Koester, M. A. Hollands, N. P. Gentile Fusillo, T. Cunningham, and K. Apps. *MNRAS*, 517(3):4557–4574, 2022.
- A. K. Elms, P.-E. Tremblay, B. T. Gänsicke, A. Swan, C. Melis, et al. *MNRAS*, 524(4):4996–5015, 2023.
- A. K. Elms, N. P. Gentile Fusillo, P.-E. Tremblay, R. C. Bohlin, M. A. Hollands, S. Sahu, M. W. O’Brien, S. Deustua, and T. Cunningham. *MNRAS*, 534(3):2758–2782, 2024.
- D. Fabricant, P. Cheimets, N. Caldwell, and J. Geary. *PASP*, 110(743):79–85, 1998.
- S. B. Fajardo-Acosta, J. D. Kirkpatrick, A. C. Schneider, M. C. Cushing, D. Stern, et al. *AJ*, 832(1):62, 2016.

- N. J. Fantin, P. Côté, A. W. McConnachie, P. Bergeron, J.-C. Cuillandre, et al. *AJ*, 887(2): 148, 2019.
- J. Farihi. *New Astronomy Review*, 71:9–34, 2016.
- J. Farihi, M. Jura, and B. Zuckerman. *ApJ*, 694(2):805–819, 2009.
- J. Farihi, B. T. Gänsicke, M. C. Wyatt, J. Girven, J. E. Pringle, and A. R. King. *MNRAS*, 424(1):464–471, 2012.
- J. Farihi, Howard E. Bond, P. Dufour, N. Haghhighipour, G. H. Schaefer, J. B. Holberg, M. A. Barstow, and M. R. Burleigh. *MNRAS*, 430(1):652–660, 2013.
- J. Farihi, J. J. Hermes, T. R. Marsh, A. J. Mustill, M. C. Wyatt, et al. *MNRAS*, 511(2): 1647–1666, 2022.
- J. Farihi, P. Dufour, and T. G. Wilson. *MNRAS*, 530(4):4446–4460, 2024a.
- J. Farihi, A. Robert, and N. Walters. *MNRAS*, 529(1):L164–L168, 2024b.
- J. Farihi, K. Y. L. Su, C. Melis, S. J. Kenyon, A. Swan, S. Redfield, M. C. Wyatt, and J. H. Debes. *ApJ,L*, 981(1):L5, 2025.
- L. Ferrario, S. Vennes, D. T. Wickramasinghe, J. A. Bailey, and D. J. Christian. *MNRAS*, 292(1):205–217, 1997.
- L. Ferrario, D. de Martino, and B. T. Gänsicke. *ASR*, 191(1-4):111–169, 2015.
- L. Ferrario, D. Wickramasinghe, and A. Kawka. *ASR*, 66(5):1025–1056, 2020.
- C. Flammarion. *Astronomical register*, 15:186–189, 1877.
- G. Fontaine and P. Brassard. *PASP*, 120(872):1043, 2008.
- G. Fontaine, P. Brassard, and P. Bergeron. *PASP*, 113(782):409–435, 2001.
- J. Fraunhofer. *Annalen der Physik*, 56(7):264–313, 1817.
- W. Freudling, M. Romaniello, D. M. Bramich, P. Ballester, V. Forchi, C. E. García-Daból, S. Moehler, and M. J. Neeser. *A&A*, 559:A96, 2013.
- S. Friedrich, R. Oestreicher, and W. Schweizer. *A&A*, 309:227–234, 1996.
- Gaia Collaboration, T. Prusti, J. H. J. de Bruijne, A. G. A. Brown, A. Vallenari, C. Babusiaux, et al. *A&A*, 595:A1, 2016.

- Gaia Collaboration, C. Babusiaux, F. van Leeuwen, M. A. Barstow, C. Jordi, A. Vallenari, et al. *A&A*, 616:A10, 2018.
- Gaia Collaboration, A. G. A. Brown, A. Vallenari, T. Prusti, J. H. J. de Bruijne, C. Babusiaux, et al. *A&A*, 649:A1, 2021a.
- Gaia Collaboration, R. L. Smart, L. M. Sarro, J. Rybizki, C. Reyl  , et al. *A&A*, 649:A6, 2021b.
- Gaia Collaboration, A. Vallenari, A. G. A. Brown, T. Prusti, J. H. J. de Bruijne, F. Arenou, et al. *A&A*, 674:A1, 2023.
- B. T. G  nsicke, T. R. Marsh, J. Southworth, and A. Rebassa-Mansergas. *Science*, 314(5807):1908, 2006.
- B. T. G  nsicke, T. R. Marsh, and J. Southworth. *MNRAS*, 380(1):L35–L39, 2007.
- B. T. G  nsicke, D. Koester, T. R. Marsh, A. Rebassa-Mansergas, and J. Southworth. *MNRAS*, 391(1):L103–L107, 2008.
- B. T. G  nsicke, D. Koester, J. Farihi, J. Girven, S. G. Parsons, and E. Breedt. *MNRAS*, 424(1):333–347, 2012.
- B. T. G  nsicke, D. Koester, J. Farihi, and O. Toloza. *MNRAS*, 481(4):4323–4331, 2018.
- B. T. G  nsicke, M. R. Schreiber, O. Toloza, N. P. Gentile Fusillo, D. Koester, and C. J. Manser. *Nature*, 576(7785):61–64, 2019.
- E. Garc  a-Berro, P. Lor  n-Aguilar, G. Aznar-Sigu  n, S. Torres, J. Camacho, et al. *ApJ*, 749(1):25, 2012.
- E. M. Garc  a-Zamora, S. Torres, and A. Rebassa-Mansergas. *A&A*, 679:A127, 2023.
- C. Genest-Beaulieu and P. Bergeron. *AJ*, 871(2):169, 2019.
- N. P. Gentile Fusillo, P.-E. Tremblay, B. T. G  nsicke, C. J. Manser, T. Cunningham, et al. *MNRAS*, 482(4):4570–4591, 2019.
- N. P. Gentile Fusillo, P.-E. Tremblay, R. C. Bohlin, S. E. Deustua, and J. S. Kalirai. *MNRAS*, 491(3):3613–3623, 2020.
- N. P. Gentile Fusillo, P.-E. Tremblay, E. Cukanovaite, A. Vorontseva, R. Lallement, M. Hollands, B. T. G  nsicke, K. B. Burdge, J. McCleery, and S. Jordan. *MNRAS*, 508(3):3877–3896, 2021.

- N. Giammichele, P. Bergeron, and P. Dufour. *ApJ, Supplement*, 199(2):29, 2012.
- A. Gianninas, P. Bergeron, and M. T. Ruiz. *AJ*, 743(2):138, 2011.
- D. R. Gies, K. V. Lester, L. Wang, A. Couperus, K. Shepard, et al. *AJ*, 902(1):25, 2020.
- S. Ginzburg, J. Fuller, A. Kawka, and I. Caiazzo. *MNRAS*, 514(3):4111–4119, 2022.
- J. Girven, C. S. Brinkworth, J. Farihi, B. T. Gänsicke, D. W. Hoard, T. R. Marsh, and D. Koester. *AJ*, 749(2):154, 2012.
- J. E. Gizis. *AJ*, 115(5):2053–2058, 1998.
- E. C. Gonzales, B. Burningham, J. K. Faherty, N. K. Lewis, C. Visscher, and M. Marley. *AJ*, 938(1):56, 2022.
- P. B. Hall and A. J. Maxwell. *AJ*, 678(2):1292–1297, 2008.
- F. Hardy, P. Dufour, and S. Jordan. *MNRAS*, 520(4):6111–6134, 2023a.
- F. Hardy, P. Dufour, and S. Jordan. *MNRAS*, 520(4):6135–6158, 2023b.
- J. H. D. Harrison, A. Bonsor, M. Kama, A. M. Buchan, S. Blouin, and D. Koester. *MNRAS*, 504(2):2853–2867, 2021.
- T. M. Heintz, J. J. Hermes, K. El-Badry, C. Walsh, J. L. van Saders, C. E. Fields, and D. Koester. *AJ*, 934(2):148, 2022.
- T. J. Henry, W.-C. Jao, J. G. Winters, S. B. Dieterich, C. T. Finch, et al. *AJ*, 155(6):265, 2018.
- M. S. Hernandez, M. R. Schreiber, J. D. Landstreet, S. Bagnulo, S. G. Parsons, M. Chavarria, O. Toloza, and K. J. Bell. *MNRAS*, 528(4):6056–6074, 2024.
- W. Herschel. *Philosophical Transactions of the Royal Society of London Series I*, 75:40–126, 1785.
- L. A. Hirsch, D. R. Ciardi, A. W. Howard, G. W. Marcy, G. Ruane, et al. *AJ*, 878(1):50, 2019.
- J. B. Holberg. *Journal for the History of Astronomy*, 40(2):137–154, 2009.
- J. B. Holberg and P. Bergeron. *AJ*, 132(3):1221–1233, 2006.
- J. B. Holberg, T. D. Oswalt, and E. M. Sion. *AJ*, 571(1):512–518, 2002.

- J. B. Holberg, E. M. Sion, T. Oswalt, G. P. McCook, S. Foran, and J. P. Subasavage. *AJ*, 135 (4):1225–1238, 2008.
- J. B. Holberg, T. D. Oswalt, E. M. Sion, M. A. Barstow, and M. R. Burleigh. *MNRAS*, 435 (3):2077–2091, 2013.
- J. B. Holberg, T. D. Oswalt, E. M. Sion, and G. P. McCook. *MNRAS*, 462(3):2295–2318, 2016.
- M. A. Hollands, D. Koester, V. Alekseev, E. L. Herbert, and B. T. Gänsicke. *MNRAS*, 467 (4):4970–5000, 2017.
- M. A. Hollands, B. T. Gänsicke, and D. Koester. *MNRAS*, 477(1):93–111, 2018a.
- M. A. Hollands, P.-E. Tremblay, B. T. Gänsicke, N. P. Gentile Fusillo, and S. Toonen. *MNRAS*, 480(3):3942–3961, 2018b.
- M. A. Hollands, P.-E. Tremblay, B. T. Gänsicke, D. Koester, and N. P. Gentile Fusillo. *Nature Astronomy*, 5:451–459, 2021.
- M. A. Hollands, P.-E. Tremblay, B. T. Gänsicke, and D. Koester. *MNRAS*, 511(1):71–82, 2022.
- M. A. Hollands, S. P. Littlefair, and S. G. Parsons. *MNRAS*, 527(3):9061–9117, 2024.
- J. R. Hurley, O. R. Pols, and C. A. Tout. *MNRAS*, 315(3):543–569, 2000.
- I. Iben, Jr. *Annual Review of A&A*, 12:215–256, 1974.
- J. Isern, E. García-Berro, B. Külebi, and P. Lorén-Aguilar. *ApJ, Letters*, 836(2):L28, 2017.
- N. Ivanova, S. Justham, X. Chen, O. De Marco, C. L. Fryer, et al. *A&A Rev.*, 21:59, 2013.
- W.-C. Jao, T. J. Henry, J. P. Subasavage, J. G. Winters, D. R. Gies, A. R. Riedel, and P. A. Ianna. *AJ*, 147(1):21, 2014.
- J. H. Jeans. *Philosophical Transactions of the Royal Society of London Series A*, 199:1–53, 1902.
- F. M. Jiménez-Esteban, S. Torres, A. Rebassa-Mansergas, G. Skorobogatov, E. Solano, C. Cantero, and C. Rodrigo. *MNRAS*, 480(4):4505–4518, 2018.
- F. M. Jiménez-Esteban, S. Torres, A. Rebassa-Mansergas, P. Cruz, R. Murillo-Ojeda, E. Solano, C. Rodrigo, and M. E. Camisassa. *MNRAS*, 518(4):5106–5122, 2023.

- M. Jura. *ApJ, Letters*, 584(2):L91–L94, 2003.
- M. Jura. *AJ*, 135(5):1785–1792, 2008.
- M. Jura and S. Xu. *AJ*, 140(5):1129–1136, 2010.
- M. Jura, J. Farihi, and B. Zuckerman. *ApJ*, 663(2):1285–1290, 2007a.
- M. Jura, J. Farihi, B. Zuckerman, and E. E. Becklin. *AJ*, 133(5):1927–1933, 2007b.
- M. Jura, M. P. Muno, J. Farihi, and B. Zuckerman. *AJ*, 699(2):1473–1479, 2009.
- B. C. Kaiser, J. C. Clemens, S. Blouin, P. Dufour, R. J. Hegedus, J. S. Reding, and A. Bédard. *Science*, 371(6525):168–172, 2021.
- E. M. Kantor and M. E. Gusakov. *MNRAS*, 381(4):1702–1710, 2007.
- M. L. Kao, K. Hawkins, L. K. Rogers, A. Bonsor, B. H. Dunlap, J. L. Sanders, M. H. Montgomery, and D. E. Winget. *ApJ*, 970(2):181, 2024.
- A. I. Karakas. In A. A. Zijlstra, F. Lykou, I. McDonald, and E. Lagadec, editors, *Asymmetric Planetary Nebulae 5 Conference*, page 144, 2011.
- W. Kausch, S. Noll, A. Smette, S. Kimeswenger, M. Barden, C. Szyszka, A. M. Jones, H. Sana, H. Horst, and F. Kerber. *A&A*, 576:A78, 2015.
- A. Kawka and S. Vennes. *AJ*, 643(1):402–415, 2006.
- A. Kawka and S. Vennes. *A&A*, 532:A7, 2011.
- A. Kawka and S. Vennes. *MNRAS*, 425(2):1394–1412, 2012.
- S. C. Keller, B. P. Schmidt, M. S. Bessell, P. G. Conroy, P. Francis, et al. *PASA*, 24(1):1–12, 2007.
- J. C. Kemp, J. B. Swedlund, J. D. Landstreet, and J. R. P. Angel. *ApJ, Letters*, 161:L77, 1970.
- E. M. R. Kempton and H. A. Knutson. *Reviews in Mineralogy and Geochemistry*, 90(1):411–464, 2024.
- S. O. Kepler, A. F. M. da Costa, O. Giovannini, and D. Koester. *Baltic Astronomy*, 9:125–132, 2000.
- M. Kilic, S. K. Leggett, P.-E. Tremblay, T. von Hippel, P. Bergeron, H. C. Harris, J. A. Munn, K. A. Williams, E. Gates, and J. Farihi. *ApJ, Supplement*, 190(1):77–99, 2010.

- M. Kilic, A. Bédard, P. Bergeron, and A. Kosakowski. *MNRAS*, 493(2):2805–2816, 2020a.
- M. Kilic, P. Bergeron, A. Kosakowski, W. R. Brown, M. A. Agüeros, and S. Blouin. *AJ*, 898(1):84, 2020b.
- M. Kilic, A. Bédard, and P. Bergeron. *MNRAS*, 502(4):4972–4980, 2021.
- M. Kilic, P. Bergeron, S. Blouin, G. Jewett, W. R. Brown, and A. Moss. *ApJ*, 965(2):159, 2024.
- M. Kilic, P. Bergeron, S. Blouin, A. Moss, W. R. Brown, A. Bédard, G. Jewett, and M. A. Agüeros. *ApJ*, 979(2):157, 2025.
- J. D. Kirkpatrick, K. Kellogg, A. C. Schneider, S. Fajardo-Acosta, M. C. Cushing, et al. *ApJ, Supplement*, 224(2):36, 2016.
- B. Klein, M. Jura, D. Koester, B. Zuckerman, and C. Melis. *AJ*, 709(2):950–962, 2010.
- B. Klein, M. Jura, D. Koester, and B. Zuckerman. *AJ*, 741(1):64, 2011.
- B. L. Klein, A. E. Doyle, B. Zuckerman, P. Dufour, S. Blouin, C. Melis, A. J. Weinberger, and E. D. Young. *ApJ*, 914(1):61, 2021.
- S. J. Kleinman, S. O. Kepler, D. Koester, I. Pelisoli, V. Peçanha, et al. *ApJ, Supplement*, 204(1):5, 2013.
- D. Koester. In Gary Wegner, editor, *IAU Colloq. 114: White Dwarfs*, volume 328, page 206. Springer Berlin, Heidelberg, 1989.
- D. Koester. *A&A*, 498(2):517–525, 2009.
- D. Koester. *Memoire della Societa Astronomica Italiana*, 81:921–931, 2010.
- D. Koester and G. Chanmugam. *Reports on Progress in Physics*, 53(7):837–915, 1990.
- D. Koester and S. O. Kepler. *A&A*, 583:A86, 2015.
- D. Koester and S. O. Kepler. *A&A*, 628:A102, 2019.
- D. Koester, H. Schulz, and V. Weidemann. *A&A*, 76:262–275, 1979.
- D. Koester, R. Napiwotzki, N. Christlieb, H. Drechsel, H. J. Hagen, et al. *A&A*, 378: 556–568, 2001.
- D. Koester, J. Girven, B. T. Gänsicke, and P. Dufour. *A&A*, 530:A114, 2011.

- D. Koester, B. T. Gänsicke, and J. Farihi. *A&A*, 566:A34, 2014.
- J. A. Kollmeier, G. Zasowski, H.-W. Rix, M. Johns, S. F. Anderson, et al. *arXiv e-prints*, art. arXiv:1711.03234, 2017.
- V. Korol, V. Belokurov, and S. Toonen. *MNRAS*, 515(1):1228–1246, 2022.
- P. M. Kowalski and D. Saumon. *ApJ, Letters*, 651(2):L137–L140, 2006.
- K. M. Kratter. In L. Schmidtbreick, M. R. Schreiber, and C. Tappert, editors, *Evolution of Compact Binaries*, volume 447 of *Astronomical Society of the Pacific Conference Series*, page 47, 2011.
- B. Külebi, S. Jordan, F. Euchner, B. T. Gänsicke, and H. Hirsch. *A&A*, 506(3):1341–1350, 2009.
- B. Külebi, S. Jordan, E. Nelan, U. Bastian, and M. Altmann. *A&A*, 524:A36, 2010.
- S. S. Kumar. *AJ*, 67:579, 1962.
- T. Kupfer, V. Korol, T. B. Littenberg, S. Shah, E. Savalle, et al. *ApJ*, 963(2):100, 2024.
- F. Kupka, F. Zaussinger, and M. H. Montgomery. *MNRAS*, 474(4):4660–4671, 2018.
- F. Lagos, M. R. Schreiber, S. G. Parsons, O. Toloza, B. T. Gänsicke, et al. *MNRAS*, 512(2):2625–2635, 2022.
- J. D. Landstreet. In Georges Meynet, Cyril Georgy, José Groh, and Philippe Stee, editors, *New Windows on Massive Stars*, volume 307 of *IAU Symposium*, pages 311–320, 2015.
- J. D. Landstreet and S. Bagnulo. *A&A*, 628:A1, 2019.
- J. D. Landstreet, E. Villaver, and S. Bagnulo. *ApJ*, 952(2):129, 2023.
- S. K. Leggett, C. V. Morley, M. S. Marley, and D. Saumon. *AJ*, 799(1):37, 2015.
- J. Liebert. *ApJ*, 210:715–720, 1976.
- J. Liebert, P. Bergeron, G. D. Schmidt, and R. A. Saffer. *AJ*, 418:426, 1993.
- J. Liebert, P. Bergeron, and J. B. Holberg. *ApJ, Supplement*, 156(1):47–68, 2005.
- M. A. Limbach, A. Vanderburg, A. Venner, S. Blouin, K. B. Stevenson, et al. *ApJ, Letters*, 973(1):L11, 2024.
- M. M. Limoges, S. Lépine, and P. Bergeron. *AJ*, 145(5):136, 2013.

- M. M. Limoges, P. Bergeron, and S. Lépine. *ApJ, Supplement*, 219(2):19, 2015.
- L. Lindegren, J. Hernández, A. Bombrun, S. Klioner, U. Bastian, et al. *A&A*, 616:A2, 2018.
- G. Lodato. *New Astronomy Reviews*, 52(2-5):21–41, 2008.
- K. Lodders. *arXiv e-prints*, art. arXiv:1912.00844, 2019.
- C. López-Sanjuan, P.-E. Tremblay, A. Ederoclite, H. Vázquez Ramió, J. M. Carrasco, et al. *A&A*, 658:A79, 2022a.
- C. López-Sanjuan, P.-E. Tremblay, A. Ederoclite, H. Vázquez Ramió, A. J. Cenarro, et al. *A&A*, 665:A151, 2022b.
- K. L. Luhman, A. J. Burgasser, and J. J. Bochanski. *ApJ, Letters*, 730(1):L9, 2011.
- W. J. Luyten. *Lick Observatory Bulletin*, 11:1–32, 1923.
- G. N. Mace, A. W. Mann, B. A. Skiff, C. Sneden, J. D. Kirkpatrick, et al. *AJ*, 854(2):145, 2018.
- N. Madhusudhan. *Annual Review of A&A*, 57:617–663, 2019.
- C. J. Manser, B. T. Gänsicke, T. R. Marsh, D. Veras, D. Koester, E. Breedt, A. F. Pala, S. G. Parsons, and J. Southworth. *MNRAS*, 455(4):4467–4478, 2016.
- C. J. Manser, B. T. Gänsicke, K. Inight, A. Robert, S. Ahlen, et al. *MNRAS*, 521(4):4976–4994, 2023.
- C. J. Manser, P. Izquierdo, B. T. Gänsicke, A. Swan, D. Koester, et al. *MNRAS*, 535(1):254–289, 2024.
- P. Marigo and L. Girardi. *A&A*, 469(1):239–263, 2007.
- T. R. Marsh, V. S. Dhillon, and S. R. Duck. *MNRAS*, 275:828, 1995.
- J. L. Marshall, S. Badsurles, I. B. Thompson, S. A. Shectman, B. C. Bigelow, et al. In Ian S. McLean and Mark M. Casali, editors, *Ground-based and Airborne Instrumentation for Astronomy II*, volume 7014 of *Society of Photo-Optical Instrumentation Engineers (SPIE) Conference Series*, page 701454, 2008.
- D. C. Martin, J. Fanson, D. Schiminovich, P. Morrissey, P. G. Friedman, et al. *ApJ, Letters*, 619(1):L1–L6, 2005.
- J. McCleery, P.-E. Tremblay, N. P. Gentile Fusillo, M. A. Hollands, B. T. Gänsicke, et al. *MNRAS*, 499(2):1890–1908, 2020.

- A. M. Meisner, J. K. Faherty, J. D. Kirkpatrick, A. C. Schneider, D. Caselden, et al. *AJ*, 899(2):123, 2020.
- P. Montegriffo, F. De Angeli, R. Andrae, M. Riello, E. Pancino, et al. *arXiv e-prints*, art. arXiv:2206.06205, 2022.
- H. Monteiro, W.-C. Jao, T. Henry, J. Subasavage, and T. Beaulieu. *AJ*, 638(1):446–453, 2006.
- A. Moss, T. von Hippel, E. Robinson, K. El-Badry, D. C. Stenning, et al. *AJ*, 929(1):26, 2022.
- J. Munday, I. Pelisoli, P.-E. Tremblay, T. R. Marsh, G. Nelemans, et al. *MNRAS*, 532(2): 2534–2556, 2024.
- J. Munday, R. Pakmor, I. Pelisoli, D. Jones, S. Sahu, et al. *Nature Astronomy*, 2025.
- R. Napiwotzki, C. A. Karl, T. Lisker, S. Catalán, H. Drechsel, et al. *A&A*, 638:A131, 2020.
- I. Newton. *Philosophical Transactions of the Royal Society of London*, 6(80):3075–3087, 1672.
- L. R. Nittler, T. J. McCoy, P.-E. Clark, M. E. Murphy, J. I. Trombka, and E. Jarosewich. *Antarctic Meteorite Research*, 17:231, 2004.
- L. Noack, C. Dorn, and P. Baumeister. *arXiv e-prints*, art. arXiv:2410.08055, 2024.
- J. Nordhaus, S. Wellons, D. S. Spiegel, B. D. Metzger, and E. G. Blackman. *Proceedings of the National Academy of Science*, 108(8):3135–3140, 2011.
- M. W. O’Brien, P.-E. Tremblay, N. P. Gentile Fusillo, M. A. Hollands, B. T. Gänsicke, et al. *MNRAS*, 518(2):3055–3073, 2023.
- M. W. O’Brien, P.-E. Tremblay, B. L. Klein, D. Koester, C. Melis, et al. *MNRAS*, 527(3): 8687–8705, 2024.
- M. W. O’Brien, P.-E. Tremblay, B. L. Klein, C. Melis, D. Koester, et al. *MNRAS*, 539(1): 171–184, 2025.
- D. O’Donoghue, D. Kilkenny, C. Koen, N. Hambly, H. MacGillivray, and R. S. Stobie. *MNRAS*, 431(1):240–251, 2013.
- J. B. Oke. *ApJ Supplement*, 27:21, 1974.

- G. Ourique, S. O. Kepler, A. D. Romero, T. S. Klippel, and D. Koester. *MNRAS*, 492(4): 5003–5010, 2020.
- C. Paquette, C. Pelletier, G. Fontaine, and G. Michaud. *ApJ Supplement*, 61:197, 1986.
- W. Pauli. *Zeitschrift fur Physik*, 31(1):765–783, 1925.
- C. Pelletier, G. Fontaine, F. Wesemael, G. Michaud, and G. Wegner. *AJ*, 307:242, 1986.
- M. A. C. Perryman, L. Lindegren, J. Kovalevsky, E. Hoeg, U. Bastian, et al. *A&A*, 323: L49–L52, 1997.
- J. L. Provencal, H. L. Shipman, D. Koester, F. Wesemael, and P. Bergeron. *AJ*, 568(1): 324–334, 2002.
- A. Putney. *ApJ, Supplement*, 112(2):527–556, 1997.
- D. Qiu, H.-J. Tian, X.-D. Wang, J.-L. Nie, T. von Hippel, G.-C. Liu, M. Foesneau, and H.-W. Rix. *ApJ, Supplement*, 253(2):58, 2021.
- R. Raddi, B. T. Gänsicke, D. Koester, J. Farihi, J. J. Hermes, S. Scaringi, E. Breedt, and J. Girven. *MNRAS*, 450(2):2083–2093, 2015.
- R. Raddi, N. P. Gentile Fusillo, A. F. Pala, J. J. Hermes, B. T. Gänsicke, et al. *MNRAS*, 472 (4):4173–4192, 2017.
- A. Rebassa-Mansergas, E. Solano, F. M. Jiménez-Esteban, S. Torres, C. Rodrigo, et al. *MNRAS*, 506(4):5201–5211, 2021.
- A. Recio-Blanco, P. de Laverny, P. A. Palicio, G. Kordopatis, M. A. Álvarez, et al. *A&A*, 674:A29, 2023.
- I. N. Reid and J. E. Gizis. *PASP*, 117(833):676–698, 2005.
- H.-W. Rix, D. W. Hogg, D. Boubert, A. G. A. Brown, A. Casey, R. Drimmel, A. Everall, M. Foesneau, and A. M. Price-Whelan. *AJ*, 162(4):142, 2021.
- M. Rocchetto, J. Farihi, B. T. Gänsicke, and C. Bergfors. *MNRAS*, 449(1):574–587, 2015.
- C. Rodrigo and E. Solano. In *XIV.0 Scientific Meeting (virtual) of the Spanish Astronomical Society*, page 182, 2020.
- C. Rodrigo, E. Solano, and A. Bayo. IVOA Working Draft 15 October 2012, 2012.
- R. D. Rohrmann, L. G. Althaus, and S. O. Kepler. *MNRAS*, 411(2):781–791, 2011.

- B. Rolland, P. Bergeron, and G. Fontaine. *AJ*, 857:56, 2018.
- R. L. Rudnick and S. Gao. *Treatise on Geochemistry*, 3:659, 2003.
- S. Sahu, B. T. Gänsicke, P.-E. Tremblay, D. Koester, J. J. Hermes, et al. *MNRAS*, 526(4): 5800–5823, 2023.
- S. Sahu, P.-E. Tremblay, R. Lallement, S. Redfield, and B. T. Gänsicke. *MNRAS*, 535(1): 1147–1162, 2024.
- D. Saumon, J. B. Holberg, and P. M. Kowalski. *AJ*, 790(1):50, 2014.
- D. Saumon, S. Blouin, and P.-E. Tremblay. *Physics Reports*, 988:1–63, 2022.
- C. Sayres, J. P. Subasavage, P. Bergeron, P. Dufour, J. R. A. Davenport, Y. AlSaiyad, and B. M. Tofflemire. *AJ*, 143(4):103, 2012.
- R. D. Scholz, M. Irwin, R. Ibata, H. Jahreiß, and O. Yu. Malkov. *A&A*, 353:958–969, 2000.
- M. R. Schreiber, D. Belloni, B. T. Gänsicke, S. G. Parsons, and M. Zorotovic. *Nature Astronomy*, 5:648–654, 2021.
- Science Software Branch at STScI. Astrophysics Source Code Library, record ascl:1207.011, 2012.
- M. J. Seaton. *MNRAS*, 132:113, 1966.
- K. J. Shen, S. Blouin, and K. Breivik. *ApJ,L*, 955(2):L33, 2023.
- B. Sibthorpe, B. Vandenbussche, J. S. Greaves, E. Pantin, G. Olofsson, et al. *A&A*, 518: L130, 2010.
- E. M. Sion, J. L. Greenstein, J. D. Landstreet, J. Liebert, H. L. Shipman, and G. A. Wegner. *AJ*, 269:253–257, 1983.
- M. F. Skrutskie, R. M. Cutri, R. Stiening, M. D. Weinberg, S. Schneider, et al. *AJ*, 131(2): 1163–1183, 2006.
- A. Smette, H. Sana, S. Noll, H. Horst, W. Kausch, S. Kimeswenger, M. Barden, C. Szyszka, A. M. Jones, A. Gallenne, J. Vinther, P. Ballester, and J. Taylor. *A&A*, 576:A77, 2015.
- E. A. Spiegel. *ApJ*, 138:216, 1963. doi: 10.1086/147628.
- J. P. Subasavage, T. J. Henry, P. Bergeron, P. Dufour, N. C. Hambly, and T. D. Beaulieu. *AJ*, 134(1):252–261, 2007.

- J. P. Subasavage, T. J. Henry, P. Bergeron, P. Dufour, and N. C. Hambly. *AJ*, 136(3): 899–908, 2008.
- J. P. Subasavage, W.-C. Jao, T. J. Henry, P. Bergeron, P. Dufour, P. A. Ianna, E. Costa, and R. A. Méndez. *AJ*, 137(6):4547–4560, 2009.
- J. P. Subasavage, W.-C. Jao, T. J. Henry, H. C. Harris, C. C. Dahn, et al. *AJ*, 154(1):32, 2017.
- M. Sun and P. Arras. *ApJ*, 858(1):14, 2018.
- A. Swan, J. Farihi, D. Koester, M. Hollands, S. Parsons, P. W. Cauley, S. Redfield, and B. T. Gänsicke. *MNRAS*, 490(1):202–218, 2019.
- A. Swan, J. Farihi, C. Melis, P. Dufour, S. J. Desch, D. Koester, and J. Guo. *MNRAS*, 526(3):3815–3831, 2023.
- K. D. Temmink, S. Toonen, E. Zapartas, S. Justham, and B. T. Gänsicke. *A&A*, 636:A31, 2020.
- W. Thomson. *The London, Edinburgh, and Dublin Philosophical Magazine and Journal of Science*, 42(281):362–377, 1871.
- S. E. Thorsett, Z. Arzoumanian, and J. H. Taylor. *ApJ, Letters*, 412:L33, 1993.
- S. Toonen, M. Hollands, B. T. Gänsicke, and T. Boekholt. *A&A*, 602:A16, 2017.
- S. Torres, P. Canals, F. M. Jiménez-Esteban, A. Rebassa-Mansergas, and E. Solano. *MNRAS*, 511(4):5462–5474, 2022.
- S. Torres, P. Cruz, R. Murillo-Ojeda, F. M. Jiménez-Esteban, A. Rebassa-Mansergas, et al. *A&A*, 677:A159, 2023.
- P.-E. Tremblay and P. Bergeron. *AJ*, 672(2):1144–1152, 2008.
- P.-E. Tremblay and P. Bergeron. *AJ*, 696(2):1755–1770, 2009.
- P.-E. Tremblay, P. Bergeron, and A. Gianninas. *AJ*, 730(2):128, 2011a.
- P.-E. Tremblay, H. G. Ludwig, M. Steffen, P. Bergeron, and B. Freytag. *A&A*, 531:L19, 2011b.
- P.-E. Tremblay, H.-G. Ludwig, M. Steffen, and B. Freytag. *A&A*, 559:A104, 2013a.
- P.-E. Tremblay, H. G. Ludwig, M. Steffen, and B. Freytag. *A&A*, 552:A13, 2013b.

- P.-E. Tremblay, S. K. Leggett, N. Lodieu, B. Freytag, P. Bergeron, J. S. Kalirai, and H. G. Ludwig. *AJ*, 788(2):103, 2014.
- P.-E. Tremblay, A. Gianninas, M. Kilic, H. G. Ludwig, M. Steffen, B. Freytag, and J. J. Hermes. *AJ*, 809(2):148, 2015.
- P.-E. Tremblay, J. Cummings, J. S. Kalirai, B. T. Gänsicke, N. Gentile Fusillo, and R. Raddi. *MNRAS*, 461(2):2100–2114, 2016.
- P.-E. Tremblay, E. Cukanovaite, N. P. Gentile Fusillo, T. Cunningham, and M. A. Hollands. *MNRAS*, 482(4):5222–5232, 2019a.
- P.-E. Tremblay, G. Fontaine, N. P. Gentile Fusillo, B. H. Dunlap, B. T. Gänsicke, et al. *Nature*, 565(7738):202–205, 2019b.
- P.-E. Tremblay, M. A. Hollands, N. P. Gentile Fusillo, J. McCleery, P. Izquierdo, et al. *MNRAS*, 497(1):130–145, 2020.
- I. L. Trierweiler, A. E. Doyle, C. Melis, K. J. Walsh, and E. D. Young. *AJ*, 936(1):30, 2022.
- I. L. Trierweiler, A. E. Doyle, and E. D. Young. *PSJ*, 4(8):136, 2023.
- K. Unglaub and I. Bues. *A&A*, 338:75–84, 1998.
- K. Unglaub and I. Bues. *A&A*, 359:1042–1058, 2000.
- W. F. van Altena, J. T. Lee, and E. D. Hoffleit. Yale University Observatory, New Haven, CT, 1995.
- E. J. M. van den Besselaar, R. Greimel, L. Morales-Rueda, G. Nelemans, J. R. Thorstensen, et al. *A&A*, 466(3):1031–1041, 2007.
- H. M. van Horn. *ApJ*, 151:227, 1968.
- F. van Leeuwen. *A&A*, 474(2):653–664, 2007.
- A. van Maanen. *PASP*, 29:258, 1917.
- Z. Vanderbosch, J. J. Hermes, E. Dennihy, B. H. Dunlap, P. Izquierdo, et al. *ApJ*, 897(2):171, 2020.
- A. Vanderburg, J. A. Johnson, S. Rappaport, A. Bieryla, J. Irwin, et al. *Nature*, 526(7574):546–549, 2015.
- A. Vanderburg, S. A. Rappaport, S. Xu, I. J. M. Crossfield, J. C. Becker, et al. *Nature*, 585(7825):363–367, 2020.

- G. Vauclair, H. Schmidt, D. Koester, and N. Allard. *A&A*, 325:1055–1062, 1997.
- A. Venner, S. Blouin, A. Bédard, and A. Vanderburg. *MNRAS*, 523(3):4624–4642, 2023.
- S. Vennes, A. Kawka, B. L. Klein, B. Zuckerman, A. J. Weinberger, and C. Melis. *MNRAS*, 527(2):3122–3138, 2024.
- D. Veras. *Oxford Research Encyclopedia of Planetary Science*, 2021.
- D. Veras and K. Heng. *MNRAS*, 496(2):2292–2308, 2020.
- D. Veras, Z. M. Leinhardt, A. Bonsor, and B. T. Gänsicke. *MNRAS*, 445(3):2244–2255, 2014.
- D. Veras, A. J. Mustill, and A. Bonsor. *Reviews in Mineralogy and Geochemistry*, 90(1): 141–170, 2024.
- J. Vernet, H. Dekker, S. D’Odorico, L. Kaper, Kjaergaard, et al. *A&A*, 536:A105, 2011.
- O. Vincent, M. A. Barstow, S. Jordan, C. Mander, P. Bergeron, and P. Dufour. *A&A*, 682: A5, 2024.
- S. S. Vogt, S. L. Allen, B. C. Bigelow, L. Bresee, B. Brown, et al. In David L. Crawford and Eric R. Craine, editors, *Instrumentation in Astronomy VIII*, volume 2198 of *Society of Photo-Optical Instrumentation Engineers (SPIE) Conference Series*, page 362, 1994.
- T. von Hippel, M. J. Kuchner, M. Kilic, F. Mullally, and W. T. Reach. *ApJ*, 662(1):544–551, 2007.
- M. Voyer, Q. Changeat, P.-O. Lagage, P. Tremblin, R. Waters, et al. *ApJ, Letters*, 982(2): L38, 2025.
- R. E. Wall, M. Kilic, P. Bergeron, B. Rolland, C. Genest-Beaulieu, and A. Gianninas. *MNRAS*, 489(4):5046–5052, 2019.
- K. Werner, N. J. Hammer, T. Nagel, T. Rauch, and S. Dreizler. In D. Koester and S. Moehler, editors, *14th European Workshop on White Dwarfs*, volume 334 of *Astronomical Society of the Pacific Conference Series*, page 165, 2005.
- D. T. Wickramasinghe and L. Ferrario. *MNRAS*, 356(4):1576–1582, 2005.
- J. T. Williams, B. T. Gänsicke, A. Swan, M. W. O’Brien, P. Izquierdo, A. M. Cutolo, and T. Cunningham. *A&A*, 691:A352, 2024.

- K. A. Williams, M. H. Montgomery, D. E. Winget, R. E. Falcon, and M. Bierwagen. *AJ*, 817(1):27, 2016.
- T. G. Wilson, J. Farihi, B. T. Gänsicke, and A. Swan. *MNRAS*, 487(1):133–146, 2019.
- D. E. Winget, E. L. Robinson, R. D. Nather, and G. Fontaine. *ApJ, Letters*, 262:L11–L15, 1982.
- D. E. Winget, D. J. Sullivan, T. S. Metcalfe, S. D. Kawaler, and M. H. Montgomery. *ApJ, Letters*, 602(2):L109–L112, 2004.
- J. G. Winters, J. M. Irwin, D. Charbonneau, D. W. Latham, A. M. Medina, et al. *AJ*, 159(6):290, 2020.
- B. Wolff, D. Koester, and J. Liebert. *A&A*, 385:995–1007, 2002.
- E. L. Wright, P. R. M. Eisenhardt, A. K. Mainzer, M. E. Ressler, R. M. Cutri, et al. *AJ*, 140(6):1868–1881, 2010.
- M. C. Wyatt, J. Farihi, J. E. Pringle, and A. Bonsor. *MNRAS*, 439(4):3371–3391, 2014.
- E. M. Zeidler-K. T., V. Weidemann, and D. Koester. *A&A*, 155:356–370, 1986.
- Z. Zhang, M. C. Liu, J. J. Hermes, E. A. Magnier, M. S. Marley, et al. *AJ*, 891(2):171, 2020.
- M. Zorotovic, M. R. Schreiber, B. T. Gänsicke, A. Rebassa-Mansergas, A. Nebot Gómez-Morán, et al. *A&A*, 536:L3, 2011.
- B. Zuckerman. *ApJ, Letters*, 791(2):L27, 2014.
- B. Zuckerman and E. E. Becklin. *Nature*, 330(6144):138–140, 1987.
- B. Zuckerman, E. E. Becklin, B. A. Macintosh, and T. Bida. *AJ*, 113:764, 1997.
- B. Zuckerman, D. Koester, I. N. Reid, and M. Hünsch. *AJ*, 596(1):477–495, 2003.
- B. Zuckerman, D. Koester, C. Melis, B. M. Hansen, and M. Jura. *AJ*, 671(1):872–877, 2007.